



Roger Barba, Isolda (2017) *Investigations into electrochemical water splitting*. PhD thesis.

<http://theses.gla.ac.uk/8228/>

Copyright and moral rights for this work are retained by the author

A copy can be downloaded for personal non-commercial research or study, without prior permission or charge

This work cannot be reproduced or quoted extensively from without first obtaining permission in writing from the author

The content must not be changed in any way or sold commercially in any format or medium without the formal permission of the author

When referring to this work, full bibliographic details including the author, title, awarding institution and date of the thesis must be given

Enlighten:Theses
<http://theses.gla.ac.uk/>
theses@gla.ac.uk

Investigations into electrochemical water splitting



Isolda Roger Barba

Submitted in fulfilment of the requirements for the
Degree of Doctor of Philosophy

School of Chemistry
College of Science and Engineering
University of Glasgow

May, 2017

Abstract

The work detailed in this thesis is organized in the following manner: In Chapter 1 we discuss electrochemical and photoelectrochemical catalysts in the context of their application for solar-to-hydrogen devices. During this introduction we will give an overview of the current state of the field, discussing the different kinds of materials that are being investigated before giving a brief description of some actual solar-to-hydrogen devices and finishing with a discussion of the current and future challenges in the field. Chapter 2 is a description of the different techniques used throughout this thesis. Once having set the bases, we shall start with the actual research, which corresponds to Chapters 3 to 5.

Chapter 3 and 4 deal with the effect of trace metal impurities in electrochemical water splitting. In Chapter 3 we show that adventitious nickel at trace levels can act as a water oxidation catalyst in mildly basic aqueous solutions at overpotentials comparable to many recently-reported water oxidation catalysts, therefore serving to raise the burden of proof required of new materials in this field. Chapter 4 shows how silver ions leaking from Ag/AgCl reference electrodes in aqueous buffers at low pH can deposit on the working electrode as Ag(0) and catalyze the hydrogen evolution reaction, calling into question the validity of any reports using these electrodes that cannot demonstrate significantly superior activity to the baseline we set in this chapter.

In Chapter 5 we describe a direct hydrothermal deposition method to prepare Cobalt-doped MoS₂ thin films onto transparent Fluorine-doped SnO₂ substrate and demonstrate that the obtained films display good activity for the hydrogen evolution reaction from acid solution.

Table of contents

Abstract.....	ii
Table of contents.....	iii
List of conferences attended.....	vi
List of publications.....	vii
Acknowledgements.....	viii
Author's Declaration.....	ix
List of abbreviations.....	x
Chapter 1:	Towards an efficient solar-to-hydrogen device
	for the storage of renewable energy
	1
Synopsis.....	2
1.1 Introduction.....	3
1.1.1 The importance of energy storing technologies.....	3
1.1.2 Technologies for the storage of energy.....	5
1.1.3 Electrochemical and Photoelectrochemical water splitting.....	7
1.2 The electrochemistry of the water splitting reaction.....	12
1.3 Earth-Abundant Hydrogen Evolution Electrocatalysts	20
1.4 Earth-Abundant Oxygen Evolution Electrocatalysts.....	26
1.4.1 OER electrocatalysts based on mixed metal oxides.....	26
1.4.2 OER electrocatalysts based on single metal oxides.....	29
1.5 Earth-Abundant Catalysts for Photoelectrochemical Water Splitting.....	37
1.5.1 Catalysts for the Photoelectrochemical HER.....	38
1.5.2 Catalysts for the Photoelectrochemical OER.....	42
1.6 Artificial Photosynthesis Systems	45
1.7 Conclusions.....	49
1.8 References.....	50
Chapter 2:	Behind the techniques used
	59
2.1 Electrochemical techniques.....	60
2.1.1 Cyclic and linear sweep voltammetry.....	60
2.1.2 Bulk electrolysis.....	61
2.1.3 Galvanostatic experiments.....	61
2.1.4 Two-electrode vs three-electrode configuration.....	62
2.1.5 Reference electrodes.....	62
2.2 Gas Chromatography.....	63

4.4.2 Electrochemical Methods.....	146
4.4.3 Headspace Hydrogen determination.....	148
4.4.4 Other analytical techniques.....	149
4.5 References.....	150

Chapter 5: The Direct Hydrothermal Deposition of Cobalt-Doped MoS₂ onto Fluorine-Doped SnO₂ substrate as electrocatalyst for the HER 155

Synopsis.....	156
5.1 Introduction.....	157
5.2 Synthesis and Characterisation of Co-doped MoS ₂ on FTO.....	158
5.3 Hydrothermally-produced Co-doped MoS ₂ on FTO as an electrocatalyst for the HER.....	170
5.3.1 Study of the performance of 300 nm thick films at low pH.....	170
5.3.2 Study of the performance of 150 nm thick films at low pH.....	172
5.3.3 Study of the performance of 150 nm thick films at other pH.....	173
5.3.4 Gas analysis and stability.....	176
5.4 Conclusions.....	177
5.5 Experimental section.....	178
5.5.1 Materials and Reagents.....	178
5.5.2 Preparation of Co ₂ Mo ₉ S ₂₆ -on-FTO.....	178
5.5.3 Morphological and Compositional characterization.....	179
5.5.4 Electrochemical Methods.....	180
5.5.5 Headspace Hydrogen determination.....	181
5.6 References.....	182
Conclusions and future work.....	185

List of conferences attended and posters/talks presented

1) Inorganic Colloquia Seminars School of Chemistry, University of Glasgow

Oral presentations: (2014 – 2016)

- a) *“Winning the silver medal: rediscovering silver as a water oxidation catalyst”*, March 2015
- b) *“Efficient Electrocatalytic Water Oxidation at Neutral and High pH by Adventitious Nickel at Nanomolar Concentrations”*, November 2015
- c) *“Silver Leakage from Ag/AgCl Reference Electrodes as a Potential Cause of Interference in the Electrocatalytic Hydrogen Evolution Reaction”*, November 2016

2) MASC 2013 [16/12/2013 – 17/12/2013] University of Glasgow

3) Dalton Meeting [19/03/2014] University of St. Andrews

4) UK Solar Fuels Symposium, University of Cambridge [22/01/2016]

Poster: *Efficient Electrocatalytic Water Oxidation at Neutral and High pH by Adventitious Nickel at Nanomolar Concentrations*

5) Renewable Energy: Solar Fuels Gordon Research Seminar and Conference

[27/02/2016 – 4/03/2016] Italy

Poster: *Adventitious Nickel at Nanomolar Concentrations as an Efficient Electrocatalytic Water Oxidation catalyst at Neutral and High pH, and for Proton Reduction at Low pH*

6) 2016 Scotland and North of England Electrochemistry Symposium (Butler

Meeting), University of Glasgow [20/04/2016]

Oral presentation: *Efficient Electrocatalytic Water Oxidation at Neutral and High pH by Adventitious Nickel at Nanomolar Concentrations*

List of publications

- “Silver Leakage from Ag/AgCl Reference Electrodes as a Potential Cause of Interference in the Electrocatalytic Hydrogen Evolution Reaction” **Roger, I.**; Symes, M. D. *ACS Appl. Mater. Interfaces* **2017**, 9, 472.
- “The Direct Hydrothermal Deposition of Cobalt-Doped MoS₂ onto Fluorine-Doped SnO₂ Substrates for Catalysis of the Electrochemical Hydrogen Evolution Reaction” **Roger, I.**; Moca, R.; Miras, H. N.; Crawford, K. G.; Moran, D. A.; Ganin, A. Y.; Symes, M. D. *J. Mater. Chem. A* **2017**, 5, 1472.
- "Earth-Abundant Catalysts for Electrochemical and Photo-Electrochemical Water Splitting" **Roger, I.**; Shipman, M.; Symes, M. D. *Nature Reviews Chemistry* **2017**, 1.
- “First Row Transition Metal Catalysts for Solar-Driven Water Oxidation Produced by Electrodeposition” **Roger, I.**; Symes, M. D. *J. Mater. Chem. A* **2016**, 4, 6724
- “Efficient Electrocatalytic Water Oxidation at Neutral and High pH by Adventitious Nickel at Nanomolar Concentrations” **Roger, I.**; Symes, M. D. *J. Am. Chem. Soc.* **2015**, 137, 13980.

Acknowledgements

I'd like to thank Dr. Mark Symes first of all for choosing me as his first PhD student, when he had just founded the Symes Group, and then for all the time he has spent teaching me electrochemistry both on paper and in the lab, and for all the valuable advice and tricks in organic and inorganic synthesis he has shared with me. It is however the other things I've learned from Mark that I will always treasure the most: the "never give up attitude", the patience and cheerfulness when explaining things to students, being constructive and always looking for the bright side of things. Whenever experimental results were discouraging or confusing, he would always manage to cheer me up and give me the strength to go back to the lab just with a few words by showing me that nothing is ever entirely black, and behind the clouds there is always a silver lining. It has been a honour to have such a cool supervisor these three years and a half, and I wish you Mark the best of lucks in your career.

I'd also like to thank Prof. Lee Cronin for his support and advice and in general to the Cronin Group for all their help.

Big thanks to the past and present members of the Symes group: Giacomo (always ready to help in anything, and quick to come up with good ideas), Mike (with whom to speak about Marvel Superheroes) and Alex (thanks for your help with impedance, but I am afraid I still do not understand it). Then to Johnny Wong, the first project student I had the pleasure to supervise, who was incredibly bright and had the best of attitudes, and to Theo, my second project student, with whom I always had a good time in the lab.

To the friends that have been there to listen to my problems and go out together on the weekends: Merce, Lluís, Vasilis, Weimin, Qi, Zied and Raul. To JiaJia, a source of invaluable help in the lab, especially whenever I broke something, and to Guillaume for his help in other matters... To Lewis, Ben, Leanne, Niall and Greig also for their help doing electrochemistry. To Ohmmid and Andrew, who were my advisors when I restarted doing syntheses, and to the Forgans, in particular to Ross (who listened to all my complaints when we first moved lab) and to Isa (with whom I've enjoyed so many evenings doing taekwondo).

To my mum, my brother, my uncle Pepe and my cousin Guille, for their love and understanding. To Elvi, who makes my life so much more fun whenever she is around and also to Vero and Miri. To Javier, the love of my life, for loving me the way I am. And to my Grandad Luis, the wisest and the best person I've ever met, whom I know would have felt so proud.

Author's declaration

I declare that, except where explicit reference is made to the contribution of others, this dissertation is the result of my own work and has not been submitted for any other degree at the University of Glasgow or any other institution.

Printed Name: ISOLDA ROGER BARBA

Signature:

List of abbreviations

AAS Atomic Absorption Spectroscopy

AFM Atomic Force Microscopy

AM Atmospheric Mass

C Charge

CE Counter Electrode

CV Cyclic Voltammogram

DI De-ionized

E Potential

ECPB Electron-Coupled-Proton Buffer

EDTA Ethylene Diamine Tetra-Acetic Acid

EDX Energy- Dispersive X-ray spectroscopy

Eq. Equation

F Faraday's constant (96485.333 C / mol)

FTO Fluorine-doped Tin Oxide

GCHA Gas Chromatography Headspace Analysis

HEC Hydrogen Evolution Catalyst

HER Hydrogen Evolution Reaction

HOR Hydrogen Oxidation Reaction

i Current

ICP-MS Inductively coupled plasmas mass spectrometry

ICP-OES Inductively coupled plasma optical emission spectroscopy

ITO Indium-doped Tin Oxide

j Current density

j_0 Exchange current density

KBi Potassium borate

NaBi Sodium Borate

NaPi Potassium phosphate

KPi Potassium phosphate

NaCi Sodium carbonate

KCi Potassium carbonate

NHE Normal Hydrogen Electrode

OEC Oxygen Evolution Catalyst

OER Oxygen Evolution Reaction

ORR Oxygen Reduction Reaction
PCET Proton-Coupled-Electron Transfer
PEM Proton Exchange Membrane
PEME Proton Exchange Membrane Electrolyzer
R Resistance
RE Reference Electrode
RHE Reversible Hydrogen Electrode
SEM Scanning Electron Microscopy
T Temperature
TEM Transmission Electron Microscopy
TLS Turnover Limiting Step
WE Working Electrode
WOC Water Oxidation Catalyst
XPS X-Ray Photoelectron Spectroscopy
 α Transfer coefficient
 β Symmetry factor
 η Overpotential

CHAPTER 1

Towards an efficient solar-to-hydrogen device for the storage of renewable energy

Acknowledgements and declaration

This chapter includes extended and updated sections from the following two papers:

"Earth-Abundant Catalysts for Electrochemical and Photo-electrochemical Water Splitting" **Roger, I.**; Shipman, M.; Symes, M. D. *Nature Reviews Chemistry* **2017**, 1.

"First Row Transition Metal Catalysts for Solar-Driven Water Oxidation Produced by Electrodeposition" **Roger, I.**; Symes, M. D. *J. Mater. Chem. A* **2016**, 4, 6724.

Said papers were written through the contributions of all the cited authors.

Synopsis

Renewable sources suffer from seasonal and diurnal fluctuations as a result of which they need to be coupled to energy storage technologies in order to be feasible alternatives to nuclear and fossil fuels plants. Electrochemical and photoelectrochemical water splitting could be a solution to this problem, as hydrogen is an excellent storable fuel that can be either burnt in air or recombined with oxygen in a fuel cell to release the stored energy. In particular, fully integrated solar-to-hydrogen devices in which sunlight is directly converted to hydrogen are particularly sought for the compactness and simplicity of their architecture. However, if these devices are to become a reality, they must be cheap to produce and operate, calling for the development of water splitting electrocatalysts based on Earth-abundant elements. In this Chapter we will discuss progress towards such electrocatalysts within the context of their application in photoelectrolytic water-splitting devices. For this, we will first comment on different architectures of solar-to-hydrogen devices and also give some insight into the electrochemistry of the water splitting reaction.

1.1 Introduction

1.1.1 The importance of energy storing technologies

In 2012 the world's energy consumption was 5.79×10^{20} J, with future energy demand projected to reach 8.60×10^{20} J in 2040¹. There are different estimations of how long fossil fuels will last and what percentage of the projected energy they will be able to cover²⁻⁵, but what it is widely agreed is that fossil fuels cannot be the major energy suppliers at this energy rate if we want to at least maintain the present CO₂ atmospheric levels. Many countries are taking measures to increase the amount of energy coming from renewable sources as well as lowering the emissions of greenhouse gases, and while most of the proposed targets⁶ will not be met in the timeframe stipulated, in recent years there has been a significant investment in renewable energies and their share of total electricity production has indeed increased.⁷ For instance, between 2014 and 2015 the input of renewable sources into electricity production in the UK increased by 25%, according to the Department for Business, Energy & Industrial Strategy,⁸ and many grants were awarded so that new plants are projected or under current construction. This should arguably be seen as an achievement, and yet there are organizations⁹ talking of the need to “cool down the overheating in the renewables sector”, pointing out that if all these projected plants are indeed built the UK will actually exceed its renewable energy's target for 2020, with bad consequences in the country's economy due to two main reasons: firstly, that apparently there will not be enough subsidy budget for all these projects, and secondly because they will result in an oversupply of electricity. While it is not the scope of this thesis to enter into the first argument or into moral and economical arguments about this, it is true that a hurried and inadequately planned implementation of renewable energies can lead to economic and social problems. We are currently seeing the effects of this in Germany, a pioneer country in the use of renewable resources. In 2010 Germany's government launched an ambitious plan (the *Energiewende*, which means an energy change or revolution), to decrease their CO₂ emissions by dramatically increasing the component of the country's electricity production that comes from renewable sources. As a result, in 2015 about one third of the electricity consumed in the country did indeed come from renewable sources. Also, although it might be surprising bearing in mind that we are talking of a northern country, Germany has become the country with the highest solar energy production in the world. And they have indeed managed to lower their carbon dioxide emissions: in 2014 they were a 27% lower than in 1990,¹⁰ still far from the initial goals they set (a cut down in greenhouse gas emissions of 40% by 2020 and

95% by 2050, always compared to the emissions in 1990),¹¹ but still quite a big improvement. And yet, they have come up against an issue they had not accounted for properly: from time to time, when strong winds coincide with sunny days, the renewable energies' share of total electricity climbs from usually less than half the total to percentages as high as 80% depending on the day of the week,¹² resulting in sudden energy production peaks that have caused the electricity prices to become "negative"¹³ for as long as the overproduction continued, which last time¹² was almost ten hours. The way media has been talking about these negative prices leads one to believe that they are actually a good thing for the customers, since in theory it is the supplier who is virtually paying the customer during the hours the renewables' oversupply lasts. However the economic mechanisms behind this phenomenon are a bit more complicated: in order to favor renewables sources, whenever the electricity price is lower than an agreed value, the German government pays renewables producers to compensate them with money coming from a budget directly fed from a tax paid by citizens. What this implies is that if these negative prices keep occurring more and more often, the tax related to them will have to be increased, so that in the end citizens are the ones paying the consequences of the oversupply. But how have they arrived to this situation?

Renewable energies suffer from seasonal and diurnal fluctuations and are therefore intermittent sources of energy. This is not compatible with the way we consume energy unless we couple them with energy-storing systems, so that any energy produced in excess at peak production times can be stored to be released as soon as a minimum in energy production is reached. This is well known, and there are different technologies available to store energy: mechanically, thermally, in batteries or as chemical bonds. We will discuss each of these options later. However, these storing technologies are not ready to be set up as quickly as a solar or a wind farm, so what has happened in Germany is that even though they have increased the renewable energy production to an extent that there are times in which they produce too much electricity, they cannot start closing any fossil fuels power plants yet because most of the time the electricity produced by renewable sources is still too low. In these times of transition between a fossil-fuels-based energy system to a renewable energies-based one, when these kind of energy peaks happen basically the easiest and cheapest thing to do is to dump to earth the excess electricity from whichever source is deemed most suitable from an economical point of view. In order to avoid this, what Germans have been trying to do is to scale down the production of electricity from some of the fossil fuels

thermal plants as soon as a peak was reached. Unfortunately, fossil fuels power plants' electricity production cannot be efficiently tailored to produce variable amounts of electricity to match the peaks and valleys in the electricity supply caused by solar and wind energy, neither from a technological nor from an economical point of view. And in any case, it simply takes too much time, so that by the time the amount of gas or coal burning has been lowered to the desired level the grid is again in need of electricity and production needs to be increased again. This example shows us the consequences of trying to increase the renewable sources' energy quota without coupling them to an equally ambitious energy storing system: If renewable sources are to become a main component of the global energy production, they *do* need to be coupled to efficient and economically viable energy storing systems. The fact that these have not yet been developed and optimized enough to be implemented at the scale they are currently needed should be seen as an urgent call for a big research effort in this area.

1.1.2 Technologies for the storage of energy

We have mentioned before four possible paths to store energy: mechanically, thermally, in batteries or as chemical bonds.² The first option refers to probably the most ancient large-scale energy storage system known by humankind: **Pumped Hydroelectric Storage**. The bases of this technology are quite simple: electricity can be used to move turbines to pump water uphill from a lower reservoir to an upper one, where it is stored as potential energy. To get the electricity back, the water is released back to the lower reservoir, converting the potential energy into kinetic energy, which is used to move the turbines the other way round (or a different system of turbines), converting the kinetic energy into electricity. Unfortunately this technique would not match well with the diurnal cycle of solar energy: we cannot realistically hope to be filling and emptying big water reservoirs daily! It could be used though as a long-term energy storage system, to serve as a back up to cover a sudden, emergency need of electricity, but that goes beyond the scope of this discussion.

The second option, **thermal storage**, refers mainly to **Solar Thermal Technology**, which uses sunlight to heat water or other fluids. On a small scale, it can be used to provide hot water and heating for a house, but it can also be applied to big buildings and even in industry, where so many processes require the use of heat and vapor. This is quite a simple and

effective option that, if effectively integrated to the buildings, would really make a difference in the fossil fuels consumption, since it has the potential to substitute for natural gas.

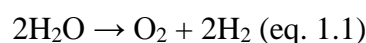
Another option are **batteries**. Batteries are everywhere nowadays, yet they are not the best option for storing the excess energy produced in a wind or solar farm. This is due mainly to their low energy density, both in terms of volume and weight. The low energy densities of batteries are not a big problem when making small devices like mobile phones or laptops, but it has proved to be a hindrance in bigger applications like electric cars. Also, continuous charge and discharge degrades little by little the components of a battery, leading to a continuous decrease in storing capacity and therefore a low durability, which combined with their prices makes it impossible to amortize their cost over the typical lifetime of a photovoltaic².

This takes us to the last option: to store energy as **chemical bonds**. This means using energy to drive an endergonic reaction whose products can be stored and subsequently recombined to release back the energy in a controlled manner when it is needed. And the best reaction to use for this is water splitting into hydrogen and oxygen. In a way, it is what plants do: they use sunlight to split water, and then they combine the hydrogen equivalents produced with carbon dioxide taken from the air to make carbohydrates. We can try to mimic the whole process and store energy as for example methanol, but given the amount of energy required to convert hydrogen and CO₂ to methanol using current industrial methods, it is a lot more efficient just to use the H₂ directly as a fuel, since present technologies allow for its proper storage and distribution. Now, how can we split water? There are actually several ways,¹⁴ including thermolysis, thermochemical water splitting, photobiological water cleavage, electrolysis and photoelectrolysis. In **thermolysis** water is thermally split at temperatures between 2000 and 2500 °C, which requires materials able to withstand these conditions as well as a cheap heat source. The need of a cheap heat source limits this process to places where geothermal energy can be used. **Thermochemical water splitting** requires more reasonable temperatures, but is based on chemical cycles like the iodine-sulfur one, and the corrosive nature of the chemicals employed makes a large scale plant design quite cumbersome. **Photobiological Water Cleavage** uses microorganisms (mainly green algae and cyanobacteria), and at least at present is a process too slow for being taken into consideration. This leaves **electrolysis and photoelectrolysis** as the most feasible water splitting processes at the time being, but a good deal of effort and investment must be

devoted to them in order to keep lowering the cost of electrolyzers so that they can compete with the non-renewable energy sources.

1.1.3 Electrochemical and Photoelectrochemical water splitting

The water splitting reaction can be written as



And it is a thermodynamically-uphill process that requires 286 kJ mol^{-1} of energy input under standard conditions of room temperature and pressure. The first water electrolyzers built in the 19th and 20th centuries were initially intended to produce H_2 for industrial applications (in particular for the Haber-Bosch process), but as a consequence of the growing need to move from fossil fuels to renewable sources of energy, over the last two decades water splitting has arisen as a promising method to store energy in the form of chemical bonds. To do this, energy is first used to drive an electrochemical or photoelectrochemical device to split water. Then, the hydrogen produced is stored so that it can be either burnt in air or recombined with oxygen in a fuel cell to give electricity when this is needed.

The two main kinds of electrolyzers commercially available at present are **proton exchange membrane** (PEM) electrolyzers and **alkaline based** electrolyzers. The formers are the most efficient ones and can achieve current densities¹⁵ up to 2000 mA cm^{-2} , whereas the alkaline electrolyzers usually reach between 100 and 300 mA cm^{-2} . However, PEM electrolyzers require very costly materials because they use precious metals as electrode catalysts, in contrast with the catalysts mainly based on Earth-abundant elements of the alkaline electrolyzers (as for example nickel based spinels and perovskites¹⁶). Both electrolyzers work at extreme pH, requiring materials that can withstand these harsh conditions. **Solid oxide electrolysis cells** (SOEC) are also being currently investigated, but they work at very high temperatures, which implies using costly materials, and if the thermal source is included in the efficiency equation this drops significantly, not to mention the corrosion, seals and thermal cycling issues yet to deal with.¹⁴

These electrolyzers are run by electricity which can be generated from any renewable source, and are currently in use in some wind and solar farms.¹⁷ We are going to focus from this

point onwards on solar energy, since “more energy strikes the earth in one hour (4.3×10^{20} J) than all of the energy currently consumed on the planet in 1 year (4.1×10^{20} J)”². In this context, electrolyzers powered by conventional solar panels constitute an **indirect** approach to solar-to-hydrogen production. A **direct** approach would be a device in which light harvesting materials coexist with water splitting catalysts, converting sunlight directly into oxygen and hydrogen. Such direct solar-to-fuels devices can be considered to perform “artificial photosynthesis”, with sunlight being captured and stored in the form of chemical bonds in a product “solar fuel” (in this case, H₂).¹⁸ An indirect approach benefits from the use of conventional, tried-and-tested technologies, but it suffers from efficiency losses due to the additional step involved (electricity is first generated in the photovoltaic cell and is then consumed in a subsequent electrolysis step in a separate device). This is why over the last decade more and more researchers have turned their efforts towards the development of **direct solar-to-fuels devices**, in the hope that these will eventually become more efficient than indirect methods.^{19,20}

From an architectural point of view there are two possible configurations for a direct solar-to-hydrogen device. In a **wireless configuration**, the light harvesting function is performed by a photovoltaic sandwiched between the water oxidation and the hydrogen evolution catalysts. Upon receiving a photon, an electron-hole pair is created and the electron moves to the Hydrogen Evolution Catalyst (HEC) while the hole moves to the Oxygen Evolution Catalyst (OEC). In a **wired configuration**, the two electrodes are spatially separated, so that an external circuit is needed for electron flow. Figure 1.1 shows these two possibilities as well as the indirect one.

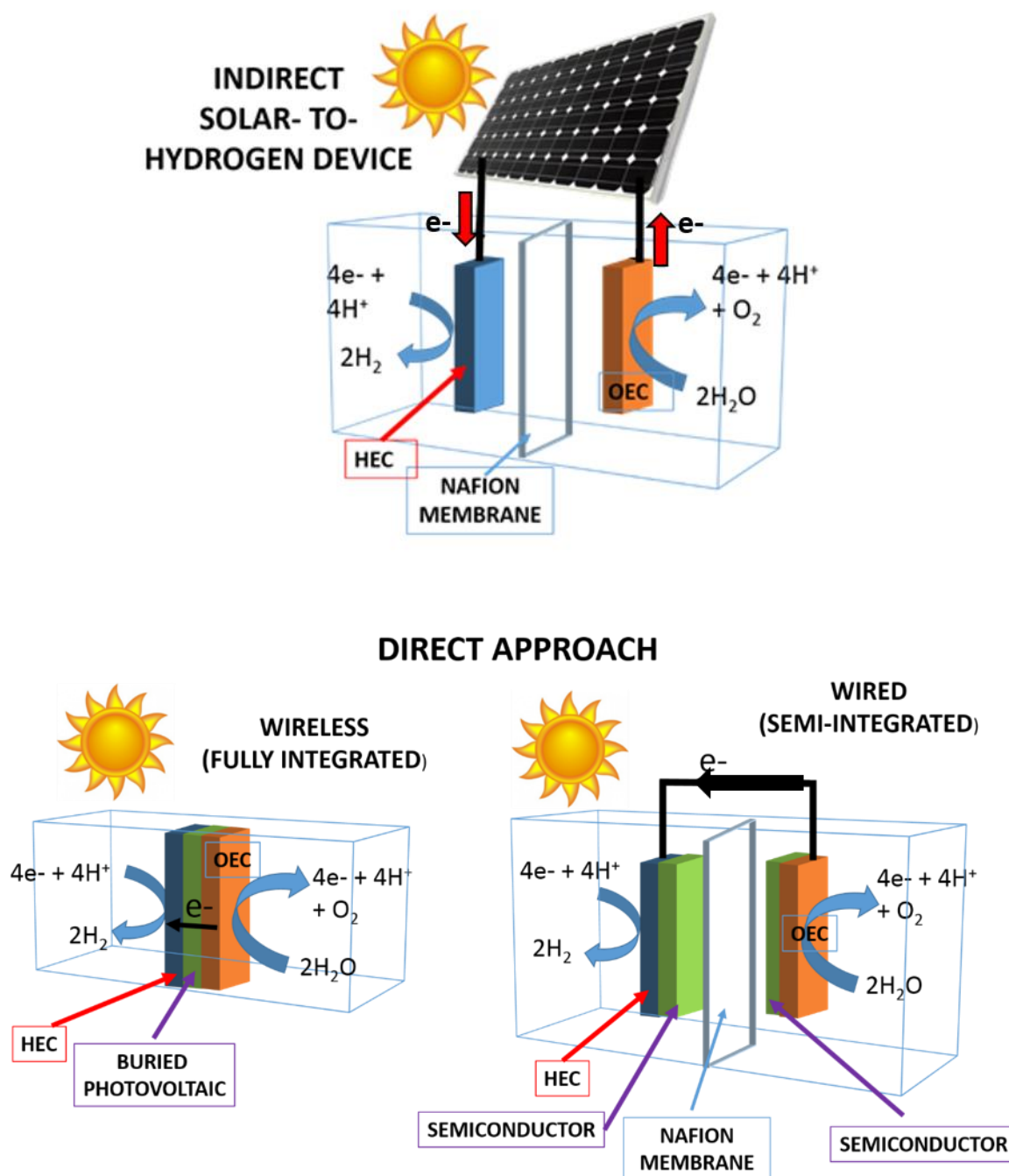


Figure 1.1 Indirect approach (up) vs two possible direct approaches (bottom): In the wireless one (left), the light harvesting material is buried between the HEC and the OEC and the electrons move through the semiconductor to the HER electrocatalyst without the need of external wires. In the wired one (right), each electrocatalyst is in contact with a light harvester, but they are spatially separated and the electrons flow through a wire.

Practical and scalable artificial photosynthesis systems will have some fairly stringent materials requirements. Firstly, the current densities that can be obtained from these devices will be limited by the power of the incident sunlight (0.1 W cm^{-2} at most) which means the highest current density that can be obtained is therefore limited to 30 mA cm^{-2} , with current densities on the order of 10 mA cm^{-2} considered realistic for artificial photosynthesis systems.²¹ This means that to make the same amount of gas per unit time a photoelectrochemical solar-to-hydrogen device would require around 50-200 times the electrode area of a conventional electrolyzer, making the use of precious metal electrocatalysts in such artificial photosynthesis systems economically unviable. Instead, the electrocatalysts in artificial photosynthesis systems will have to be both very cheap and widely available, thus restricting our choice to first row transition metals and their compounds.²²

Another issue is that conventional electrolysis works best at either very high or very low pH, where the concentration of charge carriers is greatest, but the vast majority of known semiconductors suitable for use as light-absorbers degrade rapidly at extreme pH values, meaning that neutral electrolytes are sought for many artificial photosynthesis applications. Milder pH environments in artificial photosynthesis systems would also slow the rate of degradation of other cell components (gaskets, connections, membrane separators), which is vital for long-term performance (and hence overall system cost).²³ Moreover, pH neutral electrolytes avoid many of the potential safety issues that could arise if more caustic electrolytes were employed (given that artificial photosynthesis systems will have to cover large areas in order to produce useful amounts of fuel on practical timescales, it seems almost inevitable that leaks will occur somewhere).

Whether these kind of devices will ever prove to be better than the PEM or the alkaline electrolyzers in terms of efficiency and cost is something that time will tell, but it could be that we are looking at two approaches in design connected with two different ways of producing and distributing energy. We currently rely on a system in which energy production is performed in localized places on a big scale and the produced electricity is then distributed to people. This surely looked like the best idea when the system was implemented, since the main energy sources were hydroelectric, nuclear and fossil fuels power stations. Efforts to move from fossil fuel and nuclear plants to solar energy have given rise to photovoltaic farms. But is this the most efficient way to use this energy source? Since sunlight is

everywhere, it does not really require that the electricity production is concentrated in one place. Probably the main reason it is done in this manner is because a centralized electricity distribution system that required a big inversion is already implemented, so that moving to a delocalized, small-scale energy production system is something developed countries are naturally reluctant to consider. And yet the developing countries are in time to opt for an infrastructure based on this opposite design: delocalizing the energy production to many smaller locations. And here is where artificial photosynthesis devices enter the argument. PEM and alkaline electrolyzers have outstanding performance, but the cost of the materials they are made off prevents them for being used in such a highly distributed system. It can be argued that alkaline electrolyzers are cheaper, since they are not necessarily based on precious metals catalysts, but the fact that they work in so harsh pH conditions not only raises the requirements and price of the materials in the device, but makes it dangerous due to potential leaks, making these devices potentially unsafe. These electrolyzers are better suited to a large scale operation in a specific location, which matches with the energy distribution system already in place in the developed world. Contrary to this, an artificial photosynthesis device that works at near neutral pH and is based on Earth-abundant elements is better suited to be scaled down so as to give power, for example, to just the neighbors of the same building, or even provide each family with personalized energy. This shows most promise for developing countries, where energy needs are growing fast and big centralized energy production sites with the corresponding energy-distribution infrastructure is too expensive and incompatible with their near-term needs.²⁴ It must be noted here that most of the world's total increase in energy consumption is projected to arise from the developing countries between the 2012 to 2040 period.¹

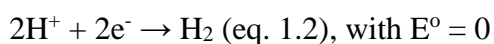
Regardless of whether we intend direct solar-to-fuel devices to be the key to personalized energy or replace PEM and alkaline electrolyzers, there is much work to be done for these devices to become a reality. Efforts are currently directed to develop cheaper and more efficient light-harvesting materials, to deal with the electron-hole separation issues in the device, and to develop stable catalysts for the two water splitting half-reactions based on Earth-abundant elements with decent enough performances that can be combined with and coupled to photocatalytic materials. The work in this thesis has focused on the electrochemical component of the problem, so in the next sections of this chapter we will examine recent progress towards the development of Earth-abundant electrocatalysts for water splitting within the context of their potential use in photoelectrochemical solar-to-

hydrogen devices. “Earth abundant” is taken here to exclude the metals Re, Ru, Os, Rh, Ir, Pd, Pt, Ag and Au. We shall examine in turn electrocatalysts for the hydrogen evolution reaction (HER) and electrocatalysts for the oxygen evolution reaction (OER), before exploring some examples of the use of particular catalysts in photoelectrochemical cells for performing the HER and OER. We note here that we are only going to cover heterogeneous electrocatalysts, leaving aside homogeneous catalysts as well as systems that use microorganisms. Each of the sections will include a table summarizing all this information by providing some of the most relevant examples of each kind of the materials discussed. Finally, we shall present some examples of complete and functional photoelectrochemical solar-to-hydrogen devices, and critically appraise the remaining challenges in this field.

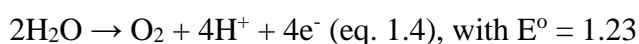
But before starting with these discussions, we will go first through some concepts and equations necessary to follow the rest of the thesis.

1.2 The electrochemistry of the water splitting reaction

The water splitting reaction can be divided into the following half-reactions:



$$E = E^\circ + \frac{0.059}{2} \log[\text{H}^+]^2 = E^\circ + 0.059 \log[\text{H}^+] = 0 - 0.059\text{pH} \text{ (eq. 1.3)}$$



$$E = E^\circ + \frac{0.059}{4} \log[\text{H}^+]^4 = E^\circ + 0.059 \log[\text{H}^+] = 1.23 - 0.059\text{pH} \text{ (eq. 1.5)}$$

As the above equations suggest, in theory in order to split water we would only need a voltage difference of 1.23 V between the anode and the cathode, but in practice it is necessary to apply a bigger potential due to the resistances present in the cell as well as the need to surpass kinetic barriers at each electrode. The difference between the potential that we really need to split water and the theoretical potential is called the **overpotential (η)**, and the voltage we need to apply becomes:

$$E_{\text{applied}} = 1.23 + \eta_{\text{anode}} + \eta_{\text{cathode}} + iR \text{ (eq. 1.6)}$$

The resistance loss can be minimized by optimizing the cell design, and to deal with the activation barriers at each of the electrodes we add catalysts to these, with the target being

to decrease the overpotential as much as possible to reduce the energy input needed to drive the reaction.

It is also important to note that the potential required to drive each of the half reactions changes with the pH. While the pH terms cancel each other in the overall equation and therefore do not matter for an electrolyzer, they *do* matter when we study the performance of a catalyst for one of the two half-reactions with a potentiostat. In this case we are applying a potential for that half-reaction only, and the value we need to apply will vary depending on the pH, as reflected by the diagram in Figure 1.2. This is why we often give the potentials referred to the **Reversible Hydrogen Electrode (RHE)**, which is a sub-type of the Normal Hydrogen Electrode (NHE) in which the measured potential does not change with pH, allowing us to compare directly the position of a redox event of interest with the standard reduction potential of hydrogen (which is always 0 V vs. RHE) regardless of the pH. The formula to convert from one to another is $E_{\text{RHE}} = E_{\text{NHE}} + 0.059 \times \text{pH}$. For example, if we want to apply a potential of 1 V vs RHE, this will be 1.41 V vs NHE at pH 7 and 1.83 V at pH 14.

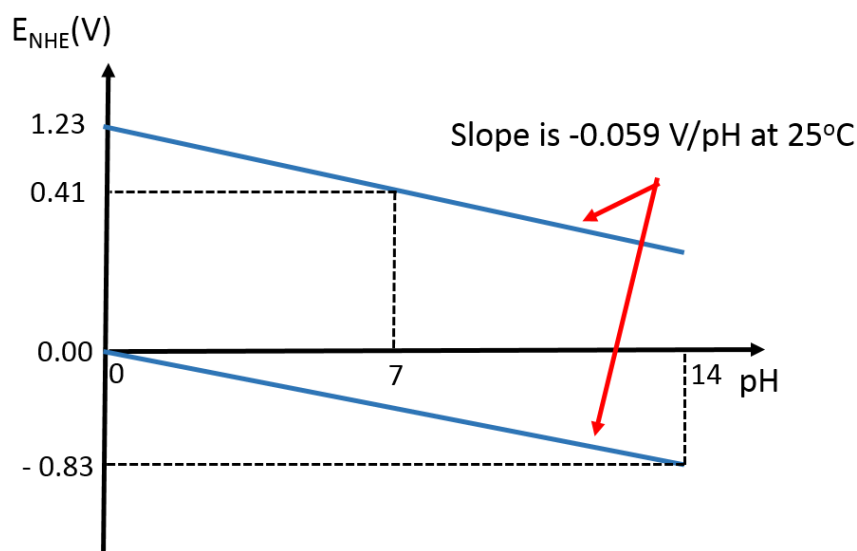


Figure 1.2 $E/p\text{H}$ diagram of the water half-reactions in aqueous medium. Adapted from reference (25).

There are a number of parameters and terms we will be constantly referring to, so in the following pages we are going to go over them explaining their significance and application within the context of water splitting:

OVERPOTENTIAL AND ONSET POTENTIAL

In order to compare different catalysts we refer to the **overpotential** required to achieve a given current density, usually **10 mA cm⁻² for HECs** and **1 mA cm⁻² for OECs**. Many researchers talk also of “**onset overpotential**”, which would be the potential at which activity for the half-reaction under study starts to manifest, but this is not a very useful term unless accompanied with a value of the current density, since there is not a clear consensus in what exactly is considered the “onset”.

TAFEL SLOPE AND EXCHANGE CURRENT DENSITY

The Tafel slope is probably the parameter that best gives an idea of the performance of an electrocatalyst. We are going to briefly explain where the equation comes from before talking of its meaning and utility.

In the absence of mass transport limitations it is generally accepted that the steady state current density follows the equation:

$$j = j_o e^{\alpha F \eta / RT} \text{ (eq. 1.7)}$$

with j_o = exchange current density, α = transfer coefficient, η = overpotential, F = Faraday constant, R = gas constant and T = temperature.

If we take napierian logarithms the equation becomes

$$\ln j = \ln j_o + \alpha F \eta / RT \text{ (eq. 1.8)}$$

and if we convert it to natural logarithms

$$2.303 \log j = 2.302 \log j_o + 2.303 \alpha F \eta / RT \text{ (eq. 1.9)}$$

And dividing by 2.303

$$\log j = \log j_o + \alpha F \eta / 2.303 RT \text{ (eq. 1.10)}$$

Which can be arranged as

$$\eta = a + b \log j \text{ (eq. 1.11)}$$

This expression is known as the Tafel equation, with a and b being constants. If we record the steady state current density given by our catalyst at different values of potential and plot it as logarithm of the current density vs the overpotential we should find a linear region that

follows this equation. Now regardless of the meaning of a and b , this kind of plot is very useful because the slope shows how the electrocatalytic performance of the catalyst under examination changes over a given potential range. Because we are using logarithms and the slope is expressed in units of mV decade^{-1} , we can see at a quick glance the overpotential increment needed to increase the current density by an order of magnitude, say for example to change from 1 to 10 mA cm^{-2} . It is therefore a useful parameter to compare different catalysts: the smaller the Tafel slope the better the catalyst, since it means that it requires smaller increments of overpotential to give increased current densities and also that we can “tune” the current density with just small changes in overpotential. We need to bear in mind that in an electrolyzer we probably will not want a fixed value of current density, so a catalyst that can operate in a range of current densities with little change in the overpotential is very desirable.²⁶

We note here that although the Tafel equation is widely accepted and applied to basically any kind of heterogeneous electrocatalysts, Equation 1.7 was originally developed for metallic electrodes, and therefore its applicability to electrodes that are not strictly metals is something one should consider with care. The reasoning behind this is that electrons in a metal follow the Fermi statistics while molecular species follow the Boltzmann statistics, and so the expression for the electrochemical potential of molecular species must include a term proportional to the logarithm of their concentration, whereas in the case of a metal it does not make sense to talk about electrons concentration.²⁷ The electrocatalysts that we will be describing in the following sections are oxides, hydroxides, phosphides, carbides and many other materials whose behavior in terms of kinetics will probably be somewhere between that of metals and that of molecular species. Since most of the electrochemical community seems to accept the validity of Equations 1.7 and 1.11 for all heterogeneous electrocatalysts we will follow lead and explain next the mechanistic information that can be extracted from the Tafel plot.

If we go back to Equation 1.11, we have that the slope, b , is

$$b = 2.303RT/\alpha F \text{ (eq. 1.12)}$$

and on the other hand for a multistep reaction that comprises a series of elementary steps,²⁶ the transfer coefficient is

$$\alpha = \frac{n_f}{\nu} + n_\Gamma \beta \text{ (eq. 1.13)}$$

Where

n_f = number of electrons transferred before the rate determining step

ν = number of times the rate determining reaction takes place in the overall reaction

n_Γ = number of electrons transferred during the rate determining step

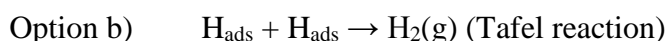
β = symmetry factor (related to the activation energy barrier and assumed to be 0.5)

This leads us to the other reason why the Tafel slope is useful: it gives information about the mechanistic pathway of the reaction under study. It may look like calculating the transfer coefficient with the slope does not give that much information since it leaves us with an equation with three unknowns, but we can rationalize what these coefficients would be in different situations, calculate with them α and with this the Tafel slope, which we can compare to the one we have obtained experimentally. This is better understood with an example, and the easiest one concerning water splitting is the HER in acidic media.

It is generally agreed that for the HER in acidic media the first step is



But then it can go through one of these two options:



If the rate determining step is the Heyrovsky reaction then $n_f = 1$ (because it happens after a Volmer step), $\nu = 1$ (there is only 1 Heyrovsky step per overall reaction), $n_\Gamma = 1$ (the Heyrovsky reaction involves the transfer of 1 electron) and we have said that $\beta = 0.5$. It follows that

$$\alpha = \frac{n_f}{\nu} + n_\Gamma \beta = 1 + 0.5 = 1.5$$

$$b = 2.303RT/\alpha F = \mathbf{40 \text{ mV decade}^{-1}}$$

If the rate determining step is the Tafel reaction then $n_f = 2$ (because we need two Volmer steps to generate two H_{ads}), $\nu = 1$ (only one Tafel step per overall reaction) and $n_r = 0$ (this step does not involve any electron transfer). So in this case:

$$\alpha = \frac{n_f}{\nu} + n_r \beta = 2 + 0 = 2$$

And therefore $b = 30 \text{ mV decade}^{-1}$

Finally, **if the rate limiting step is the Volmer reaction**, even though ν will be 1 or 2 depending on the subsequent step, because this is the first step in the reaction, $n_f = 0$ and therefore $\alpha = 0.5$ in both cases, resulting in a slope of **120 mV decade⁻¹**.

Thus depending on the Tafel slope we have obtained we can know which of these three steps is the rate limiting one and therefore which is the mechanism of reaction (except in the case in which the rate limiting step is the Volmer reaction, in which we cannot know from the Tafel slope which is the subsequent step).

We see now the importance of the Tafel slope in elucidating the mechanism of an electrode process. Now what happens is that the hydrogen evolution reaction is quite easy to rationalize, in the sense that as we have seen there are only two possible pathways. But if we think of the oxygen evolution reaction we will realize that it involves the transfer of 4 electrons and 4 protons, giving rise to many possible pathways and involving the formation of a range of adsorbed intermediates (M-O, M-OH, M-OOH...) and many different reactions. This is why one cannot find a Tafel slope classification in the literature for the OER such as the one we have described for the HER. This does not mean that the Tafel slope is therefore useless: in addition to giving us a measure of how good our catalyst is it can help us confirm or rule out a mechanism we are proposing based on complementary data (e.g. spectroscopic or DFT calculations). Some of the most typical Tafel slopes values for heterogeneous catalysts for the OER based on metal oxides are **120 mV decade⁻¹** and **60 mV decade⁻¹**. The first one is telling us that the rate determining step is also the first electron transfer, whereas the second means that the rate determining step is not an electrochemical one and that it happens right after the first electron transfer.

For most catalysts one never gets exactly one of these values, so we accept that the most likely mechanism is the one whose theoretical Tafel slope value is closer to the experimental,

but sometimes the slope we obtain is in the middle between two categories and one cannot be sure of what it means.

The other parameter that we can calculate with a Tafel plot, this time from the intercept value, is the **exchange current density (j_0)**, which represents the rate of reaction at the equilibrium potential. It reflects the intrinsic rate of electron transfer between an analyte in solution and the electrode. It can thus be viewed as a measure of the effectiveness of a catalyst for a particular electrochemical reaction under a particular set of conditions (the greater the magnitude of the exchange current density, the greater the activity of the catalyst). However, the exchange current density only applies at the thermodynamic potential, which is not the potential at which the catalyst will be working in an electrolyzer. Therefore while this is an important parameter, a Tafel slope is more useful, since it gives information about how the catalyst will behave at higher, more practical current densities.

STABILITY

It is not uncommon to find papers describing the outstanding activity of a catalyst only to read at the end that it loses half of this activity in a matter of hours. Clearly a catalyst needs to be stable to have any real application, and this stability is normally demonstrated by either maintaining a current density of at least 10 mA cm^{-2} for several hours or cycling the catalyst multiple times (typically more than 1000) with ideally negligible loss of performance at the end of the experiment. Typical problems of stability are related to exfoliation by intense bubbling and degradation at harsh pH conditions.

FARADAIC EFFICIENCY

In electrochemistry, this is the ratio between the amount of product actually detected and quantified, and the amount of that product that could theoretically have been formed based on the charge passed in the experiment. It can be written as

$$\gamma_{Faradaic} = \frac{\Delta n^{effective}}{\Delta n^{faradaic}} \quad (\text{eq 1.13})$$

Where $\Delta n^{Faradaic}$ is calculated with Faraday's law, which would be

$$\Delta n_{O_2}^{Faradaic} = \frac{\nu_{O_2}}{\nu_e F} C = \frac{1}{4F} C \quad \text{for the OER and}$$

$$\Delta n_{H_2}^{Faradaic} = \frac{\nu_{H_2}}{\nu_e F} C = \frac{1}{2F} C \quad \text{for the HER,}$$

where C is the charge passed in the electrolysis, F is Faraday constant, ν_e = stoichiometric number of electrons and n the number of moles.

The Faradaic yield tells us whether the reaction under study is the only process or if there is some other competing electrochemical process taking place. It is clearly insufficient to simply assume that a given current is producing a particular gas – one has to prove that the products of the reaction are indeed those claimed, and then compute the Faradaic yield. Hence, quantitative gas analyses are essential. For hydrogen, this means gas chromatography, whilst for quantitative oxygen detection the investigator has a choice of gas chromatography, fluorescence-quench methods or (in some cases) O_2 -sensitive electrodes such as the Clark electrode. The amount of gas produced can be quantified as well making it flow through a measuring cylinder containing water so that the total volume of gas produced can be read as it pushes the water out of the measuring cylinder. However this method does not tell us what gas is it, so it should be only used as a complementary technique accompanying another analysis method that can confirm the identity of the gas evolved.

TURNOVER FREQUENCY

The turnover frequency is the number of reactants that get converted to the desired product per catalytic site per unit of time. It is not easy to get this value for heterogeneous catalysts, since not all the catalytic sites are equally easy to access in the material, so it is often reported referred to the active sites on the surface of the catalyst only.

SOLAR-TO-HYDROGEN CONVERSION EFFICIENCY

The energy that would be released upon complete oxidation of the hydrogen produced by (for example) an artificial photosynthesis system in a given time, divided by the energy required by the artificial photosynthesis system to produce that amount of hydrogen.

BIFUNCTIONAL CATALYST

Here we will distinguish between three types of bifunctional catalysts: those that can catalyze the water oxidation reaction and its reverse, the oxygen reduction reaction (ORR); those that catalyze the hydrogen evolution reaction and its reverse, the hydrogen oxidation reaction (HOR) and finally those that can catalyze both the OER and the HER. A catalyst that can

catalyze both the OER and the ORR or the HER and the HOR would be useful for unitized regenerative fuel cells,²⁸ which work both as fuel cell and as electrolyzers, the same way that a battery can be charged and discharged. And a catalyst capable of catalyzing both the HER and the OER would be capable of catalyzing the overall water splitting on its own, so this is also desirable.

From all this it follows that an ideal catalyst would have small overpotentials, low Tafel slopes, a large exchange current density, quantitative Faradaic yield and high stability.

1.3 Earth-abundant hydrogen evolution electrocatalysts

The best known heterogeneous catalysts for the hydrogen evolution reaction are based on platinum. As this is rather expensive and rare, there has been considerable interest in hydrogen evolution electrocatalysts that use more abundant elements. Under very alkaline conditions (30% KOH in water), first row transition metals such as nickel have long been known to be effective HER catalysts. Nickel on its own deactivates progressively in alkaline media due to the formation of Ni-hydride species, so nickel alloys like Raney®-Nickel are preferred. Alloys of Ni and Co with Mo in particular display high cathodic current densities attributed to hydrogen production at only modest overpotentials (see entries 1-5 in Table 1.1).²⁹⁻³²

Among the key inspirations behind the design of new hydrogen evolution catalysts are the so-called “volcano” plots that correlate HER exchange current densities for various materials with the chemisorption energy of hydrogen on those materials. This trend was first recorded for metals in the 1970s by Trasatti,³³ who made up for the lack of experimental or theoretical data for hydrogen adsorption energies at the time by using instead the bond enthalpy of metal hydrides, as shown in Figure 1.3. While now it is known that the metals on the descending edge are actually covered by an oxide coating during the HER, which affects negatively the kinetics for this half-reaction, the ascending branch stays reasonably true in acidic media. Nowadays one can find in the literature volcano plots that have been built using values of ΔG for hydrogen adsorption obtained by DFT calculations³⁴, but in essence the position of the metals stay the same, since $\Delta G = \Delta H - T\Delta S$. While the information obtained by this kind

of plot should be treated with care, they have nonetheless been a fertile treasure map for new catalysts ever since Trasatti's first volcano plot.^{35,36} The reasoning behind this is that for the HER to happen the hydrogen atoms need to be adsorbed on the material's surface first and later the H_2 molecules need to be desorbed, but both processes are competitive: a material with too strong bonding strength will have trouble releasing the product, whereas if the hydrogen atoms adsorb weakly to the surface there will be difficulties in initiating the reaction. Therefore a balance is needed between the two processes, and these plots reveal that this is best achieved when the hydrogen adsorption free energy (ΔG) is close to 0, at which the maximum catalytic activity is obtained. Perhaps unsurprisingly, Pt lies near the apex of this volcano.

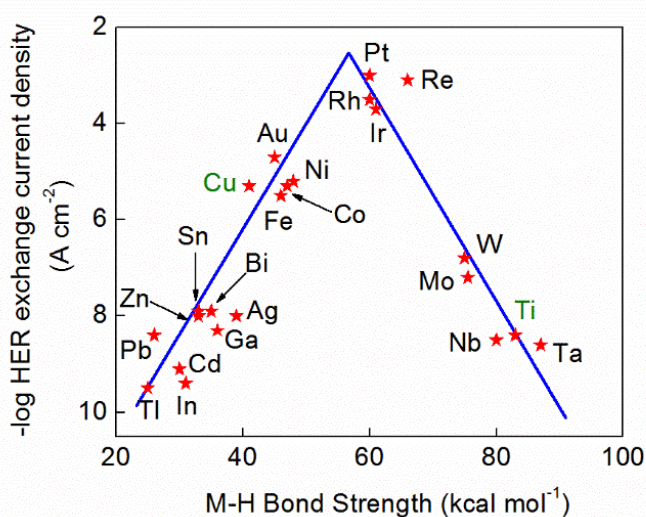


Figure 1.3 Trasatti's HER Volcano plot. The y-axis plots the exchange current densities for the HER vs. the energy of the intermediate metal-hydrogen bond formed between absorbed H and the electrode surface on the x-axis (adapted from reference 32). The positions of Ti and Cu have been highlighted in green (vide infra).

In 2005, Hinnemann *et al.* exploited this relationship by using density functional theory (DFT) to identify materials where the free energy associated with atomic hydrogen bonding to the catalyst surface was close to zero.³⁷ Their results suggested that MoS_2 would be a suitable candidate material (which they showed experimentally was indeed the case), despite bulk MoS_2 being known to be a rather poor HER catalyst.³⁸ This apparent contradiction was subsequently explained by some of the same authors, who demonstrated that hydrogen evolution occurs preferentially at edge sites on MoS_2 , with the basal plane being much less active.^{39,40} Since this discovery, various transition metal **sulfides** and **selenides** have been

prepared by numerous methods (often with a view to exposing as many edge sites as possible) and shown to have activity for the HER (see Table 1.1).⁴¹⁻⁵⁰

Similarly, transition metal **phosphides** have shown their worth as HER catalysts. Popczun *et al.* first demonstrated that Ni₂P was an effective hydrogen evolution catalyst in acidic media by noting that both Ni₂P and MoS₂ are common hydrodesulfurization catalysts.⁵¹ The key similarity here is that both hydrodesulfurization and HER require catalysts that reversibly bind and cleave H₂. The same group reported CoP as an even better catalyst a year later:⁵² only 85 mV overpotential to give 20 mA cm⁻² in 0.5 M H₂SO₄, with just a small increase of 25 mV in the overpotential after 24 h poised galvanostatically at 10 mA cm⁻², which the authors attribute to some particle desorption from the titanium substrate leading to a smaller mass loading. Other phosphides have since been shown to be active, including MoP and FeP.^{53,54} The later has the largest value for the exchange current density (0.42 mA cm⁻²) and the second smallest Tafel slope (39 mV decade⁻¹) of all reported non-noble metal HER catalysts in acidic media. Phosphides are at present among the most active materials for HER based on Earth-abundant elements, although it must be said that their stability needs to be tested for longer periods of time, since all these examples show a slight increase in the overpotential after 24-48 h of sustained electrolysis.

Meanwhile, transition metal **carbides**, **borides** and **nitrides** are also in vogue, with some of these materials functioning in both basic and acidic media as summarized in Table 1.1 (entries 21-29).⁵⁵⁻⁶⁰ DFT calculations have shown that the hybridization between transition metals and carbon or nitride atoms results in an electronic configuration resembling that of platinum, which has led to the investigation of this kind of materials. Although the first carbide found to have catalytic properties like platinum was WC in 1973,⁶¹ so far molybdenum carbides are giving better results in terms of combined stability and catalytic activity. It has been shown⁶² that the highest HER performance corresponds to hexagonal β-Mo₂C, and at the moment studies are directed to its nanostructural optimization to boost surface area and exposure of active sites. As way of example, Liao *et al.*⁵⁹ prepared highly dispersed nanowires made of Mo₂C nanocrystallites on glassy carbon electrodes and tested them in 1 M H₂SO₄, requiring just 130 mV overpotential to reach 10 mA cm⁻² and showing a Tafel slope of ≈ 53 mV decade⁻¹ (entry 26 in Table 1.1). In terms of stability it showed negligible loss after 25 h of continuous electrolysis maintaining a current density of 12 mA cm⁻², quite a promising result. Carbide-based catalysts can be made by means of reducing

the metal precursors at very high temperatures with gases like CH₄, C₂H₆ or CO, but many other carbon-containing compounds have been tried, from amines (as in the example above) to soy beans,⁶³ metal organic frameworks (MOFs) (table 1.1 entries 27 and 28), and carbon nanotubes and graphene, which can be used both as support material and carbon source. Regarding carbides with other transition metals, very recently Fan *et al.* obtained excellent metrics for the HER using a transition metal carbide (Ni/C) catalyst prepared by heating a nickel-based metal organic framework at 973 K.⁶⁴ This carbonization reaction led to the generation of carbon nanoparticles dotted with isolated Ni atoms. The activity of these materials for the HER at pH 0 was within a few mV of that exhibited by Pt for current densities less than 100 mA cm⁻². Catalysts whose activities rely on highly dispersed clusters of relatively few atoms often suffer from rapid deterioration in performance under constant potential because of the tendency for isolated metal centres to agglomerate. In this case, however, the activity of the catalysts was maintained over 25 h of continuous operation, which is a remarkable finding.

Nitrides are prepared by nitridation with NH₃ gas of metal precursors, again usually molybdenum, although the introduction of Ni⁵⁶ or Co⁵⁷ has been shown to increase the performance. For example, Cao *et al.* prepared Co_{0.6}Mo_{1.4}N₂ and obtained current densities of 10 mA cm⁻² at overpotentials of 200 mV in 0.1 M HClO₄, showing good stability after 3000 cycles.⁵⁷ These results have been outperformed with the preparation of cobalt nitrides without molybdenum: 140 mV overpotential to achieve 10 mA cm⁻² in 0.5 M H₂SO₄ with just an 11 mV increment after 5000 cycles for Liang *et al.*'s CoN_x/C catalyst.⁵⁵ An added feature of this material is that it can work over a range of pH, requiring 170 and 247 mV overpotential to achieve 10 mA cm⁻² in 1 M KOH and 1 M phosphate buffer (pH 7) respectively, also with negligible performance loss. This is particularly important since most of the best catalysts for the HER work in acidic media. As for borides, they have received much less attention, although they are also promising materials. In 2012 Hu *et al.*⁵⁸ reported an overpotential of about 225 mV to get 20 mA cm⁻² in 1 M H₂SO₄ for MoB, with reasonable stability over 48 h. Surprisingly this catalyst had a similar overpotential and Tafel slope at pH 14, which is uncommon among HECs, but it corrodes losing activity in this media in just one hour of continuous electrolysis.

These are so far the main kind of materials investigated. Interrogation of volcano-type plots allows new catalysts for the HER to be proposed by combining catalysts on opposite slopes of the volcano to produce new materials with intermediate hydrogen binding energy (and hence improved catalytic performance). Lu *et al.* recently employed this strategy and used DFT to predict that copper surfaces doped with titanium (to produce adsorption sites consisting of two copper centres and one titanium centre) would have hydrogen binding energies very similar to that of Pt.⁶⁵ Accordingly, the authors synthesised a range of bimetallic copper-titanium films by arc-melting methods and tested their activity for electro-reduction reactions in 0.1 M KOH. The optimal HER performance was obtained with films of composition Cu₉₅Ti₅, which gave current densities of -10 mA cm⁻² at an overpotential of only 60 mV (note the poor performance anticipated for Cu and Ti on their own, highlighted in green in Figure 1.3). In comparison, an overpotential of around 100 mV is required for a commercial Pt/C catalyst to achieve the same current density, suggesting that Earth-abundant HER catalysts can out-perform Pt under certain conditions. The key challenge for earth-abundant HER catalysts now remains to prove that such excellent performance can be maintained in the long term (continuous operation for tens to hundreds of thousands of hours).

Table 1.1 Overpotential (η) requirements, Tafel slopes and Faradaic yields of some selected Earth-abundant HER electrocatalysts.

Entry	Catalyst material	η at -10 mA cm $^{-2}$ (mV)	Tafel slope (mV/decade)	pH	Faradaic yield	Ref
1	Ni-Mo	200 (100 mA cm $^{-2}$)	122	14.8	N/A	29
2	Co-Mo	170 (100 mA cm $^{-2}$)	92	14.8	N/A	29
3	Ni-Mo	185 (300 mA cm $^{-2}$)	112	14.8	N/A	30
4	Ni-Mo	70 (20 mA cm $^{-2}$)	N/A	14.3	N/A	31
5	Ni-Mo	34 (20 mA cm $^{-2}$)	N/A	14	N/A	32
6	MoS $_2$	260	50	0	N/A	40
7	MoS $_2$	200 (15 mA cm $^{-2}$)	40	-0.3	100% ^a	41
8	MoS $_2$	~150	41	0	N/A	42
9	MoS $_2$	170	60	0.2	N/A	43
10	CoS $_2$	145	51	0	N/A	44
11	CoS $_2$	~175	93	7	100% ^b	45
12	CoMoS $_x$	250	85	7	~100% ^c	46
13	WS $_2$	~250	60	0	N/A	47
14	CoSe $_2$	90	39	0	N/A	48
15	MoS $_{1.0}$ Se $_{1.0}$	~200	56	0	100% ^a	49
16	NiSe $_2$	~140	49	0	N/A	50
17	Ni $_2$ P	130 (20 mA cm $^{-2}$)	46	0	100% ^a	51
18	CoP	85 (20 mA cm $^{-2}$)	50	0	100% ^a	52
19	FeP	55	38	0	100% ^c	54
20	MoP	64	N/A	0	100% ^c	53
21	CoN $_x$	170	75	14	N/A	55
22	CoN $_x$	140	30	0	N/A	55
23	NiMoN $_x$	225 (5 mA cm $^{-2}$)	35.9	1	N/A	56
24	Co $_{0.6}$ Mo $_{1.4}$ N $_2$	200	N/A	1	> 90% ^a	57
25	α -MoB	~225 (20 mA cm $^{-2}$)	55	-0.3	100% ^b	58
26	Mo $_2$ C	130	53	0	N/A	59
27	“MoC”	124	43	0	N/A	60
28	“MoC”	77	50	14	N/A	60
29	Ni/C	34	41	0	100% ^a	64
30	Cu $_{95}$ Ti $_5$	60	110	13	N/A	65
31	Pt/C	~80	55	14	N/A	66
32	Pt/C	~50	30	0	N/A	66

Notes: a) Quantified by measuring volume of gases evolved, b) Quantified by gas chromatography, c) Quantification method not stated.

1.4 Earth-Abundant Oxygen Evolution Electrocatalysts

Of the two water splitting half-reactions water oxidation to dioxygen is the most kinetically demanding step, since it involves a 4 electron transfer coupled to the removal of four protons. The difficulty of this process compared to the hydrogen evolution reaction (2 electron - 2 proton transfer) is reflected in the fact that here we talk of overpotentials to get 1 mA/cm² instead of the 10 mA/cm² benchmark in the previous section.

The main kind of materials that have been studied for the OER are metal oxides and oxyhydroxides, which we will discuss next.

1.4.1 OER electrocatalysts based on mixed metal oxides

At present, the best activities for electrochemical water splitting in alkaline media are claimed by materials based on mixed metal oxides, in particular combinations of nickel, iron and cobalt. In the 1980s, Corrigan was working with batteries when he observed that iron impurities present in nickel oxide electrodes increased the rate of the parasitical OER. This led him to change field from batteries to electrolyzers and publish a paper in 1987 showing how doping nickel oxide films with amounts of iron as low as 0.01% improved significantly their performance as catalysts for the OER.⁶⁷ On the other hand, in 2008 Merrill and Dougherty⁶⁸ set out to systematically explore the electrocatalytic activity of the first row transition metals for the OER, electrodepositing them individually or in pairs from a wide range of metal salt solutions on Pt substrates. The best result they obtained was for the **NiFe** combination, which required only 30 mV overpotential to perform the OER at 1 mA cm⁻² (or 300 mV overpotential at 500 mA cm⁻²) at pH 14, and had a Tafel slope of 15 mV decade⁻¹. A quick look at Table 1.2 will suffice to see that this catalyst is in a completely different league compared to the rest, but we cannot forget that it is on a Pt substrate. This work has encouraged further studies of mixed Ni-Fe oxides in basic media, including that of Lu and Zhao,⁶⁹ whose result arguably surpasses that of Merrill and Dougherty: even though the overpotential for their NiFe nanosheets to get 1 mA cm⁻² is higher (120 vs 30 mV decade⁻¹), their catalyst can give current densities of 500 and 1000 mA cm⁻² at overpotentials of 240 and 270 mV respectively, and more importantly, it is remarkably robust during strong oxygen evolution. In their paper they show that it maintains 500 mA cm⁻² galvanostatically for two hours without any increase in the required overpotential, and 100 mA cm⁻² for 10 h. In order for this catalyst to be able to have an application in an electrolyzer they will have to prove it is stable for much longer times, but still this is probably

the most efficient OEC in alkaline pH reported to date with potential industrial applications. Also, the substrate they use is a Nickel foam, so this is a completely noble metal-free material. The high activity of this catalyst is due to a combination of using electrodeposition as the preparation method (which tends to give more robust catalysts than those that are made as powders and held on the electrodes with polymeric binders like Nafion), and, most of all, the use of a macroporous, 3D substrate. This last one is a strategy that is becoming quite popular for the preparation of catalysts, since it allows high loadings of the catalytic material and a much higher number of accessible active sites compared to a planar material.

Other relevant works with NiFe materials are those of Gong *et al.*⁷⁰ and Li and co-workers.⁷¹ In the latter, the authors noted that while low loadings of iron gave enhanced catalysis of the OER, higher loadings reduced the performance of the resulting NiFe oxides below that exhibited by undoped nickel oxides, highlighting the importance of finding the right iron doping percentage. Bell and co-workers studied this in more detail and found that the optimal activity of NiFe oxides for the OER was obtained at a composition of 2:3 Fe: Ni in the oxide.⁷² Through electrochemical and *in situ* X-ray absorption spectroscopy measurements, it was found that the composition of these iron-doped Ni-oxide films was a good fit to the formula $\text{Ni(II)}_{1-x}\text{Fe(III)}_x(\text{OH})_2(\text{SO}_4)_{x/2}(\text{H}_2\text{O})_y$ (a layered double hydroxide structure) at the catalyst rest potential. It was also observed that the position of the Ni(III)/Ni(II) couple shifted to more anodic potentials with increasing Fe content in the films.⁷³ Using computational methods, the authors suggested that raising the potential into the zone in which the OER occurred caused the nickel in these films to become oxidised to Ni(III) (whilst the iron stayed in the Fe(III) oxidation state), but that the Fe(III) centres in these oxidised films possessed lower overpotential requirements for the OER than the Ni(III) centres (and hence the Fe(III) centres were held to be the sites of oxygen evolution). A key result in this area which has important ramifications for high pH electrochemical water splitting was supplied by Boettcher and co-workers.^{74,75} These authors prepared Ni-oxide films for the OER from ostensibly pure nickel salt precursor solutions. However, upon careful examination of their films, the authors discovered that significant traces of iron were present in the most active of their materials. Indeed, when Fe was rigorously excluded from the catalyst deposition baths, the overpotential requirement to achieve a current density of 1 mA cm^{-2} for the OER increased from 300 mV to 470 mV. Working backwards from this finding, the authors found an optimal activity for the OER at a loading of 25% Fe in Ni-oxides (in good agreement with Bell's results above). However, Boettcher's team assigned

the locus of the OER activity to the resulting highly oxidizing $\text{Ni}^{4+/3+}$ couple, rather than to the Fe centres. The same group subsequently observed similar behavior when cobalt oxides were doped with iron.⁷⁶

Other mixed metal oxides that have proved to be competent OER are **NiCo** and **NiMo** oxides, which again contain nickel. Adding Ni to Co_3O_4 is believed to increase its conductivity and surface area, and Lambert's $\text{Ni}_x\text{Co}_{3-x}\text{O}_4$ has the added feature of being a bifunctional catalyst that can also catalyze the ORR.⁷⁷ On the other hand, the NiMo hollow nanorrod array prepared by Asiri's group⁷⁸ is a bifunctional catalyst with activity for both the oxygen and the hydrogen evolution reactions, giving 10 mA/cm^{-2} at overpotentials of 310 mV for the OER and 92 mV for the HER in 1.0 M KOH, and they actually made a small alkaline electrolyzer powered by an AAA battery using this material on both electrodes.

The best catalytic performance for the OER of an earth-abundant catalyst that contains no nickel was reported in 2016 by Zhang *et al.* (see Table 1.2, entry 9).⁷⁹ These authors used DFT to predict that mixed oxides containing iron, cobalt and tungsten would display optimal binding energies of the various potential *OH, *O and *OOH intermediates on the catalyst surface (where * indicates a surface-bound species). Accordingly, the authors synthesised **FeCo oxides doped with W(VI)** ions by very carefully controlled hydrolysis of solutions of the simple metal salts. This control avoided phase-separation of the various components in the resulting catalyst gels, which displayed excellent activity for the OER for periods of continuous operation of over 500 h. The generality of this approach presents numerous opportunities for the generation of addition multi-metal catalysts for the OER. Shao-Horn and co-workers have similarly used computational methods to guide the design of OER catalysts, in their case leading them to identify and then experimentally verify the mixed-metal **perovskite $\text{Ba}_{0.5}\text{Sr}_{0.5}\text{Co}_{0.8}\text{Fe}_{0.2}\text{O}_{3-\delta}$** as an active OER catalyst in basic media.⁸⁰ An alternative approach to the identification of mixed-metal OER catalysts has been reported by Gregoire and co-workers, who used a high-throughput screen to produce 5456 discrete oxide compositions containing the elements nickel, iron, cobalt and cerium by inkjet printing.⁸¹ The best of the materials they identified (**$\text{Ni}_{0.2}\text{Co}_{0.3}\text{Ce}_{0.5}\text{O}_x$**) displays a current density for the OER of 10 mA cm^{-2} at only 310 mV overpotential. Such screening methods can be extremely useful for identifying potentially highly-active catalysts, but they do not allow the prediction of long-term stability (which must therefore be established through

more traditional means). Nevertheless, it is to be expected that many more OER catalysts will be identified through such methods in the coming years.

Very recently Fan *et al.*⁸² reported a **Fe-V** composite that gives current densities of 10 mA cm⁻² at 390 mV overpotential, with a Tafel slope of 36.7 mV decade⁻¹, close to 100% Faradaic yield for O₂ evolution and good stability (the catalyst maintains 10 mA cm⁻² galvanostatically for more than 10 h without showing any increase in the overpotential). The authors prepared this material by hydrothermal deposition using FeCl₃ and VCl₃ as precursors, obtaining a Fe-V composite as solid spheres containing a mixture of α , β and γ -FeOOH and vanadium oxides with oxidation states V(III), V(IV) and V(V). When they examined the catalyst again after testing it for oxygen evolution in 1 M KOH they found that the spheres were now “hollow”, and that all the vanadium was as V(III). Bearing in mind that the ionic radii of V(III) and Fe(III) are quite similar, so that V(III) ions can substitute some Fe(III) in the FeOOH, but those of V(IV) and V(V) are much smaller, they proposed that during the hydrothermal synthesis some of the V(III) ions are oxidized to VO₂ and V₂O₅, which forms the core of the spheres, while the rest of the V(III) integrates itself in the FeOOH structure that constitutes the shell. Upon anodization in 1 M KOH, the pure vanadium oxides at the core dissolve in the KOH, leaving a hollow V-doped FeOOH shell of composition FeV that acts as the catalyst for the OER. This is an important result, since FeOOH is unstable in alkaline media, suggesting that the incorporation of the V(III) ions chemically stabilizes this material. Also, it is the first mixed metal oxide catalyst with high activity for the OER in alkaline media in which iron is not accompanied by nickel or cobalt, one or both of which had up to now been regarded as indispensable.

1.4.2 OER electrocatalysts based on single metal oxides

The OER electrocatalysts discussed so far have all been optimized for use in rather basic media (pH 13-14). And yet, as discussed in Section 1.1.3, mild pH regimes may be advantageous in artificial photosynthesis systems. In Nature, water oxidation is carried out by a Mn₄Ca cluster embedded in a protein environment in photosystem II (PSII) and the electrons are transferred through a series of cofactors to photosystem I (PSI), where the protons are reduced to hydrogen in the form of NADPH. The Mn₄Ca cluster operates at ambient conditions of temperature and pressure from natural water sources at neutral pH. In this section we will have the chance to discuss some WOCs that approach this manganese

cluster both in structure and functionality, as well as a selection of other electrocatalysts based on single metal oxides that have been described in the last two decades.

COBALT OXIDES

In 2008 Nocera and co-workers reported a **cobalt oxy-hydroxide** catalyst that performs the OER over many hours of continuous operation at modest overpotentials in neutral buffers and whose structure resembles that of the Mn_4Ca cluster, including a self-healing mechanism (Table 1.2, entries 12-13).⁸³⁻⁸⁵ The local structure of the proposed active sites in this catalyst has been suggested to approximate to incomplete Co-oxo cubanes, as illustrated in Figure 1.4.^{86,87} Figure 1.4 also shows the proposed mechanism by which the catalyst turns over during water oxidation: Co(III) centres in the catalyst resting state undergo oxidation to Co(IV) under anodic bias, and it is these Co(IV) centres that oxidize water to give O_2 .⁸⁸ As this happens, the Co(IV) centres are themselves reduced to Co(II). Co(II) compounds tend to be substitutionally-labile, with the result that the Co(II)-oxides readily dissolve into solution. However, provided an anodic bias is maintained, these Co(II) ions are then rapidly re-oxidized by the electrode and re-deposit as Co(III)-oxides, giving the catalyst functional (rather than structural) stability.⁸⁹ Of special relevance to the development of low-cost solar-to-hydrogen devices, these cobalt catalysts were found to work effectively in both phosphate-buffered seawater and from buffered (but otherwise untreated) river water.⁹⁰ This is in contrast to most commercial electrolyzers, which require high purity water inputs.

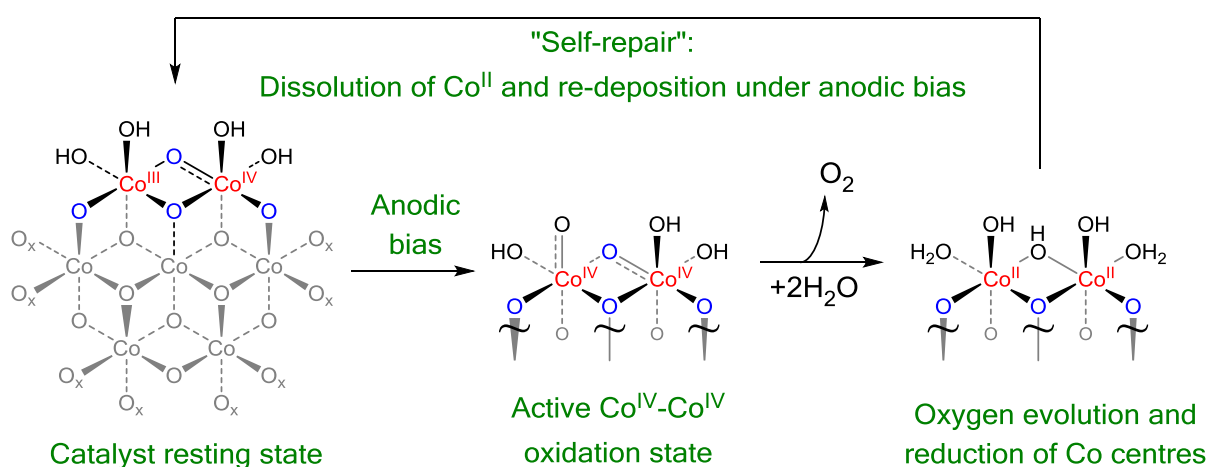


Figure 1.4 Neutral pH OER with a cobalt catalyst. The structure and OER mechanism of Nocera's Co oxy-hydroxide water oxidation electrocatalyst, showing the generation of the active Co(IV) oxidation state and the dissolution/re-deposition "self-repair" mechanism.

It is worth mentioning that Cobo *et al.*⁹¹ have extended this work to the HER upon realizing that when these CoPi-like deposits on FTO substrate are poised cathodically they do not dissolve: they are reduced instead on the electrode to cobalt metal with a thin overlayer of a cobalt-oxy-phosphate material. This new material shows moderate activity for the HER, giving 1 mA cm^{-2} of current density at around 400 mV overpotential.

Since these reports on the OER activity of cobalt oxides at neutral pH, numerous other groups have measured the performance of Co-containing materials as OER catalysts across a wide pH range (*e.g.* Table 1.2, entries 15-17). In particular, heterogeneous Co-oxides have been shown to be competent catalysts of the OER under more basic conditions. For example, Switzer and co-workers⁹² electrodeposited films of Co_3O_4 from solutions of cobalt (II) tartrate at pH 14 over a range of temperatures, and found that the films grown between 50 – 90 °C were amorphous and exfoliated from the electrode, while those deposited at 103 °C were crystalline and robust. They tested all these films in 1 M KOH and found that the crystalline ones had Tafel slopes of $49 \text{ mV decade}^{-1}$ and reached 1 mA cm^{-2} of current density at 300 mV of overpotential. Some activity for these materials has also been observed at low pH: Stahl and co-workers⁹³ obtained quite robust films of cobalt oxides from solutions of potassium fluoride containing CoSO_4 at pH 3.5, requiring about 500 mV of overpotential to get 1 mA cm^{-2} . They later expanded their investigations of cobalt oxides in a range of buffers across the whole pH range, observing that these films mediate water oxidations above pH 3.5 but below this value they dissolve to give Co(II) soluble species which mediate water oxidation to H_2O_2 instead.⁹⁴ Despite this result, a few years later Bloor *et al.* showed that both a Co-oxide water oxidation catalyst and a Co-metal based proton reduction catalyst could be electrodeposited simultaneously from 0.2 M $\text{Co}_2(\text{PO}_4)_3$ at pH 1.6 under an applied bias, being functionally stable for the two half-reactions of water splitting for as long as the potential difference across the cell was at least 2 V. If the circuit was opened the films re-dissolved with concomitant O_2 and H_2 evolution, and it was possible to redeposit them by reapplication of a suitable difference of potential between the two electrodes. The importance of this work lies in the fact that it showed that the natural tendency of first row transition metal oxides to dissolve at low pH is not an impediment for using them as heterogeneous water splitting electrocatalysts, the key being in exploiting, rather than trying to avoid the fact that they dissolve to use them as functional, metastable catalysts.⁹⁵

Apart from cobalt oxides, cobalt-containing phosphides have very recently emerged as promising heterogeneous catalysts for the OER,^{96,97} and doubtless the OER activity of many more such materials will be reported in the near future.

NICKEL OXIDES

Not long after reporting his neutral-pH cobalt-oxide OER catalyst, Nocera described its **nickel** analogue.²⁴ Detailed analysis of the performance of this catalyst for the OER revealed that the catalytic activity improved gradually over the first few hours of operation under anodic bias, with Tafel slopes of 30 mV decade⁻¹ manifesting after sufficient anodization.⁹⁸ X-ray absorption near-edge structure spectra collected on samples after various amounts of anodization revealed a shift in the average oxidation state of the Ni centres in the catalyst from +3 before any anodization to +3.6 once anodization was complete.⁹⁹ This was interpreted as indicating that Ni(IV) was the active species in the catalytic cycle (just as Co(IV) is the active site for the neutral pH cobalt-oxide water oxidation catalyst described above), with the formation of Ni(IV) from Ni(III) requiring a significant energy input (manifested in the need for anodization) on account of the reorganization energy required to overcome the Jahn-Teller distortion in the Ni(III) centres. Other Ni-only OER catalysts have subsequently been reported,^{100,101} but the fact remains that nickel oxides appear to be inferior catalysts compared to iron-doped nickel oxides.

MANGANESE OXIDES

Even though **manganese oxides** are Nature's choice of OER catalyst, they have proved much less successful as electrocatalysts of the OER. A selection of the better performing of these electrocatalysts is given in Table 1.2 (entries 23-25).¹⁰²⁻¹⁰⁴ Typically, the more active manganese oxide OER catalysts display a high degree of structural disorder and contain Mn in more than one oxidation state. Structural disorder produces smaller Mn-oxo platelets with a large number of coordinatively unsaturated and partially reduced {Mn(III)O₅} moieties at the plate boundaries which may act as hole traps, promoting the oxidation of nearby water molecules under anodic bias.^{105,106} Meanwhile, the role of the mixed Mn valence states in the catalysis displayed by these materials is much less clear-cut, with various groups suggesting that MnO₂,¹⁰⁷ Mn₂O₃⁹⁴ or mixtures of these phases¹⁰⁸ are all required for efficient catalysis of the OER.

Leaving structural discussions aside, the fact is that manganese oxides have much lower overpotentials for the OER at pH >13. Takashima *et al.* used spectroelectrochemical methods to follow the changes in the composition of Mn-oxide catalysts during electrolytic water oxidation at a range of pH values. They related the drop-off in activity below pH 8 with the disproportionation of Mn(III) into soluble Mn(II) salts and insoluble Mn^{IV}O₂ (see Figure 1.5), concluding that manganese oxides could only work as electrocatalysts for the OER at pH values well above 8 so that Mn(III)-species, which they consider the catalytically active species, are stabilized.^{109,110}

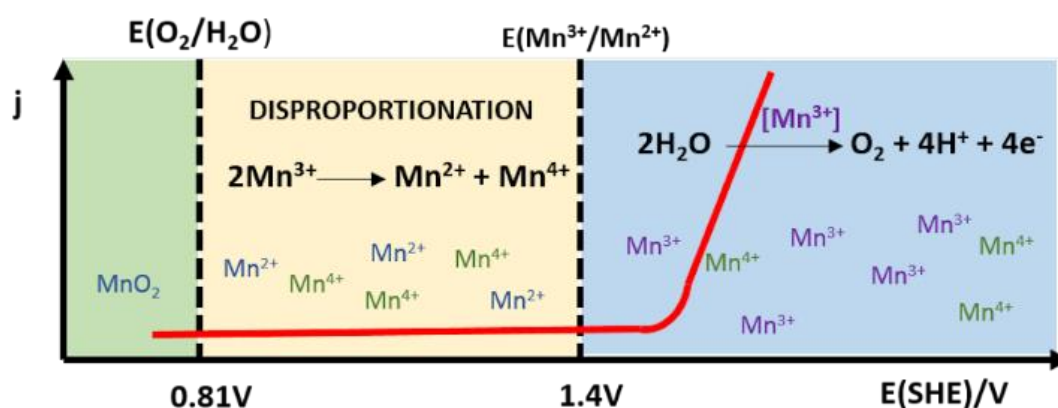


Figure 1.5 Illustration of the current density (j) vs. potential curve for MnO_2 at neutral pH according to Takashima *et al.* showing where disproportionation occurs. The dotted line at 0.81 V vs SHE denotes the standard reduction potential of the $\text{O}_2/\text{H}_2\text{O}$ couple at this pH. We see though that the onset value for water oxidation takes place at about 1.5 V, which corresponds approximately to the potential at which Mn^{3+} becomes stable, providing the basis of the hypothesis of Mn^{3+} being the catalytically active oxidation state of manganese for this reaction.

This supposition of Mn (III) ions being responsible of the catalytic activity appears to be borne out by subsequent analysis of the mechanism of the OER at manganese oxides over the pH range 0-14 undertaken by Huynh *et al.*^{111,112} As in the case of Takashima's group, Huynh *et al.* first electrodeposited the manganese oxide catalyst onto FTO and subsequently examined its electrochemical properties as a function of pH. They observed that at high pH the Tafel slopes were around 60 mV decade⁻¹ and that there was an inverse first order dependence on proton concentration. On the other hand at low pH the Tafel slopes were quasi-infinite and the reaction was independent of the proton concentration. Intermediate Tafel slopes and proton-dependency values observed at neutral pH suggested two competing mechanisms in place, one at low pH and the other at high pH, as depicted in Figure 1.6. This

alternative acid regime mechanism explains why Mn-oxides can catalyze the OER at low pH, which otherwise would contradict the results of Takashima *et al.* discussed above.

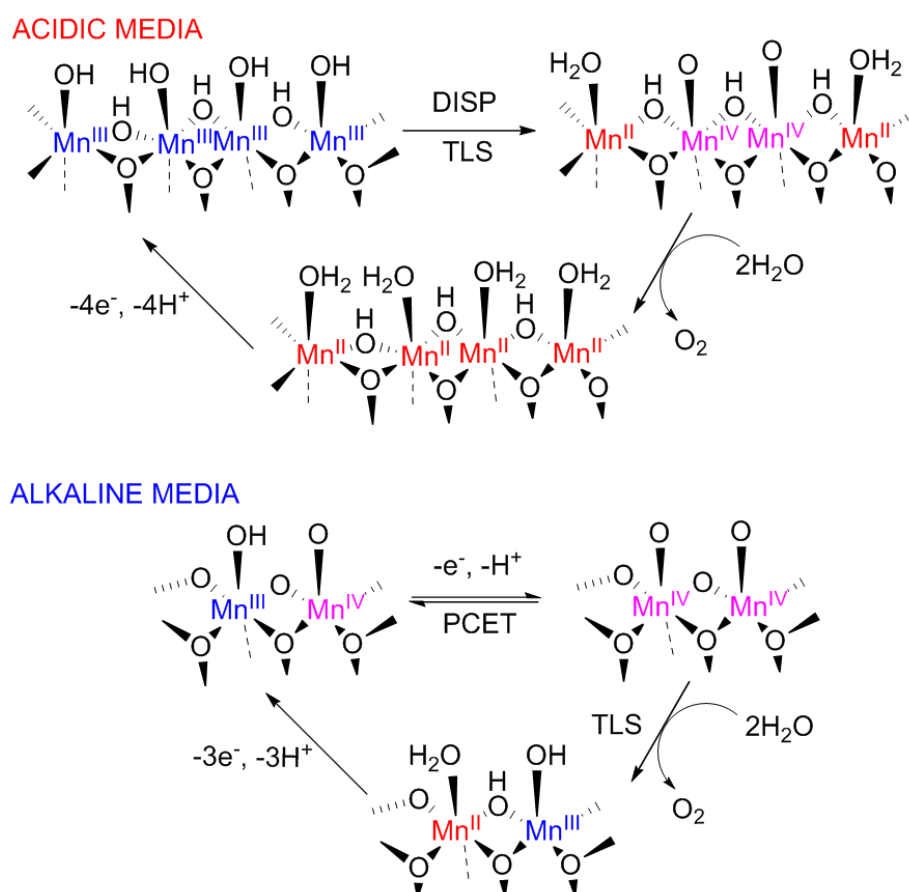


Figure 1.6 Proposed mechanisms for the OER as mediated by manganese oxides under acidic and basic conditions. DISP = disproportionation; TLS= Turnover Limiting Step; PCET = Proton-Coupled-Electron Transfer.

COPPER AND IRON OXIDES

Copper oxides have recently been shown to be active for the OER, although the catalysts reported so far require much bigger overpotentials than all the catalysts we have discussed in this section. As way of example, Yu *et al.*¹¹³ electrodeposited copper oxide films from 1 mM $Cu(NO_3)_2$ in borate buffer, which gave 1 mA cm^{-2} of current density at overpotentials between 550-600 mV. In light of our findings in Chapter 3 regarding the activity of trace nickel impurities for the OER under these conditions,¹¹⁴ one wonders if the results reported in this paper are actually due to copper oxides. Other groups are exploring the

electrodeposition of Cu-oxide films from Cu-containing metal-ligand complexes, but this strategy adds the need to synthesize the complexes, which are used only as precursors, and do not seem to be helping to lower the overpotentials.¹¹⁵ **Iron oxides** may be more promising, even though they have been studied much less than those of its neighbour metals in the periodic table, probably due to the low solubility of Fe(III) in neutral aqueous solutions. Some reports concerning this material have started to appear over the last years, though. For example, Wu *et al.* reported in 2015 an iron-oxide film electrodeposited by cyclic voltammetry from FeSO₄ solutions that requires only 530 mV to give 1 mA cm⁻² at neutral pH.¹¹⁶ This is an interesting finding, although to date it looks like iron is more useful as dopant for nickel films rather than on its own.

Table 1.2 summarizes a selection of the OER catalysts discussed in this section. Inspection of this table shows that mixed oxides containing Ni tend to give the best performance for the OER under basic conditions, whilst Ni and Co oxides are the most effective at near-neutral pH. There are currently no good Earth-abundant catalysts for the OER under acidic conditions, mainly because they tend to dissolve and degrade in this media. And yet the identification of a stable catalyst that can perform the OER at low pH would be a major advance in the field, with potential applications both in artificial photosynthesis systems and in more conventional polymer electrolyte membrane electrolyzers.

Table 1.2: Overpotential (η) requirements, Tafel slopes and Faradaic yields of some selected earth-abundant OER electrocatalysts.

Entry	Catalyst material	η at 1 mA cm ⁻² (mV)	Tafel slope (mV/decade)	pH	Faradaic yield	Ref
1	Ni-Fe oxides on Pt substrate	30	15	14	N/A	68
2	Ni-Fe oxides	≈120	32	15	N/A	69
3	Ni-Fe oxides	210	31	14	~100% ^a	70
4	Ni-Fe oxides	~180	40	14	N/A	71
5	Ni-Fe oxides	300 (10 mA cm ⁻²)	40	14	N/A	72
6	Ni-Co oxides	370	N/A	13	N/A	75
7	Ni-Mo oxides	300	47	14	N/A	78
8	Fe-Co-W oxyhydroxides	191 (10 mA cm ⁻²)	N/A	14	100% ^a	79
9	Ba _{0.5} Sr _{0.5} Co _{0.8} Fe _{0.2} O _{3-δ}	~320	~60	13	N/A	80
10	Ni-Co-Ce oxides	250	~60	14	97% ^a	81
11	V _{0.5} Fe _{0.5}	292	37	14	100% ^a	82
12	Co oxides	410	60	7	100% ^b	83
13	Co oxides	390	60	9.2	100% ^b	85
14	Co oxides	530	75	9.2	N/A	90
15	Co ₃ O ₄	300	49	14	N/A	92
16	Co oxides	~480	~120	3.5	>95% ^b	93
17	Co oxides	~900	N/A	1.6	96% (±2%) ^a	95
18	Co-P	345 (10 mA cm ⁻²)	47	14	100% ^a	96
19	CoMnP	330 (10 mA cm ⁻²)	61	14	96% ^a	97
20	Ni oxides	380	30	9.2	100% ^b	98
21	Ni oxides	450	72	9.1	N/A	100
22	Ni oxides	320 (10 mA cm ⁻²)	52	14	~100% ^a	101
23	Mn oxides	<300	N/A	13	N/A	102
24	Mn oxides	280	N/A	14	N/A	103
25	Mn oxides	300	114	14	~100% ^b	104

Notes: a) Quantified by gas chromatography, b) Quantified using a fluorescence-quench sensor.

1.5 Earth-Abundant Catalysts for Photoelectrochemical Water Splitting

Water splitting can also be performed by photolysis, whereby light energy is used to overcome the necessary energy barrier to drive the water splitting reaction. In order for a single material to split water unaided by an external bias, it must have a band gap in excess of 1.23 eV. As it must also be able to supply additional energy for overcoming various overpotentials and electron-transfer-induced losses, band gaps of between 1.6 – 2.4 eV (corresponding to wavelengths in the visible region between ~800 and 500 nm) are required for practical water-splitting applications.¹¹⁷ Various other factors (band-edge position, charge-carrier diffusion lengths, *etc.*) must then be taken into consideration when selecting an appropriate semiconductor light-absorber, as discussed in reference 117. Identifying semiconductor materials that have optimal characteristics for the above and that are stable with respect to the conditions under which they must operate (aqueous solutions, possibly at variable pH) is in fact extremely challenging. In the face of these factors, a blind eye is generally turned to the cost of these materials in the first instance, and indeed the projected costs of many artificial photosynthesis systems are therefore dominated by the cost of the light-absorbing components.

Once semiconductors with the appropriate light absorption and stability profiles have been identified, electrocatalysts are normally deposited on top of these in order to reduce overpotentials for the OER and HER, just as with a conventional electrode. In this section, we will discuss electrocatalyst-light harvester ensembles that have been used to drive the HER and OER in isolation (often with the aid of an additional external bias). Such studies are useful for optimizing a particular semiconductor-electrocatalyst combination and can be viewed as stepping-stones to the development of artificial photosynthesis systems for water splitting without external bias. Unless otherwise stated, all values of current densities and overpotentials will be referred to 1 Sun of illumination. In this context, “1 Sun” corresponds to the illumination from the Sun that hits a perpendicular surface through an air mass of 1.5, which is the air mass on a bright day accounting for an average pollution and humidity.¹¹⁸ Under these conditions, the accepted value for the received sunlight is 1 kW m^{-2} . Therefore an illumination of 10 Suns, for example, would be 10 kW m^{-2} .

1.5.1 Catalysts for the Photoelectrochemical HER

Silicon and the III-V semiconductors (namely GaAs, GaP, InP, and their solid solutions) can be used either as photocathodes when they are p-doped or as photonanodes when n-doped. Silicon is the most common choice, due to its natural abundance and low cost compared to other semiconductor materials, as well as its versatility. Silicon itself is unstable in aqueous media, but many strategies have been developed to protect it, such as covering it with layers of TiO₂, Al₂O₃ or catalysts for the HER so that its surface is protected against corrosion. At present it is probably the best photocatalytic material for working at low pH, at least in terms of stability, and the fact that most of the best HECs reported have been developed to work at pH near 0 is another reason for its popularity. A key early result in this area was established by Chorkendorff and co-workers, who deposited a molybdenum sulfide catalyst onto a p-type silicon semiconductor substrate that was optimized to absorb red light photons (wavelengths > 620 nm). The authors used photolithography to pattern the Si substrate, producing a “pillar” architecture (somewhat reminiscent of a microscale toothbrush). This design provided a large surface area for the HER catalyst whilst optimizing photocurrent collection efficiency. Compared to planar Si substrates decorated with the same electrocatalyst, the pillared Si/MoS_x arrays displayed higher current densities for the HER at all potentials, giving -10 mA cm^{-2} at 0 V vs. RHE.¹¹⁹

The first eight rows in Table 1.3^{45, 119-125} are examples of photoelectrocatalytic systems containing silicon in combination with different catalysts. Even though most of these are examples at low pH, rows 2 and 8 show examples at pH 7 and 14, respectively. This last one, a recent work by the Hu group,¹²⁵ is particularly remarkable, since it is the first report in which Si-based photocathodes are used in strongly alkaline electrolytes for the HER. The material described consisted of a molybdenum carbide catalyst in combination with an amorphous silicon light absorber and was able to perform the HER under 1 Sun illumination without any applied bias giving current densities of -11 mA cm^{-2} in both 0.1 M H₂SO₄ and 1 M KOH. It should be noted however that at pH 14 the material deactivates after 1 h, but still this opens the door to try silicon at a wider pH range than had been considered so far.

Cadmium chalcogenides have been used as photoactive substrates for the deposition of earth-abundant HER electrocatalysts,^{126,127} (rows 9-10), but the main alternatives to Si at the present time are the copper oxides.¹²⁸⁻¹³⁰ By way of example, we will consider a recent report by Morales-Guio *et al.* who used a photo-active layer of Cu₂O to harvest visible

photons (Table 1.3, entries 14 and 15).¹³¹ Cu_2O has an ideal bandgap for solar-to-hydrogen applications (~ 2 eV),¹³² but it tends to corrode rapidly in aqueous environments. Hence the authors used thin layers of aluminium-doped ZnO and TiO_2 as barriers to protect the underlying Cu_2O . Under 1 Sun irradiation at pH 0, these films performed the HER at a current density of -5.7 mA cm^{-2} at 0 V *vs.* RHE, although the films were not stable and activity declined steadily over a few hours of operation. Under slightly milder conditions, however (pH 4), the HER photocurrent at 0 V *vs.* RHE was stable at -4.5 mA cm^{-2} for at least 10 h. The effectiveness of this protection strategy bodes well for the application of Cu_2O as a photocathode in the future.

CuO has also been studied, but it has received less attention due to it having the same corrosion problems as Cu_2O and an indirect and narrower bandgap. Indirect bandgaps are less desirable than direct ones because they imply a slower rate in the light absorption process. When a photon of energy E_g (E_g being the bandgap energy) interacts with a semiconductor the energy of this photon is used to create an electron-hole pair. Photons in the visible range of the spectrum have a really tiny momentum, enough to create an electron-hole pair in a direct semiconductor, since both the valence and conduction band have basically the same momentum value and therefore the electron does not need to be given *extra* momentum, but not enough to create it in an indirect semiconductor, where the valence and conduction bands have different values of the momentum. As a result, for an electron-hole pair to be created in an indirect semiconductor, the electron needs to interact also with a phonon, which provides it with the extra momentum needed, as shown in Figure 1.7. This requirement makes light absorption in semiconductors with an indirect bandgap a slower process compared to a direct bandgap semiconductor, which is why direct ones are, if possible, preferred.

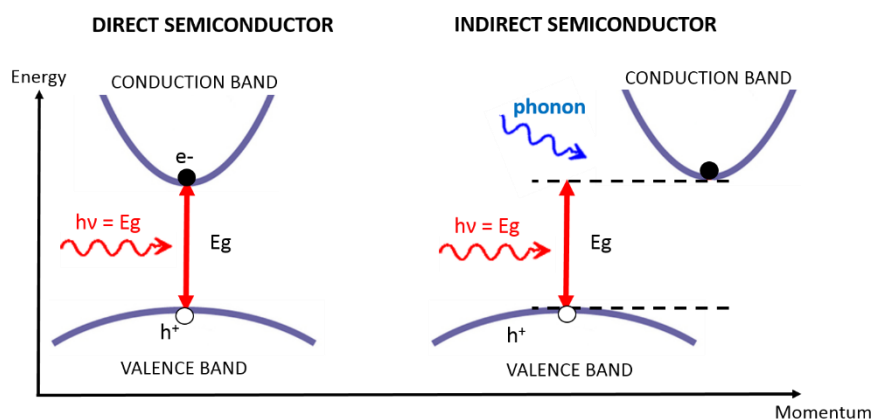


Figure 1.7 Diagram showing the process of forming an electron-hole pair in a direct (left) and indirect (right) semiconductor material upon receiving a photon of energy, E_g .

Other materials currently being explored are ternary oxide photocathodes, such as CuFeO_2 or CuInS_2 . It is important to note here that most of the catalysts in Table 1.3, which have been selected from the best publications about each type of material, suffer from serious instability issues, and are therefore far from being ready to be applied in artificial photosynthesis systems: any candidate should demonstrate stability over thousands of hours of continuous operation, whereas many of these catalysts suffer a significant reduction in efficiency over just a few hours.

Table 1.3: Photocurrents and Faradaic yields at 0 V vs. RHE of some selected earth-abundant HER photoelectrocatalytic systems.

Entry	Catalyst material	Photoactive substrate	Current density at 0 V vs. RHE and 1 Sun illumination (mA cm^{-2})	pH	Faradaic yield	Ref
1	Mo_3S_4	p-Si	-10	0	100% ^a	119
2	Co-S	planar n+/p-Si	-11	7	100% ^a	45
3	W_2C	p-Si	-4	0	N/A	120
4	MoS_2	planar n+/p-Si	-17.6	0	100% ^a	121
5	CoPS	n+-p-p+ silicon	-35	0	N/A	122
6	Co dithiolene polymer	p-type Si	-3.8	1.3	80% ($\pm 3\%$) ^a	123
7	Ni-Mo	p-type Si	-15	4.5	N/A	124
8	Mo_2C	Surface-protected Si	-11.2	14	100% ^b	125
9	Co_3O_4	CdS	-0.15 (+0.12 V)	7	N/A	126
10	NiO/CoP	CdSe	-0.15 (+0.4 V)	6.8	81% ^a	127
11	NiO _x	Cu_2O	-5	6	32% ($\pm 6\%$) ^a	128
12	Cu_2MoS_4	Cu_2O / NiO	-1.25	5	< 23% ^a	129
13	Ni	$\text{Cu}_2\text{O}/\text{CuO}$	-4.3	5	84% ^a	130
14	MoS_x	Cu_2O	-4.8	4	100% ^b	131
15	MoS_x	Cu_2O	-5.7	1	100% ^b	131

Notes: a) Quantified by gas chromatography, b) Quantified using a pressure sensor.

1.5.2 Catalysts for the Photoelectrochemical OER

If the photocathodes listed in Table 1.3 gave decent current densities without the need to apply an external bias but had serious stability problems, the situation is basically the opposite for photoanodes: as we can see in Table 1.4, all the systems listed need applied bias potentials of several hundreds of millivolts to drive the water oxidation reaction even under 1 Sun irradiation, just to give 1 mA cm^{-2} , but it is fair to say that they suffer less from stability issues. In order for a material to be used as a photoanode it needs to be an n-type semiconductor, and the first of these materials that was demonstrated to work for this application was **TiO₂**. Its excellent photostability and chemical stability at all pHs make it an excellent choice as photoanode, and it is actually used as protective layer for other photoactive materials, but its big bandgap (3 – 3.2 eV) means that its main absorbance is in the UV part of the spectrum. The same problem occurs with **WO₃**, with the added disadvantage that this has an indirect bandgap. In an effort to increase the proportion of visible light absorbed by the photoanode, Hardee and Bard used a hematite (**α -Fe₂O₃**) substrate for the OER with irradiation at wavelengths longer than 500 nm and an additional applied bias.¹³³ Hematite has key advantages in terms of its light absorption profile ($E_g = 2.0 - 2.2 \text{ eV}$), its high abundance and low cost, however, it also has a high overpotential requirement as an electrocatalyst for the OER. This is why hematite is normally used in combination with a co-catalyst in order to improve the kinetics of oxygen evolution (although see Table 1.4, entries 16 and 17). Cobalt oxides have become the OER catalyst of choice for this purpose, as they can be electrodeposited onto hematite under mild conditions and because they have been shown to be good OER catalysts at the neutral to alkaline pH values where hematite is stable. Gamelin and co-workers were among the first to deposit cobalt oxides onto Fe₂O₃ for the OER, with a reduction in the required overpotential of several hundred millivolts being obtained (Table 1.4, entries 1-3).¹³⁴⁻¹³⁶ Since this report, Co-oxides have been used as co-catalysts of the OER on numerous photoactive substrates, as shown in Table 1.4.¹³⁷⁻¹⁴³ Of these, the best performance in terms of the current density that can be obtained at a given potential was reported recently by Kim *et al.*¹⁴⁴ These authors developed a photoanode consisting of two comparatively cheap light absorbers arranged in series (a single-junction perovskite solar cell and a molybdenum-doped BiVO₄ semiconductor), onto which Co-oxides were deposited as the OER catalyst. The use of two light-harvesting systems in tandem greatly reduced the external bias that was required to achieve a given current density for the OER.

Nickel and iron-based catalysts have also been used as co-catalysts for the photoelectrochemical OER (Table 1.4, entries 12-19).¹⁴⁵⁻¹⁵¹ The best of these uses a combination of Ni and Fe oxides on a **BiVO₄** photoactive substrate and delivers a current density for the OER under illumination of 1 mA cm⁻² at only a little over 300 mV overpotential.¹⁵² The authors found that photoanodes formed by first depositing a layer of FeOOH on the BiVO₄ substrate, then depositing a layer of NiOOH on top of the FeOOH layer gave superior performance compared to photoanodes prepared using individual metal oxy-hydroxides (*i.e.* NiOOH on BiVO₄ and FeOOH on BiVO₄) or photoelectrodes formed in the order BiVO₄-NiOOH-FeOOH.

Table 1.4: Photocurrents and Faradaic yields for some selected earth-abundant OER photoelectrocatalytic systems.

Entry	Catalyst material	Photoactive substrate	Bias required to get 1 mA cm ⁻² under 1 Sun illumination (V vs. RHE)	pH	Faradaic yield	Ref
1	Co	α -Fe ₂ O ₃	1.45	13.6	N/A	134
2	Co	α -Fe ₂ O ₃	1.1	7 – 13.6	N/A	135
3	Co	α -Fe ₂ O ₃	1	13.6	N/A	136
4	Co	WO ₃	1.2 (0.5 mA cm ⁻²)	7	100% ^a	137
5	Co	npp*Si / ITO	1.2	7	100% ^a	138
6	Co	BiVO ₄	1	5.6	N/A	139
7	Co	W-doped BiVO ₄	1	5.6	N/A	140
8	Co	BiVO ₄	1.2	7	N/A	141
9	Co	TiO ₂	1.7 (0.4 mA cm ⁻²)	7	>95% ^b	142
10	Co	TiO ₂ -gC ₃ N ₄	1	6.8	N/A	143
11	Co	BiVO ₄ and perovskite PV	0.5	7	100% ^b	144
12	Ni	BiVO ₄	1	9.2	100% ^a	145
13	Ni	W-doped BiVO ₄	1.3	7	N/A	146
14	Ni	WO ₃	1.2	9.2	N/A	147
15	NiFe	Ti-doped α -Fe ₂ O ₃	1.1	14	N/A	148
16	Fe	α -Fe ₂ O ₃ (the oxide itself)	1.1	14	N/A	149
17	Fe	α -Fe ₂ O ₃ (the oxide itself)	1.15	13.6	N/A	150
18	Ni	n-Si	~1.6 (10 mA cm ⁻²)	9.5	N/A	151
19	NiOOH and FeOOH	BiVO ₄	0.32	7	>90% ^a	152

Notes: a) Quantified using a fluorescence-quench sensor, b) Quantified by gas chromatography.

1.6 Artificial Photosynthesis Systems

In Figure 1.1 we showed the two possible configurations for a direct solar-to-hydrogen device as well as an indirect one. A wireless device is desirable because of its simplicity and compactness, but an issue¹⁵³ with this configuration is that as the efficiency of the buried photovoltaic is increased, a bigger loading of the electrocatalyst materials is required to match it, blocking more sunlight and therefore decreasing the photovoltaic's absorption. This is not a big problem yet because the efficiencies of the photovoltaics used so far in artificial photosynthesis systems are quite low, but it will probably pose a challenge in design as the efficiencies get better in the following years. We will next discuss some relevant examples of artificial photosynthesis devices.

An early example of a wireless artificial photosynthesis system was described by **Rocheleau** and co-workers in 1998.¹⁵⁴ Their design called for a buried amorphous Si PV, with a CoMo alloy as the HER catalyst on one side and a NiFe_yO_x OER catalyst on the other. A useful figure of merit for artificial photosynthesis systems is their solar-to-hydrogen conversion efficiency. In Rocheleau's report, an excellent photoelectrochemical solar-to-hydrogen conversion efficiency of **7.8%** was reported **at pH 14** (for cells of area 1 cm²), with the catalysts themselves exhibiting stability for over 7200 h of operation.

More recently, **Verlage et al.** have reported an improved wireless artificial photosynthesis system device (area = 1 cm²) that also works in **1 M KOH**.¹⁵⁵ In this case, a tandem-junction GaAs/InGaP light harvester was used in combination with a NiMo HER catalyst and a nickel-based OER catalyst. Under 1 Sun illumination, a solar-to-hydrogen conversion efficiency of **8.6%** was obtained.

In terms of producing artificial photosynthesis systems suitable for operation in the field for tens or hundreds of thousands of hours, systems that use less corrosive electrolytes may be required in order to minimize degradation of the photoelectrodes and other cell components. In this regard, several devices that work at near-neutral pH have been reported. The first such system used a (somewhat costly) buried triple-junction silicon light-absorber, a cobalt oxy-hydroxide catalyst for the OER and a ternary NiMoZn HER catalyst.¹⁵⁶ Irradiation of this device (total area 2 cm²) with simulated solar light in borate buffer (**pH 9.2**) led to water splitting with a **2.5%** solar-to-hydrogen conversion efficiency.

Any practical and scalable artificial photosynthesis system will need significantly cheaper light absorbers than triple-junction Si, and some progress has been made in this regard. For example, **Janssen** and co-workers replaced the triple-junction silicon in ref 156 with a triple-junction polymer solar cell, and achieved solar-to-hydrogen conversion efficiencies **at pH 9** of 4.9% (using cells of area $<0.1 \text{ cm}^2$, which decreased to **1.3%** when the cell area was 1.2 cm^2).¹⁵⁷ The use of organic polymers as PVs offers the combined advantages of improved flexibility and lower production costs (as such materials are suitable for roll-to-roll printing) compared to inorganic photovoltaics.

These are so far the most relevant examples of fully integrated (wireless) solar-to-hydrogen devices that do not use precious metals. It has been said¹⁵⁸ that for solar water splitting to become a viable alternative in energy production, the solar-to-fuel conversion needs to be at least 10%, so there is still much work to do. Many are the problems that cause the solar-to-fuel efficiencies to be so low, highlighting the low efficiency of the photovoltaics tried so far. In this sense, a technique that may offer some improvement is to use a concentrator system so that the light intensity arriving to the photovoltaic is higher. Spiccia's group were able to obtain a solar to hydrogen efficiency of 22% in an indirect solar-to-hydrogen Device thanks to this approach. For their work they chose a GaInP/GaAs/Ge multijunction PV harvesting material and bifunctional nickel foam electrodes, placing a suitable convex lens before the incident 1 Sun sunlight to concentrate it into a focused irradiation of 100 suns. This allowed them to achieve about 22.4% solar to hydrogen efficiency at pH 7, 9 and 14 with remarkable stability over multiple 12 h cycles.¹⁵⁹ They argued that the benefits of adding a concentrator exceed by far the increase in the device cost, and that concentrators are widely available and can easily provide intensities between 2 – 300 Suns. This was an indirect approach, where the photovoltaic and the electrolyzer were two independent devices so that sunlight was first converted into electricity and then this was applied to the electrolyzer, but concentrators could be used in integrated devices too, allowing the building of artificial photosynthesis systems capable of giving current densities higher than the $20 - 30 \text{ mA cm}^{-2}$ expected of them under 1 Sun of irradiation. This could widen the range of their applications. On the other hand, it should be noted that while increasing the light intensity from 1 to 100 suns does indeed increase significantly the solar-to-hydrogen efficiency, this is not 100 times higher compared to the same device under an irradiation of 1 sun.

Another issue related to photoelectrochemical devices working at near neutral pH will be the development of pH gradients,¹⁶⁰ which cause the overpotentials at each electrode to increase even more. pH gradients are minimized both at very high and very low pH, but for intermediate values they will be unavoidable unless stirring or other means of convection are employed. Then there is the pending question regarding how hydrogen can be safely harvested from the large surface area arrays that seem to be required (if there is no solar concentration). Assuming current densities under irradiation on the order of 10 mA cm^{-2} , the permeation of both hydrogen and oxygen through membrane separators such as Nafion would be significant and could lead to extensive (and dangerous) mixing of the product gases.¹⁶¹ Although methods do exist to prevent the build-up of dangerous gas mixtures in electrolyzers, these methods would also significantly reduce the overall solar-to-hydrogen efficiencies that could be obtained.¹⁶² Then again, collecting hydrogen efficiently from a large area array (probably at close to atmospheric pressure) is not necessarily a simple task to perform. The recent development of the Electron-Coupled-Proton Buffer (ECPB) offers solutions to some of these challenges, as it allows the OER and HER to be completely decoupled from each other so that the gases are not made in the electrochemical cell at the same time.¹⁶³⁻¹⁶⁵ This remarkable finding is based on quite a simple, yet groundbreaking idea: the addition to the buffer of an intermediate redox agent capable of reversibly accepting the protons and electrons generated in the water oxidation half-reaction and “storing” them until we want to generate the hydrogen. In order to serve as ECPB, this intermediate redox agent needs to fulfill a series of conditions: it has to be very soluble in water at room temperature, so that it is present in the buffer in a significant enough concentration to afford a high storage capacity for protons and electrons. Then, it needs to have at least one reversible redox wave with a reduction potential intermediate between the OER onset and the HER onset. In addition, the ECPB’s only counterion needs to be H^+ , it should be made of Earth-abundant elements and it needs to be stable in the electrolysis conditions. It may seem that these are too many requirements, but the authors showed that all this could be achieved at low pH with commercially available phosphomolybdic acid¹⁶³ and with quinone derivatives.¹⁶⁴ The detailed operating procedure is depicted in Figure 1.8, and can be described as follows: first, a potential is applied to the cell to drive the water oxidation half-reaction. The protons cross to the other compartment through the membrane while the electrons move through an external circuit. These electrons and protons are then taken by the ECPB preferentially over the HER because the energy of the ECPB’s redox wave(s) is intermediate between the onset of the OER and the HER. The ECPB keeps “kidnapping” the

electrons and protons until the potential input is stopped, ideally more or less when all the ECPB is in its reduced form, and it will stay reduced storing these protons and electrons until we decide that we want to release the hydrogen. For this, a second potential input is applied and the ECPB goes back to its initial oxidized form with concomitant production of hydrogen, completing a cycle. Unlike “standard” electrolysis, this system works by means of applying two separated, smaller energy inputs rather than a big one.

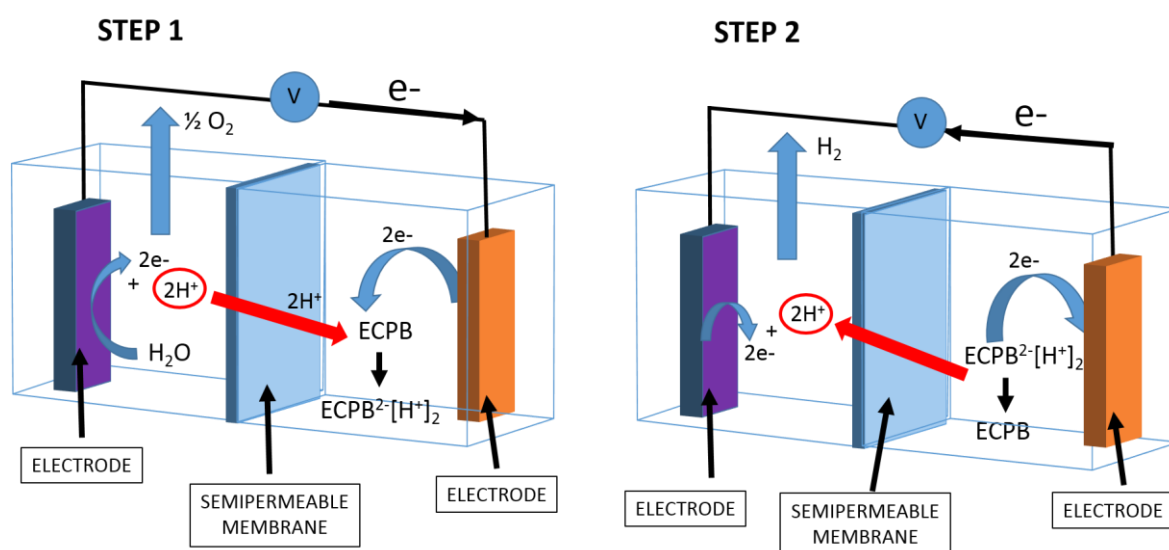


Figure 1.8 Diagram showing how the ECPB works. **Left:** During water oxidation, the protons move through the membrane to the ECPB’s compartment, where they are taken by the ECPB, which gets reduced to $\text{ECPB}^{2-}[\text{H}^+]_2$. **Right:** When all the ECPB is in its reduced form, the potential is reversed and the $\text{ECPB}^{2-}[\text{H}^+]_2$ gives back the electrons and protons, which go back to the left compartment and combine there to produce hydrogen gas.

This way, the HER and the OER are separated in time. In a later paper,¹⁶⁵ the same authors managed to also decouple the two water splitting half-reactions *spatially* by introducing an ECPB (silicotungstic acid, $\text{H}_4[\text{SiW}_{12}\text{O}_{40}]$) that is first reduced in the electrolytic cell and then transferred to a separate chamber where it spontaneously releases H_2 without having to apply the second energy input as in the initial design. As a result, hydrogen is not produced in the electrolytic cell itself, eliminating once and for all any gas mixing problems that could otherwise compromise the safety of the electrolyzer. It is to be expected that in the near future, ECPBs capable of working at near-neutral pH will be proposed, allowing for their implementation in artificial photosynthesis devices.

1.7 Conclusions and future challenges in the field

In this chapter we have explained the need of energy storage systems for the effective implementation of renewable energies, and how electrochemical and photoelectrochemical water splitting constitute one of the most attractive options for this. We have introduced the concept of solar-to-hydrogen devices with their different design approaches and discussed their suitability for different applications. We have also discussed the different kinds of materials based on Earth-abundant elements that can be used as electrocatalysts for the HER and the OER, highlighting the best results achieved so far, commenting too on a selection of photocathodes and photoanodes as well as some examples of actual solar-to-hydrogen devices. In all, we have provided an overview of the current state of the field.

Many are the challenges that remain facing the development of affordable and reliable artificial photosynthesis systems for solar-driven water splitting. In all the examples described in Section 1.6, the areas of the devices are on the order of a centimeter, and it will take a lot of effort in many areas (charge transport, catalyst performance and stability, need of cheaper components) before these devices are ready for scaling up. There is also the serious mismatch between the optimal conditions under which most of the earth-abundant OER (photo-)electrode systems operate ($\text{pH} \gg 7$), and those suitable for the HER (generally $\ll \text{pH} 7$). In practice, near-neutral pH conditions may be preferred (or even required) in artificial photosynthesis systems on account of component longevity and regulatory issues. Looking at electrocatalytic water splitting more generally, Earth-abundant HER and OER catalysts that work at very high and very low pH will also doubtless be of great utility (*e.g.* for the production of cheaper conventional electrolyzers that run using other forms of renewable energy). Electrocatalysis of the OER at high pH using NiFe oxide electrodes is well established, yet low pH water oxidation with Earth-abundant electrocatalysts presents enormous challenges in terms of catalyst stability and overpotential demands. Operation at high or low pH seems less of an issue for the HER (Table 1.1), but considerable optimization is almost certainly achievable here too. With regard to the development of new catalysts, combined computational and high-throughput methods hold great promise for identifying highly active formulations.

In all, much work is needed in this multidisciplinary and fascinating field, posing great challenges for electrocatalyst optimization, semiconductor development, device design and cost-balance considerations. And yet, if we think of how much we have advanced in the last

two decades, we may not be that far from the day in which solar-to-hydrogen devices will become a reality.

1.8 References

- (1) International Energy Outlook 2016, <https://www.eia.gov/outlooks/ieo/>
- (2) Lewis, N. S.; Nocera, D.G. *Proc. Natl. Acad. Sci. U.S.A.* **2006**, *103*, 15729.
- (3) Olah, G. A.; Prakash, G.K. S.; Goeppert, A. *J. Am. Chem. Soc.* **2011**, *133*, 12881.
- (4) Shafiee, S.; Topal, E. *Energ. Policy* **2009**, *37*, 181.
- (5) Armaroli, N.; Balzani, V. *Angew. Chem. Int. Ed.* **2007**, *46*, 52.
- (6) <https://ec.europa.eu/energy/en/topics/renewable-energy>
- (7) http://ec.europa.eu/eurostat/statistics-explained/index.php/File:Electricity_generated_from_renewable_energy_sources,_EU-28,_2004%E2%80%9314_YB16-fr.png
- (8) https://www.gov.uk/government/uploads/system/uploads/attachment_data/file/547977/Chapter_6_web.pdf
- (9) <http://www.ref.org.uk/publications/327-2015-update-on-progress-towards-2020-renewables-target>
- (10) MIT Energy Review, 2016, <https://www.technologyreview.com/s/601514/germany-runs-up-against-the-limits-of-renewables/>
- (11) <https://www.cleanenergywire.org/factsheets/germanys-greenhouse-gas-emissions-and-climate-targets>
- (12) <http://www.independent.co.uk/environment/renewable-energy-germany-negative-prices-electricity-wind-solar-a7024716.html>
- (13) <http://ceenews.info/en/negative-power-prices-during-christmas-time-in-germany/>
- (14) Holladay, J.D.; Hu, J.; King, D.L.; Wang Y. *Catal. Today* **2009**, *139*, 244.
- (15) Symes, M.D.; Cronin, L. “Materials for a sustainable future, chapter 18”, RSC Publishing, **2012**, Cambridge, UK
- (16) Du, P.; Eisenberg, R. *Energy Environ. Sci.* **2012**, *5*, 6012.
- (17) <http://www.itm-power.com/project/wind-hydrogen-development-platform>
- (18) Tachibana, Y.; Vayssieres, L.; Durrant, J. R. *Nat. Photonics*, **2012**, *6*, 511.
- (19) Le Formal, F.; Bourée, W. S.; Prévot, M. S.; Sivula, K. *Chimia*, **2015**, *69*, 789.

- (20) Joya, K. S.; Joya, Y. F.; Ocakoglu, K.; van de Krol, R. *Angew. Chem. Int. Ed.* **2013**, *52*, 10426.
- (21) McCrory, C. C. L.; Jung, S.; Ferrer, I. M.; Chatman, S. M.; Peters, J. C.; Jaramillo, T. F. *J. Am. Chem. Soc.* **2015**, *137*, 4347.
- (22) Faber, M. S.; Jin, S. *Energy Environ. Sci.* **2014**, *7*, 3519.
- (23) Nocera, D. G. *Acc. Chem. Res.* **2012**, *45*, 767.
- (24) Dinca, M.; Surendranath, Y.; Nocera, D. G. *Proc. Natl. Acad. Sci. U.S.A.* **2010**, *107*, 10337
- (25) Lefrou, C. ; Fabry, P. ; Poinet, J-C “Electrochemistry: The Basics, with examples” *Springer-Verlag Berlin Heidelberg*, **2012**.
- (26) Doyle, L.; Lyon, M. E. G. “Photoelectrochemical Solar Fuel Production” Chapter 2 (41-105).
- (27) Guidelli R.; Compton, R. G.; Feliu, J. M.; Gileadi, E.; Lipkowski, J.; Schmickler, W.; Trasatti, S. *Pure Appl Chem* **2014**, *86*, 245.
- (28) Ye, D.; Wu, T.; Cao, H.; Wang, Y.; Liu, B.; Zhang, S.; Kong, J. *RSC Adv.* **2015**, *5*, 26710.
- (29) Fan, C.; Piron, D. L.; Sleb, A.; Paradis, P. *J. Electrochem. Soc.* **1994**, *141*, 382.
- (30) Arul Raj, I.; Vasu, K. I. *J. Appl. Electrochem.* **1990**, *20*, 32.
- (31) McKone, J. R.; Sadtler, B. F.; Werlang, C. A.; Lewis, N. S.; Gray, H. B. *ACS Catal.* **2013**, *3*, 166.
- (32) Wang, Y.; Zhang, G.; Xu, W.; Wan, P.; Lu, Z.; Li, Y.; Sun, X. *ChemElectroChem.* **2014**, *1*, 1138.
- (33) Trasatti, S. *J. Electroanal. Chem.* **1972**, *39*, 163.
- (34) Quaino, P.; Juarez, F.; Santos, E.; Schmickler, W. *Beilstein J. Nanotechnol.* **2014**, *5*, 846.
- (35) Nørskov, J. K.; Bligaards, T.; Logadottir, A.; Kitchin, J. R.; Chen, J. G.; Pandalov, S.; Stimming, U. *J. Electrochem. Soc.* **2005**, *152*, J23.
- (36) Sheng, W., Myint, M., Chen, J. G.; Yan, Y. *Energy Environ. Sci.* **2013**, *6*, 1509
- (37) Hinnemann, B.; Moses, P. G.; Bonde, J.; Jorgensen, K. P.; Nielsen, J. H.; Horch, S.; Chorkendorff, I.; Nørskov, J. K. *J. Am. Chem. Soc.* **2005**, *127*, 5308.
- (38) Jaegermann, W.; Tributsch, H. *Prog. Surf. Sci.* **1988**, *29*, 1.
- (39) Jaramillo, T. F.; Jorgensen, K. P.; Bonde, J.; Nielsen, J. H.; Horch, S.; Chorkendorff, I. *Science* **2007**, *317*, 100.

- (40) Kibsgaard, J.; Chen, Z.; Reinecke, B. N.; Jaramillo, T. F. *Nat. Mater.* **2012**, *11*, 963.
- (41) Merki, D.; Fierro, S.; Vrabel, H.; Hu, X. *Chem. Sci.* **2011**, *2*, 1262.
- (42) Li, Y.; Wang, H.; Xie, L.; Liang, Y.; Hong, G.; Dai, H. *J. Am. Chem. Soc.* **2011**, *133*, 7296.
- (43) Li, H.; Tsai, C.; Koh, A. L.; Cai, L.; Contryman, A. W.; Fragapane, A. H.; Zhao, J.; Han, H. S.; Manoharan, H. C.; Abild-Pedersen, F.; Norskov, J. K.; Zheng, X. *Nat. Mater.* **2016**, *15*, 48.
- (44) Faber, M. S.; Dziedzic, R.; Lukowski, M. A.; Kaiser, N. S.; Ding, Q.; Jin, S. *J. Am. Chem. Soc.* **2014**, *136*, 10053.
- (45) Sun, Y.; Liu, C.; Grauer, D. C.; Yano, J.; Long, J. R.; Yang, P.; Chang, C. J. *J. Am. Chem. Soc.* **2013**, *135*, 17699.
- (46) Tran, P. D.; Chiam, S. Y.; Boix, P. P.; Ren, Y.; Pramana, S. S.; Fize, J.; Artero, V.; Barber, J. *Energy Environ. Sci.* **2013**, *6*, 2452.
- (47) Voiry, D.; Yamaguchi, H.; Li, J.; Silva, R.; Alves, D. B.; Fujita, T.; Chen, M.; Asefa, T.; Shenoy, V. B.; Eda, G.; Manish, C. *Nat. Mater.* **2013**, *12*, 850.
- (48) Xu, Y.-F.; Gao, M.-R.; Zheng, Y.-R.; Jiang, J.; Yu, S.-H. *Angew. Chem. Int. Ed.* **2013**, *52*, 8546.
- (49) Kiran, V.; Mukherjee, D.; Jenjeti, R. N.; Sampath, S. *Nanoscale* **2014**, *6*, 12856.
- (50) Zhou, H.; Wang, Y.; He, R.; Yu, F.; Sun, J.; Wang, F.; Lan, Y.; Ren, Z.; Chen, S. *Nano Energy* **2016**, *20*, 29.
- (51) Popczun, E. J.; McKone, J. R.; Read, C. G.; Biacchi, A. J.; Wiltout, A. M.; Lewis, N. S.; Schaak, R. E. *J. Am. Chem. Soc.* **2013**, *135*, 9267.
- (52) Popczun, E. J.; Read, C. G.; Roske, C. W.; Lewis, N. S.; Schaak, R. E. *Angew. Chem. Int. Ed.* **2014**, *53*, 5427.
- (53) Kibsgaard, J.; Jaramillo, T. F. *Angew. Chem. Int. Ed.* **2014**, *53*, 14433.
- (54) Jiang, P.; Liu, Q.; Liang, Y.; Tian, J.; Asiri, A. M.; Sun, X. *Angew. Chem. Int. Ed.* **2014**, *53*, 12855.
- (55) Liang, H.-W.; Bruller, S.; Dong, R.; Zhang, J.; Feng, X.; Mullen, K. *Nat. Commun.* **2015**, *6*, 7992.
- (56) Chen, W.-F.; Sasaki, K.; Ma, C.; Frenkel, A. I.; Marinkovic, N.; Muckerman, J. T.; Zhu, Y.; Adzic, R. R. *Angew. Chem. Int. Ed.* **2012**, *51*, 6131.
- (57) Cao, B.; Veith, G. M.; Neuefeind, J. C.; Adzic, R. R. & Khalifah, P. G. *J. Am. Chem. Soc.* **2013**, *135*, 19186.
- (58) Vrabel, H.; Hu, X. *Angew. Chem. Int. Ed.* **2012**, *51*, 12703.

- (59) Liao, L.; Wang, S.; Xiao, J.; Bian, X.; Zhang, Y.; Scanlon, M. D.; Hu, X.; Tang, Y.; Liu, B.; Girault, H. H. *Energy Environ. Sci.* **2014**, *7*, 387.
- (60) Shi, Z.; Wang, Y.; Lin, H.; Zhang, H.; Shen, M.; Xie, S.; Zhang, Y.; Gao, Q.; Tang, Y. *J. Mater. Chem. A*, **2016**, *4*, 6006.
- (61) Levy, R. B.; Boudart, M. *Science* **1973**, *181*, 547
- (62) Wan, C.; Regmi, Y. N.; Leonard, B. M. *Angew. Chem. Int. Ed.* **2014**, *53*, 6407
- (63) Chen, W.-F.; Lyer, S.; Sasaki, K.; Wang, C.-H.; Zhu, Y.; Muckerman, J. T.; Fujita, E. *Energy Environ. Sci.* **2013**, *6*, 1818
- (64) Fan, L.; Liu, P. F.; Yan, X.; Gu, L.; Yang, Z. Z.; Yang, H. G.; Qiu, S.; Yao, X. *Nat. Commun.* **2016**, *7*, 10667.
- (65) Lu, Q.; Hutchings, G. S.; Yu, W.; Zhou, Y.; Forest, R. V.; Tao, R.; Rosen, J.; Yonemoto, B. T.; Cao, Z.; Zheng, H.; Xiao, J. Q.; Jiao, F.; Chen, J. G. *Nat. Commun.* **2015**, *6*, 6567.
- (66) Ma, L.; Rui, L.; Ting, L.; Molinari, V.; Giordano, C.; Yeo, B. S. *J. Mater. Chem. A* **2015**, *3*, 8361
- (67) Corrigan, D. A. *J. Electrochem. Soc.* **1987**, *134*, 377.
- (68) Merrill, M. D.; Dougherty, R. C. *J. Phys. Chem. C* **2008**, *112*, 3655.
- (69) Lu, X.; Zhao, C. *Nat. Commun.* **2015**, *6*, 6616.
- (70) Gong, M.; Li, Y.; Wang, H.; Liang, Y.; Wu, J. Z.; Zhou, J.; Wang, J.; Regier, T.; Wei, F.; Dai, H. *J. Am. Chem. Soc.* **2013**, *135*, 8452.
- (71) Li, X.; Walsh, F. C.; Pletcher, D. *Phys. Chem. Chem. Phys.* **2011**, *13*, 1162.
- (72) Louie, M. W.; Bell, A. T. *J. Am. Chem. Soc.* **2013**, *135*, 12329.
- (73) Friebel, D.; Louie, M. W.; Bajdich, M.; Sanwald, K. E.; Cai, Y.; Wise, A. M.; Cheng, M.-J.; Sokaras, D.; Weng, T.-C.; Alonso-Mori, R.; Davis, R. C.; Bargar, J. R.; Nørskov, J. K.; Nilsson, A.; Bell, A. T. *J. Am. Chem. Soc.* **2015**, *137*, 1305.
- (74) Trotochaud, L.; Young, S. L.; Ranney, J. K.; Boettcher, S. W. *J. Am. Chem. Soc.* **2014**, *136*, 6744.
- (75) Smith, A. M.; Trotochaud, L.; Burke, M. S.; Boettcher, S. W. *Chem. Commun.* **2015**, *51*, 5261.
- (76) Burke, M. S.; Kast, M. G.; Trotochaud, L.; Smith, A. M.; Boettcher, S. W. *J. Am. Chem. Soc.* **2015**, *137*, 3638.
- (77) Lambert, T. N.; Vigil, J. A.; White, S. E.; Davis, D. J.; Limmer, S. J.; Burton, P. D.; Coker, E. N.; Beechem, T. E.; Brumbach, M. T. *Chem. Commun.* **2015**, *51*, 9511.

- (78) Tian, J.; Cheng, N.; Liu, Q.; Sun, X.; He, Y.; Asiri, A. M. *J. Mater. Chem. A* **2015**, *3*, 20056.
- (79) Zhang, B.; Zheng, X.; Voznyy, O.; Comin, R.; Bajdich, M.; Garcia-Melchor, M.; Han, L.; Xu, J.; Liu, M.; Zheng, L.; Pelayo Garcia de Arquer, F.; Dinh, C. T.; Fan, F.; Yuan, M.; Yassitepe, E.; Chen, N.; Regier, T.; Liu, P.; Li, Y. De Luna, P.; Janmohamed, A.; Xin, H. L.; Yang, H. *Science* **2016**, *352*, 333.
- (80) Suntivich, J.; May, K. J.; Gasteiger, H. A.; Goodenough, J. B.; Shao-Horn, Y. *Science*, **2011**, *334*, 1383.
- (81) Haber, J. A.; Cai, Y.; Jung, S.; Xiang, C.; Mitrovic, S.; Jin, J.; Bell, A. T.; Gregoire, J. M. *Energy Environ. Sci.* **2014**, *7*, 682.
- (82) Fan, K.; Ji, Y.; Zou, H.; Zhang, J.; Zhu, B.; Chen, H.; Daniel, Q.; Luo, Y.; Yu, J.; Sun, L. *Angew. Chem. Int. Ed.* **2017**, *56*, 1
- (83) Kanan, M. W.; Nocera, D. G. *Science* **2008**, *321*, 1072.
- (84) Lutterman, D. A.; Surendranath, Y.; Nocera, D. G. *J. Am. Chem. Soc.* **2009**, *131*, 3838.
- (85) Surendranath, Y.; Dincă, M.; Nocera, D. G. *J. Am. Chem. Soc.* **2009**, *131*, 2615.
- (86) Risch, M.; Khare, V.; Zaharieva, I.; Gerencser, L.; Chernev, P.; Dau, H. *J. Am. Chem. Soc.* **2009**, *131*, 6936.
- (87) Kanan, M. W.; Yano, J.; Surendranath, Y.; Dinca, M.; Yachandra, V. K.; Nocera, D. G. *J. Am. Chem. Soc.* **2010**, *132*, 13692.
- (88) McAlpin, J. G.; Surendranath, Y.; Dinca, M.; Stich, T. A.; Stoian, S. A.; Casey, W. H.; Nocera, D. G.; Britt, R. D. *J. Am. Chem. Soc.* **2010**, *132*, 6882.
- (89) Surendranath, Y.; Kanan, M. W.; Nocera, D. G. *J. Am. Chem. Soc.* **2010**, *132*, 16501.
- (90) Esswein, A. J.; Surendranath, Y.; Reece, S. Y.; Nocera, D. G. *Energy Environ. Sci.* **2011**, *4*, 499.
- (91) Cobo, S.; Heidkamp, J.; Jacques, P-A.; Fize, J.; Fourmond, V.; Guetaz, L.; Jusselme, B.; Ivanova, V.; Dau, H.; Palacin, S.; Fontecave, M.; Artero, V. *Nature Mater.* **2012**, *11*, 802
- (92) Koza, J. A.; He, Z., Miller, A. S.; Switzer, J. A. *Chem. Mater.* **2012**, *24*, 3567.
- (93) Gerken, J. B.; Landis, E. C.; Hamers, R. J.; Stahl, S. S. *ChemSusChem* **2010**, *3*, 1176.
- (94) Gerken, J. B.; McAlpin, J. G.; Chen, J. Y. C.; Rigsby, M. L.; Casey, W. H.; Britt, R. D.; Stahl, S. S. *J. Am. Chem. Soc.* **2011**, *133*, 14431.

- (95) Bloor, L. G.; Molina, P. I.; Symes, M. D.; Cronin, L. *J. Am. Chem. Soc.* **2014**, *136*, 3304.
- (96) Jiang, N.; You, B.; Sheng, M.; Sun, Y. *Angew. Chem. Int. Ed.* **2015**, *54*, 6251.
- (97) Li, D.; Baydoun, H.; Verani, C. N.; Brock, S. L. *J. Am. Chem. Soc.* **2016**, *138*, 4006.
- (98) Bediako, D. K.; Surendranath, Y.; Nocera, D. G. *J. Am. Chem. Soc.* **2013**, *135*, 3662.
- (99) Bediako, D. K.; Lassalle-Kaiser, B.; Surendranath, Y.; Yano, J.; Vittal, Y.; Nocera, D. G. *J. Am. Chem. Soc.* **2012**, *134*, 6801.
- (100) Wu, L.-K.; Hu, J.-M.; Zhang, J.-Q.; Cao, C.-N. *J. Mater. Chem. A* **2013**, *1*, 12885.
- (101) Zhao, Y.; Xiaodan, j.; Chen, G.; Shang, L.; Waterhouse, G. I. N.; Wu, L.-Z.; Tung, C.-H.; O'Hare, D.; Zhang, T. *J. Am. Chem. Soc.* **2016**, *138*, 6517.
- (102) Gorlin, Y.; Jaramillo, T. F. *J. Am. Chem. Soc.* **2010**, *132*, 13612.
- (103) Ramírez, A.; Hillebrand, P.; Stellmach, D.; May, M. M.; Bogdanoff, P.; Fiechter, S. *J. Phys. Chem. C* **2014**, *118*, 14073.
- (104) Zhou, F.; Izgorodin, A.; Hocking, R. K.; Armel, V.; Spiccia, L.; MacFarlane, D. R. *ChemSusChem* **2013**, *6*, 643.
- (105) Zaharieva, I.; Chernev, P.; Risch, M.; Klingan, K.; Kohlhoff, M.; Fischer, A.; Dau, H. *Energy Environ. Sci.* **2012**, *5*, 7081.
- (106) Mattioli, G.; Zaharieva, I.; Dau, H.; Guidoni, L. *J. Am. Chem. Soc.* **2015**, *137*, 10254.
- (107) Gorlin, Y.; Lassalle-Kaiser, B.; Benck, J. D.; Gul, S.; Webb, S. M.; Yachandra, V. K.; Yano, J.; Jaramillo, T. F. *J. Am. Chem. Soc.* **2013**, *135*, 8525.
- (108) Zhou, F.; Izgordin, A.; Hocking, R. K.; Spiccia, L.; MacFarlane, D. R. *Adv. Energy Mater.* **2012**, *2*, 1013.
- (109) Takashima, T.; Hashimoto, K.; Nakamura, R. *J. Am. Chem. Soc.* **2012**, *134*, 1519.
- (110) Takashima, T.; Hashimoto, K.; Nakamura, R. *J. Am. Chem. Soc.* **2012**, *134*, 18153.
- (111) Huynh, M.; Bediako, D. K.; Liu, Y.; Nocera, D. G. *J. Phys. Chem. C* **2014**, *118*, 17142.
- (112) Huynh, M.; Bediako, D. K.; Nocera, D. G. *J. Am. Chem. Soc.* **2014**, *136*, 6002.
- (113) Yu, F.; Li, F.; Zhang, B.; Li, H.; Sun, L., *ACS Catal.* **2015**, *5*, 627
- (114) Roger, I.; Symes, M. D. *J. Am. Chem. Soc.* **2015**, *137*, 13980.
- (115) a) Liu, X.; Jia, H.; Sun, Z.; Chen, Y.; Xu, P.; Du, P. *Electrochem. Commun.* **2014**, *46*, 1b) Li, T.-T.; Cao, S.; Yang, C.; Chen, Y.; Vv, X.J.; Fu, W.-F. *Inorg. Chem.* **2015**, *54*, 3061
- (116) Wu, Y.; Chen, M.; Han, Y.; Luo, H.; Su, X.; Zhang, M.-T.; Lin, X.; Sun, J.; Wang, L.; Deng, L.; Zhang, W.; Cao, R. *Angew. Chem. Int. Ed.* **2015**, *54*, 4870.

- (117) Walter, M. G.; Warren, E. L.; McKone, J. R.; Boettcher, S. W.; Mi, Q.; Santori, E. A.; Lewis, N. S. *Chem. Rev.* **2010**, *110*, 6446.
- (118) Patel, M. R. "Wind and Solar Power Systems" CRC Press, **2005**
- (119) Hou, Y.; Abrams, B. L.; Vesborg, P. C. K.; Bjoerketun, M. E.; Herbst, K.; Bech, L.; Setti, A. M.; Damsgaard, C. D.; Pedersen, T.; Hansen, O.; Rossmeisl, J.; Dahl, S.; Nørskov, J. K.; Chorkendorff, I. *Nat. Mater.* **2011**, *10*, 434.
- (120) Berglund, S. P.; He, H.; Chemelewski, W. D.; Celio, H.; Dolocan, A.; Mullins, C. B. *J. Am. Chem. Soc.* **2014**, *136*, 1535.
- (121) Ding, Q.; Meng, F.; English, C. R.; Caban-Acevedo, M.; Shearer, M. J.; Liang, D.; Daniel, A. S.; Hamers, R. J.; Jin, S. *J. Am. Chem. Soc.* **2014**, *136*, 8504.
- (122) Cabán-Acevedo, M.; Stone, M. L.; Schmidt, J. R.; Thomas, J. G.; Ding, Q.; Chang, H.-C.; Tsai, M.-L.; He, J.-H.; Jin, S. *Nat. Mater.* **2015**, *14*, 1245.
- (123) Downes, C. A.; Marinescu, S. C. *J. Am. Chem. Soc.* **2015**, *137*, 13740.
- (124) McKone, J. R.; Warren, E. L.; Bierman, M. J.; Boettcher, S. W.; Brunschwig, B. S.; Lewis, N. S.; Gray, H. B. *Energy Environ. Sci.* **2011**, *4*, 3573.
- (125) Morales-Guio, C. G.; Thorwarth, K.; Niesen, B.; Liardet, L.; Patscheider, J.; Ballif, C.; Hu, X. *J. Am. Chem. Soc.* **2015**, *137*, 7035.
- (126) Lang, D.; Cheng, F.; Xiang, Q. *Catal. Sci. Technol.* **2016**, *6*, 6207.
- (127) Meng, P.; Wang, M.; Yang, Y.; Zhang, S.; Sun, L. *J. Mater. Chem. A* **2015**, *3*, 18852.
- (128) Lin, C.-Y.; Lai, Y.-H.; Mersch, D.; Reisner, E. *Chem. Sci.* **2012**, *3*, 3482.
- (129) Yang, C.; Tran, P. D.; Boix, P. P.; Bassi, P. S.; Yantara, N.; Wong, L. H.; Barber, J. *Nanoscale*, **2014**, *6*, 6506.
- (130) Dubale, A. A.; Pan, C.-J.; Tamirat, A. G.; Chen, H.-M.; Su, W.-N.; Chen, C.-H.; Rick, J.; Ayele, D. W.; Aragaw, B. A.; Lee, J.-F.; Yang, Y.-W.; Hwang, B.-J. *J. Mater. Chem. A* **2015**, *3*, 12482.
- (131) Morales-Guio, C. G.; Tilley, S. D.; Vrubel, H.; Grätzel, M.; Hu, X. *Nat. Commun.* **2014**, *5*, 3059
- (132) Paracchino, A.; Laporte, V.; Sivula, K.; Grätzel, M.; Thimsen, E. *Nat. Mater.* **2011**, *10*, 456
- (133) Hardee, K. L.; Bard, A. J. *J. Electrochem. Soc.* **1976**, *123*, 1024.
- (134) Zhong, D. K.; Sun, J.; Inumaru, H.; Gamelin, D. R. *J. Am. Chem. Soc.* **2009**, *131*, 6086.
- (135) Zhong, D. K.; Gamelin, D. R. *J. Am. Chem. Soc.* **2010**, *132*, 4202.

- (136) Zhong, D. K.; Cornuz, M.; Sivula, K.; Grätzel, M.; Gamelin, D. R. *Energy Environ. Sci.* **2011**, *4*, 1759.
- (137) Seabold, J. A.; Choi, K.-S. *Chem. Mater.* **2011**, *23*, 1105.
- (138) Pijpers, J. J. H.; Winkler, M. T.; Surendranath, Y.; Buonassisi, T.; Nocera, D. G. *Proc. Natl. Acad. Sci. U.S.A.* **2011**, *108*, 10056.
- (139) Abdi, F. F.; van de Krol, R. *J. Phys. Chem. C* **2012**, *116*, 9398.
- (140) Abdi, F. F.; Firet, N.; van de Krol, R. *ChemCatChem* **2013**, *5*, 490.
- (141) Pilli, S. K.; Deutsch, T. G.; Furtak, T. E.; Turner, J. A.; Brown, L. D.; Herring, A. M. *Phys. Chem. Chem. Phys.* **2012**, *14*, 7032.
- (142) Khnayzer, R. S.; Mara, M. W.; Huang, J.; Shelby, M. L.; Chen, L. X.; Castellano, F. N. *ACS Catal.* **2012**, *2*, 2150.
- (143) Li, Y.; Wang, R.; Li, H.; Wei, X.; Feng, J.; Liu, K.; Dang, Y.; Zhou, A. *J. Phys. Chem. C* **2015**, *119*, 20283.
- (144) Kim, J. H.; Jo, Y.; Kim, J. H.; Jang, J. W.; Kang, H. J.; Lee, Y. H.; Kim, D. S.; Jun, Y.; Lee, J. S. *ACS Nano* **2015**, *9*, 11820.
- (145) Choi, S. K.; Choi, W.; Park, H. *Phys. Chem. Chem. Phys.* **2013**, *15*, 6499.
- (146) Pilli, S. K.; Summers, K.; Chidambaram, D. *RSC Adv.* **2015**, *5*, 47080.
- (147) Jin, T.; Diao, P.; Xu, D.; Wu, Q. *Electrochim. Acta* **2013**, *114*, 271.
- (148) Kleiman-Shwarsstein, A.; Hu, Y.-S.; Stucky, G. D.; McFarland, E. W. *Electrochem. Commun.* **2009**, *11*, 1150.
- (149) Zeng, Q.; Bai, J.; Li, J.; Xia, L.; Huang, K.; Li, X.; Zhou, B. *J. Mater. Chem. A* **2015**, *3*, 4345.
- (150) Tilley, S. D.; Cornuz, M.; Sivula, K.; Grätzel, M. *Angew. Chem. Int. Ed.* **2010**, *49*, 6405.
- (151) Kenney, M. J.; Gong, M.; Li, Y.; Wu, J. Z.; Feng, J.; Lanza, M.; Dai, H. *Science* **2013**, *342*, 836.
- (152) Kim, T. W.; Choi, K.-S. *Science* **2014**, *343*, 990.
- (153) Okamoto, S.; Deguchi, M.; Yotsushashi J. *J. Phys. Chem. C* **2017**, *121*, 1393
- (154) Rocheleau, R. E.; Miller, E. L.; Misra, A. *Energy Fuels* **1998**, *12*, 3.
- (155) Verlage, E.; Hu, S.; Liu, R.; Jones, R. J. R.; Sun, K.; Xiang, C.; Lewis, N. S.; Atwater, H. A. *Energy Environ. Sci.* **2015**, *8*, 3166.
- (156) Reece, S. Y.; Hamel, J. A.; Kimberly, S.; Jarvi, T. D.; Esswein, A. J.; Pijpers, J. J. H.; Nocera, D. G. *Science* **2011**, *334*, 645.

-
- (157) Esiner, S.; Willems, R. E. M.; Furlan, A.; Weiwei, L.; Wienk, M. M.; Janssen, R. A. *J. J. Mater. Chem. A* **2015**, *3*, 23936.
- (158) Cox, C. R.; Lee, J. Z.; Nocera, D. G.; Buonassisi, T. *Proc. Natl. Acad. Sci. U. S. A.* **2014**, *39*, 14057.
- (159) Bonke, S. A.; Wiechen, M.; MacFarlane, D. R.; Spiccia, L. *Energy Environ. Sci.* **2015**, *8*, 2791
- (160) Lewis, N. S. *Nat. Nanotechnol.* **2016**, *11*, 1010
- (161) Barbir, F. *Sol. Energy* **2005**, *78*, 661.
- (162) Berger, A.; Segalman, R. A.; Newman, J. *Energy Environ. Sci.* **2014**, *7*, 1468.
- (163) Symes, M. D.; Cronin, L. *Nature Chem.* **2013**, *5*, 403.
- (164) Rausch, B.; Symes, M. D.; Cronin, L. *J. Am. Chem. Soc.* **2013**, *135*, 13656.
- (165) Rausch, B.; Symes, M. D.; Chisholm, G.; Cronin, L. *Science* **2014**, *345*, 1326.

CHAPTER 2**BEHIND THE TECHNIQUES USED****Synopsis**

In this chapter we will briefly explain the main experimental techniques used in Chapters 3 to 5 so as to have a theoretical background prior to encountering them in the text. This way it will be clear why they were chosen in each case and how they complement each other for different applications.

2.1 Electrochemical techniques

Electrochemical techniques can be divided in three main groups depending on whether we control the potential, the current or the charge, leaving impedance techniques in a fourth group. In this section we will briefly explain the main techniques used throughout this thesis focusing on the information we can get from them and in which cases we use one or another within the context of the study of electrocatalysts for water splitting. Also, we will explain the use of reference electrodes in the experiments and compare two and three-electrode set ups.

2.1.1 Cyclic and linear sweep voltammetry

In a linear sweep voltammetry the potential is linearly swept at a constant rate from a potential E_1 to a potential E_2 . If at this point the scan is reversed back to E_1 keeping the same scan rate, then it makes a whole cycle, and the technique is called cyclic voltammetry (see Figure 2.1). The data is recorded as current vs potential, and this representation is called a voltammogram, an example of which can be found on the right panel of Figure 2.1. Both techniques are used to first evaluate the activity of a material for the HER or the OER, comparing its voltammogram to that of the substrate on its own and with those of reported catalysts. Linear sweep voltammetry at slow scan rates ($\approx 2 \text{ mV s}^{-1}$) can be used to obtain tafel slopes (although this data is more reliably obtained through electrolysis). Cyclic voltammetry can be used for example to electrodeposit metal oxides /oxohydroxides onto conductive substrates from metal-salt solutions, the number of cycles determining the mass loading and the morphology of the catalyst depending on the scan rate and the range of potentials. It is also used to see whether the activity of the catalyst changes with cycling: sometimes the catalyst undergoes a “conditioning” over the first scans upon testing in a specific media, which can be due for example to an structural rearrangement, or to a change in the oxidation number of some of the metal centers in the material. Often, multiple cycling (> 1000 cycles) is used to evaluate the stability of a catalyst, although this is better demonstrated with continuous electrolysis keeping an specific current density.

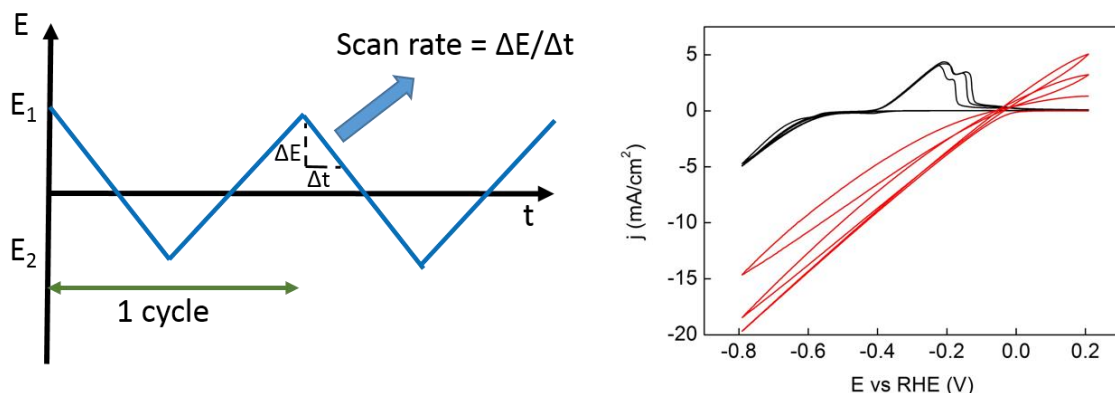


Figure 2.1 *Left:* Waveform of a cyclic voltammogram. **Right:** Example of the cyclic voltammogram (3 cycles) of a catalyst (red) compared to the substrate on its own (black). In this example the catalyst loses activity after each cycle.

2.1.2 Bulk electrolysis

In a bulk electrolysis an specific potential value is maintained over time, recording current vs time. This can be used again to electrodeposit a catalyst, the thickness of the deposit depending on the total charge passed (charge = current \times time), and the morphology and composition on the potential applied (leaving aside other parameters like temperature, stirring...). It is also used to make tafel plots, applying a potential for 5 – 10 min, then increasing or decreasing it 20 or 30 mV and maintaining it for another 5 – 10 min, doing what we call “potential steps”. A several-days bulk electrolysis at a potential that gives a representative current density is the most reliable way to examine the stability of a catalyst in a particular media. It is also used in closed cells to generate enough amounts of hydrogen and oxygen to be detected by a suitable technique like for example gas chromatography.

2.1.3 Galvanostatic experiments

Sometimes it is preferable to fix a current and see how the potential required to keep that current varies over time. For example, if we want to have a quick look at how our catalyst behaves at different values of pH, we can set up a galvanostatic experiment in phosphate buffer (or any other buffer, but phosphate has the advantage that it has three buffering points), imposing a

value of the current so that we have a relevant current density (e.g. 10 mA cm^{-2}), and record how the potential required to keep that current value varies as we add to the electrolyte aliquots of acid or base to slowly change the pH. We can also use this kind of experiment to test the stability of a catalyst with time instead of using bulk electrolysis. In general, it can be said that galvanostatic experiments offer complementary information to controlled potential bulk electrolysis.

2.1.4 Two-electrode vs three-electrode configuration

In the lab we normally work with three electrodes: the working electrode is the one connected to the catalyst we want to test, and will work as a cathode or as an anode depending on the potential we apply to it. The opposite reaction (an oxidation or a reduction) occurs at the counter electrode, which closes the circuit and is made of an inert material so that it does not participate in the electrochemical reaction under study, its function being limited to just transfer electrons as required. The counter electrode's surface area needs to be higher than that of the working electrode, or otherwise it will be a limiting factor in the kinetics of the reaction. Although the circuit can be closed with just the two of them, we normally use a third one, the reference electrode, to compare the potential we apply (or measure) to (at) the working electrode (we will explain this in more detail in the next section). It is possible to work without the reference electrode in a two-electrode configuration, but in this case what we apply/measure is the *difference of potential* between working and counter. This set up is used to analyze the performance of the whole electrochemical cell rather than to test a catalyst for one of the half-reactions.

2.1.5 Reference electrodes

In order to be able to compare the electrochemical potentials of different species we use the half-reaction of the reduction of protons to hydrogen ($2\text{H}^+ + 2\text{e}^- \rightarrow \text{H}_2$) as the reference point, so that its standard reduction potential receives the value of 0 ($E^\circ = 0.00 \text{ V}$) and all other reduction potentials are referred to it. It would therefore seem as the obvious choice to build a reference electrode based on this reaction, but while this electrode exists it is quite cumbersome

to use in the lab, so reference electrodes based on other electrochemical systems are used instead and data is reported referencing it either to the electrode that has been used specifying which one it is and its characteristics or it is converted to the NHE. There are several options as the reference electrode. Probably the most common one is the Ag/AgCl, which consists on a silver wire immersed in an aqueous solution of AgCl, its standard value depending on the concentration of silver ions in the solution. There is also the Hg/HgO, the Hg/Hg₂SO₄ and the calomel electrode, all based on mercury. Which reference electrode is used depends on each particular case, especially on the pH and on whether or not chlorides can be an interference, as well as on the availability. The important thing is that it needs to be able to keep a constant potential during the experiment so that the working electrode's potential can be constantly referenced to it, that is, it has to be non-polarizable. And obviously the reaction in which it is based needs to be reversible, so that we can apply the Nernst equation.

2.2 Gas Chromatography

Gas chromatography is a separation technique in which the components of a gas sample are separated as a function of their retention coefficients in a liquid or solid stationary phase held in a column. Unlike in liquid chromatography, here the mobile phase does not interact with the analytes, its function being just to push them through the chromatograph. A calibrated micro-syringe is used to take a sample from the headspace of the electrochemical cell and inject it in the injection port. Depending on whether it is a packed column or a capillary one the injection mode changes: for a packed column we inject in “splitless mode”, which means that the whole sample gets inside the column, whereas when using a capillary column only a tiny fraction of the sample is taken to the column and the rest of it is vented to the room, as can be seen in Figure 2.2. This is the split mode. Many gas chromatographs allow to switch between the two modes depending on the column in use. As the flux of inert gas carries the sample through the column the different analytes separate arriving therefore to the detector at different times depending on their retention coefficient. There are many kinds of detectors, each of them suitable for different types of samples. We use a thermal conductivity detector, which senses changes in the thermal conductivity of the gas coming out of the column and compares it to a reference flow of Ar. The

detector sends a signal to the computer and this is plotted as a function of time, so that each analyte appears in the chromatogram as a peak at a specific time. The time serves to identify the peaks, and the area of the peaks is correlated with the % of that gas in the headspace of the electrochemical cell by means of calibration lines that have been made for each gas using commercial gas cylinders that contain specific percentages of them in Argon. These percentages are then translated into number of mols knowing the volume of the headspace, and then compared to the theoretical amount of mols that should have been made if all the passed charge is used for water splitting.

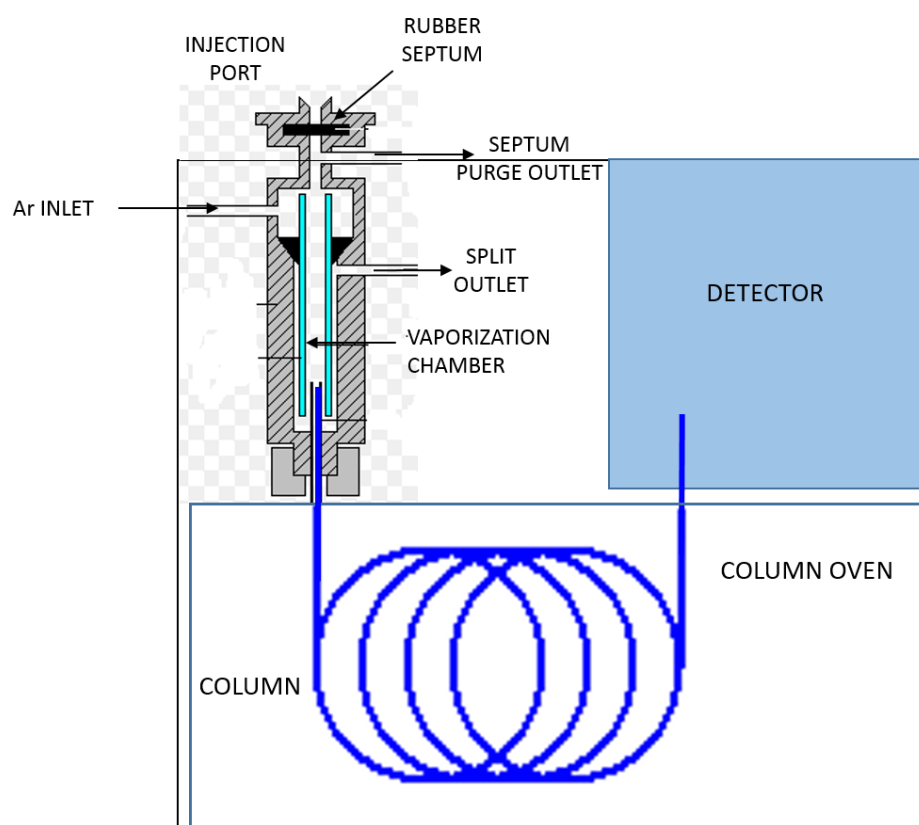


Figure 2.2 Diagram showing the main parts of a gas chromatograph

2.3 X-Ray Photoelectron Spectroscopy (XPS)

This technique is based on the photoelectric effect, whereby a radiation beam of sufficient energy impacting on a material causes the ejection of photoelectrons. Upon measuring the kinetic energy (E_k) of these photoelectrons we can calculate their binding energy (E_b), since

$$E_k = h\nu - E_b \text{ (eq. 2.1)}$$

Depending on the kind of radiation source used we actually distinguish between two techniques: if using UV rays, the energy of these photons can eject electrons from the valence levels, providing information about the bonding in molecules. This is called UPS (Ultraviolet Photoelectron spectroscopy). In order to expel electrons from the core levels we need to irradiate the sample with soft X-rays (200-2000 eV), the technique being then called XPS (X-ray photoelectron spectroscopy).

Removing an electron from a core level leaving behind a “hole” is not a stable situation, so this hole is quickly filled with an electron that “drops” from a higher level. This transition releases energy either as an Auger electron or as fluorescence, as depicted in Figure 2.3. The probability of one event or the other depends on both the atomic number of the element and the (sub)-shell from which the electron “drops”, with the Auger probability dominating significantly over that of fluorescence for light elements.¹

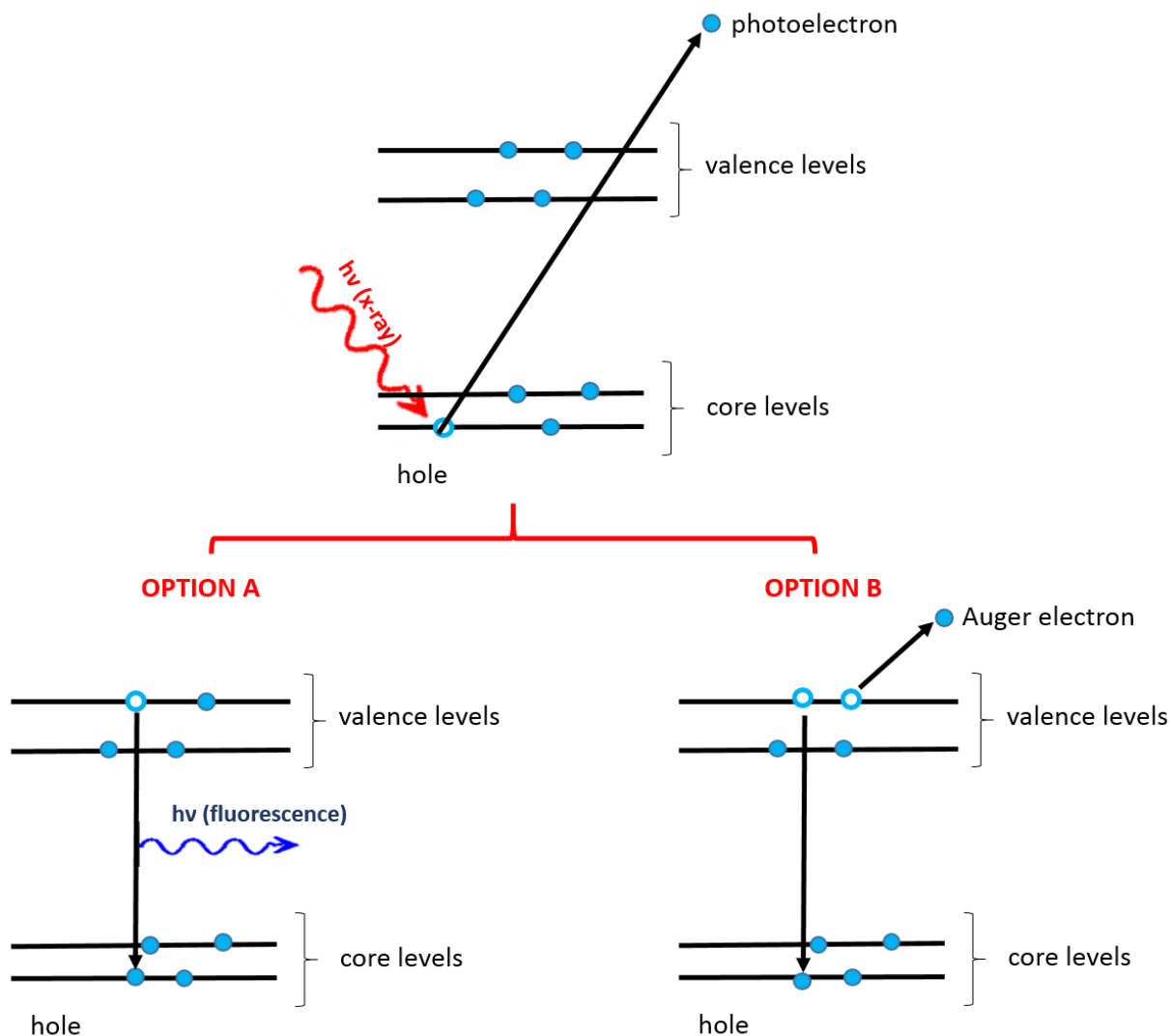


Figure 2.3 Representation of the photoelectric effect in which XPS is based. Upon receiving an X-ray photon a core electron is expelled leaving a hole behind and this is immediately filled by an electron dropping from a valence level releasing energy either as fluorescence (option A, left) or using it to expel an Auger electron from the same valence level (option B, right).

In order to be able to apply Equation 2.1 and obtain the binding energies of the elements in the sample we need to irradiate this with a monochromatic beam of X-rays. The two most common sources are either magnesium ($\text{Mg } K_{\alpha}$ $h\nu = 1.25 \text{ keV}$) or aluminium ($\text{Al } K_{\alpha}$ $h\nu = 1.49 \text{ keV}$). When this monochromatic beam hits the sample it penetrates it a few nanometres (3 – 10 nm for an $\text{Al } K_{\alpha}$) and the emitted electrons are directed to the analyzer's entrance thanks to a set of

electrostatic and/or magnetic lenses. The architecture of the analyzer is crucial so that electrons with different kinetic energies travel through it following different paths until they reach the detector slits, where their kinetic energies are measured. Detected electrons include photoelectrons and also Auger electrons, which can be useful to help identify the element and the oxidation state. It is important to note here that while the kinetic energy of the photoelectron will depend on the X-ray source used, the energy of Auger electrons is independent, that is, if we plot the data in terms of kinetic energies, the position of the peaks corresponding to photoelectrons will vary depending on the source used whereas the Auger peaks will not shift². It is often preferred to plot the data in terms of binding energy, already accounting for the energy of the X-ray photons, but in this case the Auger peaks are moved. This is why it is very important to specify the X-ray source used. The energy values of the different possible transitions for each element are tabulated, so that the presence of peaks at particular energies suggest the identity of the element and its oxidation state and their intensity allows to quantify that element in the sample.

Regarding applications, XPS is most often used for surface scanning of solid materials, providing the elemental composition of it (up to depths of 10 nm usually), the electronic state of each element and the distribution of these elements across the surface, allowing therefore to “map” the composition of the surface (which gives information about its uniformity) and even get an empirical formula of it. It can also show contamination of trace elements on the material.

2.4 Raman Spectroscopy

Let's imagine that we direct a laser beam in the visible part of the spectrum onto a material. The visible range of the electromagnetic spectrum interacts with matter causing electronic transitions. However, because we are applying a monochromatic radiation, chances are that its energy will not correspond with the exact value of any electronic transition. As a result, electrons in the ground state are forced to a "virtual" excited level³ (see Figure 2.4), but this is an unstable situation and so they will quickly jump back to the ground level, emitting back light of the same frequency they received. This is the same as saying that photons are scattered elastically by the sample, and it is the main component we will see in the spectrum: the Rayleigh component. While most of the electrons in the sample will go back to their initial state, some of them (about 1 in 30 millions, actually) may lose some energy in the interaction process and end up in the ground electronic state but in a higher vibrational level, emitting therefore a photon with a slightly lower energy than the one they received. This is the Stokes component of the spectrum. A few electrons may be initially in an excited vibrational state and when returning to the electronic ground state arrive at the ground vibrational state. In this case, the emitted photon will have a slightly higher frequency than the incident one, and this is the Anti-Stokes component. Stokes and Anti-Stokes processes are what we refer to as the Raman Effect, which gives name to the technique that benefits from it. A Stokes process is more probable than an anti-Stokes one, since at room temperature most electrons will be in their ground vibrational state. This is way normally we take only the Stokes component of the spectrum and replot it as Intensity of scattered light vs the difference in energy between the incident and the emitted photons.

The main trouble of this technique is to filter out the Rayleigh component in the spectrum, which tends to hide the Raman scattering, and with that and other interferences like parasitical fluorescence processes we require enhancement techniques in order to be able to uncover and analyze the Stokes peaks. And yet they can provide really useful information, since the Raman spectrum is characteristic of each material, allowing to distinguish between different phases, say if a material is amorphous or crystalline, or polymorphous, spot defects and inhomogeneities...⁴

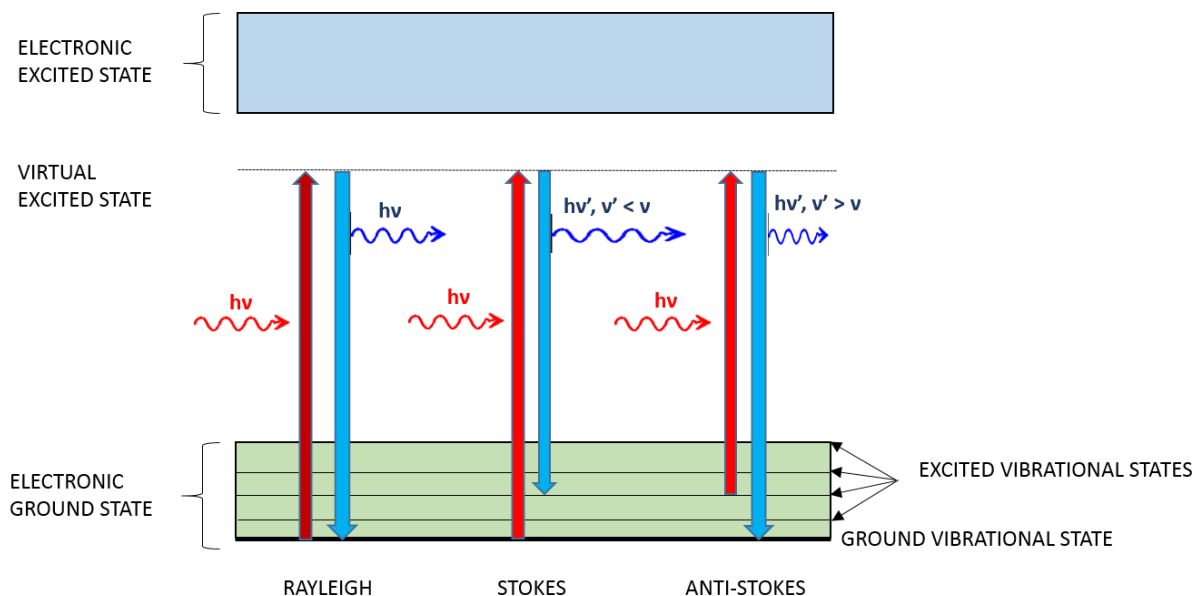


Figure 2.4 Diagram showing the Raman effect in the scattering of a monochromatic ray of energy $h\nu$ by a sample. In the first case the excited electron returns to the electronic and vibrational ground states, so that the ray is scattered elastically without any change of energy: this is the Rayleigh component. In the second, the electron returns to the electronic ground state but in an excited vibrational level, resulting in an emitted ray with a frequency ν' slightly smaller than that of the incident ray: this is the Stokes component. In the last one, the excited electron was initially in an excited vibrational level, and when it goes back to the electronic ground state it also goes back to the vibrational ground state, releasing a photon with ν' slightly higher than that of the incident photon.

Nowadays there are many options to enhance the intensity of the Raman signals, like resonance Raman scattering, surface enhanced RS (SERS), transmission RS, tip-enhanced RS... resonance Raman can only be used in very specific situations, since the wavelength of the laser used has to be close to an electronic transition in the material, but it enhances the intensity of the signals several orders of magnitude.

It is important to note that not all the vibrations and motions in a crystal lattice are Raman active: only those that imply a deformation of the lattice with a change in polarizability are observed. This makes it complementary to infrared spectroscopy, in which only transitions that imply a change in dipole moment are permitted, with the advantage (among others) that Raman is a non-destructive technique.

2.5 SEM/EDX

Scanning electron microscopy (SEM) is a technique that uses a focused beam of high-energy electrons to obtain high-resolution images of the surface of materials. The minimum separation between two discrete objects that can be resolved by any kind of microscope is given by the formula

$$d = \lambda/2n\sin\theta \text{ (eq. 2.2)}$$

where n is the refractive index of the transmission medium and λ the wavelength. It follows that the lower the wavelength, the highest the resolution. While an optical microscope cannot go beyond the limits of the visible range of the spectrum, since our eyes cannot detect photons with wavelengths smaller than ≈ 400 nm, we can generate a beam of highly energetic electrons that behave as waves of lower wavelength compared to that of visible light. The wavelength of the electrons depends on their speed, and this on the accelerating voltage we apply to them, which is a parameter we can control.⁵ As a result of this, while optical microscopes have their resolution limited to about 200 nm, most SEMs can go down to 10 nm nowadays. (If more resolution is required, a Transmission Electron Microscope (TEM) can go down even further, to about 0.2 nm).⁶

The scanning electron microscope works in the following manner: a beam of electrons is generated by a suitable source (a tungsten filament in our case) and then it is accelerated through a high voltage (1 – 30 kV) so that they acquire enough kinetic energy. Here the “lenses” that focus the electron beam are magnetic fields, resulting in all the electrons converging in a highly-focused beam. All this happens inside a vacuum chamber, since otherwise any particles carried by the air could interact with the electrons.⁷ When the electron beam hits the sample it penetrates to a depth of a few microns producing a variety of signals, as can be seen in Figure 2.5. The most relevant here are secondary and backscattered electrons, which are collected by one or more detectors and combined to form images on the computer screen.

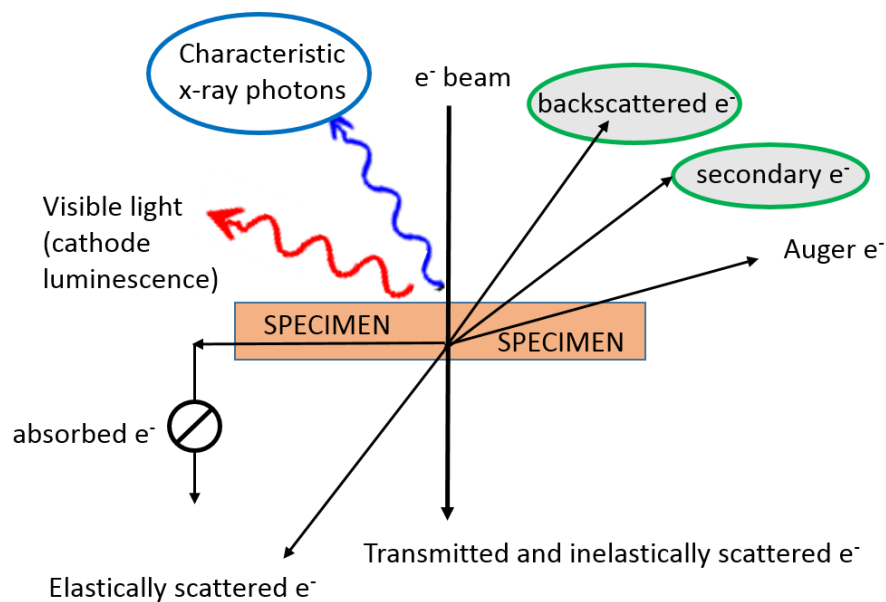


Figure 2.5. Diagram showing all possible processes occurring when a highly energetic electronic beam hits a solid sample.

SEM is often complemented with **energy-dispersive X-ray spectroscopy (EDX)**, enabling the user to determine the composition of the features in the SEM figure. This is achieved by positioning an X-ray detector to intercept the X-rays emitted by the sample. When these enter the detector they generate a small current which is converted to a voltage pulse, the size of this proportional to the frequency of the X-rays. This way, while we take pictures of the sample's surface exploring its topography we can select specific features and obtain their composition as well as get an average composition of a wider area.

2.6 ICP-MS and Atomic Absorption Spectroscopy (AAS)

Both these techniques follow the same initial sequence: volatilize and atomize the sample to produce gas-phase atoms and ions. This can be achieved with different atomization techniques: a flame, a plasma, an electrothermic atomizer. Then, with the sample decomposed into gaseous ions and atoms, there are different possibilities for analyzing them: fluorescence, absorption or emission spectroscopy and mass spectrometry, giving rise to a range of different techniques

depending on which combination of atomization and analysis methods are chosen. Although in some of these combinations it is possible to analyze directly a solid sample by means of laser ablation,⁸ both ICP-MS and AAS require the sample to be initially in solution, so when they are used to analyze an heterogeneous catalyst deposited on a substrate the deposit needs to be either manually scratched from the substrate or digested and then dissolved, preferably in water.

2.6.1 Atomic Absorption Spectroscopy (AAS)

AAS exploits the fact that each element in the periodic table has its own set of absorption lines, which serves as its fingerprint to identify it. Among these lines, those that correspond to the most probable electronic transitions are therefore the most intense and are the ones used to identify the element, the idea being to irradiate the atomized sample with a beam of monochromatic light of exactly the same frequency as one of these lines and quantify how much of it is absorbed. And the only way of doing this is by using a lamp made of the same element that we want to quantify in the sample, since otherwise we would never reach the resolution required to distinguish between the lines of different elements, not even with the best monochromator. This has the disadvantage that we need to change the lamp for each element, and this technique is therefore used for the determination of single elements and cannot be used to screen a sample (normally one has a number of lamps for different elements, and changing from one to another does not take too long but they need a bit of time to “warm up”). On the bright side, because we are talking of atoms, there are no complications with vibration or rotational modes, and when using a flame as atomization technique, which is the most common choice, it is quite a straightforward and quick technique that does not require much training, and relatively cheap in terms both of apparatus cost and maintenance. We will next explain briefly how a flame-AAS works:

The sample, in solution, is first drawn through a straw into the nebulizer, where it becomes a suspension composed of tiny drops. The gas flux, which is a mixture of an oxidant and a fuel, carries this suspension to a flame where it will be atomized. Atomization consists of a series of steps: first the solvent is evaporated, so that we end up with a finely divided molecular aerosol, and then these molecules are dissociated into atoms, most of which are also ionized, so that we end up with a gas formed of cations and electrons. It is unavoidable to produce some other

molecules and ions during the atomization due to the interactions of the species in the sample with the oxidant and fuel gases, the extent of which will vary a lot depending on the kind of flame and other parameters. This gas is irradiated with a beam of monochromatic light of the wavelength of the selected line of the element we want to quantify from a lamp made of this element, and the portion of light that has been absorbed tells as the concentration of that element present in the sample using Beer's law:

$$A = abc \text{ (eq. 2.3)}$$

With A = absorbance, a = absorption coefficient (λ dependent), b = path length and c = concentration of the absorbing species.

All this is schematized in figure 2.6:

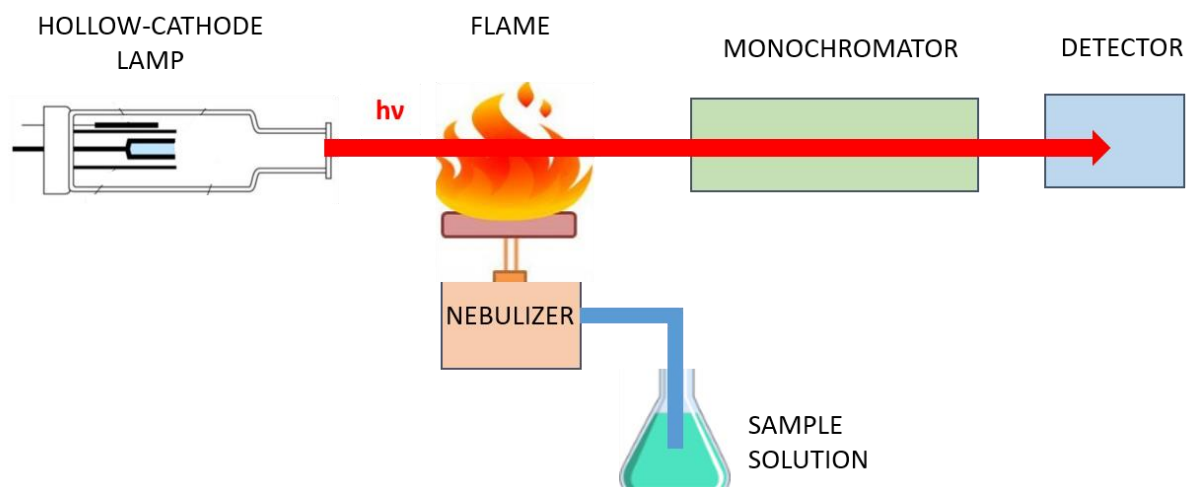


Figure 2.6 Diagram showing the components of a flame-atomic absorption spectrometer.

The detection limits of this technique can be improved by a factor of up to 1000 using an electrothermal atomizer instead of a flame: this is called ETAAS or GFAAS (graphite furnace absorption spectroscopy).

2.6.2 ICP-MS

ICP-MS combines an inductively-coupled plasma as atomizer with mass spectrometry as the analysis technique. As with AAS, the sample is first nebulized and then atomized and ionized, this time in a plasma. Then the carrier gas (Ar), pushes this plasma through a differential vacuum interphase, where it expands cooling down and a fraction of it goes to another chamber where the cations are separated from the electrons and the molecular species. The cations are then accelerated and focused to the quadrupole mass analyzer, which separates and quantifies them as a function of their m/z (mass-charge ratio), so that in the end we obtain a mass spectra comprising the isotopic peaks of all the analytes present in our sample. To quantify the elements of interest we refer to calibration lines made with standards of these elements in the concentrations range we expect them to be, preferably in the same matrix as the sample.

The whole procedure is schematized in Figure 2.7.

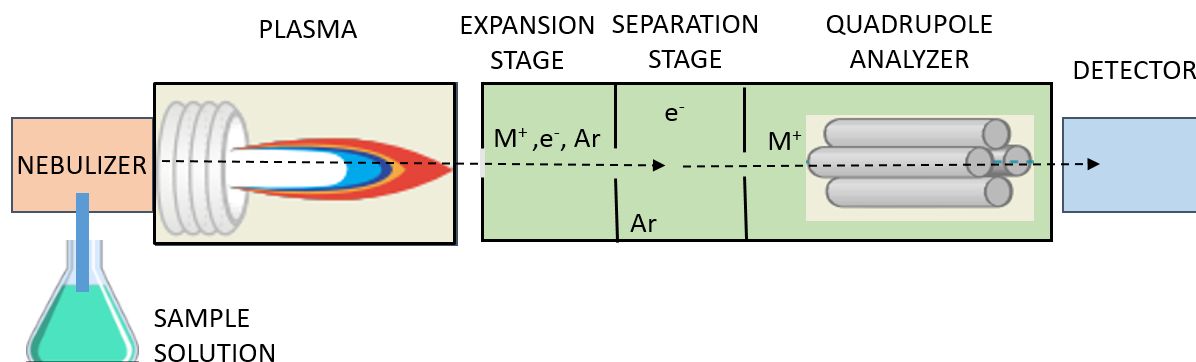


Figure 2.7 Diagram showing the components of a flame-atomic absorption spectrometer.

The main attractive of ICP-MS is that the use of a mass spectrometer as the analysis technique gives ICP-MS better detection limits than FAAS and ICP-OES (same atomizer as ICP-MS but uses atomic emission spectroscopy), and comparable to those of ETAAS (electrothermic atomic absorption spectroscopy), with the advantage that ICP-MS is a multielemental technique, allowing sample screening. Another advantage is that mass spectra are usually easier to interpret than the corresponding optical spectra, and this is particularly true for lanthanides and actinides, which have thousands of emission lines. One may think that having so many lines could actually be an advantage, but in practice they are so many that they have lots of interferences with other

elements present in the sample, atmospheric pollutants or even the carrier gas, and the resulting spectrum is often a mess of lines that cannot be distinguished from the background, especially for mixtures of these heavy elements. This does not mean that ICP-MS is free of interferences: there are isobaric interferences when different elements have an isotope of the same mass. Most elements in the periodic table have at least one or two isotopes that cannot be mistaken with an isotope of another element, so that in case of doubt between two elements we can always look for the other isotopic lines of each of them and measure the relative intensities. An example relevant to chapter three is the mutual interference between nickel and iron: $^{58}\text{Ni}^+$, nickel's most abundant isotope, overlaps with $^{58}\text{Fe}^+$, so that to check which of the two elements we are seeing we need to look for some of their other isotope lines. $^{60}\text{Ni}^+$ does not suffer from any isobaric interference, but unfortunately it overlaps with CaO^+ , a polyatomic specie often formed in calcium-containing samples. And $^{56}\text{Fe}^+$ overlaps with ArO^+ , another polyatomic cation that forms due to interactions between the sample matrix and the plasma. It would seem that measuring nickel or iron is therefore a lost cause, but nowadays most of these interferences can be automatically corrected with the right software: isobaric overlapping can be predicted from relative abundances databases, and polyatomic ions interferences can be removed with a blank, so in the end both nickel and iron can be unequivocally identified and quantified.

2.7 Powder X-Ray Diffraction (PXRD)

When an X-ray travels through a crystalline sample its electric component interacts with the electronic density of the ions in the lattice and as a result it is diffracted. A crystalline lattice has a layered, ordered structure in which a “unit cell” is repeated periodically in the three dimensions, so if the incoming ray forms an angle Θ with a group of planes, it will be diffracted with the same angle, as shown in Figure 2.8. Now if we imagine a whole beam of X-rays travelling through this crystalline lattice, some of them will be diffracted upon hitting the first layer of atoms, while others will travel further and will be diffracted by the second one, and others by the third one, and so on. If we compare a ray that is diffracted upon hitting the first layer with one that is diffracted at the second, the later has travelled a slightly longer distance, depicted by the blue lines AB and BC in Figure 2.8.

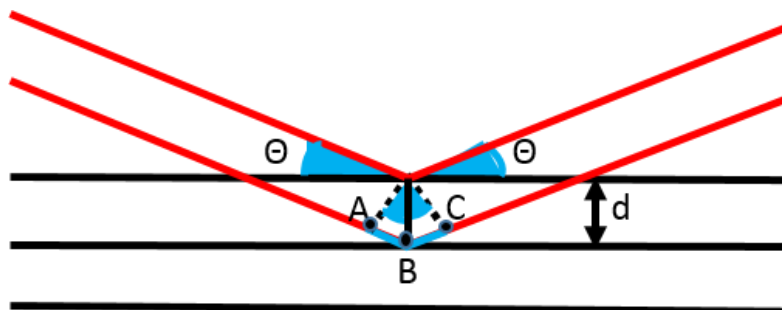


Figure 2.8 A representation of two X-rays being diffracted by the first and the second layer in a crystalline lattice. Θ is the angle between the incident ray and the planes, and the two blue lines show the additional distance that the second ray travels compared to the one diffracted by the first layer.

For these two rays to come out of the lattice with the same phase and result in a constructive interference, they need to follow the relation:

$$AB + BC = n\lambda \text{ (eq. 2.4)}$$

With n being a whole number and λ the wavelength of the X-ray source. Since $AB = BC = d\sin\Theta$, we can rewrite the above relation as

$$2d\sin\Theta = n\lambda \text{ (eq. 2.5)}$$

Which is known as Bragg's law. Extrapolating this back to the whole X-ray beam, the result is that we will only see the effect of it being diffracted when Bragg's law is obeyed, that is, only for some specific values of Θ . In all other cases the individual diffracted rays will be out of phase and will cancel each other (destructive interference). A second condition is that the distance between layers, d , must be of the same order of magnitude as the wavelength of the X-rays, but this is already accounted for when choosing the X-ray source.

The important thing for us from an application point of view is that the values of Θ and the intensities of the diffracted rays are characteristic of each crystal lattice, allowing for the identification of different compounds and phases.

For this technique the sample is first milled to make it into a thin, homogeneous powder. This way the tiny crystals that compose it will be randomly orientated in all possible directions, and when we irradiate it with an X-ray beam Bragg's law will work in all directions and we will get all possible interplanar distances.⁹ Some diffractometers allow for the sample holder to rotate to increase the randomness in the crystals' orientation. The sample is irradiated with a beam of monochromatic X-rays, which originate from an X-ray tube and pass through a monochromator before arriving at the sample (otherwise we would not have a well-defined λ to apply in Bragg's law!). Usually the $K\alpha$ line of copper or molybdenum is used as the source.

The distance between the X-ray focal spot and the sample and between the sample and the detector are the same. There are two possible configurations¹⁰ for scanning the sample: in some diffractometers the X-ray source does not move, while the sample moves by the angle Θ and the detector by 2Θ ; this is depicted in the upper diagram of Figure 2.9. In others, the sample holder is stationary (which is actually better if the powder is very loose, so that it doesn't fall!), and both X-ray tube and detector move by Θ simultaneously, as represented in the lower diagram of Figure 2.9. The obtained diffraction spectrum is a plot of the intensities of the peaks vs the detector angle (Θ or 2Θ depending on the configuration). For almost all directions the diffracted waves will be out of phase resulting in a destructive interference and we will not see any peak, but for a few values of the angle, which are characteristic of the crystalline material under examination, we will have a resulting constructive interference and we will see a peak whose intensity will depend on the number and type of atomic scattering points in each plane.

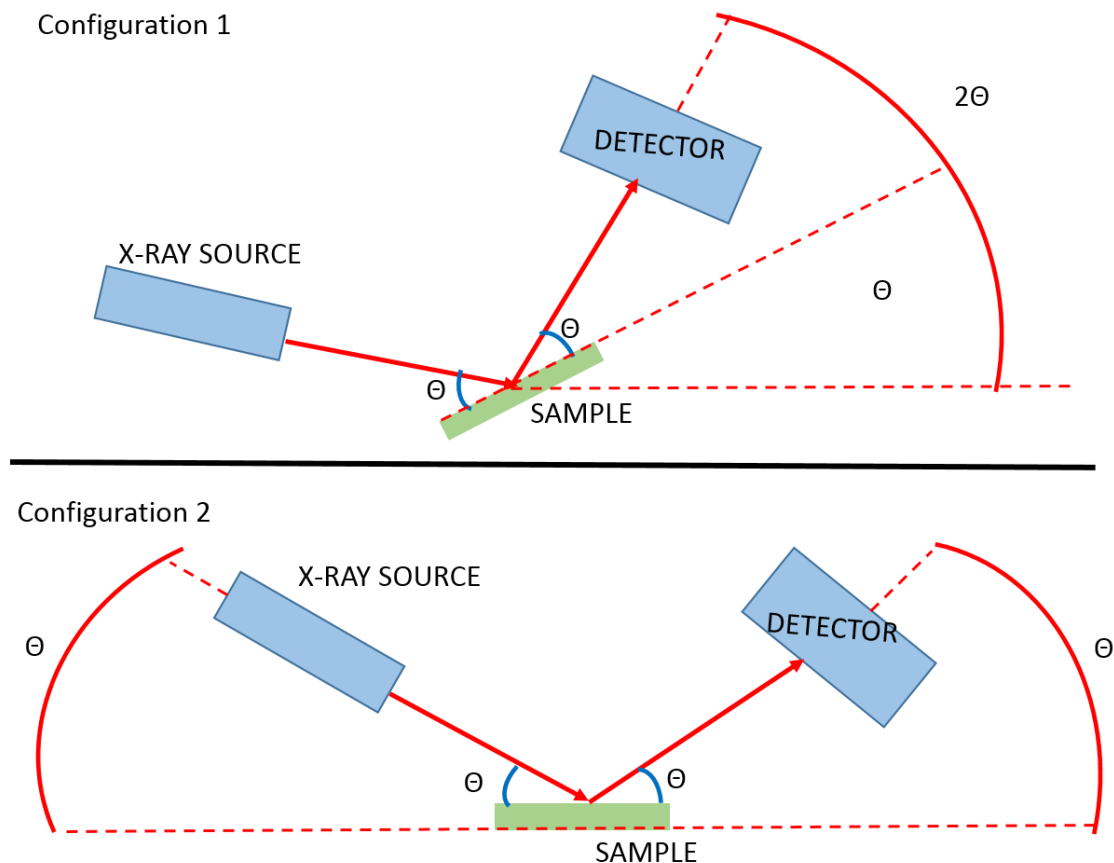


Figure 2.9 Diagram showing the two possible configurations in a powder X-ray diffractometer. In the upper one the X-ray source is fixed and the sample moves a value of the angle Θ while the detector moves 2Θ . In the lower one, both the X-ray source and the detector move simultaneously over the angular range Θ while the sample holder stays static.

The main application of PXRD is to identify and quantify components in a sample by search/match procedure thanks to the extensive databases available, since in a mixture of crystalline compounds/phases, each will produce a pattern that is characteristic and independent of the others: the powder X-ray diffraction pattern is like its fingerprint. On the other hand, it does not give enough information to characterize a new compound, since we can only obtain the distances between layers and get an idea of what the unit cell looks like, but cannot localize the individual position of each atom.

2.8 Atomic Force Microscopy (AFM)

AFM is a useful imaging technique to explore the topography of the surface of a material. Briefly, a cantilever with a very sharp tip scans the sample, keeping very close to the surface. As the tip approaches this, Van der Waal forces attract it closer due to the formation of temporal dipoles in the electronic clouds of both the tip and the sample, until a point in which the tip is too close (from a macroscopic point of view, when it touches the surface of the sample) and the repulsive coulombic forces overcome the attractive ones pushing the tip away. This repulsion and attraction effects between the tip and the surface result in subtle deflections in the cantilever, which behaves as a spring and follows Hook's law ($F = k x$, where k is the spring's constant and x the cantilever deflection). This way, we can detect hollows and raising features as the tip moves across the surface, obtaining a topographic map. The detection system is based on a laser beam that is constantly irradiating on the flat top of the cantilever and getting reflected from it: any subtle deflections of the cantilever result in an also subtle change in the direction of the reflected beam, which is collected by a position-sensitive photodiode (see Figure 2.10). Depending on the set up, in some microscopes it is the sample holder that moves in the plane perpendicular to the cantilever, whereas in other models the cantilever is attached to an arm that moves. The tip of the cantilever is usually made of silicon and it is either pyramidal or tetrahedral in shape. The sharper the tip, the higher the resolution of the AFM image.

There are basically three possible working modes in AFM: contact mode, tapping mode and non-contact mode.¹¹ In contact mode there is actual contact between the tip and the sample surface, whereas in the tapping mode the cantilever oscillates above it and only touches it lightly at the lowest point of the oscillation. In contact mode the feedback circuit tries to maintain a constant force, for which it constantly corrects the height as the tip is deflected. In tapping mode the amplitude of the cantilever's oscillation changes depending on the tip-surface separation, so that here the system tries to maintain a constant amplitude. The non-contact mode is somewhat similar to the tapping one except that the tip never touches the sample. Each of these modes has advantages and drawbacks, and one or other will be better suited depending on the kind of sample under study. In our case, we used tapping mode to characterize the Co-doped MoS₂ catalyst materials described in Chapter 5.

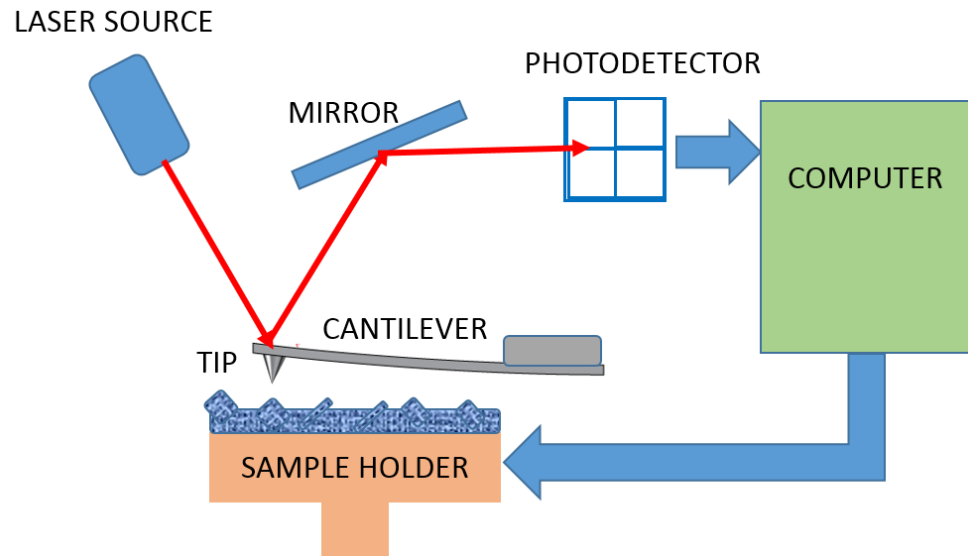


Figure 2.10 Diagram showing the main components of an atomic force microscope.

Other than topography applications, there are variants of AFM in which this is used for the measurement of mechanical, electrical and magnetic properties.¹² For example, in MFM (Magnetic Force Microscopy) the tip is strongly magnetized and is used to scan a magnetic material.

2.9 References

- (1) “X-Ray Photoelectron Spectroscopy (XPS): An Introduction” by David J. Morgan
- (2) http://www.casaxps.com/help_manual/XPSInformation/IntroductiontoXPS.htm
- (3) Supplementary Information of Ferrari, A. C.; Basko, D. M. *Nat. Nanotechnol.* **2013**, *8*, 235.
- (4) Cantarero, A. *Procedia Mater. Sci.* **2015**, *9*, 113
- (5) <http://advanced-microscopy.utah.edu/education/electron-micro/index.html>
- (6) <http://hypertextbook.com/facts/2000/IlyaSherman.shtml>
- (7) <http://www.azonano.com/article.aspx?ArticleID=3995>
- (8) Skoog, D. A.; Holler, J.; Nieman, T. A. “Principles of Instrumental Analysis”, chapter 9.
- (9) Skoog, D. A.; Holler, J.; Nieman, T. A. “Principles of Instrumental Analysis”, chapter 12
- (10) <http://prism.mit.edu/xray/oldsite/Basics%20of%20X-Ray%20Powder%20Diffraction.pdf>
- (11) <https://www.doitpoms.ac.uk/tlplib/afm/printall.php>
- (12) <http://www.parkafm.com/index.php/medias/nano-academy/how-afm-works>

CHAPTER 3

Efficient Electrocatalytic Water Oxidation at Neutral and High pH by Adventitious Nickel at Nanomolar Concentrations

Published as “Efficient Electrocatalytic Water Oxidation at Neutral and High pH by Adventitious Nickel at Nanomolar Concentrations” Roger, I.; Symes, M. D. *J. Am. Chem. Soc.* **2015**, *137*, 13980

Acknowledgements and declaration

The following people are acknowledged for their contribution to this chapter: Mr. Alexander Clunie (University of Strathclyde) for ICP-MS measurements, Mr. Jim Gallagher (University of Glasgow) for assistance with the SEM measurements. X-ray photoelectron spectra were obtained at the National EPSRC XPS Users' Service (NEXUS) at Newcastle University, an EPSRC Mid-Range Facility. IR performed all the other experimental work (unless stated otherwise) and IR and MDS co-wrote the paper.

Synopsis

This chapter is the account of an unusual research project, in the sense that it starts with the observation of an unexplained, unusually high activity for the water oxidation half-reaction in a control experiment, leading to the “detective work” of trying to find out the source of this activity. We will show the initial observations that led to these investigations and then we will explain the hypothesis we devised and the experiments we performed to check the validity of these hypothesis. As the chapter goes on, we will consider and eliminate different possibilities as experiments provide new clues and show the extent of the initial “anomalous control behavior”, which turns out to be wider than initially thought. As incorrect hypotheses are discounted we will start to see clearly the nature of this phenomenon and by the end of the chapter there will be proof solid enough to unequivocally assign the activity to its rightful agent: trace nickel present in the buffers as an impurity. We will show that this adventitious nickel, at concentrations as low as 17 nM, can act as a water oxidation catalyst in mildly basic aqueous solutions, achieving stable (tens of hours) current densities of 1 mA cm^{-2} at overpotentials as low as 540 mV at pH 9.2 and 400 mV at pH 13. This nickel was not added to the electrolysis baths deliberately, but was found to be present in the electrolytes as an impurity by ICP-MS. The presence of nickel on anodes from extended-time bulk electrolysis experiments was confirmed by XPS. In showing that such low levels of nickel can perform water oxidation at overpotentials comparable to many recently reported water oxidation catalysts, this work serves to raise the burden of proof required of new materials in this field: contamination by adventitious nickel at trace loadings must be excluded as a possible cause of any observed water oxidation activity.

3.1 Introduction

There has been much interest recently in electrocatalytic and photocatalytic water splitting as routes toward storing intermittent renewably-generated power (especially solar power) as chemical fuels such as hydrogen.¹⁻³ Acid regime Proton-Exchange Membrane Electrolyzers (PEMEs) have been proposed for this purpose as they respond well to fluctuations in power inputs.⁴ However, the most effective catalysts yet identified for PEMEs are based on very rare elements.⁵ This presents a challenge for photo-driven water splitting in particular, as the low photocurrents typically afforded by solar irradiation will require large electrode surface areas in order to produce useful amounts of fuel on practical timescales. Hence, if widespread solar-driven water splitting is to become a reality, then the loading of rare water-splitting catalysts must be lowered and/or less rare alternatives must be found.⁶ Alkaline electrolysis represents a possible solution to the issues of catalyst scarcity (porous Ni and steel electrodes in commercial electrolyzers allow current densities of 0.5 A cm^{-2} to be achieved at $\sim 300 \text{ mV}$ overpotential)⁷ but there is also a need to move away from the extreme pH regimes characteristic of such traditional commercial devices (pH ~ 0 for proton exchange membrane electrolyzers and pH > 14 for alkaline electrolyzers),⁴ because such corrosive conditions limit the types of photoelectrodes and cell components that can be used.^{8,9}

Studies on heterogeneous water oxidation catalysts that operate under the mild pH conditions that are compatible with existing photoelectrodes have therefore focused largely on first row transition metals due to their relatively high abundance in the Earth's crust. Some recent notable examples of such heterogeneous catalysts include cobalt oxides and oxyhydroxides,¹⁰⁻¹⁸ nickel oxides,¹⁹⁻²⁴ manganese oxides,²⁵⁻³³ copper oxides,³⁴⁻³⁶ and mixed oxides of first row transition metals.³⁷⁻⁴⁴ Some of these potential catalysts have already been used in conjunction with light-harvesting substrates to produce photoanodes competent for light-driven water oxidation.⁴⁵⁻⁵⁵ Meanwhile, catalysis with second and third row transition metals has been largely limited to compounds based on more scarce elements such as rhodium,⁵⁶ ruthenium⁵⁷ and iridium.^{48,58-62}

A typical strategy that is adopted when assessing the efficacy of such heterogeneous catalysts is to obtain current density *vs.* overpotential profiles and then to compare the overpotential required to reach some benchmark current density (often 1 or 10 mA cm^{-2}) with that required

to reach the same current density with other materials. Under basic conditions, an overpotential of between 0.33 and 0.5 V (to achieve a current density of 10 mA cm^{-2} for water oxidation) is considered as promising for solar-to-hydrogen applications.⁶³ However, this remains a somewhat challenging target, and many materials with overpotential requirements in excess of this 0.33 V to 0.5 V window have been (and continue to be) reported. Perhaps on account of the difficulty of demonstrating stable and sustained heterogeneous water oxidation catalysis at such comparatively low overpotentials, many studies assume that the background activity for water oxidation must be negligible, and control experiments may consist simply of a cyclic voltammogram in the absence of the material under investigation. However, such short-duration experiments may be insufficient to rule out the agency of trace metal impurities in any longer-term water oxidation catalysis observed with the proposed catalyst systems.

The issue of what the true catalyst for a given reaction actually is under a given set of conditions has been highlighted in seminal reviews by Finke⁶⁴ and Crabtree.⁶⁵ The latter paper in particular describes the effect that impurities can have in catalytic reactions, stating, “The phenomenally low loadings of metal that can give high activity is a major hazard in this area.” In recent years, the true nature of a range of catalysts with specific reference to water splitting has been explored,^{66,67} with special attention paid to the role that low levels of simple Co(II) salts (formed from the degradation of higher nuclearity homogeneous species) could have in electrocatalytic water oxidation.⁶⁸⁻⁷⁰ The effect that iron impurities have on nickel oxide water oxidation catalysts has also been reported.^{40,71-75} In this context, establishing the cause of any unexpectedly high water oxidation activity – including the potential agency of trace impurities in this catalysis – remains vital for advancing the field.

Herein, we show that nickel at very low concentrations (17 nM, giving an electrode surface loading of less than 1 nmol per cm^2) constitutes a competent catalyst for water oxidation over the pH range 9.2 - 13, delivering stable current densities of 1 mA cm^{-2} at overpotentials of 540 mV at pH 9.2 and 400 mV at pH 13 for periods of several tens of hours. This nickel was not added to the electrolysis baths deliberately. Rather, it was present as a trace impurity in the supporting electrolyte salts (and possibly even in the ostensibly de-ionized (DI) water used to prepare the electrolytes), and its water oxidation activity only manifested after several minutes of anodic polarization in electrolysis experiments. Furthermore, at these low

loadings, the nickel oxide catalyst layer on the anode was undetectable by eye or by SEM/EDX, and the presence of nickel was only evident by ICP-MS analysis of the electrolyte and by comparison of XPS spectra run in as-prepared and carefully washed electrolyte solutions. Although we cannot exclude the possibility that the nickel oxide deposits formed do not also contain traces of Fe,⁷¹⁻⁷³ we show that the concentration of nickel in the electrolyte solution is a critical determinant of the extent of water oxidation catalysis. The very low levels of nickel required to produce respectable and reproducible activities for electrochemical water oxidation serve to raise the bar when investigating the activity of heterogeneous water oxidation catalysts at neutral and basic pH: other materials that display similar current densities at these overpotentials must demonstrate that adventitious nickel contamination is not a cause of the observed activity.

3.2 An anomalous control experiment

As part of our ongoing studies of electrocatalytic water oxidation using Earth-abundant elements,¹⁶ we had occasion to conduct control experiments in which a fluorine-doped tin oxide (FTO) on glass working electrode was poised at overpotentials of around 600 mV in a single chamber electrolysis cell, along with a Pt wire counter electrode and an Ag/AgCl reference electrode. Under stirring in potassium borate buffer (0.5 M, pH = 9.2), the current first declined gently for the first few hundred seconds, much as expected. However, we were surprised to observe a subsequent steady rise in current, the onset of which typically occurred between 60 and 600 s after the beginning of the polarization, and which continued for several hours before reaching a plateau at between 1 and ~ 4 mA cm⁻² (Figure 3.1).

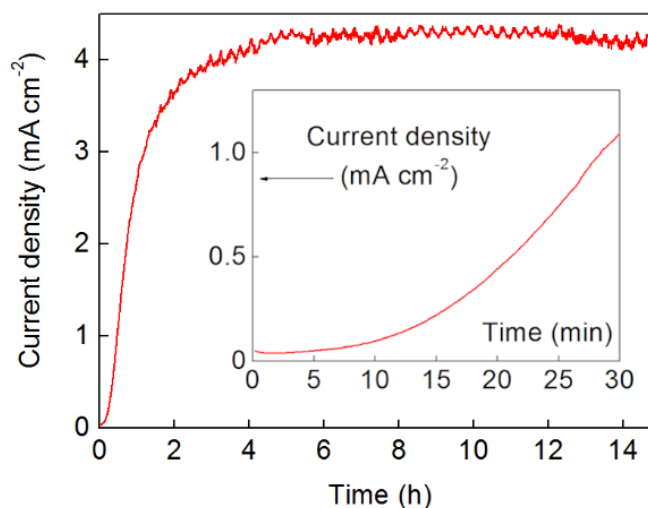


Figure 3.1 Main: A bulk electrolysis experiment performed with a 1 cm^2 FTO working electrode, Ag/AgCl reference electrode and a Pt wire counter electrode in 0.5 M potassium borate (pH 9.2) at room temperature. A single chamber cell was used and the electrolyte was stirred throughout. A potential of 1.4 V vs. NHE was maintained, and the data is not corrected for solution resistance ($R = 31 \Omega$). Inset: An expansion of the first 30 min of the main panel, showing the steady rise of the current density after an initial lag phase.

This phenomenon was found to be highly reproducible and could be observed on both FTO electrodes poised anodically in fresh solutions and FTO electrodes poised anodically in solutions that had previously displayed this behavior. Figure 3.1 shows that this high current was maintained for periods of over 10 h, and in some cases current densities well in excess of 1 mA cm^{-2} were sustained for up to 72 h, showing no sign of decreasing. During this time, steady bubbling could be observed from the FTO anode, which appeared identical by eye to fresh FTO. In the absence, to our knowledge, of any previous reports of similar behavior for FTO without the addition of catalysts, and intrigued by these large “control” currents (in many cases outperforming the substances we were trying to assess), we began a systematic study of these electrochemical processes in the hope of finding the cause of this activity.

3.3 Looking for the source of the activity observed

One of the first experiments we did was to collect points for a Tafel plot before and after anodization. Figure 3.2 compares Tafel plots obtained for FTO electrodes that had been polarized anodically in 0.5 M potassium borate buffer at 700 mV overpotential until the current density had reached a plateau with the behavior of fresh FTO electrodes that had not been subjected to prior anodization in this fashion. Pre-anodized electrodes displayed reproducible Tafel slopes of 57 mV (± 2 mV) over nearly three decades of log current density, whilst non-anodized electrodes gave slopes in the region of 120 mV per decade at low current densities (less than 0.1 mA cm^{-2}).

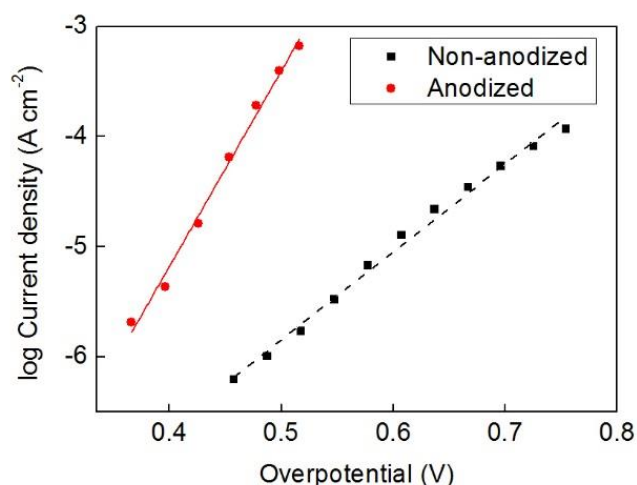


Figure 3.2 Representative Tafel plots of anodized (red line and circles) and non-anodized FTO films (black squares and dashed line) in 0.5 M potassium borate solution at pH 9.2. Anodization was conducted at 1.4 V vs. NHE for 24 h. Overpotentials have been corrected for resistance.

We also compared cyclic voltammograms (CVs) of anodized and non-anodized (fresh) films in the presence of 1 mM ferricyanide in order to determine if there was any significant increase in the surface area of the electrode as a result of anodization. If the electrode surface area was increasing with prolonged anodization, then a larger reversible wave for the Fe(III)/Fe(II) redox couple should be evident for the anodized electrodes. As a control, CVs of non-anodized electrodes having a range of known geometric surface areas were first obtained, which allowed a linear relationship between electrode surface area and peak current in the CV to be established (Figure 3.3). We then compare in Figure 3.4 a CV taken before with one taken after anodization at +1.0 V vs. NHE for 24 h, during which time the current density rose to a steady 2.3 mA cm^{-2} . No significant changes in the size or shape of

the ferricyanide redox wave were evident, in turn implying that the surface area of the electrode was not significantly altered by anodization (certainly not to an extent that would explain the increase in apparent current density seen in Figure 3.1 on its own). In contrast, a catalytic oxidation event highly suggestive of water oxidation seems to occur at a much lower onset potential after anodization than before.

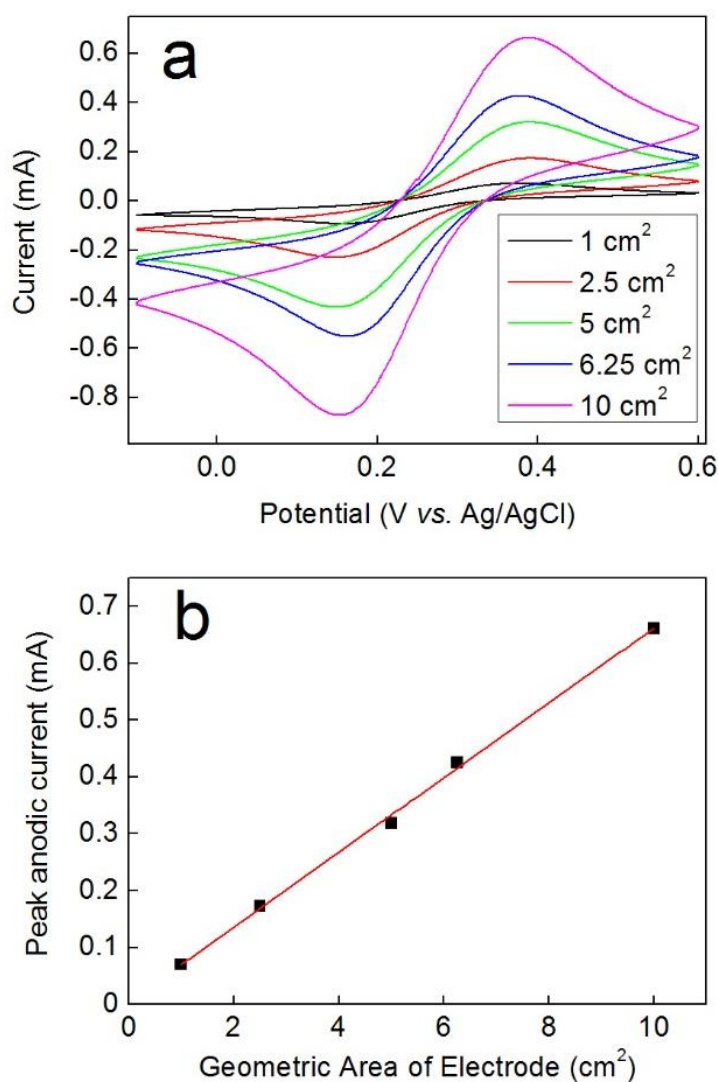


Figure 3.3 *a)* Comparison of CVs of an ITO working electrode (various geometric areas as indicated) at a scan rate of 50 mV s^{-1} at room temperature. Ag/AgCl reference and Pt counter electrodes were used. The electrolyte was 0.5 M sodium phosphate ($\text{pH } 12.9$) containing 1 mM potassium ferricyanide. *b)* Peak anodic currents from the CVs in the above panel plotted as a function of electrode geometric surface area.

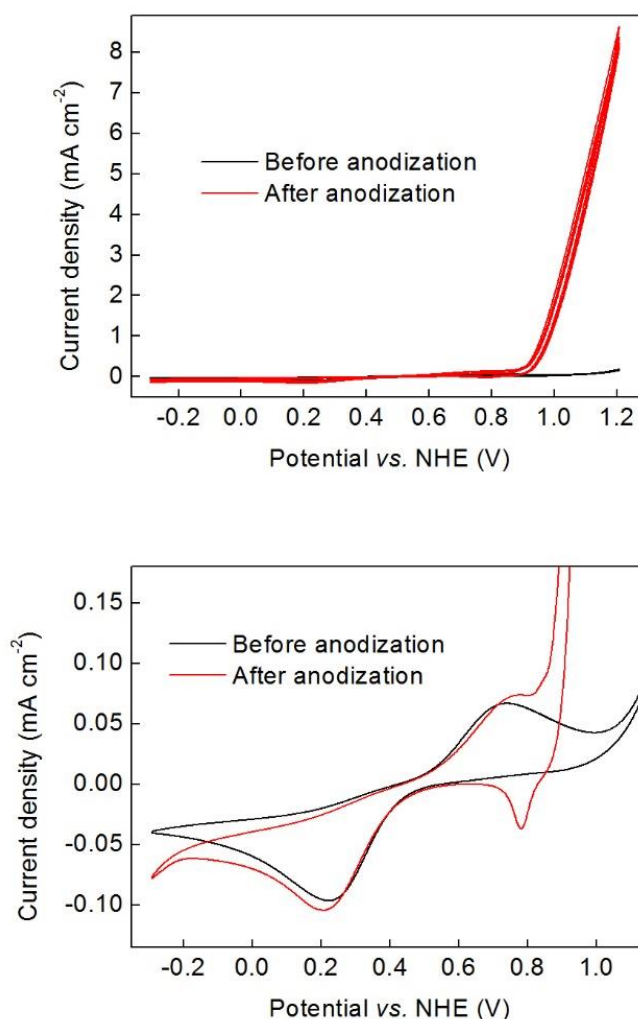


Figure 3.4 Top: Comparison of CVs of an FTO working electrode (area = 1 cm²) before and after anodization at a scan rate of 50 mV s⁻¹ at room temperature. Ag/AgCl reference and Pt counter electrodes were used. The electrolyte was 0.5 M sodium phosphate (pH 12.9) containing 1 mM potassium ferricyanide. After the first CV (black line) was recorded in this electrolyte, the working electrode was removed, rinsed with water and anodized in 0.5 M sodium phosphate (pH 12.9) electrolyte without ferricyanide for 24 h at a constant voltage of +1.0 V vs. NHE. After the anodization, ferricyanide was added to this electrolyte to give a 1 mM solution and the second voltammogram (red) was taken using the same conditions as the black trace. **Bottom:** Expansion of the CVs above.

With no evidence to support an increase in surface area being the cause of the increased current density, and in light of our Tafel data suggesting that the nature of the electrode was radically altered, it seemed plausible that the electrodeposition of some species from solution

onto the electrode could be the cause of the increased activity observed. This would also explain the slowly rising current after an initial lag phase observed in Figure 3.1. Accordingly, we analyzed anodized electrodes by SEM and EDX (Figure 3.5):

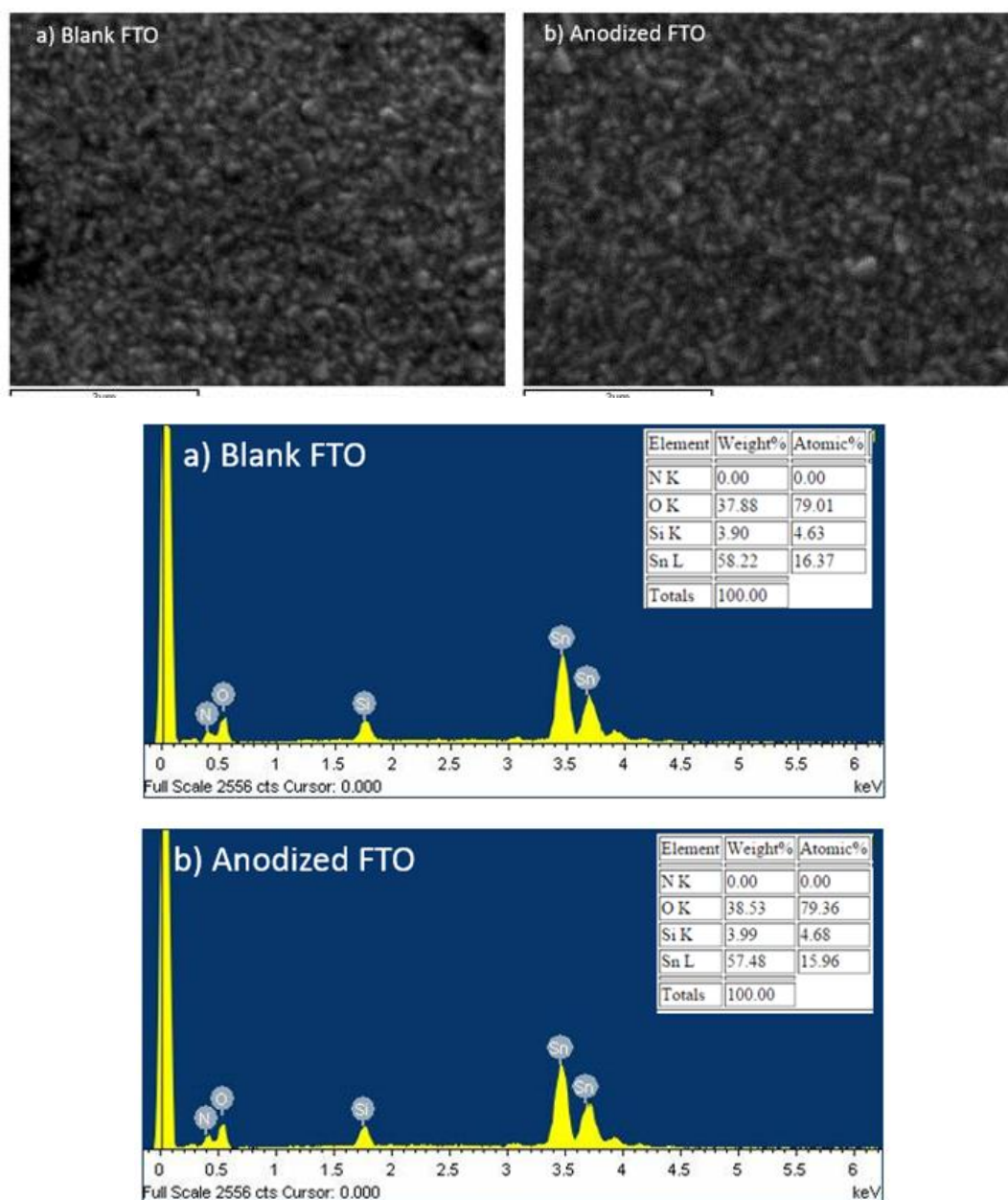


Figure 3.5 SEM images (top) and EDX spectra (below) comparing a blank FTO-glass slide with an FTO-glass slide that had been anodized for 24 h in sodium phosphate buffer at pH 12.9. For anodization, a potential of 1.0 V vs. NHE (not corrected for resistance) was applied with stirring at room temperature in a single chamber cell. The counter electrode was a Pt wire and the reference electrode was Ag/AgCl. SEM indicates that there are no obvious deposits on the surface, whilst EDX gives peaks consistent with bare FTO in both cases. Other areas of both films were analyzed and found to give the same results.

These results evinced no hints as to the presence of any surface deposits, suggesting that if any electrodeposition of catalytically-active species had occurred then the amounts deposited were very low. However, it was still possible that minute traces of impurities in the electrolyte were depositing onto the surface at very low levels. In this regard, we note that electrocatalytic water oxidation using ultra-low loadings of cobalt were recently reported by Meyer and co-workers,⁷⁶ who were able to achieve a current density for water oxidation of 0.16 mA cm^{-2} at an overpotential of 0.8 V using phosphate buffer at pH 7.2 and loadings of cobalt on planar FTO as low as $7 \times 10^{-11} \text{ mol cm}^{-2}$ (as judged by integration of cyclic voltammograms). Nocera and co-workers have also reported catalytic water oxidation at appreciable levels by heterogeneous cobalt oxides deposited from Co(II) impurities present in solutions of cobalt coordination complexes.⁷⁰ In this study, the authors found that only $9 \times 10^{-8} \text{ nmol}$ of cobalt (in the form of heterogeneous cobalt oxy-hydroxides) could give rise to current densities of 0.11 mA cm^{-2} (at $\sim 0.9 \text{ V}$ overpotential) at pH 7. Hence there is strong precedence for detectable and sustained water oxidation electrocatalysis in the presence of very small amounts of first row transitions metal ions.

Accordingly, we altered our electrolyte, and chose to probe sodium phosphate as an alternative buffer. Current densities were significantly lowered in this electrolyte at low and near-neutral pH, but more complete study of the overpotential required to achieve a current density of 1 mA cm^{-2} over the pH range 1-13 evinced an extraordinary shift at high pH to much lower values (see Figure 3.6).

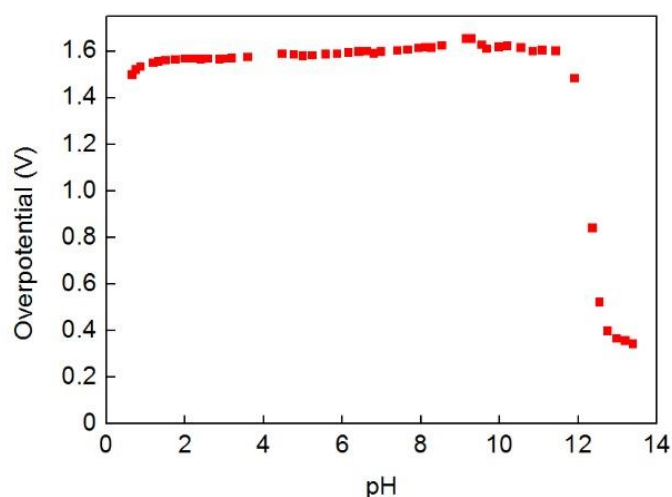


Figure 3.6 Galvanostatic overpotential vs. pH profile (at a current density of 1 mA cm^{-2}) for an FTO working electrode (area = 1 cm^2) that had previously been anodized in 0.5 M potassium borate at pH 9.2 overnight at $V = 1.2 \text{ V}$ vs. Ag/AgCl ($R = 31.5 \Omega$). A Pt wire counter electrode and an Ag/AgCl reference electrode were used at room temperature. The overpotential required to achieve a current density of 1 mA cm^{-2} was then gauged when the voltage reading had stabilized (typically around 5 min after addition of each aliquot). The electrolyte for the galvanostatic experiment was initially $1 \text{ M H}_3\text{PO}_4$, to which aliquots of NaOH solution were added.

Indeed, we found that the overpotential requirement was lowered to only 400 mV at pH 12.9 (for 1 mA cm^{-2}). Moreover, similar trends could be observed in 1 M sodium carbonate buffer (Figures 3.8, 3.11, 3.13), suggesting that any impurity present in the electrolyte was possibly common to all these salts.

Some authors have suggested that tin oxide-based electrodes can undergo compositional changes when poised anodically in aqueous solutions, with a lowered overpotential for oxygen evolution and electrode corrosion manifesting as a result of an increase in the number of oxygen vacancies in the lattice.⁷⁷ In order to test whether this was a possible cause of the activity seen in the present case, we repeated the anodization procedure using a range of alternative substrates: commercial indium tin oxide on glass (ITO), glassy carbon, boron doped diamond and platinum (see Figures 3.7 to 3.13). We also replaced our Pt counter electrode with carbon felt, in order to exclude the possibility of Pt leaching from the counter electrode and forming Pt oxides at the working electrode. Despite these changes, all combinations of substrate electrode and counter electrode that were examined displayed the

familiar initial lag phase followed by a prolonged period of rising current resulting in final current densities between 4 and 1.5 mA cm⁻² at overpotentials of between 540 and 660 mV (not corrected for resistance). These results seemed to rule out any changes in the structure or stoichiometry of the FTO electrode as the root cause of the high currents observed and eliminated Pt leached from the cathode as a source of activity.

We next repeated our standard anodization procedure in a two compartment cell, where the working and counter electrodes were in different chambers separated by a Nafion membrane. The rationale behind this was to prevent any impurities in solution from undergoing redox cycling between the anode and cathode. This division of the cell made no difference whatsoever to the rate of increase of current density upon anodization and did not alter the final current density reached (Figure 3.11). Likewise, rates of current density increase and peak current densities were again unaffected by changing the Pt counter electrode for a carbon cloth counter electrode in this two-chamber electrolysis cell. On the other hand, substituting the Ag/AgCl reference electrode for a Hg/HgO reference electrode (to exclude the possibility of trace silver acting as a water oxidation catalyst, as reported recently by some authors),⁷⁸⁻⁸⁰ gave rates of current density increase and peak current densities similar to those seen with the Ag/AgCl reference electrode (see Figures 3.10 and 3.13). Furthermore, experiments undertaken in a two-electrode configuration with an FTO working electrode and carbon felt counter electrode also showed the now familiar current density profiles (see Figure 3.12). These results suggested that the nature of the reference electrode (if any) was not the cause of the currents observed.

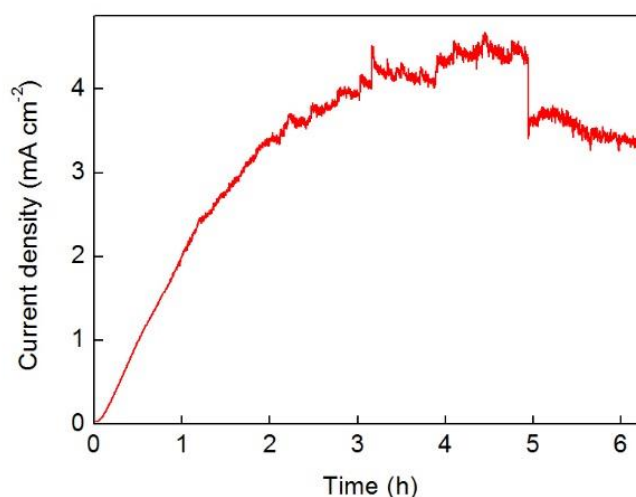


Figure 3.7 Bulk electrolysis with stirring of an aqueous solution of 0.5 M sodium phosphate (pH 12.9) on a Pt disc working electrode (area = 0.031 cm²). A Pt wire counter electrode and an Ag/AgCl reference electrode were used at room temperature. An overpotential of 0.54 V was applied (not corrected for solution resistance). The lower current after ~4.8 h is due to bubble formation on the electrode.

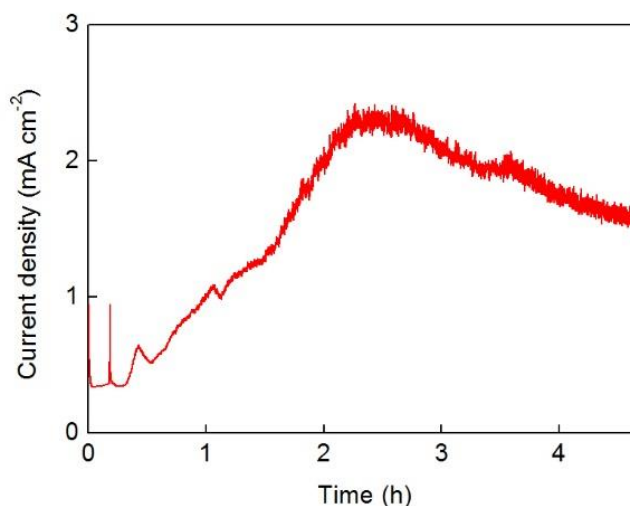


Figure 3.8 Bulk electrolysis with stirring of an aqueous solution of 1 M sodium carbonate (pH 11.5) on a glassy carbon working electrode (area = 0.071 cm²). A carbon felt counter electrode and an Ag/AgCl reference electrode were used at room temperature. An overpotential of 0.66 V was applied (not corrected for solution resistance). The current decay after around 2 h is accompanied by a darkening and apparent roughening of the electrode surface, which we attribute to oxidation of the underlying carbon substrate at these high potentials.

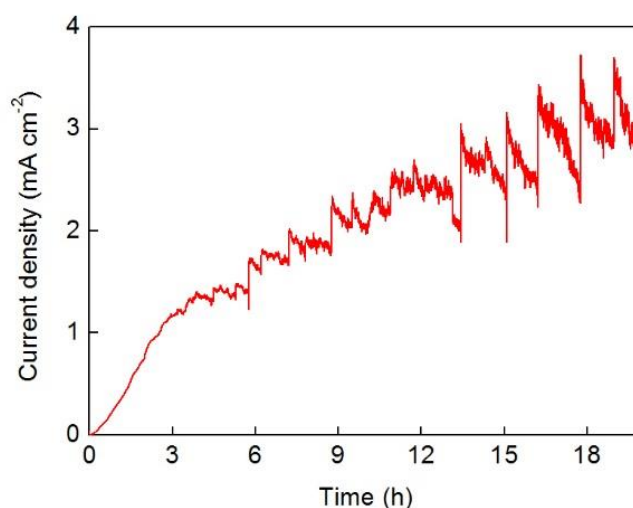


Figure 3.9 Bulk electrolysis with stirring of an aqueous solution of 0.5 M sodium phosphate (pH 12.9) on a boron-doped diamond disc working electrode (area = 0.071 cm², Windsor Scientific Ltd., UK). A Pt wire counter electrode and an Ag/AgCl reference electrode were used at room temperature. An overpotential of 0.54 V was applied (not corrected for solution resistance). The oscillations apparent in the graph are due to bubble formation at the working electrode.

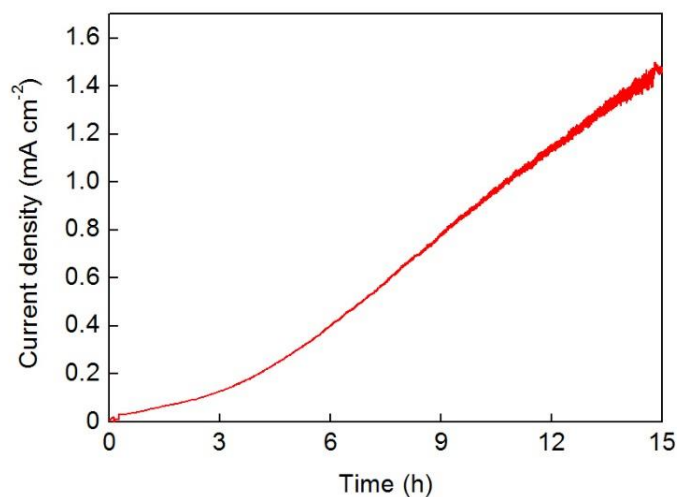


Figure 3.10 Bulk electrolysis with stirring of an aqueous solution of 0.5 M sodium borate (pH 9.2) on a boron-doped diamond disc working electrode (area = 0.071 cm², Windsor Scientific Ltd., UK). A carbon cloth counter electrode and an Hg/HgO reference electrode were used at room temperature. An overpotential of 0.66 V was applied (after correction for solution resistance).

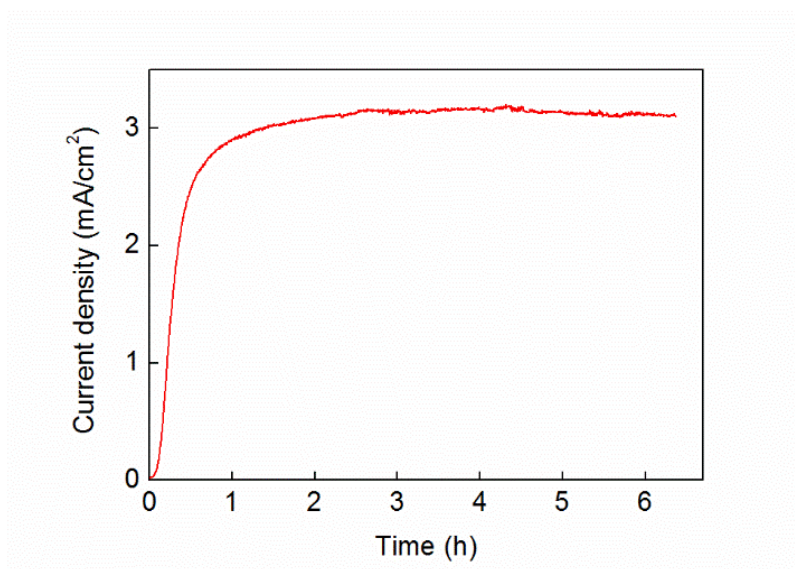


Figure 3.11 Bulk electrolysis with stirring of an aqueous solution of 1 M sodium carbonate (pH 11.5) on an FTO working electrode (area = 1.5 cm²). A two compartment cell was used, with the chambers separated by a Nafion membrane. Along with the FTO electrode, an Ag/AgCl reference electrode was used in the working electrode compartment. The counter electrode compartment contained a carbon felt counter electrode, also in 1 M sodium carbonate solution. The experiment was performed at room temperature. An overpotential of 0.66 V was applied (not corrected for solution resistance, which was on the order of 40 Ω).

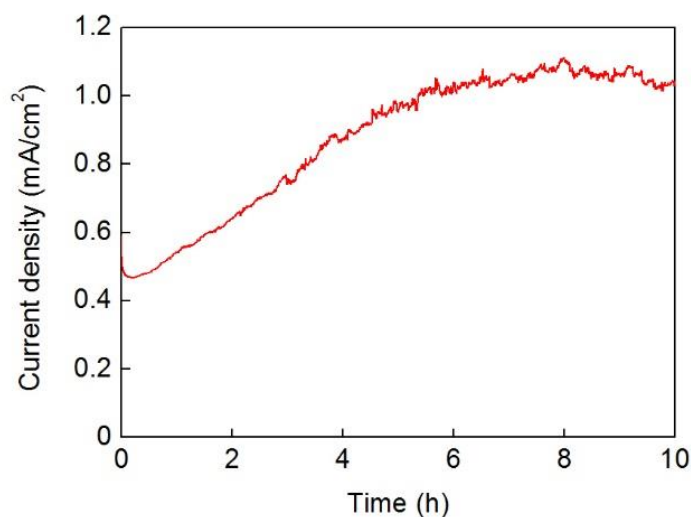


Figure 3.12 Bulk electrolysis with stirring in a two-electrode configuration of an aqueous solution of 0.5 M sodium phosphate (pH 12.9). A potential of 1.9 V (not corrected for resistance, which was on the order of 25 Ω) was applied between an FTO working electrode (area \sim 1 cm²) as the positive electrode and a carbon felt negative electrode (area \sim 1 cm²). A single compartment cell was used, and the experiment was performed at room temperature.

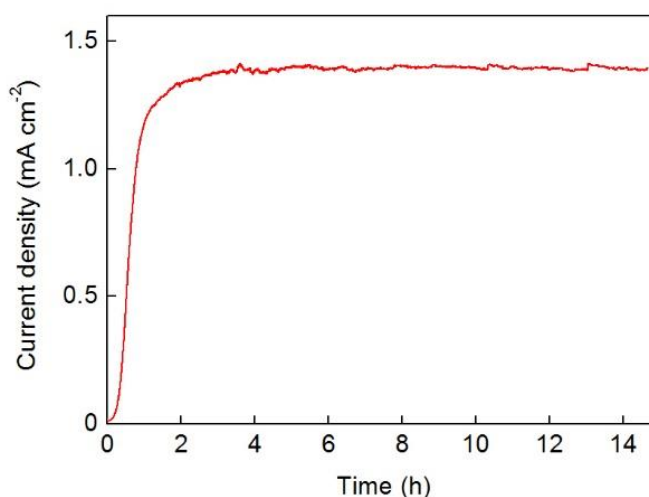


Figure 3.13 Bulk electrolysis with stirring of an aqueous solution of 1 M sodium carbonate (pH 11.5) on an ITO working electrode (area = 2.5 cm²). A carbon felt counter electrode and an Hg/HgO reference electrode were used at room temperature. An overpotential of 0.66 V was applied (not corrected for solution resistance, which was found to be 9 Ω).

The experiments in two-chambered cells suggested that the currents were not caused by redox-cycling of species in solution. We had also observed that slow bubbling was evident at the working electrode when current densities exceeded ~ 1 mA cm⁻². To determine if oxygen production would account for the observed currents, we analyzed the headspace of sealed, airtight cells containing an FTO working electrode by gas chromatography. In all, three separate sets of conditions were probed: sodium phosphate buffer with an Hg/HgO reference electrode at pH 13.0 and an overpotential for water oxidation of 580 mV (Figure 3.14), sodium phosphate buffer with an Ag/AgCl reference electrode at pH 12.9 and an overpotential for water oxidation of 540 mV (Figure 3.15), and potassium borate buffer with an Ag/AgCl reference electrode at pH 9.1 and an overpotential for water oxidation of 570 mV (Figure 3.16). All three sets of conditions showed that the currents observed were indeed due overwhelmingly to oxygen production, with Faradaic efficiencies for these processes being 95% ($\pm 6\%$) for sodium phosphate buffer with an Hg/HgO reference electrode at pH 13.0, 90% ($\pm 3\%$) for sodium phosphate buffer with an Ag/AgCl reference electrode at pH 12.9 and 94% ($\pm 8\%$) for potassium borate buffer with an Ag/AgCl reference electrode at pH 9.2.

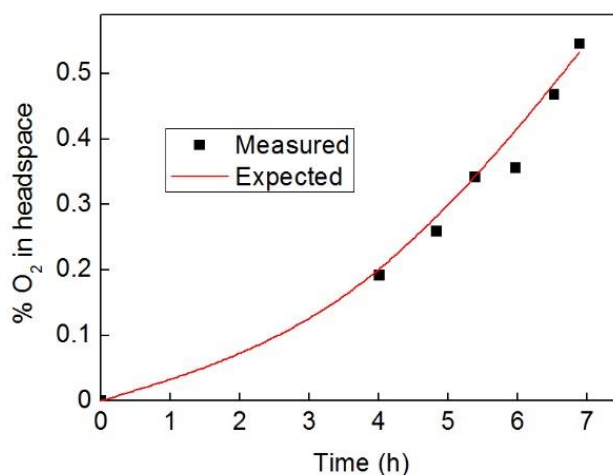


Figure 3.14 A representative trace showing gas chromatographic analysis of the headspace of an airtight cell during electrolysis of a solution of 0.5 M sodium phosphate at pH 13. An FTO working electrode, carbon felt counter electrode and an Hg/HgO (1 M NaOH) reference electrode were used at an overpotential for water oxidation of 0.58 V (not corrected for resistance). The solid red line indicates the % of oxygen expected in the cell headspace based on the charge passed during electrolysis (24 C in this case). Black squares indicate actual measurements of the % of O₂ in the cell headspace as determined by gas chromatography.

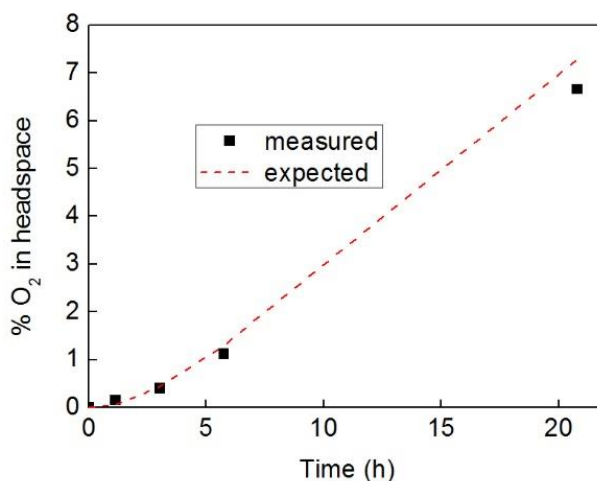


Figure 3.15 A representative trace showing gas chromatographic analysis of the headspace of airtight cells during electrolysis of a solution of 0.5 M sodium phosphate at pH 12.9. An FTO working electrode, carbon felt counter electrode and an Ag/AgCl reference electrode were used at an overpotential for water oxidation of 0.54 V (not corrected for resistance). The red dashed line indicates the % of oxygen expected in the cell headspace based on the charge passed during electrolysis (230 C in this case). Black squares indicate actual measurements of the % of O₂ in the cell headspace as determined by gas chromatography. A Faradaic yield for oxygen production of 90% ($\pm 3\%$) was determined.

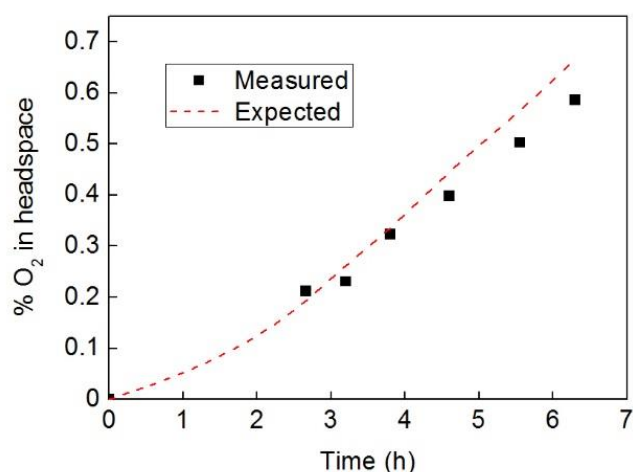


Figure 3.16 A representative trace showing gas chromatographic analysis of the headspace of airtight cells during electrolysis of a solution of 0.5 M potassium borate at pH 9.1. An FTO working electrode, carbon felt counter electrode and an Ag/AgCl reference electrode were used at an overpotential for water oxidation of 0.61 V (not corrected for resistance, or 0.57 V after correction for resistance). The red dashed line indicates the % of oxygen expected in the cell headspace based on the charge passed during electrolysis (27 C in this case). Black squares indicate actual measurements of the % of O₂ in the cell headspace as determined by gas chromatography. A Faradaic yield for oxygen production of 94% ($\pm 8\%$) was determined.

With evidence to suggest that catalytic water oxidation was occurring, but still without firm evidence of the agent(s) responsible, we next turned our attention to analysis of our electrolyte solutions. Addition of the disodium salt of ethylene diamine tetra-acetic acid (EDTA) to anodization reactions that were underway was observed to lead to a rapid and lasting reduction in current density (Figure 3.17).

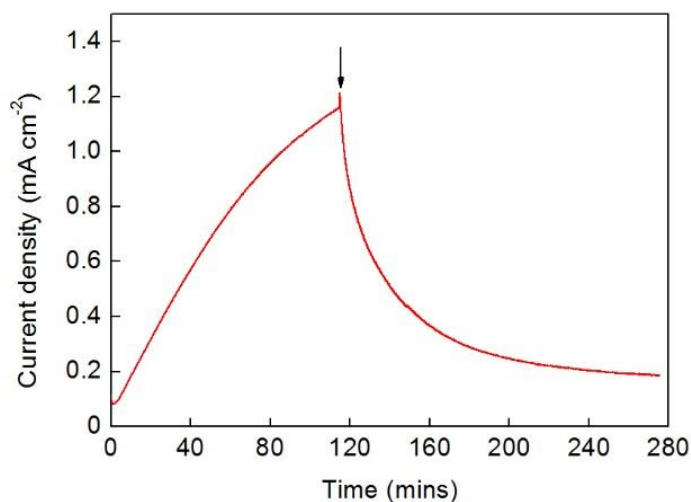


Figure 3.17 Bulk electrolysis with stirring of an aqueous solution of 0.5 M potassium borate (pH 9.2) on an FTO working electrode (area = 1 cm²). A Pt wire counter electrode and an Ag/AgCl reference electrode were used at room temperature. An overpotential of 0.72 V was applied (not corrected for solution resistance, which was on the order of 40 Ω). After 114 min (indicated by the black arrow), around 20 mg of EDTA (sodium salt) were added as a solid.

This suggested that metal ions were indeed implicated in the water oxidation catalysis. However, our previous results mentioned above implied that these metal ions did not originate from any of the electrodes. Accordingly, we analyzed both fresh solutions and those that had previously supported anodization of electrodes by ICP-MS. This revealed relatively high (hundreds of ng L⁻¹ – μg L⁻¹) levels of several transition metals to be present (including Fe, Ni, Mo, Cu and Mn) in these buffer solutions, which were prepared with deionized water of 18.2 MΩ × cm resistivity (see Table 3.1)⁸¹. In order to remove these metal ions from solution without introducing soluble agents (such as EDTA) that would remain in solution and potentially interfere with our analysis, we treated our buffer solutions with Amberlite IRC748 resin (an iminodiacetic acid chelating cation exchange resin for metal removal). In this way, it was hypothesized that any metal ions in the solution would be retained by the resin, which could then be separated from the electrolyte by filtration (see Experimental Section for the detailed procedure). Electrolysis experiments performed as before in such “washed” electrolytes did indeed evince significant attenuation in the rate of current density increase and a lowering of the peak current densities obtained, as can be seen in Figure 3.18:

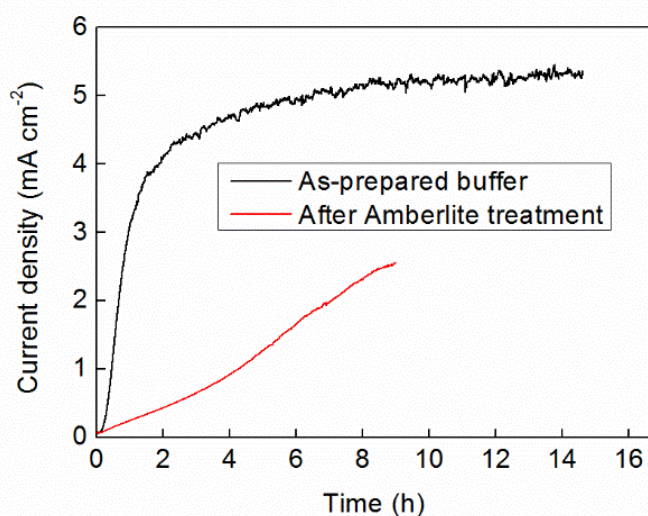


Figure 3.18 Comparison of electrolysis with and without pre-treatment of the electrolyte with Amberlite (see procedure in section 3.5.5). Red line: Bulk electrolysis with stirring of an aqueous solution of 0.5 M potassium borate (pH 9.2) that had previously been washed once with Amberlite IRC-748 resin. Black line: Bulk electrolysis with stirring of an aqueous solution of as-prepared 0.5 M potassium borate (pH 9.2) that had not previously been washed with Amberlite IRC-748 resin. In both cases, the working electrode was FTO (area = 1 cm²). Single compartment cells were used. Along with the FTO electrode, an Ag/AgCl reference electrode and a Pt wire counter electrode were employed. The experiments were performed at room temperature. An overpotential of 0.72 V was applied in each case (not corrected for solution resistance).

Metal	Content in 1% HNO ₃ blank (ng L ⁻¹)	Average content of as-prepared buffer (ng L ⁻¹)	Average content after one cleaning cycle (ng L ⁻¹)
Na	897	-	-
K	5850	-	-
Ca	30200	-	-
Sc	1.2	3.6 (±2.8)	3.3 (±2.4)
Ti	21.3	94.6 (±28.3)	89.8 (±6.5)
V	2.2	14.9 (±2.9)	12.2 (±1.8)
Cr	18.6	42.5 (±11.6)	36.7 (±7.1)
Mn	27.6	469.4 (±51.6)	250.5 (±42.5)
Fe	424.0	502.6 (±52.9)	994.8 (±75.2)
Co	1.5	2.8 (±1.4)	4.3 (±1)
Ni	43.4	1065.7 (±85.5)	778.5 (±91.1)
Cu	81.5	187.9 (±6.8)	320.8 (±55.0)
Zn	218.6	380.6 (±63.0)	457.1 (±12.4)
Y	1.0	1.7 (±1.5)	3.9 (±1)
Zr	11.5	343.5 (±24.8)	314.5 (±4.7)
Nb	<1	<1	<1
Mo	3.0	7383.3 (±144)	49.3 (±32.2)
Ru	1.6	3.1 (±1)	2.8 (±1)
Rh	<1	<1	<1
Pd	1.4	3.5 (±1)	3.0 (±1)
Ag	1.6	4.9 (±1.8)	5.7 (±2.4)
Cd	<1	9.1 (±8)	1.1 (±1)
Ce	25.0	90.6 (±10.9)	1.7 (±1)
Hf	1.7	4.9 (±3.1)	3.6 (±1.5)
Ta	<1	<1	<1
W	1.2	742.6 (±32.1)	102.2 (±10.9)
Re	<1	<1	<1
Os	<1	<1	<1
Ir	<1	<1	<1
Pt	<1	1.5 (±1)	1.2 (±1)
Au	<1	<1	<1
Hg	<1	<1	<1
Pb	17.5	23.3 (±1.1)	<1

Table 3.1: Summary of the ICP-MS data for selected metal ions collected for 0.5 M potassium borate solutions after spiking with 1% HNO₃ (averages of three runs). Errors shown are standard deviations of the replicate runs. Background data showing just 18.2 MΩ-cm water spiked with 1% HNO₃ are shown for comparison. Cleaning was achieved by washing the solution once with Amberlite resin (see Experimental Section).

Films that had been anodized in as-prepared electrolyte (until a steady current density had been reached) were subjected to analysis by CV in that electrolyte, and these CVs were compared to those obtained after the films had been removed from the as-prepared electrolyte and placed into electrolyte that had been washed with Amberlite resin. CVs were recorded in the washed electrolyte every five minutes, with stirring of the electrolyte in the intervals. No bias was applied to the working electrode during these stirring periods. Figure 3.19 shows how the peak current obtained decays gradually over time under these conditions, implying that an electrode-bound deposit has indeed formed on the electrode during anodization (or else the current density obtained on moving to the washed electrolyte would be much lower from the outset). However, these results also suggest that this deposit is not stable when allowed to rest without applied bias in washed electrolyte solution under stirring.

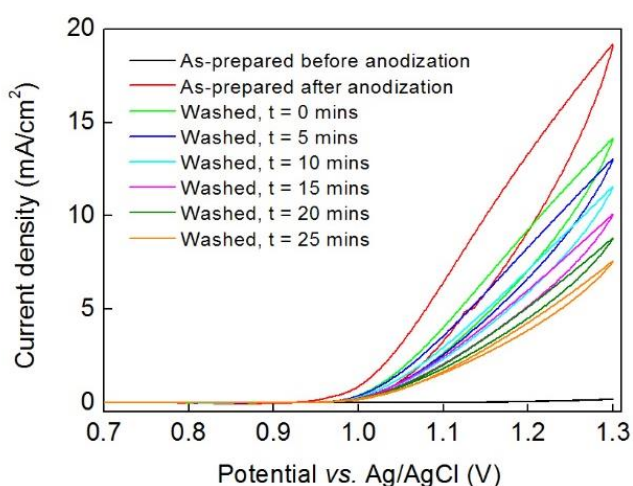


Figure 3.19 Comparison of CVs of an FTO working electrode (area = 1 cm²) after anodization at an uncorrected voltage of 1.2 V vs. Ag/AgCl for 18 h (during which time the current density reached a steady value of 4 mA cm⁻²). The scan rate in all cases was 100 mV s⁻¹ and CVs were collected at room temperature. Ag/AgCl reference and Pt counter electrodes were used for the anodization and the CVs. The electrolyte for anodization and the first CV (red line) was as-prepared 0.5 M potassium borate (pH 9.2). The working electrode was then removed from this electrolyte and rinsed thoroughly with 18.2 MΩ-cm resistivity deionized water and allowed to dry in air for 10 min. The working electrode was then placed in 0.5 M potassium borate (pH 9.2) that had been washed once with Amberlite resin according to the procedure outlined in Section 3.5.5. A CV (green line) was then immediately recorded using the same conditions as used for the CV in as-prepared buffer. CVs were subsequently recorded every 5 min, with stirring of the solution in the intervals but no bias applied. The second scan of each set of CVs is shown. The results suggest that a deposit on the electrode has been formed, but that it is not stable when allowed to rest without applied bias in washed electrolyte solution. A CV of the same electrode prior to anodization is shown for comparison (black trace).

When washed electrolytes were analyzed by ICP-MS and the concentrations of the various metal ions compared to those found in the electrolytes prior to washing with the Amberlite resin, only six metals were found to have significantly and consistently lower concentrations in the washed electrolytes (which gave correspondingly lower current densities) than in the as-prepared electrolytes: Pb, W, Mn, Mo, Ce and Ni (highlighted in Table 3.1). Of these metals, Ni and Mn have previously been shown to display catalytic water oxidation activity under neutral and near-neutral conditions.¹⁹⁻³³ However, we re-examined all of these candidate metals for water oxidation activity by adding small amounts of various solids containing these ions to electrolysis experiments in 0.5 M sodium phosphate at pH 12.9 (see Figures 3.20 to 3.25).

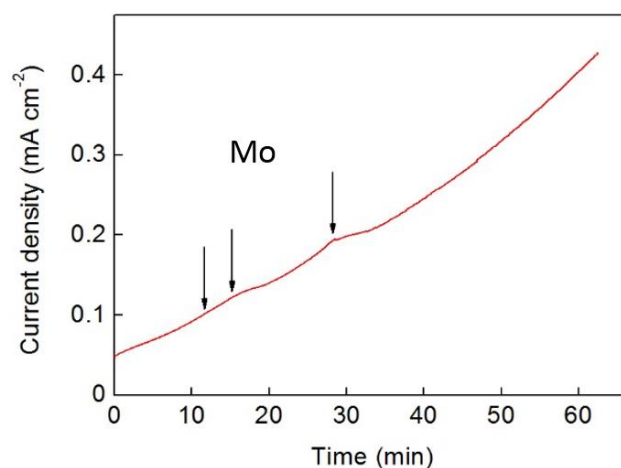


Figure 3.20 Bulk electrolysis with stirring of an aqueous solution of 0.5 M sodium phosphate (pH 12.9) on an FTO working electrode (area = 1 cm²). A carbon felt counter electrode and an Ag/AgCl reference electrode were used at room temperature in a single chamber cell. An overpotential of 0.64 V was applied (not corrected for solution resistance). Solid samples of Na₂MoO₄·2H₂O (Aldrich) were added at the times indicated by the arrows: ~20 mg at 700 s, a further 20 mg at 900 s and ~60 mg at 1700 s. Addition of this Mo salt did not affect the background current trajectory to any great extent.

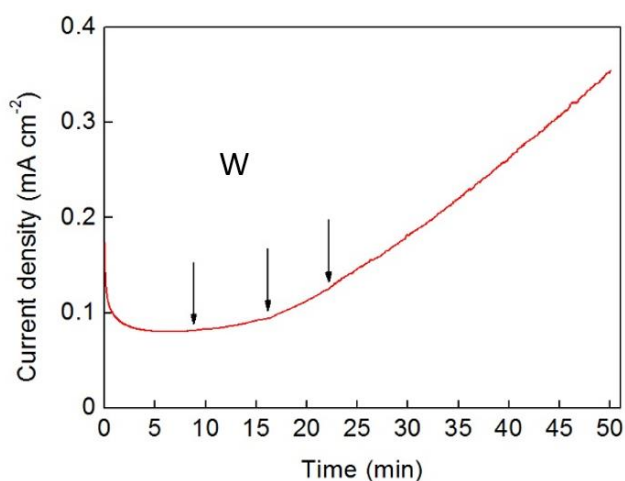


Figure 3.21 Bulk electrolysis with stirring of an aqueous solution of 0.5 M sodium phosphate (pH 12.9) on an FTO working electrode (area = 1 cm²). A carbon felt counter electrode and an Ag/AgCl reference electrode were used at room temperature in a single chamber cell. An overpotential of 0.64 V was applied (not corrected for solution resistance). Solid samples of Na₂WO₄·2H₂O were added at the times indicated by the arrows: ~20 mg at 530 s, ~50 mg at 970 s and a further 50 mg at 1330s. Addition of this W salt did not affect the expected current trajectory to any great extent.

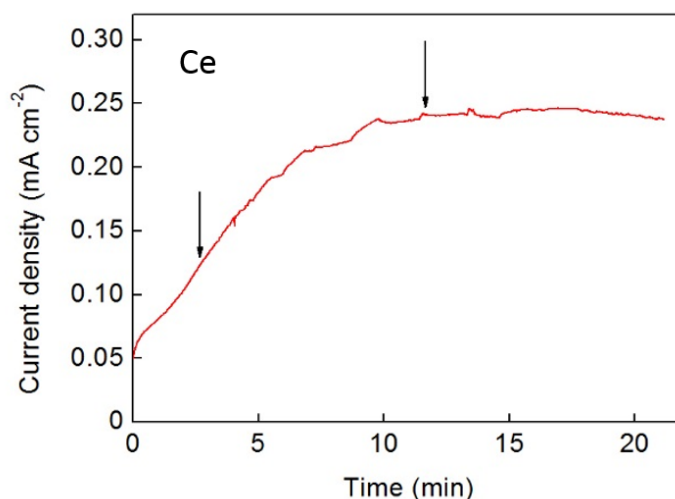


Figure 3.22 Bulk electrolysis with stirring of an aqueous solution of 0.5 M NaPi (pH 12.9) on an FTO working electrode (area = 1 cm²). A carbon felt counter electrode and an Ag/AgCl reference electrode were used at room temperature in a single chamber cell. An overpotential of 0.64 V was applied (not corrected for solution resistance). A solid sample (20 mg) of cerium(III) chloride heptahydrate was added at 160 s, and a further 60 mg was added at 700 s, as indicated by the black arrows. Dissolution was not total. Addition of this Ce salt does not seem to cause any increase in the current density. A similar result was obtained using cerium(III) acetate hydrate as the salt.

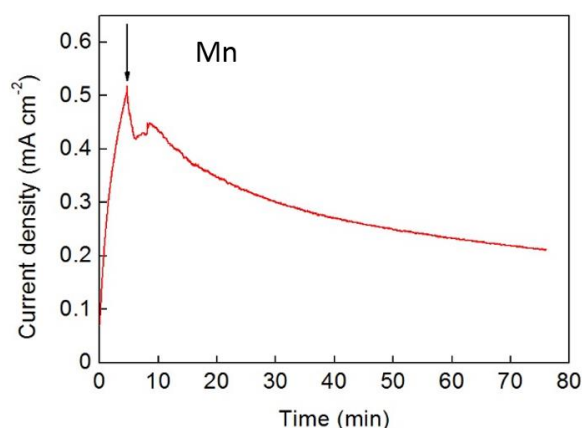


Figure 3.23 Bulk electrolysis with stirring of an aqueous solution of 0.5 M sodium phosphate (pH 12.9) on an FTO working electrode (area = 1 cm²). A carbon felt counter electrode and an Ag/AgCl reference electrode were used at room temperature in a single chamber cell. An overpotential of 0.64 V was applied (not corrected for solution resistance). A solid sample of manganese(II) perchlorate was added at the time indicated by the arrows: ~20 mg at 280 s. Dissolution was not total. Addition of this Mn salt caused the current density to decrease after addition. A similar result was obtained using manganese(II) acetate as the salt.

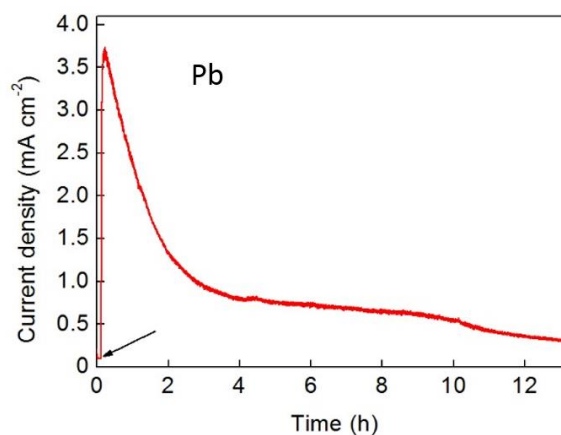


Figure 3.24 Bulk electrolysis with stirring of an aqueous solution of 0.5 M NaPi (pH 12.9) on an FTO working electrode (area = 1 cm²). A carbon felt counter electrode and an Ag/AgCl reference electrode were used at room temperature in a single chamber cell. An overpotential of 0.64 V was applied (not corrected for solution resistance). A solid sample of Pb(NO₃)₂ (20 mg) was added at the time indicated by the arrow (430 s). The current density increased at once, peaking at 3.7 mA, but this current density was not sustained over long time periods and currents decayed to only 0.3 mA after 13 h. Furthermore, a brown/red deposit was clearly visible on the working electrode just 2 minutes after addition of the lead salt (by 13 h this deposit was black). These data are not consistent with the activity reported in the main text (sustained current densities well in excess of 1 mA cm⁻² for tens of hours and no visible deposits on the electrodes), implying that lead is not the cause of this activity.

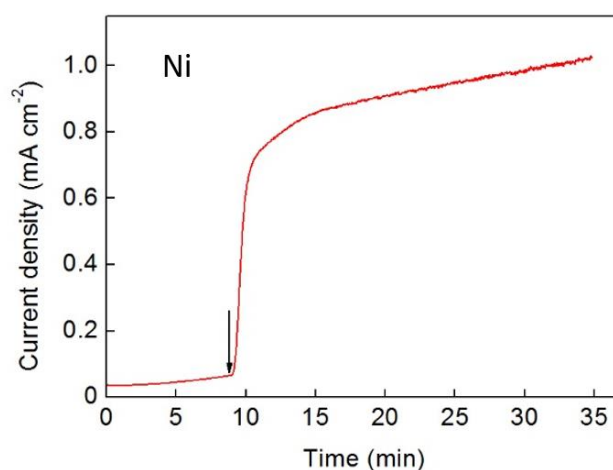


Figure 3.25 Bulk electrolysis with stirring of an aqueous solution of 0.5 M sodium phosphate (pH 12.9) on an FTO working electrode (area = 1 cm²). A carbon felt counter electrode and an Ag/AgCl reference electrode were used at room temperature in a single chamber cell. An overpotential of 0.64 V was applied (not corrected for solution resistance). A solid sample of nickel(II) chloride was added at the time indicated by the arrows: ~20 mg at 530 s. Dissolution was not total. The current density increased rapidly after the addition of this salt. At the end of the experiment, no deposit was evident on the working electrode by eye.

These experiments showed that Mo, W and Ce salts had little or no effect on the trajectory of the current, whilst Mn actually caused the current density to diminish. Only Ni and Pb gave any increase in the current density above that which manifested in all such electrolyses. Of these two metals, Ni seemed the more likely water oxidation catalyst for several reasons. Firstly, Ni has already been shown to be a competent water oxidation catalyst by Nocera and co-workers, who were able to deposit thin (transparent) films of Ni-oxides from 0.4 mM solutions of nickel salts.²² These authors also noted an increase in current density of these films with anodization, which they attributed to structural changes in the nickel oxide film upon oxidation, and a pH-overpotential profile highly reminiscent of that shown in Figure 3.6. Lead and its oxides meanwhile have been shown to give very high overpotentials for water oxidation,⁸²⁻⁸⁴ and the oxides of lead tend to form red/brown anode deposits. The anodes in our anodization reactions were, by contrast, always transparent (Figure 3.26).

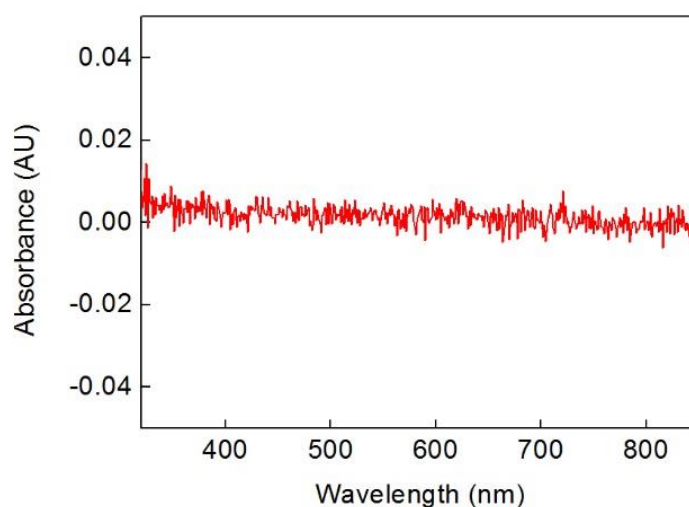


Figure 3.26 UV-vis difference spectrum showing the change in absorption in the visible part of the spectrum for an FTO electrode polarized at an overpotential of 550 mV (not corrected for resistance) in 1 M sodium phosphate buffer at pH 12.9, relative to a fresh, unused FTO electrode. Polarization was conducted from a single chamber cell (with stirring), using an Ag/AgCl reference electrode and a Pt wire counter electrode over 72 h.

To confirm that Ni was indeed responsible for the water oxidation activity seen in the experiments described above, XPS (AlK α source) was performed on FTO electrodes that had been subjected to electrolysis in as-prepared 0.5 M sodium phosphate (pH 12.9), as-prepared 0.5 M potassium borate (pH 9.2) and 0.5 M potassium borate (pH 9.2) that had previously been washed with Amberlite resin. A control FTO electrode that had not been subjected to any electrolysis was also analyzed. Although weak, signals characteristic of nickel hydroxide and/or nickel oxy-hydroxide (a larger peak at 856 eV and a smaller, broader peak 863 eV corresponding to the 2p_{3/2} spectra of Ni(OH)₂ and the β - and γ -polymorphs of NiOOH)⁸⁵ were clearly visible on the electrodes used in un-washed buffers, whilst these peaks were absent from the control and washed-buffer electrodes (Figure 3.27).

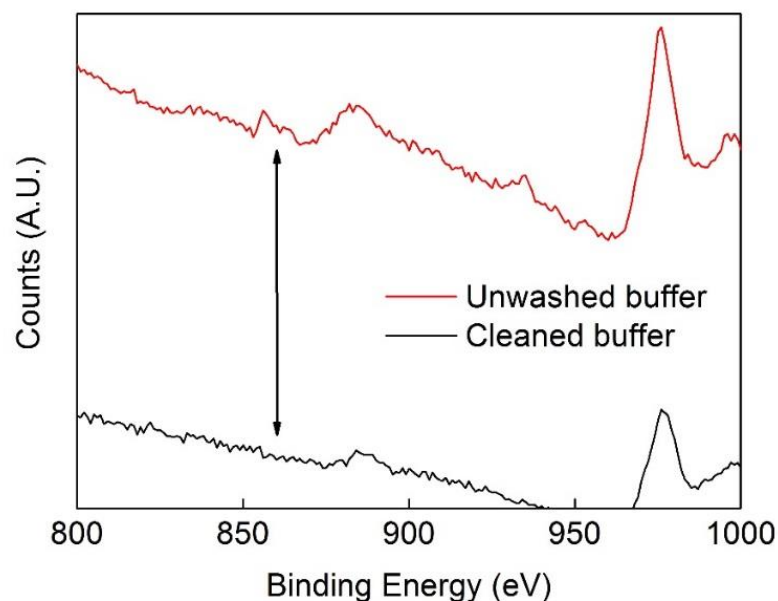


Figure 3.27 Comparison of the XPS spectra of an FTO electrode that had been anodized at a potential of +1.4 V vs. NHE overnight in an aqueous solution of 0.5 M potassium borate (pH 9.2) that had previously been washed with Amberlite resin (black line) and an FTO electrode that had been treated identically, save for the anodization occurring in an aqueous solution of 0.5 M potassium borate (pH 9.2) that had **not** been washed with Amberlite resin (red line). The characteristic peaks of the $2p_{3/2}$ spectra for nickel hydroxide/oxyhydroxide (856 and 863 eV) are present when the electrolyte is unwashed, but not when it is washed to remove Ni ions from solution.

The presence of low levels of Fe (as low as 0.01%) in nickel oxide films has been shown by Corrigan to have an observable effect on the oxygen evolution overpotential shown by such films.⁷¹ This work has recently been re-visited by both Boettcher⁷²⁻⁷⁴ and Bell and co-workers,^{40,75} who have reported excellent water oxidation electrocatalysis metrics for Fe-doped nickel oxides, with current densities of 10 mA cm^{-2} being achieved at 336 mV overpotential with $\text{Ni}_{0.9}\text{Fe}_{0.1}\text{O}_x$ in 1 M KOH,⁷² and a similar effect manifesting in near-neutral borate solutions.⁷⁴ Given the presence of Fe in the electrolyte solutions used in this work (both as-prepared and after washing), it thus seemed likely that similar Fe-doping could be occurring in this case. In order to investigate this possibility further, we examined glassy carbon electrodes that had been anodized in both as-prepared and washed sodium phosphate buffer (0.5 M, pH 12.9) using an $\text{MgK}\alpha$ source. These changes in both substrate and X-ray source from the aforementioned XPS analyses were necessary in order to obtain spectra

where the characteristic Fe 2p peaks at ~ 707 and 720 eV would not be obscured by any interference from Sn (in the FTO substrates) or Ni LMM Auger peaks.⁷³ No peaks that can be reliably assigned to Fe were observed; however, we note that the sensitivity of the MgK α X-ray source is not as high as that of the AlK α source used previously. Hence it is possible (perhaps even likely, given that ICP-MS suggests that significant Fe is present in the electrolytes investigated) that iron is present in these deposits, but at levels that are too low to be detected with the Mg source. It is interesting to note that washing the electrolyte with Amberlite resin removes Ni (and therefore reduces the peak current densities that are obtained), but does not seem to decrease the amount of Fe in solution (see Table 3.1). We note however, that a single wash with Amberlite resin is generally insufficient to remove all the Ni from solution, or to prevent the associated current density increase upon polarization (see Table 3.1 and Figure 3.18). Hence, if Ni-Fe oxides are forming, it seems that the amount of nickel present in solution is a critical determinant of the water oxidation activity that is observed. This agrees with the results obtained by Corrigan and Boettcher, which suggest that the most active catalysts are predominantly Ni oxides containing a few % Fe oxides.⁷¹⁻⁷³

ICP-MS analysis of the electrolytes had suggested a nickel concentration of around $1 \mu\text{g L}^{-1}$ in the as-prepared potassium borate buffer solutions. Washing with Amberlite resin should lower this concentration, and multiple successive washes should cause the concentration of nickel to fall even further. This is borne out by Figure 3.28, which shows the effect that up to three washing cycles has on the rate of current density increase and the peak current density that is obtained. Starting in as-prepared 0.5 M sodium phosphate solution at pH 12.9, ICP-MS gave a nickel concentration of $0.5 \mu\text{g L}^{-1}$ ($\pm 20 \text{ ng L}^{-1}$) and bulk electrolysis in this solution produced a current density of 2.6 mA cm^{-2} after 8 h (Figure 3.28, black trace). The current density fell after one wash with Amberlite resin to around 1.3 mA cm^{-2} after 8 h (red line) and to only 0.1 mA cm^{-2} after 8 h after two washes (green line). ICP-MS suggested that the nickel content of these washed solutions was 250 ($\pm 10 \text{ ng L}^{-1}$) and 200 ng L^{-1} ($\pm 8 \text{ ng L}^{-1}$) respectively. After three washes, the current density barely rose at all over the 8 h period of electrolysis, reaching only 0.02 mA cm^{-2} after this time (Figure 3.28, blue line), and reliable values for the concentration of nickel in this solution could not be obtained by ICP-MS, possibly as the levels of nickel present were too low. These results suggest that iterative removal of the nickel present in solution causes an iterative decrease in the rate at which the current density increases and the maximum current density that can be achieved within a

certain time window. In conjunction with the electrochemical and XPS data, this again implies that nickel is a cause of the water oxidation activity observed.

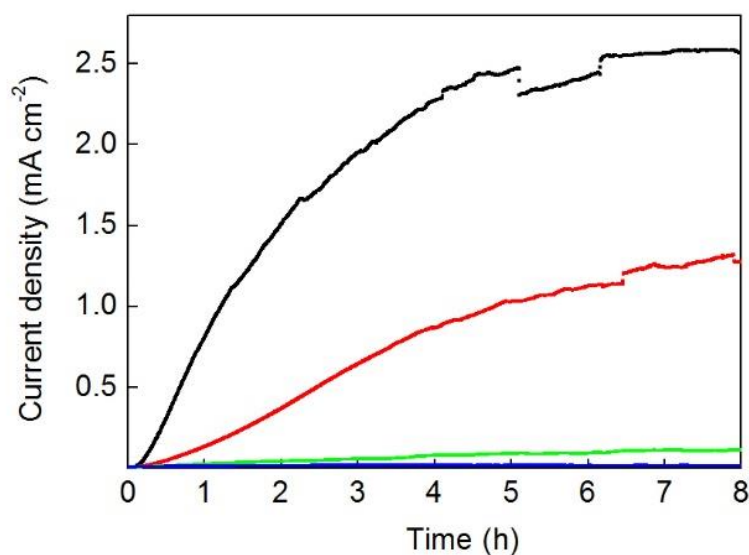


Figure 3.28 Bulk electrolysis experiments performed in 0.5 M sodium phosphate solution (pH 12.9), using an FTO working electrode (area = 1 cm²), an Hg/HgO reference and a Pt wire counter electrode. In all cases, an overpotential of 0.43 V (not corrected for resistance) was applied. The solutions had been subjected to washing with Amberlite resin to remove metal ion impurities as follows: black line, no washes (i.e. as prepared); red line, one wash; green line, two consecutive washes; blue line, three consecutive washes.

A nickel concentration in solution of 1 $\mu\text{g L}^{-1}$ corresponds to around 3.4×10^{-10} mol of nickel ions present in the 20 mL of electrolyte typically used in the electrolysis experiments described in this report. This in turn equates to a nickel concentration of ~ 17 nM, or over 23,000 times less nickel than that used by Nocera and co-workers when depositing their ultra-thin nickel oxide films.²² We note, however, that if the explicit intention is to deposit a nickel-oxide film for water oxidation, then the concentrations used in such earlier reports are likely to be more effective: our interest here merely extends to showing that 17 nM solutions of nickel *can* give rise to catalysis, and we do not claim that films deposited at these lower concentrations of nickel give superior (or even comparable) performance to films deposited from more concentrated solutions.

Assuming that all the nickel present in the electrolyte becomes deposited on the working electrode during electrolysis (and this is a significant over-estimate of the amount of Ni that is deposited, as “used” solutions are still capable of causing fresh working electrodes to become activated in this way), then a *maximum* coverage of about $0.34 \text{ nmol cm}^{-2}$ of nickel is obtained, or approximately one close-packed monolayer.⁷⁶ This is about 10,000 times lower loading of nickel than reported recently by Zhang and co-workers,²⁴ and ~20 times lower loading than that reported by Nocera and co-workers for their ultra-thin films. As the actual coverage in our case may be significantly less than one monolayer, this might also explain why the Tafel slopes obtained for anodized films in this work are somewhat higher than those previously reported.²³ In this regard, reporting the activity of trace nickel in terms of overpotential to get 1 mA cm^{-2} is probably not making justice to the importance of their effect, since there could be a significant area of substrate that is not covered with Ni. If the activity was to be described in terms of turnover frequency it would probably appear to be much more significant, superior even than that of many reported catalysts. This result could actually have important implications in the way we conceive electrocatalysts. Without enough nickel atoms on the substrate to form a monolayer it would follow that these nickel cations are evenly spread on the substrate forming tiny nanoclusters so small that cannot be seen by SEM (one would not expect to have isolated nickel atoms since to catalyze the OER 4 e^- and 4 H^+ need to be transferred). It could be interesting to perform further experiments deliberately adding tiny amounts of nickel salts to un-cleaned electrolytes (starting for example with $5 \text{ } \mu\text{g L}^{-1}$), to see how the activity increases and whether some more structural insight can be gained by SEM and XPS.

3. 4 Conclusions

Herein, we have shown that loadings of nickel of below 1 nmol cm^{-2} are effective for water oxidation across the pH range 9.2 – 13, displaying an overpotential requirement of 400 mV in order to achieve a current density of 1 mA cm^{-2} at pH 13. These are very low loadings of nickel, and indeed (as in our own case) such small amounts of nickel can be found in many common electrolyte salts. It is also possible that adventitious iron is co-depositing with nickel to produce highly active water oxidation catalysts. However, it appears that the amount of nickel present in solution is a critical determinant of catalytic activity, inasmuch as removal of Ni leads to a reduction in catalytic current despite high levels of Fe remaining in solution. In view of the number of investigators undertaking similar work in this field, it

is thus essential that the agency of trace metal ions, and nickel in particular, is excluded from any future reports of water oxidation catalysis within the pH range 9.2 - 13. It also remains critical that the nature of the true catalyst performing water oxidation is firmly established in all cases,^{69,70} noting that catalysis can manifest from extremely low levels of impurities.⁶⁵ This must be held to be especially true in cases where the measured activity for water oxidation is comparable to or below that reported in this manuscript. In these cases, ever more rigorous control experiments must be performed in order to demonstrate genuine catalysis by the species under consideration.

3. 5 Experimental Section

3.5.1 Materials and reagents

Nickel (II) hexahydrate, potassium ferricyanide(III), potassium hydroxide (90%), sodium hydroxide (98-100.5%), sodium phosphate dibasic (98.5%), potassium nitrate (90%), sodium carbonate (99.95-100%) and ethylene diamine tetra-acetic acid (sodium salt) were purchased from Sigma Aldrich. 0.180 mm-thick Nafion N-118 membrane, boric acid 99.99%, Amberlite® IRC-748 and phosphoric acid (85%) were supplied by Alfa Aesar. All chemical reagents and solvents were used as purchased, except the Amberlite resin, which was stirred for 45 min in ultrapure water and filtered before use, in order to remove any non-bound chelating agent from the beads.

All electrolyte solutions were prepared with reagent grade water (18.2 M Ω -cm resistivity), obtained from a Sartorius Arium Comfort combined water system. pH determinations were made with a Hanna HI 9124 waterproof pH meter. UV-Vis spectra were collected in the solid state on a JASCO V-670 spectrophotometer. Fluorine-doped tin oxide on glass (FTO) coated plain float electrodes (7 ohms per sheet) were purchased from Hartford Glass Co., Inc. Indium Tin Oxide on glass (ITO) coated plain float electrodes (12-15 ohms per square) were purchased from Optical Filters. All other materials were obtained as stated in the text. Experiments performed at “room temperature” were carried out at 20 °C.

3.5.2 Electrochemical Methods

Electrochemical studies were performed in a three-electrode configuration (unless otherwise stated) using both CH Instruments CHI760D potentiostats and Biologic SP-150 potentiostats. A Pt wire was used as the counter electrode (unless otherwise stated), and either an Ag/AgCl (NaCl, 3 M) reference electrode (RE 5B, BASi) or an Hg/HgO (1 M NaOH) reference electrode (CH Instruments CHI-152) was used as reference electrode as specified. Working electrodes were washed with acetone and deionized water prior to use. Pt wire was washed with HCl and rinsed in water after every experiment to remove any metal that may have deposited on its surface. Carbon felt counter electrodes (Alfa Aesar) were not re-used. Three-electrode potentials were converted to the NHE reference scale using $E(\text{NHE}) = E(\text{Ag/AgCl}) + 0.209 \text{ V}$ and $E(\text{NHE}) = E(\text{Hg/HgO}) + 0.098 \text{ V}$. Unless otherwise stated, the active area of all FTO and ITO electrodes was set to 1 cm^2 .

Bulk electrolysis and *in situ* catalyst formation: Bulk electrolyses were performed in a three-electrode configuration (unless otherwise stated) in both single compartment and two-compartment electrochemical cells. In the latter case, the compartments of the H-cell were separated by a 0.180 mm-thick Nafion N-118 membrane, with this membrane being held in place by judicious application of Araldite epoxy glue (Bostik Findley, Ltd., UK). Solutions were stirred, keeping the same stirring rate for all experiments. Where voltages have been corrected for ohmic resistances, the effective voltage ($V_{\text{effective}}$) is given by:⁸⁶

$$V_{\text{effective}} = V_{\text{applied}} - iR$$

where i is the current flowing through the cell and R is the resistance of the cell. Cell resistances were measured by the iR test function available on the CH potentiostats, using the general method developed by He and Faulkner.⁸⁷ Briefly, the iR test function works by examining the current response to small step changes in voltage relative to a test potential at which no faradaic current flows. In our case, the step change (ΔV) was 0.05 V and the test potential was selected as 0 V vs. Ag/AgCl. Other test voltages over the range 0 to 1 V vs. Ag/AgCl gave answers for the solution resistance that were within error of the values obtained at 0 V. The iR test function on the potentiostat then extrapolates the signal-averaged currents at 54 and 72 ps after the voltage-step edge backwards to obtain a current at $t = 0$, where this current can also be expressed as $\Delta V/R$. R in this case is the solution resistance that is sought. The final parameter that the user must select with this function is the

acceptable stability limit of the system at the value of R measured (“% overshoot”): in our case a value of 2% was chosen (default setting on the potentiostat). The error associated with this iR -correction is dominated by the error associated with gauging the resistance of the solution, where values were found to vary over a range of $R_{\text{measured}} \pm 3\%$. Resistances could be automatically compensated on the biologic potentiostats, using the ZIR function.

Cyclic Voltammetry: Cyclic voltammograms were collected in a single chamber cell using a three-electrode setup at room temperature, using the scan rates and electrolytes specified in the text. Measurements were conducted without stirring and with iR compensation.

Tafel Plots: Tafel plots were obtained in single chamber cells with stirring. The working electrode was FTO (1 cm^2) and the reference electrode was Ag/AgCl. A Pt wire was used as the counter electrode and solutions were kept at room temperature. “Anodized” electrodes were subjected to anodic polarization overnight at the potentials indicated in the text. Controls were performed with electrodes that had not been anodized. At each potential for anodized films, the current density was allowed to stabilize for 10 min before the stable current density was recorded. For non-anodized films the value of the current density used was that of the minimum for each potential applied (typically obtained within 5 min), on account of the tendency for the current density to rise with extended electrolysis at a given potential. Potential increments were set at 30 mV between measurements and the reported Tafel slopes are averages of several runs. The overpotentials reported have been corrected for resistive losses.

3.5.3 Headspace Oxygen Determination

Gas chromatography was conducted in airtight single-chamber cells using a variety of buffer systems and reference electrodes as detailed in the captions of Figures 3.14 – 3.16 using an Agilent Technologies 7890A GC system. During electrolysis, the solution was stirred and the headspace was sampled by gas-tight syringe (volume taken per sampling event = $50 \mu\text{L}$) and introduced onto the GC column by direct injection at various intervals. The column used was a 30 metre-long 0.320 mm widebore HP-molesieve column (Agilent). The GC oven temperature was set to $27 \text{ }^\circ\text{C}$ and the carrier gas was Ar. The front inlet was set to $100 \text{ }^\circ\text{C}$. The GC system was calibrated for O_2 using certified standards of oxygen at a range of

volume % in argon supplied by CK Gas Products Limited (UK). Linear fits of volume % vs. peak area were obtained, which allowed peak areas to be converted into volume % of O₂ in the cell headspace. A small air leak into the cell introduced during sampling was corrected for by calibrating the amount of O₂ and N₂ in air and then applying appropriate corrections for these based on the amount of N₂ observed in the chromatographs. Total system headspaces were calculated by filling the cells with water at room temperature. Typical headspaces were on the order of 200-250 mL in airtight cells. Charges passed were converted into expected volume percentages of oxygen in the headspace by converting charges to an expected number of moles of gas (by dividing by 4F for O₂, where F is the Faraday constant), and then taking the volume of 1 mole of an ideal gas at room temperature and pressure to be 24.5 L. Faradaic efficiencies were then calculated by taking the ratio of gas volume % based on the charge passed to the gas volume % measured by gas chromatography. Faradaic efficiencies were based on the total amount of charge passed, uncorrected for any background or capacitance currents. All gas determinations were performed at least twice, and average Faradaic efficiencies are reported in the main text.

3.5.4 Other analytical techniques

SEM and EDX: Scanning electron microscopy was performed with a Philips XL30 ESEM instrument equipped with an Oxford Instruments Energy 250 energy dispersive spectrometer system at an acceleration voltage of 25 kV. Following electrolysis experiments on FTO, the electrodes were rinsed gently with de-ionized (DI) water and allowed to dry in air before loading onto 12 mm AGAR scientific conductive carbon tabs. Images and EDX spectra were obtained with acceleration voltages between 12 kV and 20 kV. Spectra were analysed using Oxford Instrument INCA 4.09 Microanalysis Suite – Issue 17b.

X-ray photoelectron analysis (XPS): Following electrolysis, the electrodes were rinsed gently with deionized water and allowed to dry in air. These electrodes were then carefully packed and sent to the National EPSRC XPS Users' Service (NEXUS) at Newcastle University, UK. XPS spectra on FTO electrodes were acquired with a K-Alpha instrument (Thermo Scientific, East Grinstead, UK), using a micro-focused monochromatic AlK α source (X-ray energy 1486.6 eV, spot size 400 × 800 microns). Three positions were analyzed per sample. XPS spectra on glassy carbon substrates (Carbon-Vitreous 3000C (C)

foil, 1.0 mm thickness, GoodFellow) were collected using an MgK α source on an Omicron Nanoprobe instrument fitted with a SPECS dual anode Al/Mg X-ray source and a SPECS PHOIBOS 100 electron energy analyzer. The analyzed area on each sample was on the order of 2 x 0.7 mm. The resulting spectra were referenced to the adventitious C 1s peak (285.0 eV) and were analyzed using the free-to-download CasaXPS software package.

Elemental analysis: Samples of various electrolytes were analyzed by Inductively Coupled Plasma Mass Spectrometry on an Agilent 7700 ICP-MS instrument at the Department of Pure and Applied Chemistry at the University of Strathclyde (UK). Both semi-quantitative (all-element) and quantitative analyses (for nickel) were performed. All samples were spiked with 1% nitric acid to aid analysis, and a summary table for 0.5 M potassium borate with and without washing is given in Table 3.1, along with analysis of the 18.2 M Ω -cm resistivity deionized water with 1% nitric acid spiking.

3.5.5 Procedure for washing electrolyte with Amberlite resin

The washing procedure for the electrolyte was as follows. Firstly, the Amberlite resin was stirred for 45 min in ultrapure water and then filtered, in order to remove any unbound iminodiacetic acid. After drying in air, 5 g of this cleaned Amberlite resin were added to 400 mL of electrolyte and the mixture stirred for 5 min. After this time, the resin was removed by filtration and the electrolyte either used in this state (after “1 wash”) or else treated with a fresh 5 g of cleaned resin, in order to give doubly-washed electrolyte. Up to three washings were performed in some cases (see main text).

3.6 References

- (1) Lewis, N. S.; Nocera, D. G. *Proc. Natl. Acad. Sci. USA*, **2006**, *103*, 15729.
- (2) Tachibana, Y.; Vayssieres, L.; Durrant, J. R. *Nat. Photonics* **2012**, *6*, 511.
- (3) Dasgupta, S.; Brunschwig, B. S.; Winkler, J. R.; Gray, H. B. *Chem. Soc. Rev.* **2013**, *42*, 2213.
- (4) Carmo, M.; Fritz, D. L.; Mergel, J.; Stolten, D. *Int. J. Hydrogen Energy* **2013**, *38*, 4901.
- (5) Holladay, J. D.; Hu, J.; King, D. L.; Wang, Y. *Catal. Today* **2009**, *139*, 244.
- (6) Cook, T. R.; Dogutan, D. K.; Reece, S. Y.; Surendranath, Y.; Teets, T. S.; Nocera, D. G. *Chem. Rev.* **2010**, *110*, 6474.
- (7) Pletcher, D.; Li, X. *Int. J. Hydrogen Energy* **2011**, *36*, 15089.
- (8) McKone, J. R.; Lewis, N. S.; Gray, H. B. *Chem. Mater.* **2014**, *26*, 407.
- (9) Symes, M. D.; Cronin, L. Materials for Water Splitting. In *Materials for a Sustainable Future*, Cambridge (UK); RSC Publishing, 2012; pp 592-614.
- (10) Kanan, M. W.; Nocera, D. G. *Science* **2008**, *321*, 1072.
- (11) Lutterman, D. A.; Surendranath, Y.; Nocera, D. G. *J. Am. Chem. Soc.* **2009**, *131*, 3838.
- (12) Kanan, M. W.; Surendranath, Y.; Nocera, D. G. *Chem. Soc. Rev.* **2009**, *38*, 109
- (13) Gerken, J. B.; Landis, E. C.; Hamers, R. J.; Stahl, S. S. *ChemSusChem* **2010**, *3*, 1176.
- (14) Gerken, J. B.; McAlpin, J. G.; Chen, J. Y. C.; Rigsby, M. L.; Casey, W. H.; Britt, R. D.; Stahl, S. S. *J. Am. Chem. Soc.* **2011**, *133*, 14431.
- (15) Cobo, S.; Heidkamp, J.; Jacques, P.-A.; Fize, J.; Fourmond, V.; Guetaz, L.; Jusselme, B.; Ivanova, V.; Dau, H.; Palacin, S.; Fontecave, M.; Artero, V. *Nature Mater.* **2012**, *11*, 802.
- (16) Bloor, L. G.; Molina, P. I.; Symes, M. D.; Cronin, L. *J. Am. Chem. Soc.* **2014**, *136*, 3304.
- (17) Risch, M.; Ringleb, F.; Kohlhoff, M.; Bogdanoff, P.; Chernev, P.; Zaharieva, I.; Dau, H. *Energy Environ. Sci.* **2015**, *8*, 661.
- (18) Hutchings, G. S.; Zhang, Y.; Li, J.; Yonemoto, B. T.; Zhou, X.; Zhu, K.; Jiao, F. *J. Am. Chem. Soc.* **2015**, *137*, 4223.
- (19) Dincă, M.; Surendranath, Y.; Nocera, D. G. *Proc. Natl. Acad. Sci. U.S.A.* **2010**, *107*, 10337.

- (20) Risch, M.; Klingan, K.; Heidkamp, J.; Ehrenberg, D.; Chernev, P.; Zaharieva, I.; Dau, H. *Chem. Commun.* **2011**, *47*, 11912.
- (21) Singh, A.; Chang, S.; Hocking, R. K.; Bach, U.; Spiccia, L. *Energy Environ. Sci.* **2013**, *6*, 579.
- (22) Bediako, D. K.; Lassalle-Kaiser, B.; Surendranath, Y.; Yano, J.; Yachandra, V. K.; Nocera, D. G. *J. Am. Chem. Soc.* **2012**, *134*, 6801.
- (23) Bediako, D. K.; Surendranath, Y.; Nocera, D. G. *J. Am. Chem. Soc.* **2013**, *135*, 3662.
- (24) Wang, J.; Li, K.; Zhong, H.-X. Xu, D.; Wang, Z.-L.; Jiang, Z.; Wu, Z.-J.; Zhang, X.-B. *Angew. Chem. Int. Ed.* **2015**, *54*, 10530.
- (25) Jiao, F.; Frei, H. *Chem. Commun.* **2010**, *46*, 2920.
- (26) Gorlin, Y.; Jaramillo, T. F. *J. Am. Chem. Soc.* **2010**, *132*, 13612.
- (27) Zaharieva, I.; Chernev, P.; Risch, M.; Klingan, K.; Kohlhoff, M.; Fischer, A.; Dau, H. *Energy Environ. Sci.* **2012**, *5*, 7081.
- (28) Izgorodin, A.; Izgorodina, E.; MacFarlane, D. R.; *Energy Environ. Sci.* **2012**, *5*, 9496.
- (29) Najafpour, M. M.; Ehrenberg, T.; Wiechen, M.; Kurz, P. *Angew. Chem. Int. Ed.* **2010**, *49*, 2233.
- (30) Takashima, T.; Hashimoto, K.; Nakamura, R. *J. Am. Chem. Soc.* **2012**, *134*, 1519.
- (31) Takashima, T.; Hashimoto, K.; Nakamura, R. *J. Am. Chem. Soc.* **2012**, *134*, 18153.
- (32) Indra, A.; Menezes, P. W.; Zaharieva, I.; Baktash, E.; Pfrommer, J.; Schwarze, M.; Dau, H.; Driess, M. *Angew. Chem. Int. Ed.* **2013**, *52*, 13206.
- (33) Jin, K.; Park, J.; Lee, J.; Yang, K. D.; Pradhan, G. K.; Sim, U.; Jeong, D.; Jang, H. L.; Park, S.; Kim, D.; Sung, N.-E.; Kim, S. H.; Han, S.; Nam, K. T. *J. Am. Chem. Soc.* **2014**, *136*, 7435.
- (34) Du, J.; Chen, Z.; Ye, S.; Wiley, B. J.; Meyer, T. J. *Angew. Chem. Int. Ed.* **2015**, *54*, 2073.
- (35) Yu, F.; Li, F.; Zhang, B.; Li, H.; Sun, L. *ACS Catal.* **2015**, *5*, 627.
- (36) Li, T.-T.; Cao, S.; Yang, C.; Chen, Y.; Lv, X.-J.; Fu, W.-F. *Inorg. Chem.* **2015**, *54*, 3061.
- (37) Smith, R. D. L.; Prévot, M. S.; Fagan, R. D.; Zhang, Z.; Sedach, P. A.; Siu, M. K. J.; Trudel, S.; Berlinguette, C. P. *Science* **2013**, *340*, 60.
- (38) Smith, R. D. L.; Prévot, M. S.; Fagan, R. D.; Trudel, S.; Berlinguette, C. P. *J. Am. Chem. Soc.* **2013**, *135*, 11580.
- (39) Gong, M.; Li, Y.; Wang, H.; Liang, Y.; Wu, J. Z.; Zhou, J.; Wang, J.; Regier, T.; Wei, F.; Dai, H. *J. Am. Chem. Soc.* **2013**, *135*, 8452.

- (40) Friebel, D.; Louie, M. W.; Bajdich, M.; Sanwald, K. E.; Cai, Y.; Wise, A. M.; Cheng, M.-J.; Sokaras, D.; Weng, T.-C.; Alonso-Mori, R.; Davis, R. C.; Bargar, J. R.; Nørskov, J. K.; Nilsson, A.; Bell, A. T. *J. Am. Chem. Soc.* **2015**, *137*, 1305.
- (41) Burke, M. S.; Kast, M. G.; Trotochaud, L.; Smith, A. M.; Boettcher, S. W. *J. Am. Chem. Soc.* **2015**, *137*, 3638.
- (42) Hunter, B. M.; Blakemore, J. D.; Deimund, M.; Gray, H. B.; Winkler, J. R.; Müller, A. M. *J. Am. Chem. Soc.* **2014**, *136*, 13118.
- (43) Fominykh, K.; Chernev, P.; Zaharieva, I.; Sicklinger, J.; Stefanic, G.; Döblinger, M.; Müller, A.; Pokharel, A.; Böcklein, S.; Scheu, C.; Bein, T.; Fattakhova-Rohlfing, D. *ACS Nano* **2015**, *9*, 5180.
- (44) Cady, C. W.; Gardner, G.; Maron, Z. O.; Retuerto, M.; Go, Y. B.; Segan, S.; Greenblatt, M.; Dismukes, G. C. *ACS Catal.* **2015**, *5*, 3403.
- (45) Zhong, D. K.; Sun, J.; Inumaru, H.; Gamelin, D. R. *J. Am. Chem. Soc.* **2009**, *131*, 6086.
- (46) Reece, S. Y.; Hamel, J. A.; Sung, K.; Jarvi, T. D.; Esswein, A. J.; Pijpers, J. J. H.; Nocera, D. G. *Science* **2011**, *334*, 645.
- (47) Barroso, M.; Cowan, A. J.; Pendlebury, S. R.; Grätzel, M.; Klug, D. R.; Durrant, J. R. *J. Am. Chem. Soc.* **2011**, *133*, 14868.
- (48) Seabold, J. A.; Choi, K.-S. *Chem. Mater.* **2011**, *23*, 1105.
- (49) Yang, J.; Walczak, K.; Anzenberg, E.; Toma, F. M.; Yuan, G.; Beeman, J.; Schwartzberg, A.; Lin, Y.; Hettick, M.; Javey, A.; Ager, J. W.; Yano, J.; Frei, H.; Sharp, I. D. *J. Am. Chem. Soc.* **2014**, *136*, 6191.
- (50) Li, R.; Chen, Z.; Zhao, W.; Zhang, F.; Maeda, K.; Huang, B.; Shen, S.; Domen, K.; Li, C. *J. Phys. Chem. C* **2013**, *117*, 376.
- (51) Eisenberg, D.; Ahn, H. S.; Bard, A. J. *J. Am. Chem. Soc.* **2014**, *136*, 14011.
- (52) Kenney, M. J.; Gong, M.; Li, Y.; Wu, J. Z.; Feng, J.; Lanza, M.; Dai, H. *Science* **2013**, *342*, 836.
- (53) Sun, K.; McDowell, M. T.; Nielander, A. C.; Hu, S.; Shaner, M. R.; Yang, F.; Brunschwig, B. S.; Lewis, N. S. *J. Phys. Chem. Lett.* **2015**, *6*, 592.
- (54) Abdi, F. F.; Han, L.; Smets, A. H. M.; Zeman, M.; Dam, B.; van de Krol, R. *Nat. Commun.* **2013**, *4*, 2195.
- (55) Sun, K.; Saadi, F. H.; Lichterman, M. F.; Hale, W. G.; Wang, H.-P.; Zhou, X.; Plymale, N. T.; Omelchenko, S. T.; He, J.-H.; Papadantonakis, K. M.; Brunschwig, B. S.; Lewis, N. S. *Proc. Natl. Acad. Sci. USA* **2015**, *112*, 3612.

- (56) Harriman, A.; Pickering, I. J.; Thomas, J. M.; Christensen, P. A. *J. Chem. Soc. Faraday Trans. 1* **1988**, *84*, 2795.
- (57) Tsuji, E.; Imanishi, A.; Fukui, K.-I.; Nakato, Y. *Electrochim. Acta* **2011**, *56*, 2009.
- (58) Ouattara, L.; Fierro, S.; Frey, O.; Koudelka, M.; Comninellis, C. *J. Appl. Electrochem.* **2009**, *39*, 1361.
- (59) Tilley, S. D.; Cornuz, M.; Sivula, K.; Grätzel, M. *Angew. Chem. Int. Ed.* **2010**, *49*, 6405.
- (60) Schley, N. D.; Blakemore, J. D.; Subbaiyan, N. K.; Incarvito, C. D.; D'Souza, F.; Crabtree, R. H.; Brudvig, G. W. *J. Am. Chem. Soc.* **2011**, *133*, 10473.
- (61) Blakemore, J. D.; Mara, M. W.; Kushner-Lenhoff, M. N.; Schley, N. D.; Konezny, S. J.; Ivan Rivalta, I.; Negre, C. F. A.; Snoeberger, R. C.; Kokhan, O.; Huang, J.; Stickrath, A.; Tran, L. A.; Parr, M. L.; Chen, L. X.; Tiede, D. M.; Batista, V. S.; Crabtree, R. H.; Brudvig, G. W. *Inorg. Chem.* **2013**, *52*, 1860.
- (62) Minguzzi, A.; Lugaresi, O.; Achilli, E.; Locatelli, C.; Vertova, A.; Ghigna, P.; Rondinini, S. *Chem. Sci.* **2014**, *5*, 3591.
- (63) McCrory, C. C. L.; Jung, S.; Ferrer, I. M.; Chatman, S. M.; Peters, J. C.; Jaramillo, T. F. *J. Am. Chem. Soc.* **2015**, *137*, 4347.
- (64) Widegren, J. A.; Finke, R. G. *J. Mol. Catal. A: Chem.* **2003**, *198*, 317.
- (65) Crabtree, R. H. *Chem. Rev.* **2012**, *112*, 1536.
- (66) Artero, V.; Fontecave, M. *Chem. Soc. Rev.* **2013**, *42*, 2338.
- (67) Fukuzumi, S.; Hong, D. *Eur. J. Inorg. Chem.* **2014**, 645.
- (68) Stracke, J. J.; Finke, R. G. *J. Am. Chem. Soc.* **2011**, *133*, 14872.
- (69) Stracke, J. J.; Finke, R. G. *ACS Catal.* **2014**, *4*, 909.
- (70) Ullman, A. M.; Liu, Y.; Huynh, M.; Bediako, D. K.; Wang, H.; Anderson, B. L.; Powers, D. C.; Breen, J. J.; Abruña, H. D.; Nocera, D. G. *J. Am. Chem. Soc.* **2014**, *136*, 17681.
- (71) Corrigan, D. A. *J. Electrochem. Soc.* **1987**, *134*, 377.
- (72) Trotochaud, L.; Ranney, J. K.; Williams, K. N.; Boettcher, S. W. *J. Am. Chem. Soc.* **2012**, *134*, 17253.
- (73) Trotochaud, L.; Young, S. L.; Ranney, J. K.; Boettcher, S. W. *J. Am. Chem. Soc.* **2014**, *136*, 6744.
- (74) Smith, A. M.; Trotochaud, L.; Burke, M. S.; Boettcher, S. W. *Chem. Commun.* **2015**, *51*, 5261.
- (75) Louie, M. W.; Bell, A. T. *J. Am. Chem. Soc.* **2013**, *135*, 12329.

- (76) Kent, C. A.; Concepcion, J. J.; Dares, C. J.; Torelli, D. A.; Rieth, A. J.; Miller, A. S.; Hoertz, P. G.; Meyer, T. J. *J. Am. Chem. Soc.* **2013**, *135*, 8432.
- (77) Kraft, A.; Hennig, H.; Herbst, A.; Heckner, K.-H. *J. Electroanal. Chem.* **1994**, *365*, 191.
- (78) Wang, W.; Zhao, Q.; Dong, J.; Li, J. *Int. J. Hydrogen Energy* **2011**, *36*, 7374.
- (79) Zhao, Q.; Yu, Z.; Hao, G.; Yuan, W.; Li, J. *Int. J. Hydrogen Energy* **2014**, *39*, 1364.
- (80) Du, J.; Chen, Z.; Chen, C.; Meyer, T. J. *J. Am. Chem. Soc.* **2015**, *137*, 3193.
- (81) The main metal impurities in the de-ionized water itself (which should contain between 30 and 40 $\mu\text{g L}^{-1}$ total dissolved solids on the basis of a resistivity of 18.2 $\text{M}\Omega\text{-cm}$) appear to be Na, K and Ca (see Table S1), although low ng L^{-1} levels of other impurities cannot be ruled out.
- (82) Ho, J. C. K.; Tremiliosi Filho, G.; Simpraga, R.; Conway, B. E. *J. Electroanal. Chem.* **1994**, *366*, 147.
- (83) Amadelli, R.; Maldotti, A.; Molinari, A.; Danilov, F. I.; Velichenko, A. B. *J. Electroanal. Chem.* **2002**, *534*, 1.
- (84) Sirés, I.; Low, C. T. J.; Ponce-de-León, C.; Walsh, F. C. *Electrochim. Acta*, **2010**, *55*, 2163.
- (85) Grosvenor, A. P.; Biesinger, M. C.; Smart, R. St.C.; McIntyre, N. S. *Surf. Sci.* **2006**, *600*, 1771.
- (86) Hamann, C. H., Hamnett, A. & Vielstich, W. *Electrochemistry* (2nd. Edition). Wiley-VCH, Weinheim.
- (87) He, P.; Faulkner, L. R. *Anal. Chem.* **1986**, *58*, 517.

Silver Leakage from Ag/AgCl Reference Electrodes as a Potential Cause of Interference in the Electrocatalytic Hydrogen Evolution Reaction

Published as “Silver Leakage from Ag/AgCl Reference Electrodes as a Potential Cause of Interference in the Electrocatalytic Hydrogen Evolution Reaction” Roger, I.; Symes, M. D. *ACS Appl. Mater. Interfaces* **2017**, *9*, 472.

Acknowledgements and declaration

The following people are acknowledged for their contribution to this chapter: Mr. Jim Gallagher (University of Glasgow) for assistance with the SEM measurements, Dr. Alexey Ganin (University of Glasgow) for assistance with processing the XPS data, Dr. Lorna Eades (University of Edinburgh) for ICP-MS measurements. X-ray photoelectron spectra were obtained at the National EPSRC XPS Users' Service (NEXUS) at Newcastle University, an EPSRC Mid-Range Facility. IR performed all the other experimental work (unless stated otherwise) and IR and MDS co-wrote the paper.

Synopsis

In view of the findings described in Chapter 3, we asked ourselves whether a similar phenomenon could be observed for the HER, and so we set out to study long duration bulk electrolysis control experiments under the conditions in which most new electrocatalysts are assessed for this reaction to ascertain whether metal impurities played a role here too. This led us to see that under conditions commonly employed in identifying new electrocatalysts for this reaction (using Ag/AgCl reference electrodes in 1 M H₂SO₄), silver ions can leak from the reference electrode into solution and then deposit on the working electrode as Ag(0), giving current densities for the HER of over 5 mA cm⁻² at ~500 mV overpotential. While we saw in Chapter 1 that the best electrocatalysts reported at present give current densities of about 10 mA cm⁻² at overpotentials much lower, there is still a number of materials being reported every year whose activity falls within the range obtained with these silver traces. This calls into question the validity of any reports using Ag/AgCl reference electrodes which either fail to explicitly exclude silver as a cause of the electrocatalytic activity, or else cannot demonstrate significantly superior activity to this baseline.

4.1 Introduction

Electrolytic water splitting continues to attract significant attention as a sustainable route by which to generate hydrogen to use as a fuel and chemical feedstock.¹⁻⁴ In this regard, solar-to-hydrogen devices hold great promise for generating hydrogen from water using only renewable power inputs.⁵⁻¹² On account of the diffusivity of solar irradiation, a current density for hydrogen evolution on the order of 10 mA cm^{-2} is seen as a feasible target for a practical solar-to-fuel system.¹³ This current density target is rather low in comparison to the current densities typically found in commercial electrolyzers ($\sim 0.5 - 2 \text{ A cm}^{-2}$),¹⁴ which means that solar-to-hydrogen devices that can produce useful amounts of hydrogen on practical timescales will have to have rather large surface areas. Currently, the best known electrocatalyst for the HER is Pt. However, this is considered too rare and expensive to be deployed in large-area solar-to-fuels systems.¹⁵ This has led to sustained efforts to develop hydrogen evolution electrocatalysts that are based on more abundant elements, with cost, rather than electrochemical performance, being the chief motivator in many of these studies. Recent reviews suggest that the most promising of these earth-abundant hydrogen evolution electrocatalysts evolve H_2 at a current density of 10 mA cm^{-2} at overpotentials at or below 250 mV .¹⁶⁻¹⁹ However, numerous hydrogen evolution electrocatalysts that require overpotentials in excess of 500 mV in order to reach this benchmark current density have been (and continue to be) reported.

In the previous Chapter it was shown that nanomolar concentrations of nickel impurities in a number of commonly-used electrolytes can give rise to current densities for the oxygen evolution reaction (OER) in basic media in excess of 1 mA cm^{-2} at overpotentials as low as 400 mV .²⁰ The conditions used in this original report mirrored those generally employed in the characterization of new electrocatalysts for the OER, providing a baseline which any newly-discovered material must exceed if it is to be considered as a genuine catalytic agent for this reaction.

Following this line of reasoning, we have now expanded the scope of our studies to include the effects of impurities on electrocatalysis of the HER. The conditions we chose to investigate in the greatest detail are those which are arguably the most commonly employed in the literature: a three-electrode configuration using an Ag/AgCl reference electrode, an inert counter electrode and $1 \text{ M H}_2\text{SO}_4$ as the electrolyte. In support of this assertion, an

analysis of 46 papers describing new HER electrocatalysts (predominantly from the last five years, as summarized in Table 1 of ref. 17) reveals that 80% of these reports used either 0.5 M H₂SO₄ or 1 M H₂SO₄ as the supporting electrolyte. In these 37 publications, the choice of reference electrode used can be broken down as follows: reversible hydrogen electrode; 1 report,²¹ Hg/Hg₂SO₄ electrode; 8 reports,²²⁻²⁹ calomel electrode; 14 reports,³⁰⁻⁴³ Ag/AgCl reference; 15 reports^{22,44-57} (we note that one publication uses both Hg/Hg₂SO₄ and Ag/AgCl references, but it is not stated when each electrode is used²²). In most cases, these 15 reports that use Ag/AgCl reference electrodes are not suspect as the performance of these catalysts comfortably exceeds the 5 mA cm⁻² at ~500 mV overpotential threshold that we establish in this work (see below). Clearly, however, the use of Ag/AgCl reference electrodes in sulfuric acid electrolytes at low pH is a widespread, perhaps even the predominant, practice when assessing the activity of heterogeneous electrocatalysts for the HER.

Herein, we show that the use of Ag/AgCl reference electrodes in sulfuric acid is susceptible to the generation of “false positives” for electrocatalysis of the HER. In this case, the agent giving rise to the hydrogen evolution activity is not an impurity present in the as-prepared electrolyte, but in fact Ag⁺ ions that leach from the reference electrode and deposit on the working electrode under cathodic bias. We show that this effect can give rise to current densities for the HER in excess of 5 mA cm⁻² after several hours’ polarization at overpotentials of around 500 mV, well within the range of many reported hydrogen evolution electrocatalysts. The leakage of silver ions from Ag/AgCl reference electrodes has previously been invoked to explain the instability of these electrodes in organic solvents.⁵⁸ Contamination of aqueous electrolytes by such electrodes might also be expected,⁵⁹ but is rarely (if ever) considered in papers dealing with the HER. Indeed, in our own search of the manufacturer literature, we could not find any proscriptions against the use of Ag/AgCl reference electrodes in sulfuric acid electrolytes (although direct enquiries did sometimes elicit the advice to use these electrodes only within the pH interval 3-10).⁶⁰ Hence it seems that the possible pitfalls of silver leakage from Ag/AgCl reference electrodes under the conditions used in this paper are either not common knowledge in the HER electrocatalysis community, or else are widely ignored. As a consequence, the potential for silver from the reference electrode to interfere in electrocatalytic reactions (and in the HER in particular) is very real. This work therefore serves to increase the burden of proof required when a new electrocatalyst for the HER is claimed, and highlights once again the perils of overlooking potential sources of contamination in catalysis^{61,62} and electrocatalysis.^{63,64}

4.2 Results and discussion

Our suspicions regarding possible interference in electrocatalysis of the HER at low pH when using Ag/AgCl reference electrodes were raised by behavior such as that shown in Figure 4.1. To obtain this data, we placed a clean glassy carbon working electrode (area = 0.071 cm²), an Ag/AgCl reference electrode and a graphite counter electrode in a two-compartment electrolysis cell, both chambers of which were then charged with 1 M H₂SO₄ (see Section 4.4.2). An overpotential of 540 mV for the HER was applied (with stirring), at which potential the current density for hydrogen evolution on glassy carbon electrodes of this type should be no more than 0.1 mA cm⁻².⁶⁵ Glassy carbon was selected as the working electrode in these studies as it is a commonly used and inert substrate for many HER catalysts. However, Figure 4.1 shows that under these conditions the current density for hydrogen evolution increases steadily, sometimes exceeding 5 mA cm⁻² after 10 h of polarization (red line). This increase in current density is accompanied by significant bubbling at the working electrode. Gas chromatography on the headspace of sealed cells (Figure 4.2) indicated that this current was due essentially entirely to the formation of hydrogen (Faradaic yield for H₂ production = 95% ± 2%). Moreover, increases in current density with time were also evident (albeit of smaller magnitude) after several hours' electrolysis under the same conditions, but at 400 or 250 mV overpotential for the HER (Figure 4.1).

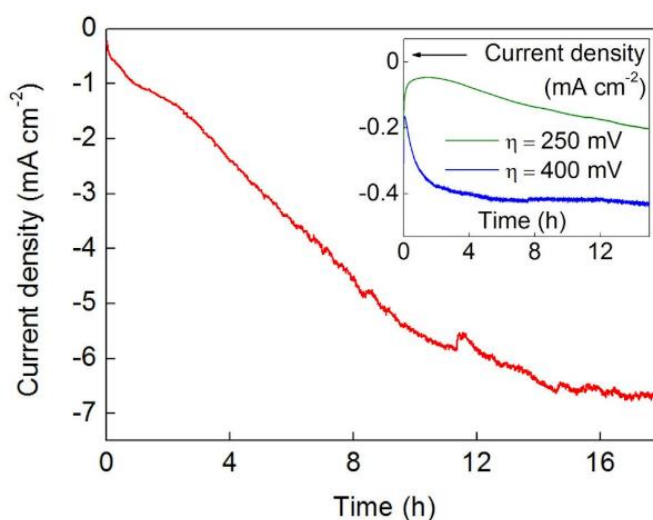


Figure 4.1 A comparison of the current densities for the HER at a glassy carbon working electrode in 1 M H₂SO₄ obtained using an Ag/AgCl reference electrode at 540 mV overpotential for the HER (main panel, red line) and at 400 and 250 mV overpotential (inset, blue and green lines respectively).

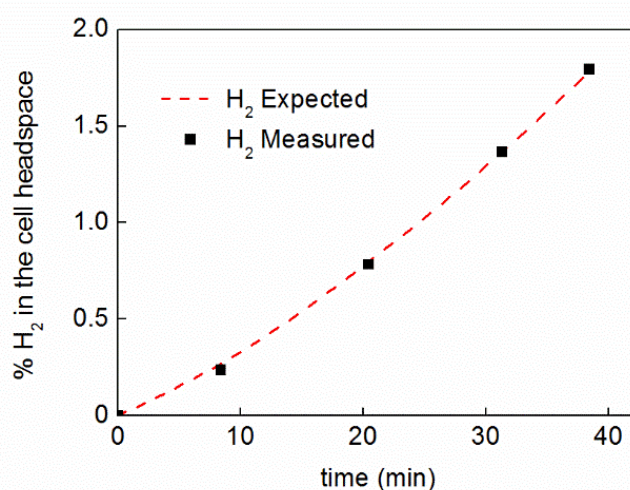


Figure 4.2. A representative trace showing gas chromatographic analysis of the headspace of airtight cells during electrolysis of a solution of 1 M sulfuric acid. A piece of graphite sheet was used for the working electrode, and another as counter electrode. An Ag/AgCl reference electrode was used at an overpotential for the hydrogen evolution reaction of 540 mV (not corrected for resistance). The red dashed line indicates the % of hydrogen expected in the cell headspace based on the charge passed during electrolysis (16 C in this case). Black squares indicate actual measurements of the % of H₂ in the cell headspace as determined by gas chromatography. In this case, 1% H₂ in the cell headspace corresponds to 46 μmol of H₂ and 83 μmol of H₂ was present in the cell headspace at the termination of electrolysis.

In our previous report,²⁰ we found that pre-treating the electrolyte solution with a chelating Amberlite resin was an effective means to remove dissolved metal impurities from the electrolyte and hence mitigate the increased current densities to which these impurities gave rise. However, in the current work, this method proved ineffective, and electrolytes that had been washed with Amberlite behaved similarly to unwashed electrolytes. This in turn suggested that any trace impurities that might have caused the increase in activity evident in Figure 4.1 did not originate from the sulfuric acid electrolyte.

Electrodes that had been subjected to extended-time electrolyses under the conditions of Figure 4.1 were then analyzed by SEM and compared to fresh carbon foil substrates (Figure 4.3). These experiments showed that electrodes that had been polarized at -0.59 V vs. RHE for several hours became covered in sub-micrometer-sized particles (white spots in Figures

4.3B, 4.3C and 4.3D). Analysis of these particles by EDX (Figure 4.4) suggested that they contained significant amounts of silver.

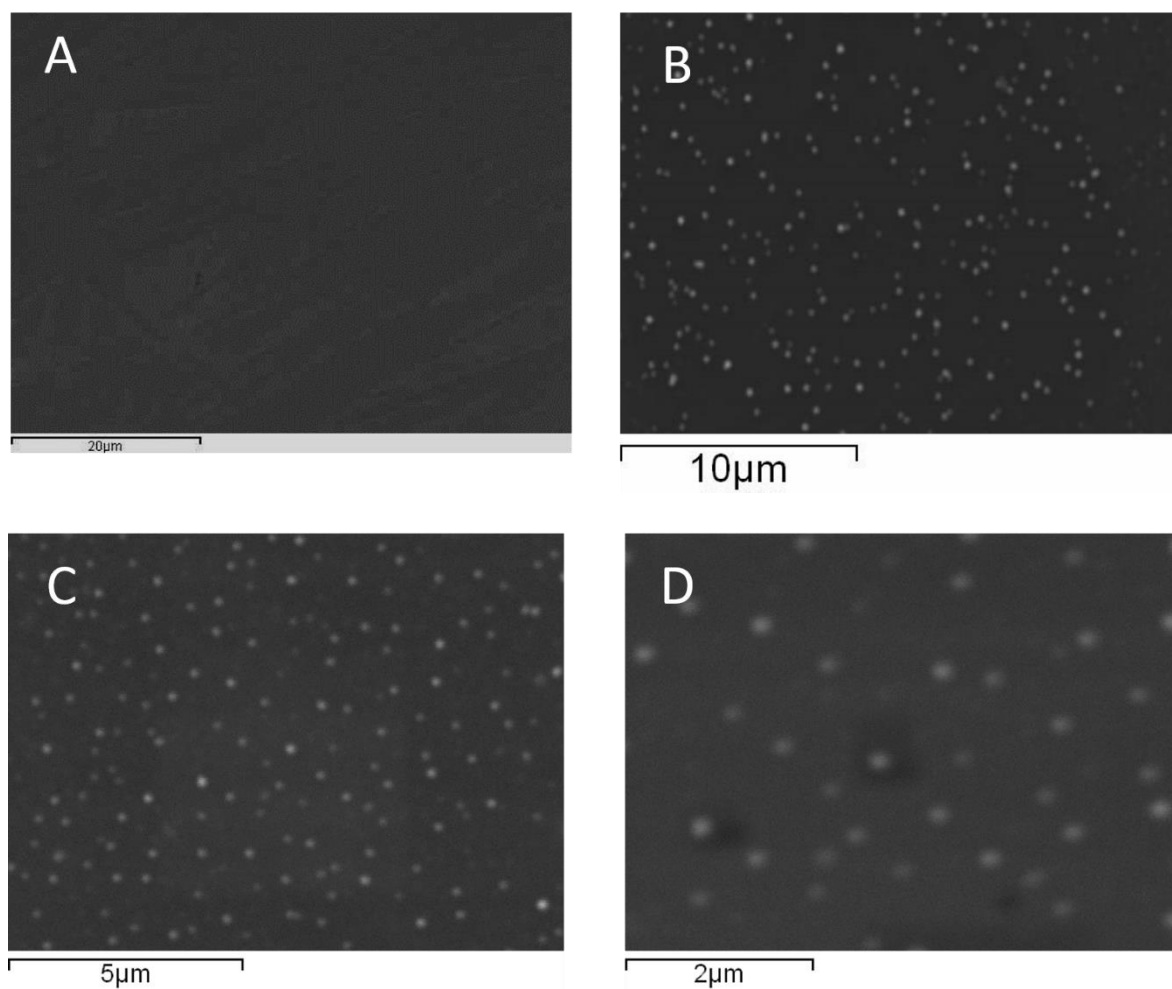


Figure 4.3. SEM images of a bare, unused glassy carbon foil (A, left hand side) and glassy carbon foils that had been subjected to electrolysis in 1 M H_2SO_4 in the presence of an Ag/AgCl reference electrode at -0.59 V vs. RHE for 24 h (panels B, C and D).

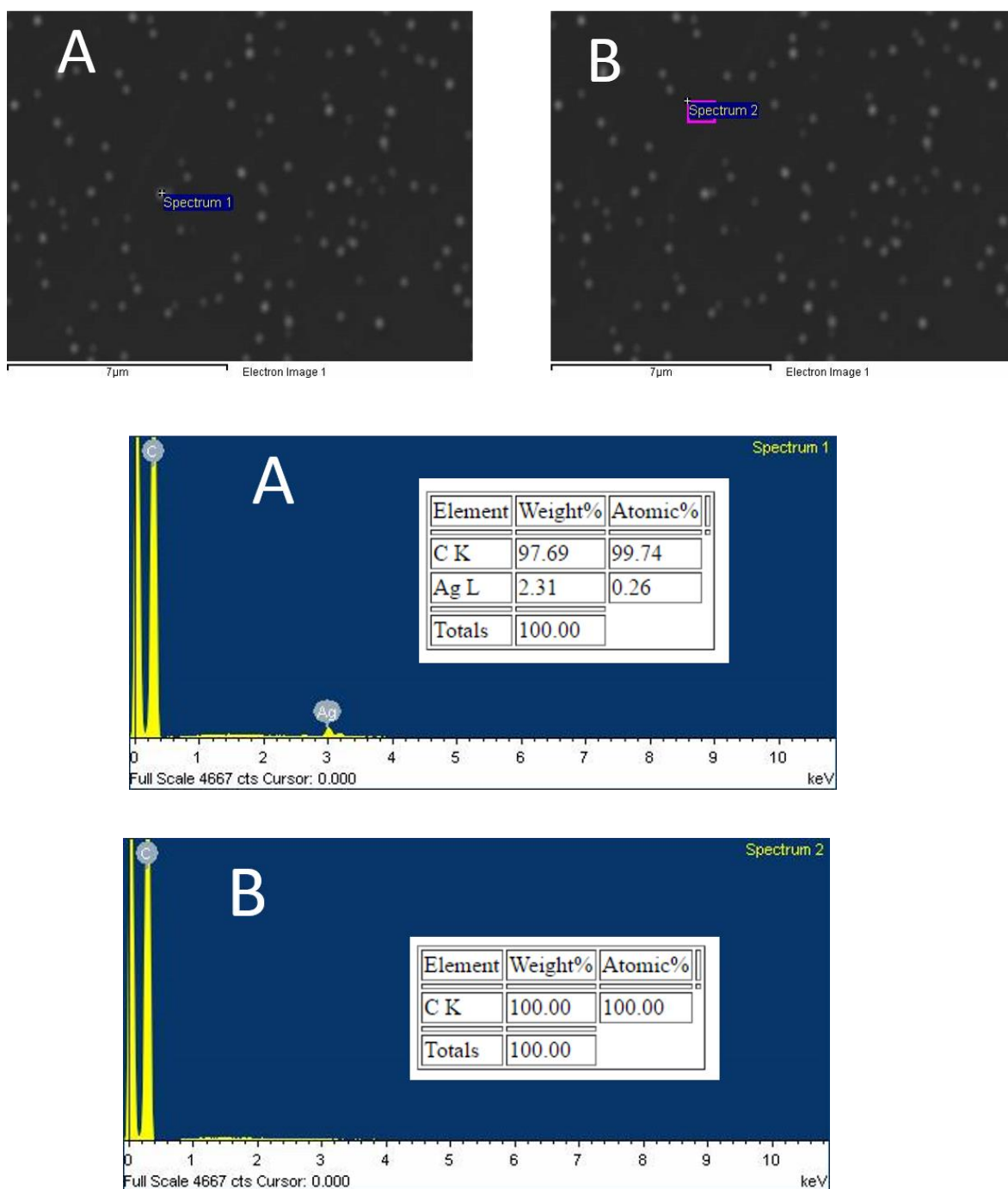


Figure 4.4 Combined SEM/EDX spectra of a glassy carbon foil after this was subjected to electrolysis in 1 M H_2SO_4 in the presence of an Ag/AgCl reference electrode at -0.59 V vs. RHE for 24 h. Panel A gives a highlighted area on one of the white dots observed on the foil after electrolysis that was examined by EDX (the results of which are shown in EDX spectrum A). These data show that silver is present in these dots (peak at ~ 3 keV). In contrast, panel B highlights an area of the foil in which there are no white dots. EDX examination of this area (EDX spectrum B), shows it to be free of silver.

Accordingly, we investigated the surface of these electrodes by XPS (Figure 4.5). This revealed two peaks for the Ag 3d core level at 368.4 and 374.4 eV, corresponding to the Ag 3d_{5/2} and Ag 3d_{3/2} signals in metallic silver respectively.^{66,67}

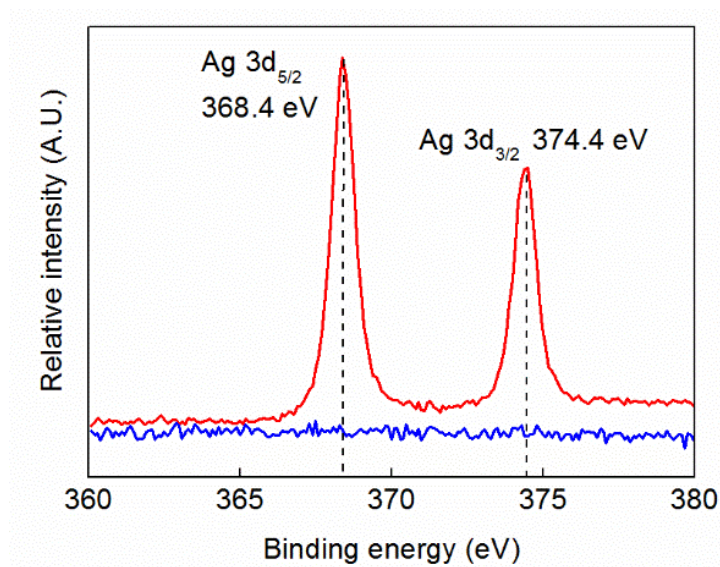


Figure 4.5 The XPS spectrum of a glassy carbon foil that had been subjected to electrolysis in 1 M H₂SO₄ in the presence of an Ag/AgCl reference electrode at -0.59 V vs. RHE for 24 h, showing the Ag 3d signals (red line) and the XPS spectrum of a glassy carbon foil electrode prior to any electrolysis for comparison (blue line).

Survey spectra were also obtained over a wider range of binding energies for these electrodes (Figure 4.6), suggesting that Ag is the only catalytically-active metallic element deposited on the electrode surface during electrolysis under these conditions. Taken together, these surface analysis data suggested that silver depositing on the cathode could be a source of the hydrogen evolution activity observed.

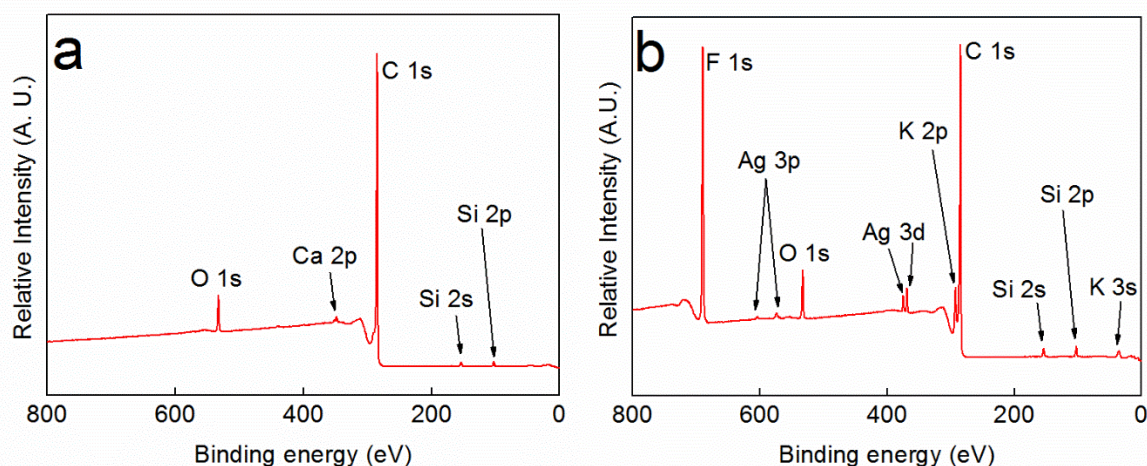


Figure 4.6 XPS survey spectra of a glassy carbon foil prior to any electrolysis as received from the manufacturer (panel (a), left hand side) and a glassy carbon foil electrode that had been subjected to electrolysis in 1 M H_2SO_4 in the presence of an Ag/AgCl reference electrode at -0.59 V vs. RHE for 24 h (panel (b), right hand side). In addition to peaks for carbon, oxygen and a small silicon impurity, the electrode after electrolysis shows several peaks attributable to silver and peaks for fluorine and potassium (probably emanating from the aqueous electrolyte).

Electrocatalytic H_2 evolution on silver has previously been demonstrated in numerous systems. For example, Ag nanoparticle/bacteriorhodopsin ensembles have been shown to be active catalysts for the HER,⁶⁸ and various alloys and composites of silver are also effective.⁶⁹⁻⁷³ Moreover, silver metal itself in unalloyed form has been studied as an electrocatalyst for the HER under both basic⁷⁴⁻⁷⁷ and acidic⁷⁸⁻⁸⁵ conditions. With regard to the latter, a recent study by Amin and co-workers⁸⁶ regarding H_2 evolution from silver nanoparticles on inert Ti supports is particularly relevant, with current densities for the HER of 1 mA cm^{-2} manifesting at overpotentials of around 400 mV for a range of loadings. Hence there is good precedent for silver acting as a moderately effective electrocatalyst for proton reduction in aqueous media.

As our efforts to attenuate the increase in current density for the HER by washing the electrolytes with a chelating resin were unsuccessful (see above), it appeared that the silver was not present in the electrolyte from the outset. It seemed logical, therefore, to hypothesize that the silver was emanating from the Ag/AgCl reference electrode. In support of this hypothesis, electrolyses performed under the same conditions as those used in Figure 4.1,

but using an Hg/Hg₂SO₄ reference electrode (which contains no silver) did not lead to any significant increase in current density (red line in the panel above in Figure 4.7), and SEM of a carbon foil after electrolysis under these conditions indicated that the electrode was free from any deposited material (bottom panels in figure 4.7).

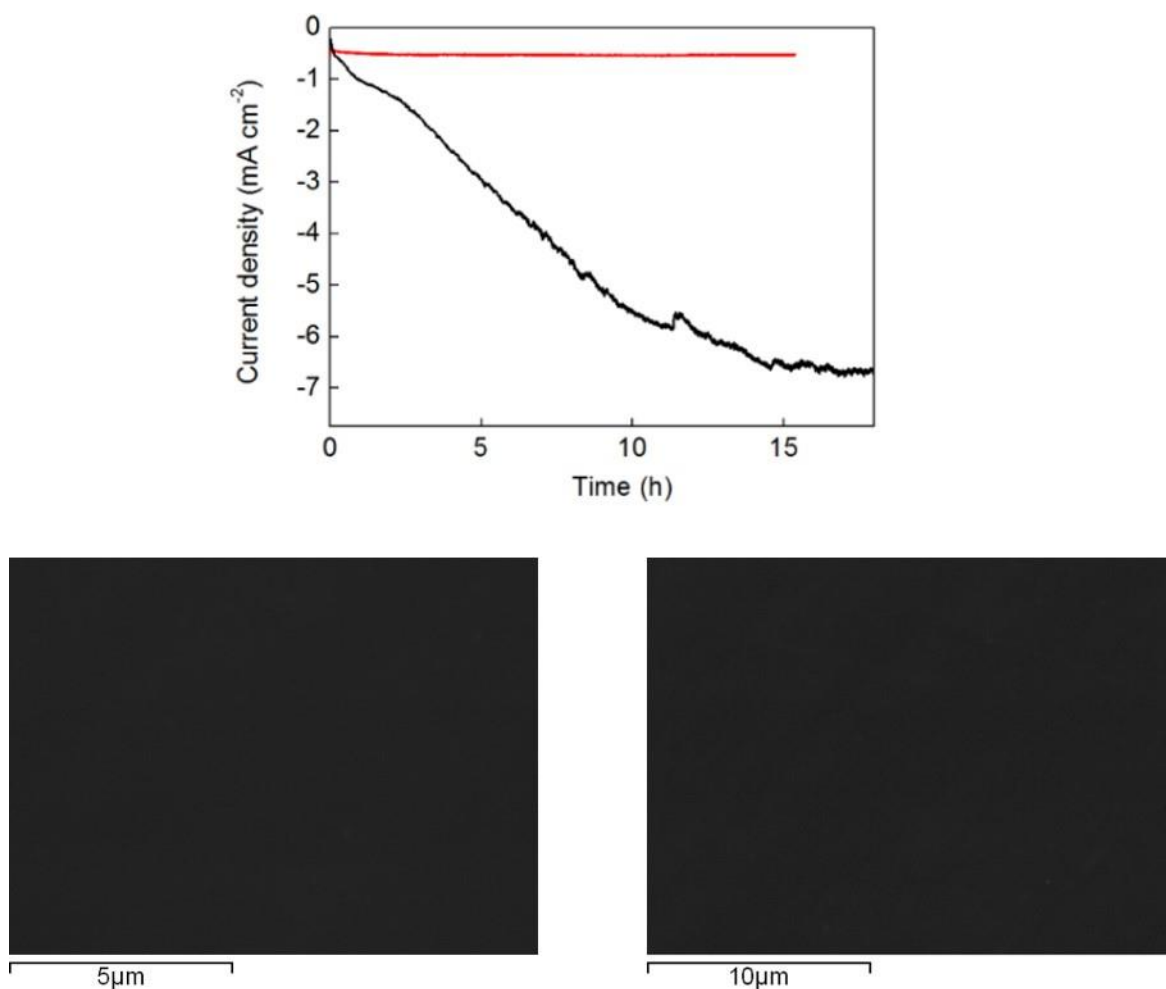


Figure 4.7 Top: A comparison of the current densities for the HER at a glassy carbon working electrode in 1 M H₂SO₄ obtained using an Ag/AgCl reference electrode (black line, reproduced from Figure 1) and using an Hg/Hg₂SO₄ reference electrode (red line). In both cases, the overpotential for the HER was 540 mV. **Bottom:** Representative SEM images of a glassy carbon foil after this was subjected to electrolysis in 1 M H₂SO₄ in the presence of an Hg/Hg₂SO₄ reference electrode at -0.59 V vs. RHE for 24 h. No dots indicative of electrodeposition are evident

Likewise, if electrolysis was performed in a two-electrode configuration (without any reference electrode at all), then again the current density did not rise significantly over the time course of several hours (Figure 4.8a). XPS analysis of an electrode subjected to such an electrolysis in a two-electrode configuration revealed that no silver was present on the electrode surface after electrolysis (Figures 4.8b and 4.8c).

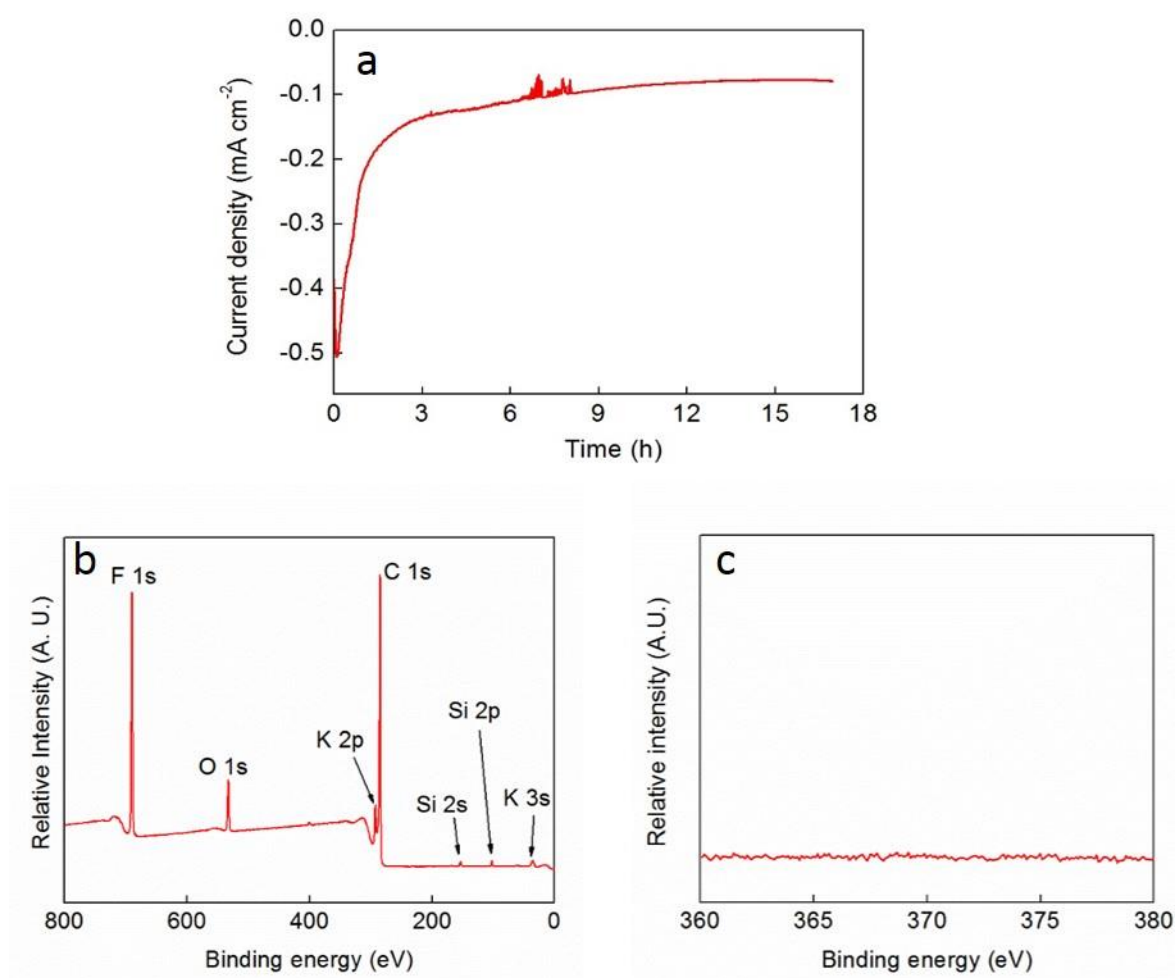


Figure 4.8 (a) Bulk electrolysis in a two-chamber, two-electrode configuration, employing a glassy carbon working electrode (cathode) and a graphite counter electrode in 1 M H₂SO₄ with stirring. A fixed potential of -1.5 V (working electrode negative) was applied across the cell. (b) XPS survey spectrum of the glassy carbon foil used in a. In addition to peaks for carbon, oxygen and a small silicon impurity, the electrode after electrolysis shows only peaks attributable to fluorine and potassium (probably emanating from the aqueous electrolyte). (c) An expansion of the region of b where the characteristic Ag 3d signals would be expected to appear were any Ag present.

Leakage of silver ions (Ag^+) from the reference electrode into solution, followed by reductive electrodeposition of Ag^+ onto the working electrode (which would then lower the overpotential requirements for the HER) thus seemed plausible. If this was indeed the mechanism by which silver was arriving at the cathode, then the rate of current density increase ought to be sensitive to the solubility of Ag^+ in the electrolyte bath, with higher solubility leading to a greater availability of Ag^+ in solution and hence a more rapid increase in current density. This appears to be borne out by the data shown in Figure 4.9: when sulfuric acid is replaced by phosphoric acid at the same concentration, the current density for the HER falls dramatically. This can be explained on the basis of the solubility constants of the relevant salts in water at 298 K ($K_{\text{sp}} \text{Ag}_3\text{PO}_4 = 8.89 \times 10^{-17}$ vs. $K_{\text{sp}} \text{Ag}_2\text{SO}_4 = 1.20 \times 10^{-5}$).⁸⁷

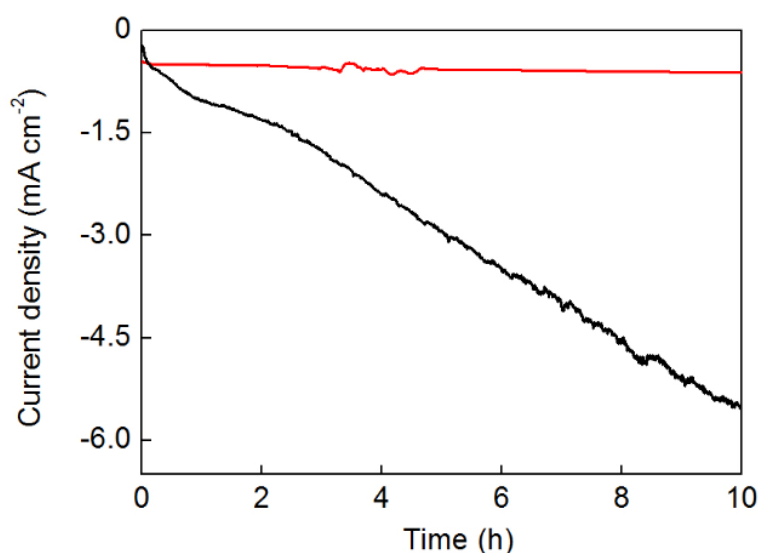


Figure 4.9 A comparison of the current densities for the HER at a glassy carbon working electrode obtained using an Ag/AgCl reference electrode in 1 M H_2SO_4 (black line, reproduced from Figure 4.1) and using an Ag/AgCl reference electrode in 1 M H_3PO_4 (red line). In both cases, graphite counter electrodes were used and the overpotential for the HER was 540 mV

SEM/EDX analysis of an electrode subjected to bulk electrolysis in 1 M phosphoric acid at -590 mV vs. RHE for 16 h using an Ag/AgCl reference electrode shows that a small amount of silver is deposited on the working electrode under these conditions (Figure 4.10). However, the loading of silver on the electrode is much lower than when sulfuric acid is used as the electrolyte.

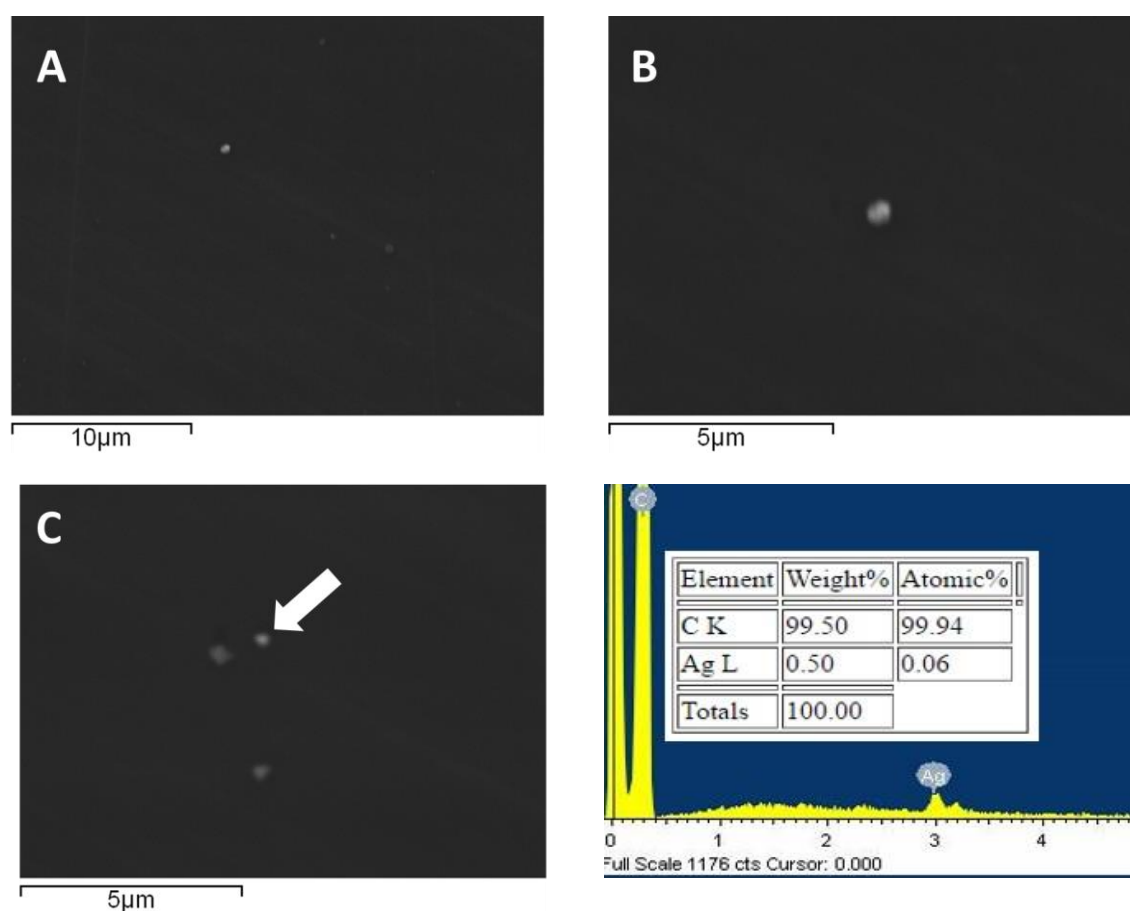


Figure 4.10 SEM/EDX spectra of a glassy carbon foil after this was subjected to electrolysis in 1 M H_3PO_4 in the presence of an Ag/AgCl reference electrode at -0.59 V vs. RHE for 16 h. Panels A-C show representative SEM images. Panel C then shows the white dot selected for analysis by EDX in the last panel. These data show that silver is present in this dot (peak at ~ 3 keV).

Likewise, Figure 4.11 shows the effect of performing electrolysis in perchloric acid. As $AgClO_4$ is around 100 times more soluble in water at room temperature than Ag_2SO_4 ,⁸⁷ a more rapid increase in current density might be expected in perchlorate electrolytes compared to sulfate electrolytes. This indeed seems to be borne out by the data in Figure 4.11.

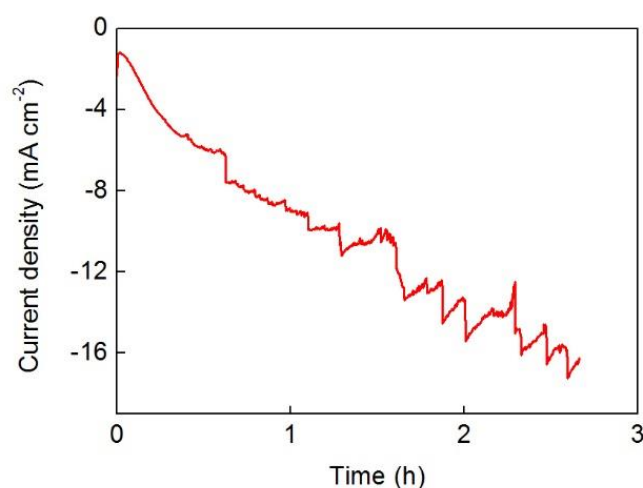


Figure 4.11 The current density for the HER at a glassy carbon working electrode obtained using an Ag/AgCl reference electrode in 0.1 M HClO₄. A graphite counter electrode was used and the overpotential (uncorrected for resistance) for the HER was 540 mV. The undulations after 1 h of electrolysis are due to bubble formation at the working electrode.

Further evidence for the leakage of silver from Ag/AgCl reference electrodes into solution was obtained by ICP-MS analysis of sulfuric acid electrolytes, both before any electrolysis and after several hours of electrolysis using an Ag/AgCl reference electrode. Electrolytes prior to electrolysis were found to contain silver at concentrations within error of the background (3.5 ± 0.8 nM, compared to a background level of 3.8 ± 0.8 nM). After electrolysis, however, the concentration of silver in the electrolyte was found to have risen to 20 ± 2.4 nM. This data again supports a mechanism whereby silver ions leak from the Ag/AgCl reference electrode into solution during electrolysis, prior to electroreduction at the working electrode.

In order to determine if such leakage of silver ions from an Ag/AgCl electrode would have a significant impact on the potential of that reference electrode, we calibrated our reference electrodes against a master reference electrode used only for calibration purposes according to a procedure recommended by the manufacturer (see Section 4.4.2).⁸⁸ This revealed that all the Ag/AgCl reference electrodes used in this work displayed potentials within ± 20 mV of the master reference, which is within the error limits for this type of electrode specified

by the manufacturer (BASi in this case). Hence all the reference electrodes used in this study were functioning within the bounds deemed acceptable by the manufacturers.

Having thus identified silver from the Ag/AgCl reference electrode as the source of the hydrogen evolution activity observed under cathodic bias, we set out to determine the loading of silver on the surface of the working electrode necessary to give a given current density under these conditions. As Figure 4.1 shows, the current density is not stable with time, but increases as more silver leaks from the reference electrode and deposits on the working electrode. Using potential stripping voltammetry, the graph shown in Figure 4.12 was constructed, which shows that there is a (roughly) linear correlation between the current density for the HER that can be obtained from a glassy carbon electrode in the presence of an Ag/AgCl reference electrode and the loading of silver on the surface of that electrode (see example stripping voltammogram shown in the inset to Figure 4.12). Hence to achieve a current density of 1 mA cm^{-2} for hydrogen evolution from $1 \text{ M H}_2\text{SO}_4$ at 540 mV overpotential, a loading of only $\sim 7 \text{ nmol}$ of silver cm^{-2} is required. This equates to somewhere between four and five monolayers (based on a covalent radius for silver of approximately 150 pm),⁸⁹ although Figure 4.3 suggests that the silver is more likely to be present in the form of nano scale islands rather than as a uniform deposit.

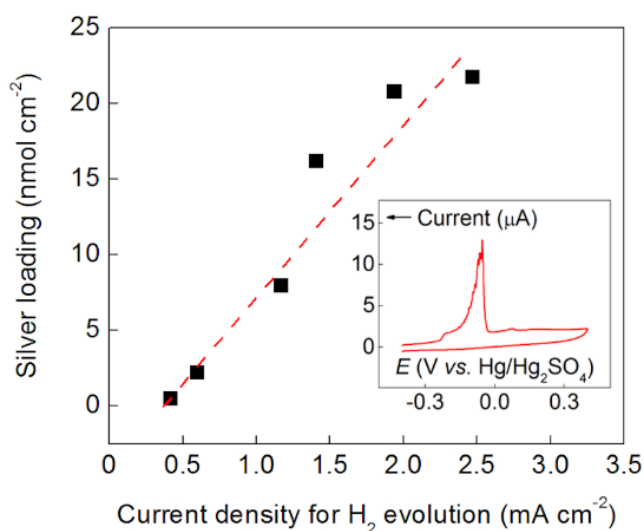


Figure 4.12 Main panel: A graph showing the relationship between the current density for hydrogen evolution achieved after poisoning a glassy carbon electrode at -0.54 V vs. RHE in $1 \text{ M H}_2\text{SO}_4$ (using an Ag/AgCl reference electrode) and the loading of silver calculated to be on the electrode surface by stripping voltammetry. Inset: A representative stripping voltammogram from which the data in the main panel were extracted.

Tafel analysis on a glassy carbon working electrode that had been polarized at -0.54 V vs. RHE (until a current density for hydrogen evolution of 1.2 mA cm $^{-2}$ had been reached) evinced a slope of 82 mV decade $^{-1}$ for the hydrogen evolution process (Figure 4.13). This value is in close agreement with that previously reported for the HER on silver disk electrodes (85 mV decade $^{-1}$),⁴³ suggesting that at this level of coverage (~ 10 nmol cm $^{-2}$), the carbon electrode behaves similarly to bulk Ag with regard to the kinetics of electrochemical proton reduction.

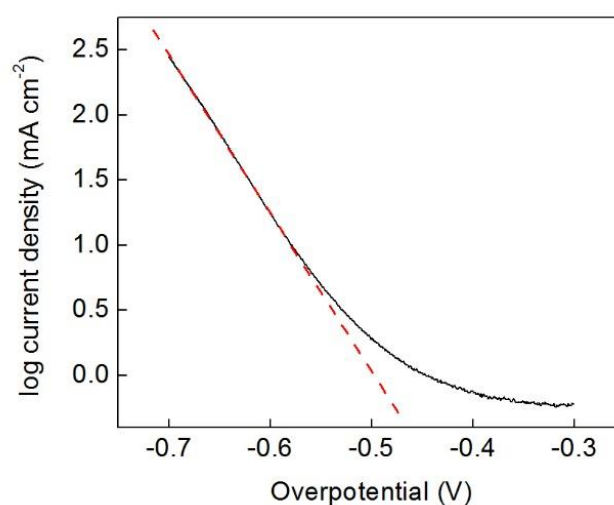


Figure 4.13 Representative Tafel plot of a glassy carbon working electrode in 1 M H_2SO_4 after bulk electrolysis in the presence of an Ag/AgCl reference electrode according to the general procedure given above. The current density for the hydrogen evolution reaction reached during the bulk electrolysis was 1.24 mA cm $^{-2}$. The red line is a linear fit of the slope (82 mV decade $^{-1}$) and is provided as a guide to the eye. Overpotentials in the figure have been corrected for resistance.

We note here that such silver deposition phenomena are not limited to glassy carbon electrodes: very similar behavior manifests when a boron-doped diamond working electrode is employed or when a titanium electrode is used (Figure 4.14).

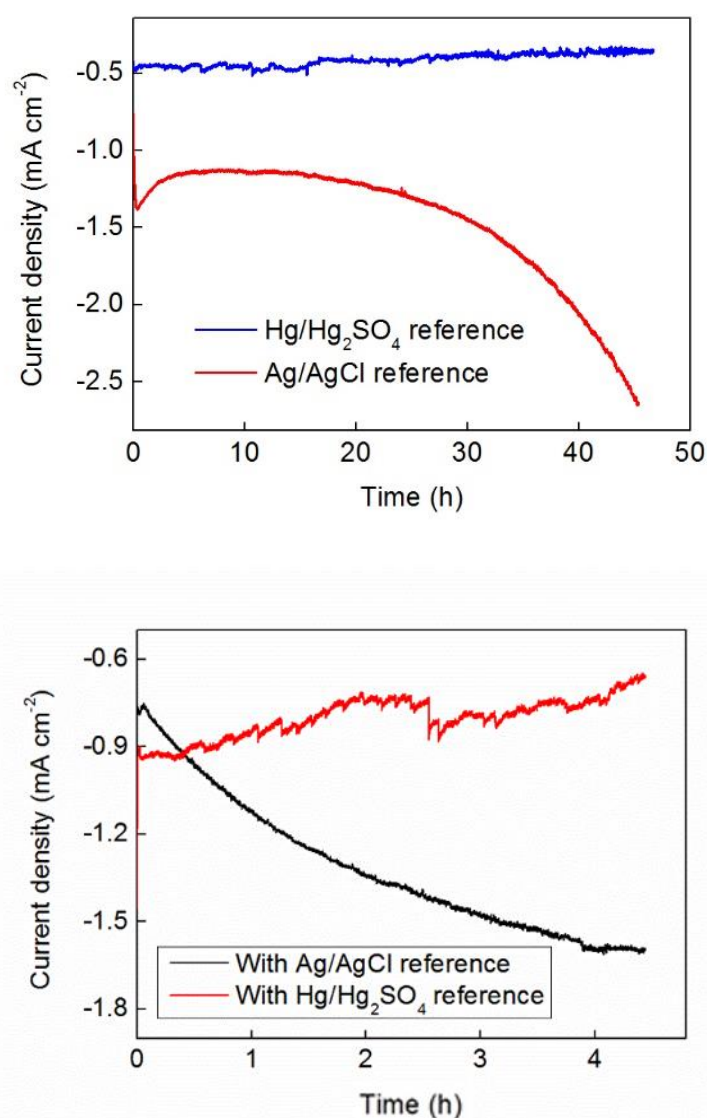


Figure 4.14 Top: A comparison of the current densities for the HER at a boron-doped diamond working electrode (area = 0.071 cm²) obtained in 1 M H₂SO₄ using either an Ag/AgCl reference electrode (red line) or an Hg/Hg₂SO₄ reference electrode (blue line). **Bottom:** A comparison of the current densities for the HER at a titanium working electrode (area = 0.7 cm²) obtained in 1 M H₂SO₄ using either an Ag/AgCl reference electrode (black line) or an Hg/Hg₂SO₄ reference electrode (red line).

The various effects reported above were observed using multiple different Ag/AgCl reference electrodes of two different designs (BASi RE-5B reference electrodes and CH Instruments CHI 111 reference electrodes). The effects observed therefore seem to be general to this class of reference electrode. However, a brand new BASi RE-5B reference electrode (after preparation for first use according to the supplier's instructions) gave only

minimal background activity for the HER (black line in Figure 4.15) when compared to the electrodes we had hitherto employed (all of which, while in apparently good condition and passing the calibration test described above, had been used on a regular basis for several months). This prompted us to investigate the conditions necessary for silver leakage from these electrodes to become appreciable.

Our strategy was to compare the current density for the HER obtained in a standard experiment before and after the reference electrode had been exposed to various conditions. The standard experiment chosen was bulk electrolysis at -0.54 V *vs.* RHE at room temperature in 1 M H_2SO_4 , using the pristine Ag/AgCl reference electrode, a freshly-polished glassy carbon working electrode and a graphite counter electrode (see Experimental Section). These tests showed that the current density reached in the standard experiment remained at background levels after the reference electrode had been used as a reference in multiple CV cycles in 1 M H_2SO_4 (over the range -2 to $+1.5$ V *vs.* Ag/AgCl). Likewise, using the Ag/AgCl electrode in bulk electrolyses overnight in the following electrolytes also failed to produce any discernable increase in the current density reached in subsequent standard experiments: 1 M H_2SO_4 , 1 M H_3PO_4 , 1 M potassium phosphate buffer (pH 7), 1 M potassium borate buffer (pH 9.2) and 1 M sodium phosphate buffer (pH 12). However, despite the current density in the standard experiments remaining at background levels after the above electrolyses, silver had indeed leaked out of the Ag/AgCl reference electrode, as shown by stripping voltammetry (Figure 4.16). Clearly then, silver leakage from even pristine Ag/AgCl reference electrodes is potentially a significant source of interference in electrocatalysis in general.

More significant increases in current density in the standard experiment were obtained after running bulk electrolyses using the Ag/AgCl reference electrode at slightly elevated temperature. The black line in Figure 4.15 shows the current density for the HER obtained at -0.54 V *vs.* RHE in 1 M H_2SO_4 at 293 K using a pristine Ag/AgCl reference electrode. The other traces then give the current densities for the HER that can be reached under the same conditions as the black line, but after the reference electrode has been used in one (red line) or two (blue line) 90-minute bulk electrolyses at -0.54 V *vs.* RHE in 1 M H_2SO_4 at 313 K (note that the working electrode was thoroughly cleaned after each experiment at 293 and

313 K). These data suggest that using Ag/AgCl reference electrodes at even very modest elevated temperatures leads to significant leakage of silver from the reference into solution when the reference electrode is subsequently used for bulk electrolysis at room temperature. The solubility of silver chloride in NaCl solutions (such as that used in the fill-solution of this type of electrode) roughly doubles over the interval 293 – 313 K.⁹⁰ Hence it could be that at higher temperatures, more silver becomes soluble in the electrode fill-solution, leading to an increased rate of silver leakage into the electrolyte in subsequent experiments. This rather dramatic increase in silver leakage in the standard experiment after an increase in temperature of just 20 K (still close to standard laboratory conditions) could have important implications for how such Ag/AgCl reference electrodes are used.

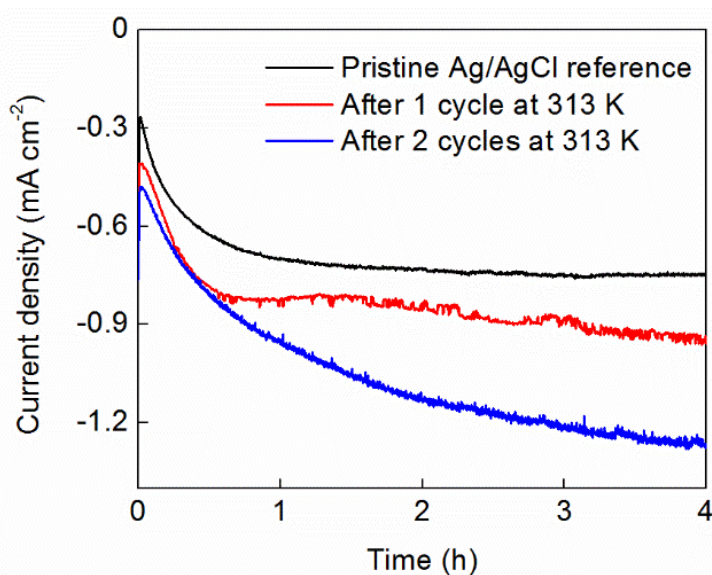


Figure 4.15 A comparison of the current densities for the HER at room temperature at a glassy carbon working electrode in 1 M H₂SO₄ obtained using an Ag/AgCl reference electrode at 540 mV overpotential. Prior to each experiment, the Ag/AgCl reference electrode had been treated as follows: pristine (black line), used in a single bulk electrolysis in 1 M H₂SO₄ at 313 K for 90 min (red line), used in two bulk electrolyses in 1 M H₂SO₄ at 313 K, each for 90 min (blue line). The reference electrode was thoroughly rinsed and allowed to cool to room temperature after each experiment at elevated temperature.

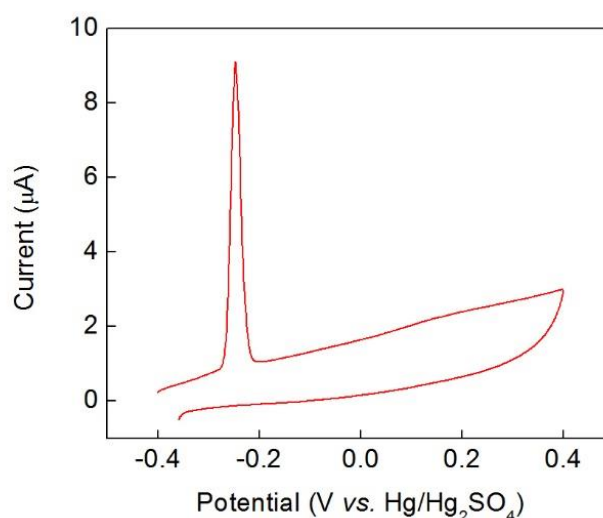


Figure 4.16 Stripping voltammogram obtained in 1 M H₂SO₄ using a glassy carbon working electrode (area = 0.071 cm²) that had previously been subjected to a galvanostatic bulk electrolysis in 1 M H₂SO₄ using a pristine Ag/AgCl reference electrode. During this bulk electrolysis, a current density of -20 mA cm^{-2} was maintained for 16 h (the potential required was around -0.8 V vs. RHE). The working electrode was rinsed with de-ionized water before the stripping voltammogram, but was not polished. The calculated loading of silver on the surface of this electrode by integration of the stripping peak is 2.8 nmol cm^{-2} .

4.3 Conclusions

In summary, we have shown that silver ions leaking from commercially available Ag/AgCl reference electrodes under conditions often employed for exploring the HER can give rise to current densities for proton reduction on the order of 5 mA cm^{-2} at overpotentials of $\sim 500 \text{ mV}$. This level of activity falls within the zone of many recently reported proton reduction electrocatalysts, and calls into question whether the activity ascribed to such catalysts originates from the materials under investigation at all. Clearly, in cases where the HER proceeds at current densities exceeding 5 mA cm^{-2} at overpotentials significantly below 500 mV , then the electrocatalytic activity cannot be attributed solely to silver, and silver contamination (if present) could well have no effect on the reported activity in such cases. However, to avoid any ambiguity when assessing catalysts that produce hydrogen at around the 5 mA cm^{-2} at 500 mV overpotential benchmark, we recommend that one or all of the following practices are adopted as standard procedure: (i) the use of phosphoric acid as the

electrolyte instead of sulfuric acid, (ii) the use of an alternative reference electrode such as Hg/Hg₂SO₄, (iii) if an Ag/AgCl reference must be used, then using a “double junction” design to attenuate Ag⁺ leakage into solution, and (iv) if an Ag/AgCl reference must be used, then undertaking a rigorous examination of the electrode surface *after* extended-time bulk electrolysis in order to show that no silver is present (by stripping voltammetry, SEM/EDX, XPS, or preferably all of these techniques).

On account of the growing body of literature concerned with electrocatalytic hydrogen evolution, it is essential that the community is fully aware of the limitations of the equipment and methods commonly used to investigate the HER. In particular, it is essential that silver is eliminated as a cause of any proton reduction activity that is observed, especially given the ease with which silver ions can be induced to leak from otherwise pristine Ag/AgCl reference electrodes.

4.4 Experimental Section

4.4.1 Materials and reagents

Sulfuric acid (95%) was purchased from Fisher. 0.180 mm-thick Nafion N-118 membrane, carbon graphite sheet (0.25mm diameter), boric acid 99.99%, Amberlite® IRC-748 and phosphoric acid (85%) were supplied by Alfa Aesar. Potassium hydroxide (90%), perchloric acid, sodium hydroxide (98-100.5%) and sodium phosphate dibasic (98.5%) were purchased from Sigma Aldrich. All chemical reagents were used as purchased. All electrolyte solutions were prepared with reagent grade water (18.2 MΩ-cm resistivity), obtained from a Sartorius Arium Comfort combined water system. pH determinations were made with a Hanna HI 9124 waterproof pH meter. ICP-MS analyses were undertaken at the University of Edinburgh. Glassy carbon foil substrates (Carbon-Vitreous 3000C (C) foil, 1.0 mm thickness) were obtained from GoodFellow. All other materials were obtained as stated in the text. Experiments performed at “room temperature” were carried out at 20 °C.

4.4.2 Electrochemical Methods

Electrochemical studies were performed in a three-electrode configuration (unless otherwise stated) using a CH Instruments CHI760D potentiostat. Strips of graphite sheet were used as the counter electrode and were not re-used. Ag/AgCl (NaCl, 3 M, from both BASi and CH Instruments) and Hg/ Hg₂SO₄ (saturated K₂SO₄, CH Instruments) reference electrodes were used as specified. A glassy carbon button electrode was used as the working electrode (unless otherwise stated) except when preparing samples for SEM and XPS analysis, in which case a piece of glassy carbon foil was used. Both working and counter electrodes were washed with acetone and deionized water prior to use. Three-electrode potentials were converted to the NHE reference scale using $E(\text{NHE}) = E(\text{Ag}/\text{AgCl}) + 0.209 \text{ V}$ and $E(\text{NHE}) = E(\text{Hg}/\text{Hg}_2\text{SO}_4) + 0.658 \text{ V}$.

Bulk electrolysis: Bulk electrolyses were performed in a three-electrode configuration (unless otherwise stated) in two-compartment electrochemical cells unless otherwise stated, the compartments of the H-cell being separated by a 0.180 mm-thick Nafion N-118 membrane, with this membrane being held in place by judicious application of Araldite epoxy glue (Bostik Findley, Ltd., UK). Solutions were stirred, keeping the same stirring rate for all experiments. Where voltages have been corrected for ohmic resistances, the effective voltage ($V_{\text{effective}}$) has been calculated as stated in section 3.5.2.

Stripping Voltammetry: Prior to stripping voltammetry, glassy carbon working electrodes (area = 0.071 cm²) were first decorated with silver by running bulk electrolyses using such an electrode, an Ag/AgCl reference electrode and graphite counter electrode in 2-compartment cells in 1 M H₂SO₄ at -0.54 V vs. RHE for various times, such that different current densities for hydrogen evolution were obtained. Once the desired current density had been reached, electrolysis was terminated and the working electrode was removed from solution and washed carefully with de-ionized water. The decorated electrode was then immersed in fresh 1 M H₂SO₄ in a two-compartment cell. The working electrode compartment was further equipped with an Hg/Hg₂SO₄ reference electrode and was stirred. The counter electrode compartment was equipped with a graphite counter electrode. Stripping voltammograms were then collected at room temperature at a scan rate of 5 mV s⁻¹, starting from -0.4 V vs. Hg/Hg₂SO₄. Measurements were conducted without *i*R compensation. A second scan was performed in all cases to ensure that all the Ag had been stripped in the first scan. The loading of silver on the electrode surface was then obtained by

integrating the peak occurring between -0.2 V and $+0.1$ V *vs.* Hg/Hg₂SO₄ in the stripping voltammogram to find the total charge passed during stripping. This was converted to a number of moles of Ag(0) stripped from the surface by dividing this charge by Faraday's constant (assuming a monoelectronic oxidation of Ag(0) to Ag⁺ under these conditions).

Tafel Plots: Glassy carbon working electrodes (area = 0.071 cm²) were subjected to bulk electrolysis applying -0.54 V *vs.* RHE in a 2-compartment cell in 1 M H₂SO₄ in the presence of an Ag/AgCl reference electrode until the current density reached a value of between 1 - 2 mA cm⁻². A graphite counter electrode was used. Immediately after the end of electrolysis, and without changing anything in the experimental set-up, Tafel plots were obtained by linear sweep voltammetry, sweeping the potential from -0.51 V to -1.0 V *vs.* Ag/AgCl at a scan rate of 2 mV s⁻¹ with stirring. A repeat scan under the same conditions gave an essentially identical result.

Bulk electrolysis activity tests with a pristine Ag/AgCl reference electrode: A clean and freshly polished glassy carbon working electrode (area = 0.071 cm²) was subjected to bulk electrolysis applying -0.54 V *vs.* RHE in a 2-compartment cell in the presence of a pristine Ag/AgCl reference electrode and a graphite counter electrode overnight. A range of electrolytes was screened in this way: 1 M sulfuric acid, 1 M phosphoric acid, 1 M potassium phosphate buffer (pH 7), 1 M potassium borate buffer (pH 9.2) and 1 M sodium phosphate buffer (pH 12). After this overnight electrolysis, the working electrode was again thoroughly cleaned and polished, in order to remove any silver deposited on its surface. Meanwhile, the reference electrode was rinsed and a new counter electrode was obtained. The cleaned glassy carbon working electrode was then subjected to bulk electrolysis applying -0.54 V *vs.* RHE in a 2-compartment cell in the presence of the Ag/AgCl reference electrode and a graphite counter electrode in fresh 1 M sulfuric acid. The profile of the resulting current density *vs.* time profile in 1 M sulfuric acid was then compared to that obtained for the pristine Ag/AgCl reference electrode during its first use in 1 M H₂SO₄.

Calibration of Reference Electrodes: Reference electrodes were calibrated versus a master reference electrode used only for this purpose, according to a procedure on BASI's website.⁹¹ Briefly, the master reference electrode and the reference electrode to be checked were immersed in 3 M NaCl solution. The master reference was connected to a potentiostat's reference electrode cable and the Ag/AgCl electrode undergoing calibration was connected

to the working electrode cable. The open circuit potential between the two electrodes was then measured. Ideally the difference between the two electrodes should be zero, but a value ± 20 mV is considered by the suppliers as within the error of this type of electrode.

4.4.3 Headspace Hydrogen Determination

Gas chromatography was conducted in airtight single-chamber and 2-compartment cells using 1 M H₂SO₄ as the electrolyte and an Ag/AgCl reference electrode, using an Agilent Technologies 7890A GC system. During electrolysis, the solution was stirred and the headspace was sampled by gas-tight syringe (volume taken per sampling event = 25 μ L) and introduced onto the GC column by direct injection at various intervals. The column used was a 30 metre-long 0.320 mm widebore HP-molesieve column (Agilent). The GC oven temperature was set to 27 °C and the carrier gas was Ar. The front inlet was set to 100 °C. The GC system was calibrated for H₂ using certified standards of hydrogen at a range of volume % in argon supplied by CK Gas Products Limited (UK). Linear fits of volume % vs. peak area were obtained, which allowed peak areas to be converted into volume % of H₂ in the cell headspace. Total system headspaces were calculated by filling the cells with water at room temperature. Typical headspaces were on the order of 113 mL for the single chamber cell and 11 mL for the 2-compartment cell. Charges passed were converted into expected volume percentages of hydrogen in the headspace by converting charges to an expected number of moles of gas (by dividing by 2F for H₂, where F is the Faraday constant), and then taking the volume of 1 mole of an ideal gas at room temperature and pressure to be 24.5 L. Faradaic efficiencies were then calculated by taking the ratio of gas volume % based on the charge passed to the gas volume % measured by gas chromatography. Faradaic efficiencies were based on the total amount of charge passed, uncorrected for any background or capacitance currents. All gas determinations were performed three times, and average Faradaic efficiencies are reported in the main text.

4.4.4 Other analysis techniques

Scanning electron microscopy (SEM) and energy-dispersive X-ray analysis (EDX).

Scanning electron microscopy was performed with a Philips XL30 ESEM instrument equipped with an Oxford Instruments Energy 250 energy dispersive spectrometer system at an acceleration voltage of 25 kV. Following electrolysis experiments on glassy carbon foil, the electrodes were rinsed gently with deionized water and allowed to dry in air before loading onto 12 mm AGAR scientific conductive carbon tabs. Images and EDX spectra were obtained with acceleration voltages between 12 kV and 20 kV. Spectra were analyzed using Oxford Instrument INCA 4.09 Microanalysis Suite – Issue 17b.

X-ray photoelectron analysis (XPS). Following electrolysis, the electrodes were rinsed gently with deionized water and allowed to dry in air. These electrodes were then carefully packed and sent to the National EPSRC XPS Users' Service (NEXUS) at Newcastle University, UK. XPS spectra on glassy carbon substrates (Carbon-Vitreous 3000C (C) foil, 1.0 mm thickness, GoodFellow) were acquired with a K-Alpha instrument (Thermo Scientific, East Grinstead, UK), using a micro-focused monochromatic AlK α source (X-ray energy 1486.6 eV). Three positions were analyzed per sample. The resulting spectra were referenced to the adventitious C 1s peak (285.0 eV) and were analyzed using the free-to-download CasaXPS software package.

4.5 References

- (1) Lewis, N. S.; Nocera, D. G. *Proc. Natl. Acad. Sci. U.S.A.* **2006**, *103*, 15729.
- (2) Armaroli, N.; Balzani, V. *Chem. Eur. J.* **2016**, *22*, 32.
- (3) Roger, I.; Symes, M. D. *J. Mater. Chem. A*, **2016**, *4*, 6724.
- (4) Xiang, C.; Weber, A. Z.; Ardo, S.; Berger, A.; Chen, Y.; Coridan, R.; Fountaine, K. T.; Haussener, S.; Hu, S.; Liu, R.; Lewis, N. S.; Modestino, M. A.; Shaner, M. M.; Singh, M. R.; Stevens, J. C.; Sun, K.; Walczak, K. *Angew. Chem. Int. Ed.* **2016**, *55*, 12974.
- (5) Gust, D.; Moore, T. A.; Moore, A. L. *Acc. Chem. Res.* **2009**, *42*, 1890.
- (6) Andreiadis, E. S.; Chavarot-Kerlidou, M.; Fontecave, M.; Artero, V. *Photochem. Photobiol.* **2011**, *87*, 946.
- (7) Nocera, D. G. *Acc. Chem. Res.* **2012**, *45*, 767.
- (8) Tachibana, Y.; Vayssieres, L.; Durrant, J. R. *Nat. Photonics* **2012**, *6*, 511.
- (9) Dasgupta, S.; Brunschwig, B. S.; Winkler, J. R.; Gray, H. B. *Chem. Soc. Rev.* **2013**, *42*, 2213.
- (10) Joya, K. S.; Joya, Y. F.; Ocakoglu, K.; van de Krol, R. *Angew. Chem. Int. Ed.* **2013**, *52*, 10426.
- (11) Shaner, M. R.; Atwater, H. A.; Lewis, N. S.; McFarland, E. W. *Energy Environ. Sci.* **2016**, *9*, 2354.
- (12) Crespo-Quesada, M.; Pazos-Outón, L. M.; Warnan, J.; Kuehnel, M. F.; Friend, R. H.; Reisner, E. *Nat. Commun.* **2016**, *7*, 12555.
- (13) McCrory, C. C. L.; Jung, S.; Ferrer, I. M.; Chatman, S. M.; Peters, J. C.; Jaramillo, T. F. *J. Am. Chem. Soc.* **2015**, *137*, 4347.
- (14) Carmo, M.; Fritz, D. L.; Mergel, J.; Stolten, D. *Int. J. Hydrogen Energy* **2013**, *38*, 4901.
- (15) Zheng, Y.; Jiao, Y.; Jaroniec, M.; Qiao, S. Z. *Angew. Chem. Int. Ed.* **2015**, *54*, 52.
- (16) Zou, X.; Zhang, Y. *Chem. Soc. Rev.* **2015**, *44*, 5148.
- (17) Zeng, M.; Li, Y. *J. Mater. Chem. A* **2015**, *3*, 14942.
- (18) Chia, X.; Eng, A. Y. S.; Ambrosi, A.; Tan, S. M.; Pumera, M. *Chem. Rev.* **2015**, *115*, 11941.
- (19) He, Z.; Que, W. *Appl. Mater. Today* **2016**, *3*, 23.
- (20) Roger, I.; Symes, M. D. *J. Am. Chem. Soc.* **2015**, *137*, 13980.

- (21) Tavakkoli, M.; Kallio, T.; Reynaud, O.; Nasibulin, A. G.; Johans, C.; Sainio, J.; Jiang, H.; Kauppinen, E. I.; Laasonen, K. *Angew. Chem. Int. Ed.* **2015**, *54*, 4535.
- (22) Kibsgaard, J.; Chen, Z. B.; Reinecke, B. N.; Jaramillo, T. F. *Nat. Mater.* **2012**, *11*, 963.
- (23) Kong, D. S.; Wang, H. T.; Cha, J. J.; Pasta, M.; Koski, K. J.; Yao, J.; Cui, Y. *Nano Lett.* **2013**, *13*, 1341.
- (24) Benck, J. D.; Chen, Z. B.; Kuritzky, L. Y.; Forman, A. J.; Jaramillo, T. F. *ACS Catal.* **2012**, *2*, 1916.
- (25) Popczun, E. J.; McKone, J. R.; Read, C. G.; Biacchi, A. J.; Wiltrout, A. M.; Lewis, N. S.; Schaak, R. E. *J. Am. Chem. Soc.* **2013**, *135*, 9267.
- (26) Popczun, E. J.; Read, C. G.; Roske, C. W.; Lewis, N. S.; Schaak, R. E. *Angew. Chem. Int. Ed.* **2014**, *53*, 5427.
- (27) McEnaney, J. M.; Crompton, J. C.; Callejas, J. F.; Popczun, E. J.; Read, C. G.; Lewis, N. S.; Schaak, R. E. *Chem. Commun.* **2014**, *50*, 11026.
- (28) McEnaney, J. M.; Crompton, J. C.; Callejas, J. F.; Popczun, E. J.; Biacchi, A. J.; Lewis, N. S.; Schaak, R. E. *Chem. Mater.* **2014**, *26*, 4826.
- (29) Kibsgaard, J.; Jaramillo, T. F. *Angew. Chem. Int. Ed.* **2014**, *53*, 14433.
- (30) Li, Y. G.; Wang, H. L.; Xie, L. M.; Liang, Y. Y.; Hong, G. S.; Dai, H. J. *J. Am. Chem. Soc.* **2011**, *133*, 7296.
- (31) Lukowski, M. A.; Daniel, A. S.; Meng, F.; Forticaux, A.; Li, L. S.; Jin, S. *J. Am. Chem. Soc.* **2013**, *135*, 10274.
- (32) Voiry, D.; Yamaguchi, H.; Li, J. W.; Silva, R.; Alves, D. C. B.; Fujita, T.; Chen, M. W.; Asefa, T.; Shenoy, V. B.; Eda, G.; Chhowalla, M. *Nat. Mater.* **2013**, *12*, 850.
- (33) Lukowski, M. A.; Daniel, A. S.; English, C. R.; Meng, F.; Forticaux, A.; Hamers, R. J.; Jin, S. *Energy Environ. Sci.* **2014**, *7*, 2608.
- (34) Cheng, L.; Huang, W. J.; Gong, Q. F.; Liu, C. H.; Liu, Z.; Li, Y. G.; Dai, H. J. *Angew. Chem. Int. Ed.* **2014**, *53*, 7860.
- (35) Wang, H. T.; Kong, D. S.; Johanes, P.; Cha, J. J.; Zheng, G. Y.; Yan, K.; Liu, N. A.; Cui, Y. *Nano Lett.* **2013**, *13*, 3426.
- (36) Liao, L.; Wang, S. N.; Xiao, J. J.; Bian, X. J.; Zhang, Y. H.; Scanlon, M. D.; Hu, X. L.; Tang, Y.; Liu, B. H.; Girault, H. H. *Energy Environ. Sci.* **2014**, *7*, 387.
- (37) Jiang, P.; Liu, Q.; Ge, C. J.; Cui, W.; Pu, Z. H.; Asiri, A. M.; Sun, X. P. *J. Mater. Chem. A* **2014**, *2*, 14634.
- (38) Tian, J. Q.; Liu, Q.; Asiri, A. M.; Sun, X. P. *J. Am. Chem. Soc.* **2014**, *136*, 7587.

- (39) Jiang, P.; Liu, Q.; Liang, Y. H.; Tian, J. Q.; Asiri, A. M.; Sun, X. P. *Angew. Chem. Int. Ed.* **2014**, *53*, 12855.
- (40) Tian, J.; Liu, Q.; Cheng, N.; Asiri, A. M.; Sun, X. *Angew. Chem. Int. Ed.* **2014**, *53*, 9577.
- (41) Xiao, P.; Sk, M. A.; Thia, L.; Ge, X. M.; Lim, R. J.; Wang, J. Y.; Lim, K. H.; Wang, X. *Energy Environ. Sci.* **2014**, *7*, 2624.
- (42) Xing, Z. C.; Liu, Q.; Asiri, A. M.; Sun, X. P. *Adv. Mater.* **2014**, *26*, 5702.
- (43) Cui, W.; Liu, Q.; Cheng, N. Y.; Asiri, A. M.; Sun, X. P. *Chem. Commun.* **2014**, *50*, 9340.
- (44) Deng, J.; Ren, P.; Deng, D.; Bao, X. *Angew. Chem. Int. Ed.* **2015**, *54*, 2100.
- (45) Xie, J. F.; Zhang, H.; Li, S.; Wang, R. X.; Sun, X.; Zhou, M.; Zhou, J. F.; Lou, X. W.; Xie, Y. *Adv. Mater.* **2013**, *25*, 5807.
- (46) Merki, M.; Fierro, S.; Vrubel, H.; Hu, X. *Chem. Sci.* **2011**, *2*, 1262.
- (47) Garcia-Esparza, A. T.; Cha, D.; Ou, Y. W.; Kubota, J.; Domen, K.; Takanebe, K. *ChemSusChem*, **2013**, *6*, 168.
- (48) Hunt, S. T.; Nimmanwudipong, T.; Román-Leshkov, Y. *Angew. Chem. Int. Ed.* **2014**, *53*, 5131.
- (49) Pan, L. F.; Li, Y. H.; Yang, S.; Liu, P. F.; Yu, M. Q.; Yang, H. G. *Chem. Commun.* **2014**, *50*, 13135.
- (50) Youn, D. H.; Han, S.; Kim, J. Y.; Park, H.; Choi, S. H.; Lee, J. S. *ACS Nano*, **2014**, *8*, 5164.
- (51) Xie, J.; Li, S.; Zhang, X.; Zhang, J.; Wang, R.; Zhang, H.; Pan, B.; Xie, Y. *Chem. Sci.* **2014**, *5*, 4615.
- (52) Vrubel, H.; Hu, X. *Angew. Chem. Int. Ed.* **2012**, *51*, 12703.
- (53) Feng, L. G.; Vrubel, H.; Bensimon, M.; Hu, X. *Phys. Chem. Chem. Phys.* **2014**, *16*, 5917.
- (54) Zheng, Y.; Jiao, Y.; Li, L. H.; Xing, T.; Chen, Y.; Jaroniec, M.; Qiao, S. Z. *ACS Nano*, **2014**, *8*, 5290.
- (55) Ito, Y.; Cong, W.; Fujita, T.; Tang, Z.; Chen, M. *Angew. Chem. Int. Ed.* **2015**, *54*, 2131.
- (56) Zheng, Y.; Jiao, Y.; Zhu, Y. H.; Li, L. H.; Han, Y.; Chen, Y.; Du, A. J.; Jaroniec, M.; Qiao, S. Z. *Nat. Commun.* **2014**, *5*, 3783.
- (57) Zhao, Y.; Zhao, F.; Wang, X.; Xu, C.; Zhang, Z.; Shi, G.; Qu, L. *Angew. Chem. Int. Ed.* **2014**, *53*, 13934.

- (58) See, for example: a) Janz, G. J. *Reference Electrodes: Theory and Practice*, Chapter 4 (Eds.: Ives, D. J. G.; Janz, G. J.), New York: Academic Press, 1961; pp. 179-230; b) Bhatt, A. I.; Snook, G. A. *Handbook of Reference Electrodes*, Chapter 7 (Eds.: Inzelt, G.; Lewenstam, A.; Scholz, F.), Heidelberg: Springer-Verlag, 2013; pp. 189-228.
- (59) Noel, M.; Vasu, K. I. *Cyclic Voltammetry and the Frontiers of Electrochemistry*, London: Aspect Publications Ltd. 1990; pp 78-79.
- (60) Jenkins, I. IJ Cambria Ltd., UK – personal communication.
- (61) Widegren, J. A.; Finke, R. G. *J. Mol. Catal. A: Chem.* **2003**, *198*, 317.
- (62) Crabtree, R. H. *Chem. Rev.* **2012**, *112*, 1536.
- (63) Strmcnik, D.; Li, D.; Lopes, P. P.; Tripkovic, D.; Kodama, K.; Stamenkovic, V. R.; Markovic, N. M. *Top. Catal.* **2015**, *58*, 1174.
- (64) Wong, C. H. A.; Sofer, Z.; Kubešová, M.; Kučera, J.; Matějková, S.; Pumera, M. *Proc. Natl. Acad. Sci. U.S.A.* **2014**, *111*, 13774.
- (65) Rausch, B.; Symes, M. D.; Chisholm, G.; Cronin, L. *Science* **2014**, *345*, 1326.
- (66) Seah, M. P.. *Surf. Interface Anal.* **1989**, *14*, 488.
- (67) Jin, M.; Zhang, X.; Nishimoto, S.; Liu, Z.; Tryk, D. A.; Emeline, A. V.; Murakami, T.; Fujishima, A. *J. Phys. Chem. C* **2007**, *111*, 658.
- (68) Zhao, Z.; Wang, P.; Xu, X.; Sheves, M.; Jin, Y. *J. Am. Chem. Soc.* **2015**, *137*, 2840.
- (69) Qin, Y.; Dai, X.; Zhang, X.; Huang, X.; Sun, H.; Gao, D.; Yu, Y.; Zhang, P.; Jiang, Y.; Zhuo, H.; Jin, A.; Wang, H. *J. Mater. Chem. A*, **2016**, *4*, 3865.
- (70) Ren, H.; Xu, W.; Zhu, S.; Cui, Z.; Yang, X.; Inoue, A. *Electrochim. Acta*, **2016**, *190*, 221.
- (71) Cheah, A. J.; Chiu, W. S.; Khiew, P. S.; Nakajima, H.; Saisopa, T.; Songsiriritthigul, P.; Radiman, S.; Hamid, M. A. *Catal. Sci. Technol.* **2015**, *5*, 4133.
- (72) Tang, M. H.; Hahn, C.; Klobuchar, A. J.; Ng, J. W. D.; Wellendorff, J.; Bligaard, T.; Jaramillo, T. F. *Phys. Chem. Chem. Phys.* **2014**, *16*, 19250.
- (73) Xia, X.; Zhao, X.; Ye, W.; Wang, C. *Electrochim. Acta* **2014**, *142*, 173.
- (74) Lacconi, G. I.; Gioda, A. S.; Macagno, V. A. *Electrochim. Acta* **1985**, *30*, 211.
- (75) Villullas, H. M.; Lacconi, G. I.; Gioda, A. S.; Macagno, V. A. *Electrochim. Acta* **1987**, *32*, 1657.
- (76) Uchida, T.; Mogami, H.; Yamakata, A.; Sasaki, Y.; Osawa, M. *J. Am. Chem. Soc.* **2008**, *130*, 10862.

- (77) Qian, X.; Hang, T.; Shanmugam, S.; Li, M. *ACS Appl. Mater. Interfaces* **2015**, *7*, 15716.
- (78) Bockris, J. O'M.; Conway, B. E. *Trans. Faraday Soc.* **1952**, *48*, 724.
- (79) Bockris, J. O'M.; Ammar, I. A.; Huq, A. K. M. S. *J. Phys. Chem.* **1957**, *61*, 879.
- (80) Frese, U.; Stimming, U. *J. Electroanal. Chem.* **1986**, *198*, 409.
- (81) Diesing, D.; Winkes, H.; Otto, *Phys. Status Solidi A* **1997**, *159*, 243.
- (82) Eberhardt, D.; Santos, E.; Schmickler, W. *J. Electroanal. Chem.* **1999**, *461*, 76.
- (83) Campbell, F. W.; Belding, S. R.; Baron, R.; Xiao, L.; Compton, R. G. *J. Phys. Chem. C* **2009**, *113*, 14852.
- (84) Ruderman, A.; Juarez, M. F.; Avalle, L. B.; Beltramo, G.; Giesen, M.; Santos, E. *Electrochem. Commun.* **2013**, *34*, 235.
- (85) Ruderman, A.; Juarez, M. F.; Soldano, G.; Avalle, L. B.; Beltramo, G.; Giesen, M.; Santos, E. *Electrochim. Acta* **2013**, *109*, 403.
- (86) Amin, M. A.; Fadlallah, S. A.; Alosaimi, G. S. *Int. J. Hydrogen Energy* **2014**, *39*, 19519.
- (87) Lide, D. R. *CRC Handbook of Chemistry and Physics: A Ready-Reference Book of Chemical and Physical Data*. Boca Raton: CRC Press, 2009; pp. 8-128.
- (88) https://www.basinc.com/manuals/LC_epsilon/Maintenance/Reference/reference#testing (accessed October, 2016).
- (89) Sanderson, R. T. *J. Am. Chem. Soc.* **1983**, *105*, 2259.
- (90) Fritz, J. J. *J. Solution Chem.* **1985**, *14*, 865.
- (91) https://www.basinc.com/manuals/LC_epsilon/Maintenance/Reference/reference#testing (accessed October, 2016).

CHAPTER 5

The Direct Hydrothermal Deposition of Cobalt-Doped MoS₂ onto Fluorine-Doped SnO₂ Substrates as electrocatalyst for the HER

Published as “*The Direct Hydrothermal Deposition of Cobalt-Doped MoS₂ onto Fluorine-Doped SnO₂ Substrates for Catalysis of the Electrochemical Hydrogen Evolution Reaction*”

Roger, I.; Moca, R.; Miras, H. N.; Crawford, K. G.; Moran, D. A.; Ganin, A.; Symes, M.D.

J. Mater. Chem. A **2017**, *5*, 1472

Acknowledgments and declaration

The project covered in this chapter was a collaboration with several researchers from other groups at University of Glasgow. Roberta Moca and Dr. Alexey Ganin prepared the Cobalt-doped MoS₂ films and characterized them with RAMAN and SEM/EDX while I did all (unless otherwise stated) the electrochemistry as well as the gas analysis measurements. The following people contributed also: Mr. Michael Beglan did the AAS and UV/vis measurements, the staff at the James Watt Nanofabrication Centre (University of Glasgow) assisted with the AFM measurements and Mr. Jim Gallagher assisted with the SEM measurements. X-ray photoelectron spectra were obtained at the National EPSRC XPS Users' Service (NEXUS) at Newcastle University, an EPSRC Mid-Range Facility.

Synopsis

In this chapter we describe an efficient hydrothermal method to prepare Cobalt-doped MoS₂ thin films onto transparent FTO substrates. Metal chalcogenides, and doped molybdenum sulfides in particular, have considerable potential as Earth-abundant electrocatalysts for the hydrogen evolution reaction. In order to integrate them in an artificial photosynthesis device, the ability to deposit these materials on transparent substrates is therefore desirable. Hydrothermal methods are perhaps the most common route by which metal chalcogenide materials suitable for the hydrogen evolution reaction are produced, since such methods are simple and scalable. However, to the best of our knowledge, the direct hydrothermal deposition of metal chalcogenides on transparent oxide electrodes has hitherto never been reported. Such an advance would greatly facilitate the expansion of the field by removing the requirement for separate hydrothermal synthesis and catalyst deposition steps. The films we describe here display good activity for the hydrogen evolution reaction from acid solution, achieving current densities of 10 mA cm⁻² at 260 mV overpotential with a Tafel slope of 64 mV decade⁻¹. Moreover, the resulting films can be made to be translucent, a very useful property which would allow light to be transmitted through the catalyst to an underlying light-harvesting array in any solar-to-hydrogen device employing this material at the cathode.

5.1 Introduction

Metal chalcogenides are a fascinating class of materials with properties conducive to catalysis,¹⁻³ energy storage,⁴⁻⁷ photovoltaics,^{8,9} electronic devices¹⁰⁻¹² and sensing applications.^{13,14} Amongst the more promising potential applications of metal chalcogenides, their use as cathodes for electrochemical water splitting has attracted significant attention in recent years.¹⁵ Much of this interest stems from the prospect of replacing platinum as the cathode in solar-driven water splitting devices with materials that are both cheaper and more abundant. In this regard, molybdenum sulfides of various compositions (Mo_xS_y) have been shown to be highly effective hydrogen evolution catalysts from aqueous solution over a wide pH-range.^{16,17} Moreover, doping of molybdenum sulfides with other transition metals has been proposed as a route to improving electrocatalytic activity for hydrogen evolution.^{18,19} This is especially true in the case of cobalt, with various CoMoS_x -type materials having been prepared and shown to outperform undoped MoS_2 .²⁰⁻²⁴

With regard to the synthesis of metal chalcogenides, hydrothermal routes are particularly desirable due to their relative simplicity and scalability. Mo_xS_y species have been synthesised on glassy carbon and other non-transparent supports by hydrothermal methods on several occasions (for examples, see references 25-30), but the direct hydrothermal synthesis of MoS_2 on transparent oxide electrodes has yet to be reported. Such an advance would be of great utility in integrating Mo_xS_y -based materials into solar-to-fuel devices, as it would allow this promising class of hydrogen evolution catalysts to be deposited directly onto the electrode substrate hydrothermally without the need for further processing steps. However, the harsh environment that characterizes aqueous solutions under typical hydrothermal conditions tends to strip the transparent conductive metal-oxide layer from the electrode support (often glass), and hence the direct hydrothermal formation of Mo_xS_y species on transparent electrodes has hitherto been overlooked or assumed to be impractical.

Herein, however, we show that the hydrothermal synthesis of metal chalcogenides directly onto transparent metal oxide electrodes is indeed possible, and that the resulting decorated electrodes remain conductive and have metrics for the hydrogen evolution reaction from 0.5 M H_2SO_4 that are comparable to those obtained from similar materials on transparent metal-oxide electrodes but that were prepared by other (non-hydrothermal) methods. In particular, we demonstrate the potential of this approach by synthesising a ternary chalcogenide with

composition $\text{Co}_2\text{Mo}_9\text{S}_{26}$ directly on fluorine-doped tin oxide (FTO) electrodes, which we then show to display good activity for the hydrogen evolution reaction in aqueous solution, achieving current densities of 10 mA cm^{-2} at 260 mV overpotential.

5.2 Synthesis and Characterization of Co-doped MoS_2 on Fluorine-doped Tin Oxide (FTO)

Samples of Co-doped molybdenum sulfide were prepared directly on FTO substrates by hydrothermal methods. Briefly, aqueous solutions containing the simple metal salts (cobalt sulfate and ammonium heptamolybdate) were mixed with thiourea in the appropriate ratios before being transferred to 20 mL Teflon-lined bombs. Into each bomb was placed a single $1 \times 2.5 \text{ cm}^2$ FTO-on-glass slide (with the FTO coating on one side of the slide only) at a 45° angle to both the base and side of the reaction chamber. The bombs were then sealed and heated at a rate of $1 \text{ }^\circ\text{C min}^{-1}$ up to a temperature of $180 \text{ }^\circ\text{C}$. Films heated to $230 \text{ }^\circ\text{C}$ adhered very poorly to the FTO substrate, and delaminated rapidly upon subsequent immersion in electrolyte solutions. Hence a temperature of $180 \text{ }^\circ\text{C}$ was used for producing all the films reported in this manuscript. This temperature was then maintained for 72 h before cooling at a rate of $10 \text{ }^\circ\text{C min}^{-1}$ back to room temperature. After extrication of the FTO slides from the bombs and washing with water to remove loosely-held material, robust, grey-black films were evident on the conductive (FTO) side of the substrates only. This was true whether the FTO side of the substrate faced upwards or downwards in the bomb, and indeed the properties of the films (described below) showed no dependence on whether the FTO side of the substrate faced upwards or downwards.

Removal of the deposited film from the FTO side of the substrate by mechanical scratching revealed that the underlying FTO layer was still conductive. In contrast, FTO-on-glass slides that were heated hydrothermally in the same manner but in the absence of any metal salts suffered degradation of their FTO layer and became non-conductive. When samples were prepared using a solution containing only ammonium heptamolybdate and thiourea (*i.e.* without the addition of cobalt salts to the deposition solution), black films were again produced on the conductive side of the FTO substrates, but these films delaminated from the substrate almost instantly upon immersion in electrolyte solutions (in contrast to films formed from solutions containing both molybdenum and cobalt precursors). Moreover, no

film formation was observed from precursor solutions that contained only cobalt sulfate and thiourea (*i.e.* in the absence of molybdenum). Hence it was concluded that the formation of metal chalcogenide films on these FTO substrates was possible without the degradation of the FTO layer under hydrothermal conditions, and that the presence of both cobalt and molybdenum in the precursor solutions was required in order to produce films stable enough for subsequent electrochemical analysis (see below). However, it is not apparent whether the FTO substrate is actively protected by the deposited films, or whether the reaction medium from which these films are deposited is inherently less corrosive towards FTO than reaction media that lack these metal ions.

Films formed on FTO hydrothermally from solutions containing 2.3 mM Co(II), 13.6 mM Mo(VI) and 34.1 mM thiourea were examined by Atomic Force Microscopy (AFM) and found to have an average thickness on the order of 300 nm (± 50 nm), as represented in Figure 5.1. Analysis of these films by atomic absorption spectroscopy evinced an average relative weight percentage of Mo 47.4 wt. % and Co 6.5 wt. %. This translates to a Co:Mo ratio of 1:4.5 (somewhat below the ratio of 1:6 in the deposition solution). CHN analysis of the films indicated that the levels of carbon, hydrogen and nitrogen present were all negligible. Therefore, assuming that the residual mass in the atomic adsorption data is due to sulfur, we assign a formula of $\text{CoMo}_{4.5}\text{S}_{13}$ ($\text{Co}_2\text{Mo}_9\text{S}_{26}$) to this hydrothermally-produced material. Assuming a crystallographic density of $\text{Co}_2\text{Mo}_9\text{S}_{26}$ of 4.87 g cm^{-3} (estimated using the Diamond 3.0 program³¹), the typical mass loading of this material on the FTO substrates thus equates to $\sim 0.15 \text{ mg cm}^{-2}$.

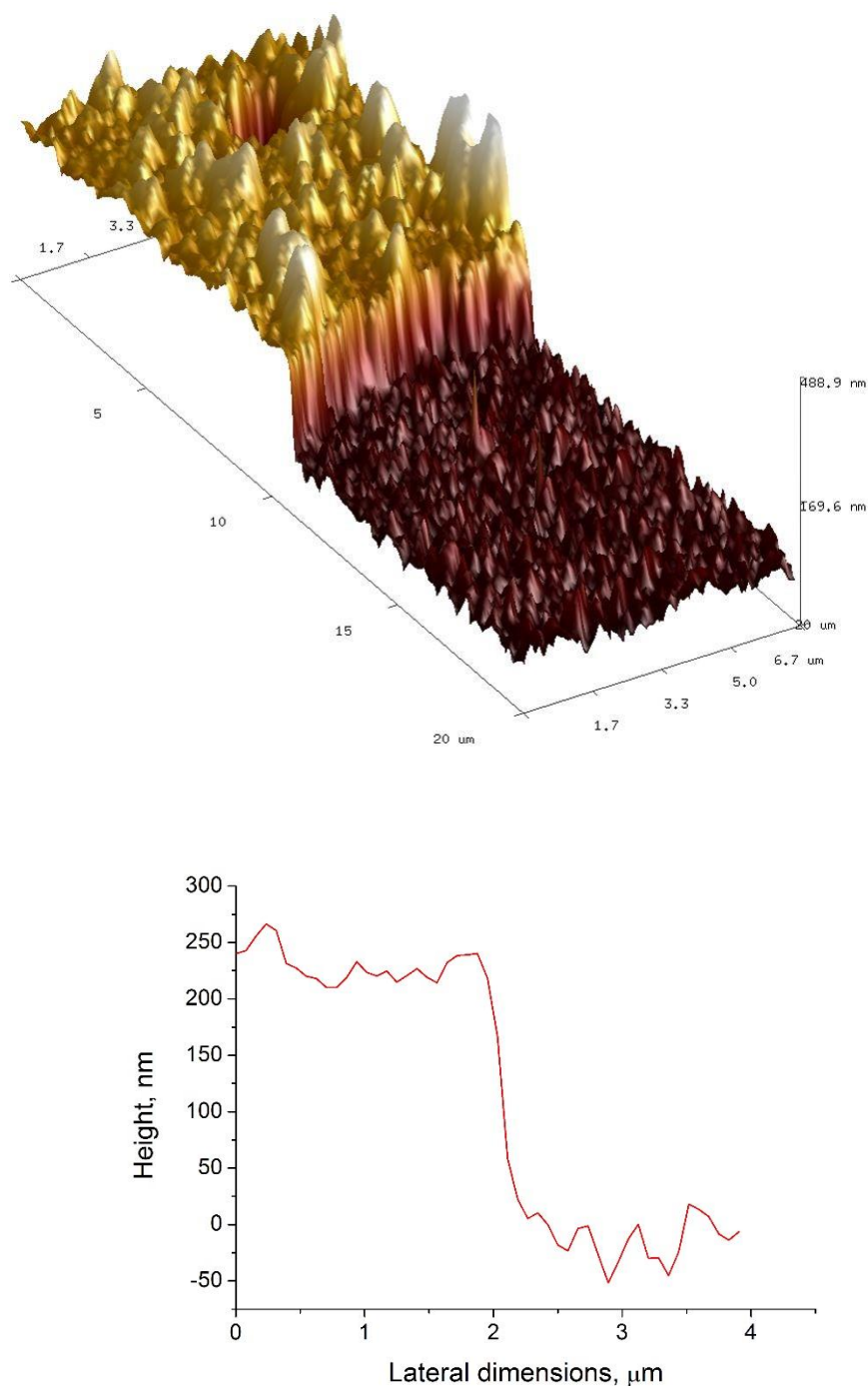


Figure 5.1 Representative AFM data collected on a film of around 300 nm in thickness. Top: 3D topographical profile of the substrate/deposit step. Bottom: A line scan showing the variation in height measured over the step shown in the upper panel.

According to X-ray diffraction (XRD) (Figure 5.2), these films are polycrystalline in nature and show a broad (002) reflection peak corresponding to the layered hexagonal structure of MoS₂. The PXRD pattern of a blank FTO slide is given for comparison

(Figure 5.2b), showing that the majority of the reflections arise from the underlying FTO substrate. This is in line with our observation that the deposition of the metal chalcogenide film is possible without the degradation of the substrate FTO layer. Due to the lack of significant reflections, the only parameter that could be estimated for the metal chalcogenide films was $c = 12.36 \text{ \AA}$, which nevertheless is in good agreement with the value expected for a MoS_2 phase. No reflections from adversary crystalline phases were observed within the pattern, suggesting that both Co and Mo are incorporated within the same structure.

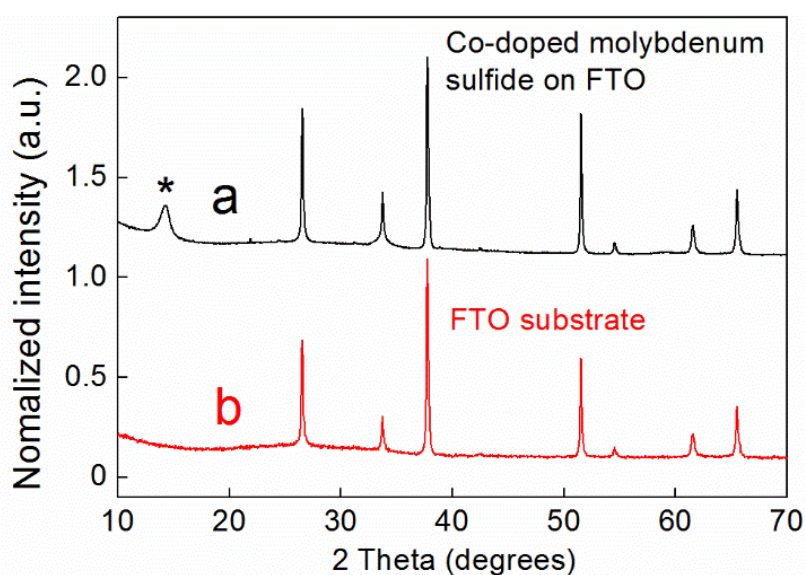


Figure 5.2 (a) XRD pattern of a Co-doped molybdenum sulfide film grown on an FTO substrate (black). The peak associated with the hexagonal structure of MoS_2 is highlighted with the asterisk. (b) The XRD pattern of a blank FTO substrate for comparison (red).

Two dominant peaks were observed by Raman spectroscopy of the bulk sample at 374 and 403 cm^{-1} , corresponding to the in-plane (E_{2g}^1) vibration and the out-of-plane A_{1g} mode respectively – values which are typical for MoS_2 (Figure 5.3).^{32,33} The peak separation ($\Delta k = 29 \text{ cm}^{-1}$) agrees with values reported for bulk MoS_2 .³⁴ Furthermore, no peaks associated with the presence of either CoS_x or MoO_x were observed in the Raman spectrum.

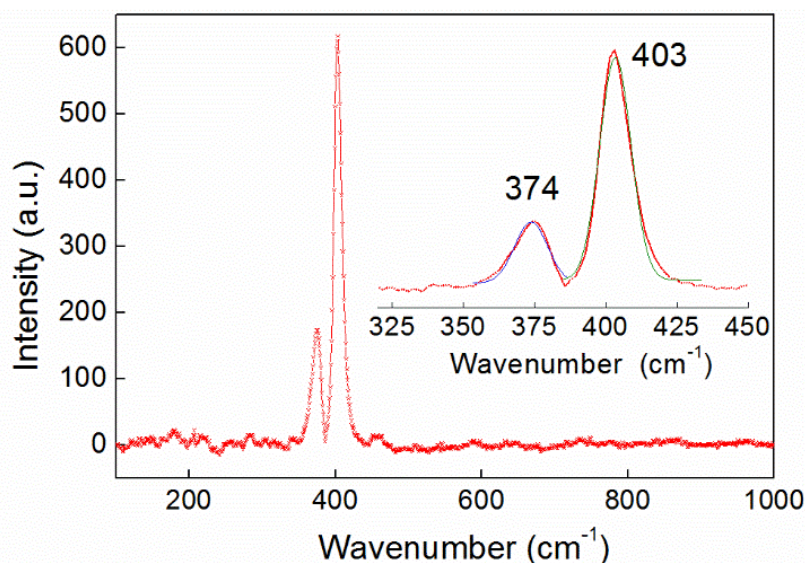


Figure 5.3 A wide range Raman spectrum of a 300 nm-thick film deposited on an FTO substrate, which only shows peaks associated with the $\text{Co}_2\text{Mo}_9\text{S}_{26}$ phase. The sample penetration depth was over 100 nm. Inset: A magnified region showing the two peaks associated with the Raman-active in-plane ($E_{2g}^1 = 374 \text{ cm}^{-1}$) and out-of-the-plane ($A_{1g} = 403 \text{ cm}^{-1}$) modes fitted with Gaussians. The peak separation ($\Delta k = 29 \text{ cm}^{-1}$) is consistent with the bulk character of the film.

XPS spectroscopy of the films revealed that Mo, Co and S were all present on the surface of the deposited materials. The valence state of molybdenum could be ascertained by examination of the 3d region of the XPS spectrum (Figure 5.4), which revealed two dominant peaks associated with Mo (IV) ions (corresponding to about 87 atomic % of the total molybdenum). Other minor components were also observed, and were attributed to Mo (V) and Mo (VI) ions, probably associated with the presence of 6.5 atomic % MoO_2OH and 6.5 atomic % MoO_3 on the surface of the sample, in agreement with reported XPS spectra of MoS_2 (for example, see ref 35 and 36).

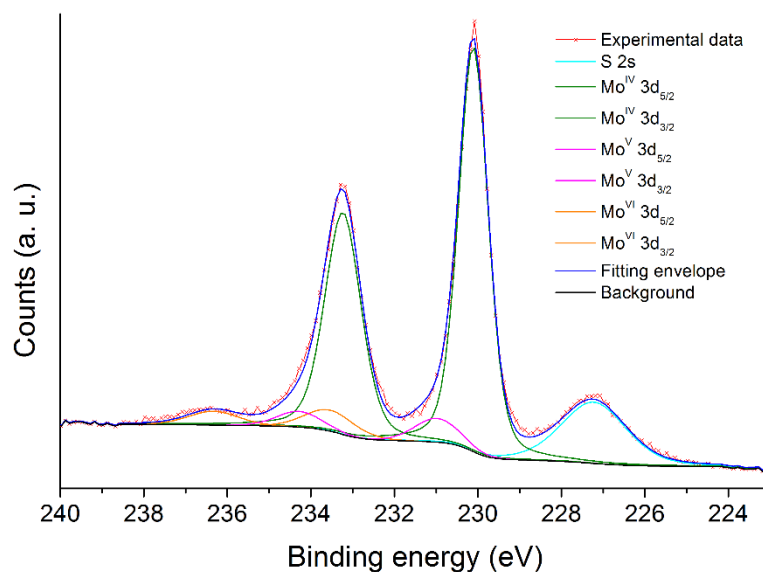


Figure 5.4 The Mo 3d region and S 2s region of the XPS spectrum for a 600 nm-thick film. The peaks were fitted with a combination of Gaussian-Lorentzian profile functions corresponding to a mixed-valence oxidation state of the molybdenum (Mo^{2+} 87 at. %; Mo^{5+} 6.5 at. % and Mo^{6+} 6.5 at. %).

The presence of cobalt on the surface of the films was confirmed by a high resolution spectrum in Co 2p region, which showed two doublets (suggesting a mixed valence state of 57 atomic % Co (II) and 43 atomic % Co (III), Figure 5.5a). Again, it is possible that there is some contribution from Co-oxides to this signal. The peaks in the S 2p_{3/2} region of the spectrum could be fitted with a single doublet (with binding energies 162.2 and 163.4 eV), which agrees with an assignment of the sulfur's oxidation state on the surface as being S²⁻ (Figure 5.5b).

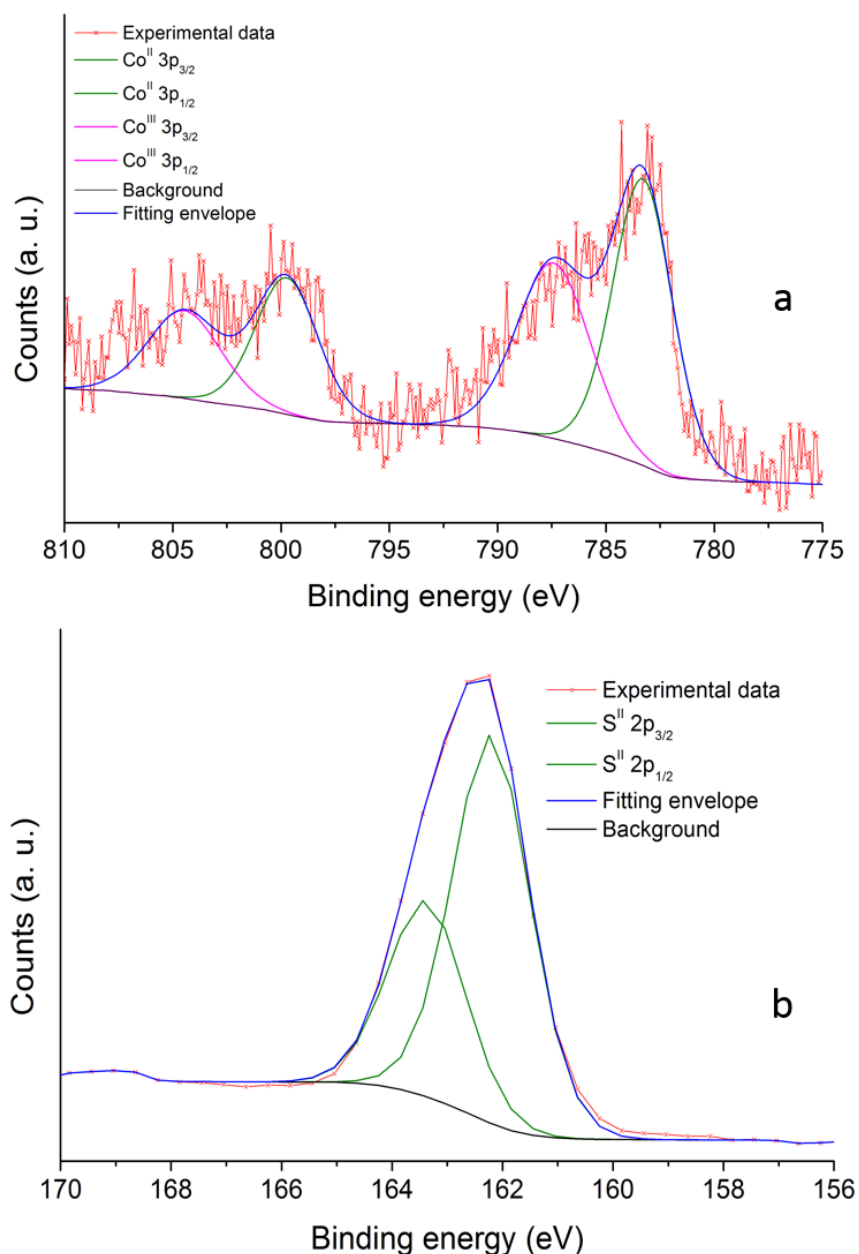


Figure 5.5(a). The 3p region of the Co XPS spectrum for a 600 nm-thick film with peaks fitted with a combination of Gaussian-Lorentzian profile functions and representing a mixed-valence oxidation state for cobalt (Co (II) 57 at. % and Co (III) 43 at. %). **5.5(b)** S 2p region of the XPS spectrum for a 600 nm-thick film. The peaks could be fitted with a single doublet using a combination of Gaussian-Lorentzian profiles, attributable to a sole S²⁻ oxidation state within the film.

The morphology of the products as assessed by scanning electron microscopy (SEM) showed the films to be homogeneous (Figure 5.6). The higher-magnification images indicate that the product films consist of a large number of discrete “sea-urchin-type” blocks probably consisting of randomly-aligned chalcogenide platelets. The presence

of such morphology is in agreement with significant peak broadening observed in the PXRD pattern (Figure 5.2), which is due to the misalignment of layers along the c -axis of the hexagonal structure. Such misfit between the layers is important for the electrochemical properties of these materials, as it generally leads to an increased number of catalytic sites (predominately located at the interfaces and edges of the MoS₂ sheets).¹⁵

Elemental mapping by EDX analysis showed a homogeneous distribution of Co, Mo and S on the surface of the films (Figure 5.7), in turn suggesting that Co-atoms replace some of the Mo-atoms within the hexagonal structure of MoS₂. These results agree with those obtained by PXRD where no significant reflections associated with Co-S or Co-O phases were present. Elemental analysis using EDX spectroscopy showed an average Co:Mo ratio of 1:5. Whilst it should be noted that EDX can only be used on an indicative, semi-quantitative basis in this case due to the overlapping of the Mo and S peaks in the spectra (see Figure 5.6), this data provides further evidence for the nature of the hydrothermally-deposited material being a ternary chalcogenide with a stoichiometry close to Co₂Mo₉S₂₆.

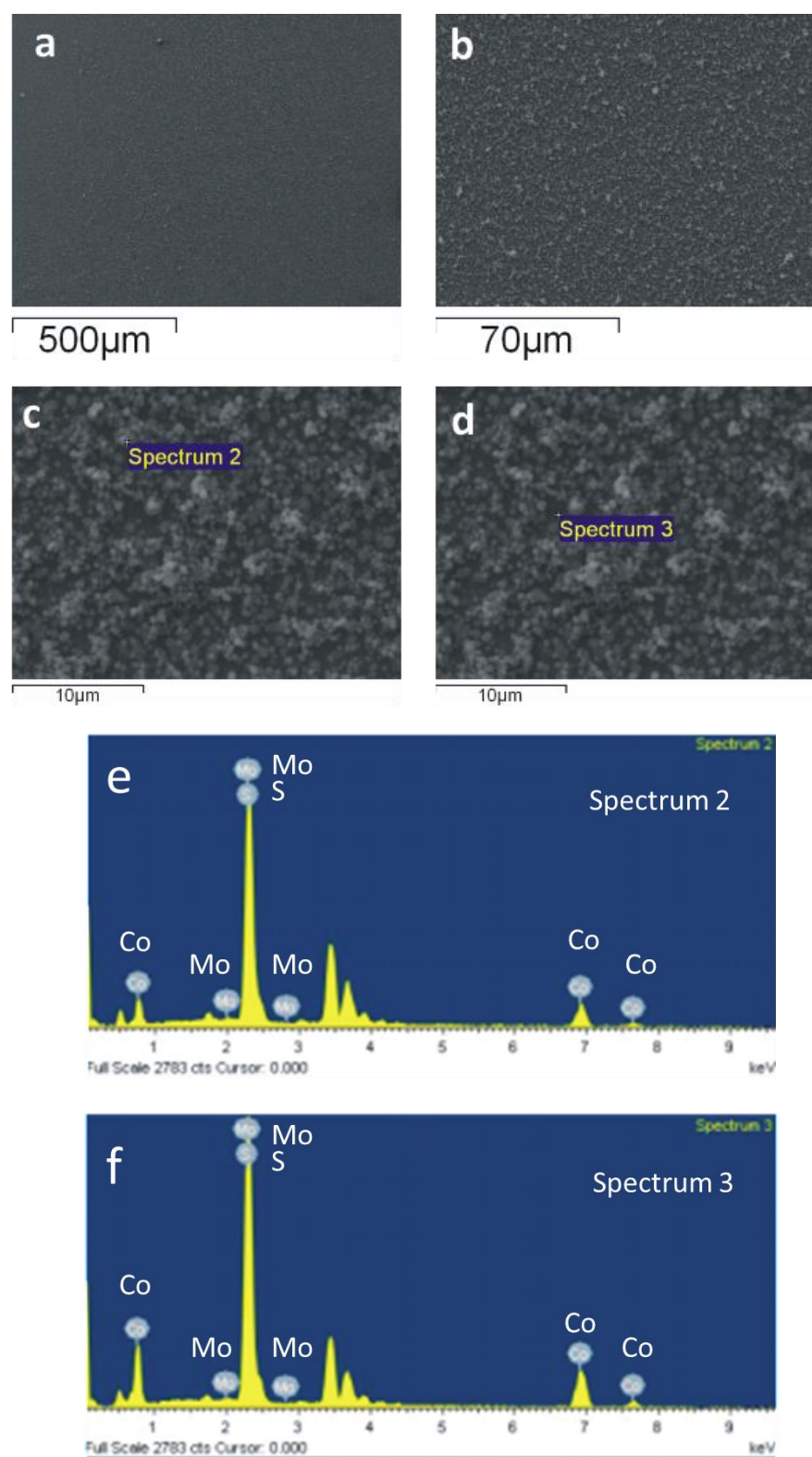


Figure 5.6 (a-b) SEM images showing the surface of the prepared films various magnifications. **(c-d)** Magnified region with the probed points. **(e,f)** The corresponding EDX spectra with Co, S and Mo peaks marked. The strong triplet of the peaks at 3-4 keV originate from Sn due to the FTO substrate.

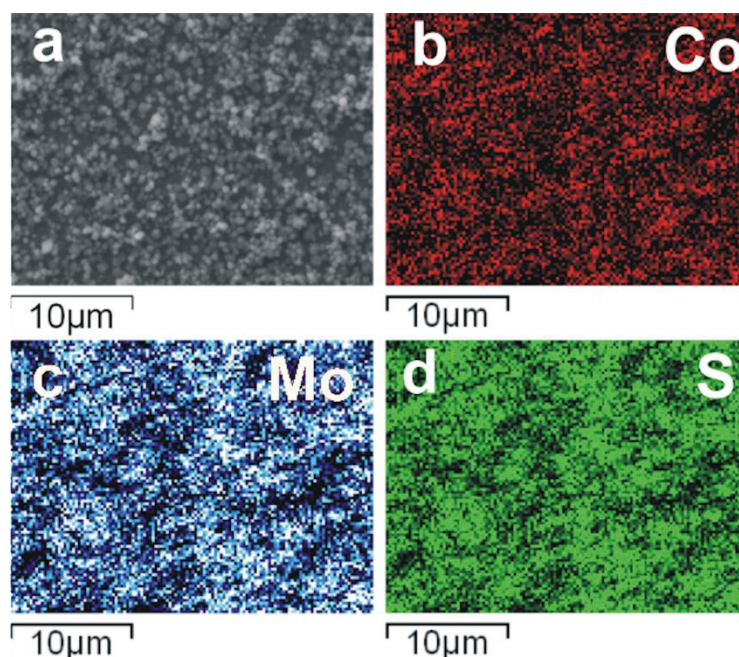


Figure 5.7 SEM images and the corresponding elemental mapping for Co, Mo and S in a $\text{Co}_2\text{Mo}_9\text{S}_{26}$ film, indicating the homogeneous distribution of Co atoms within the sample.

Modification of the standard synthetic procedure by using lower concentrations of cobalt, molybdenum and thiourea in the deposition solutions led to the formation of somewhat thinner films, through which the transmission of light was more evident as shown in Figure 5.8, which compares the transmission of light through a 150 nm-thick film with that of a 300 nm-thick film on FTO and a bare FTO substrate. Indeed, employing the same general hydrothermal method described above, but with concentrations of cobalt, molybdenum and sulfur in the deposition solution that were all lower by a factor of 2.5 compared to the standard procedure, films on the order of 150 nm (± 50 nm) thick could be produced, as seen by AFM (Figure 5.9). However, further dilution of the precursor solution failed to produce films that covered the FTO substrate in a uniform manner.

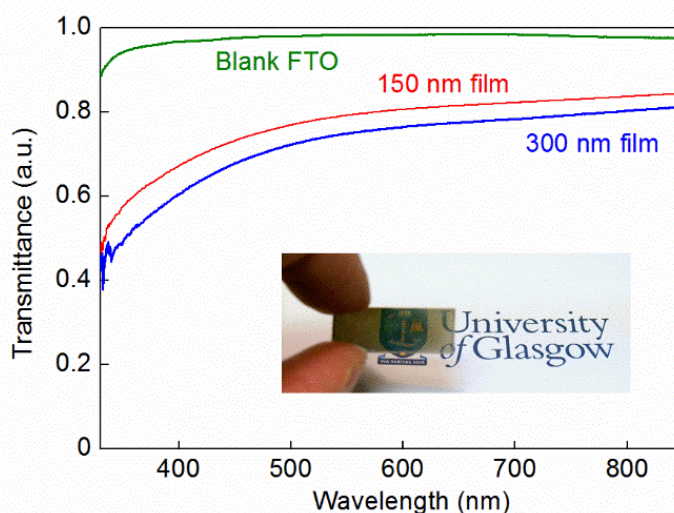


Figure 5.8 UV-vis transmission spectra of a 300 nm-thick Co-doped molybdenum sulfide film on FTO (blue line), a 150 nm-thick Co-doped molybdenum sulfide film on FTO (red line), and a blank FTO substrate for comparison (green line). A 1 mm-thick solid metal plate had a transmittance of zero on this scale (data not shown). Inset: a photograph of a 150 nm-thick Co-doped molybdenum sulfide film on FTO showing its translucent nature.

Thin, translucent, Co-doped molybdenum sulfide films such as those shown in Figure 5.8 are of considerable interest given that ternary metal chalcogenides have been proposed as cathode catalysts in solar-to-hydrogen devices (where transmission of light through the electrocatalyst to the underlying light-harvesting material would be desirable). We next, therefore, assessed the competence of our hydrothermally produced Co-doped molybdenum sulfide films as hydrogen evolution electrocatalysts in aqueous solution.

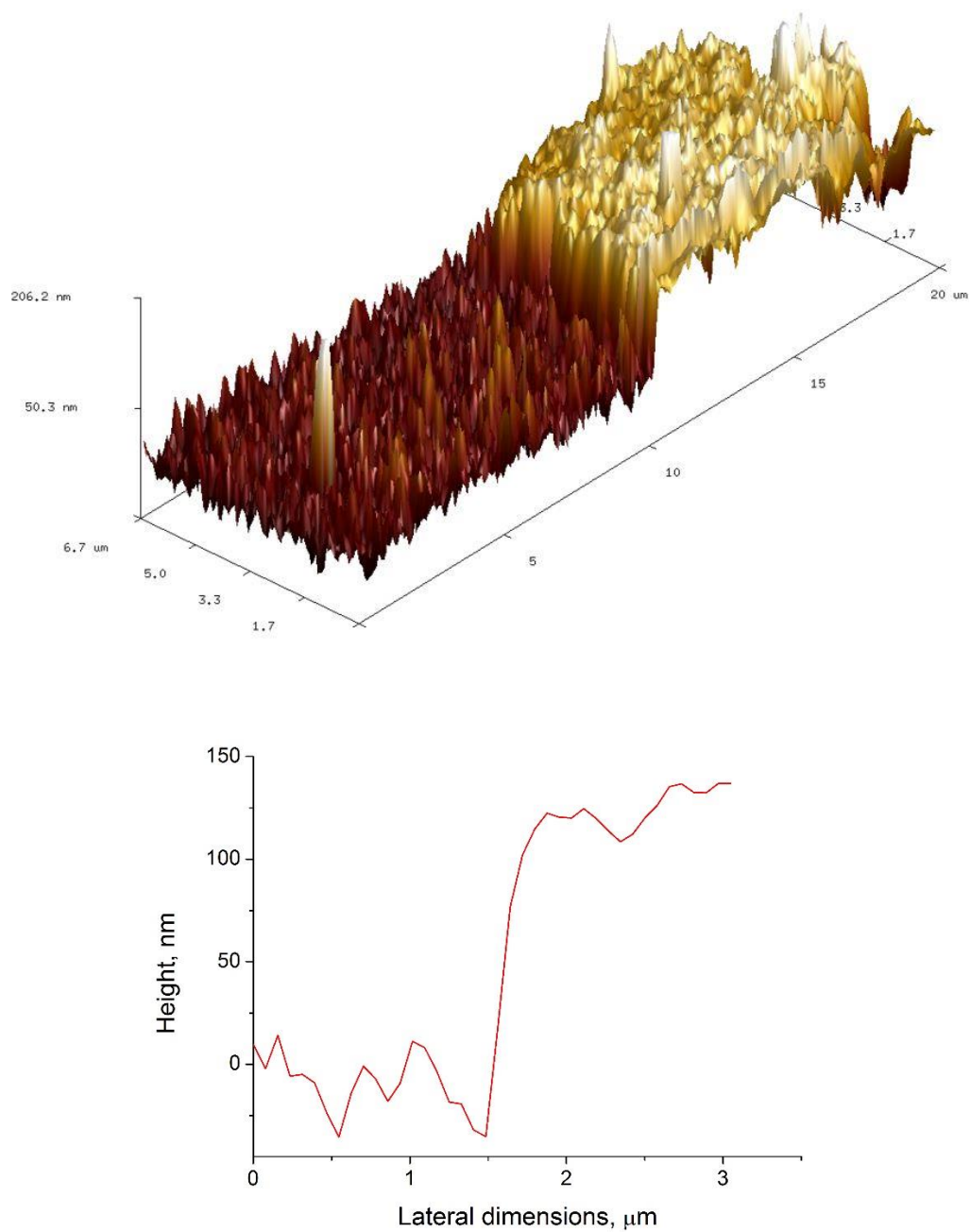


Figure 5.9 Representative AFM data collected on a film of around 150 nm in thickness. Top: 3D topographical profile of the substrate/deposit step. Bottom: A line scan showing the variation in height measured over the step shown in the upper plot.

5.3 Hydrothermally-produced Co-doped MoS₂ on FTO as an electrocatalyst for the HER

5.3.1 Study of the performance of 300 nm thick films at low pH

The performance of these hydrothermally-produced, Co-doped molybdenum sulfide-on-FTO slides as cathodes for the electrochemical hydrogen evolution reaction was probed in 0.5 M H₂SO₄. Figure 5.10 shows how the current density varied with applied potential for these electrodes as compared to a blank FTO slide:

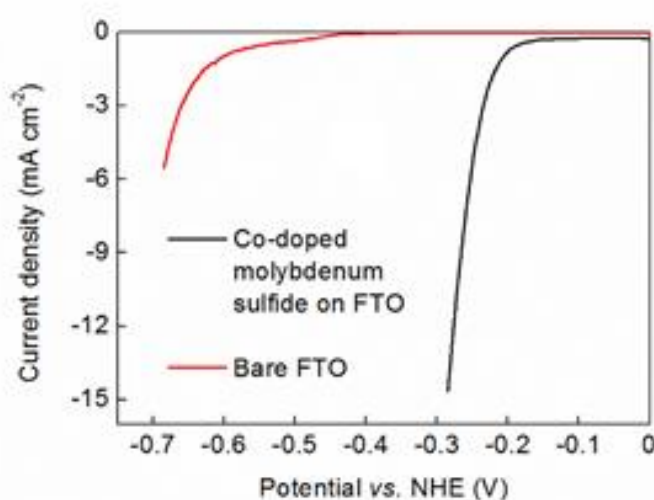


Figure 5.10 Comparison of the current densities at pH 0 delivered by a 300 nm-thick Co₂Mo₉S₂₆ film prepared by the methods described above on an FTO support (black line) and a bare FTO electrode (red line) obtained by linear sweep voltammetry at a scan rate of 2 mV s⁻¹.

Hence 300 nm-thick Co₂Mo₉S₂₆-on-FTO cathodes were found to deliver a current density of 10 mA cm⁻² at ~260 mV overpotential (262 mV ± 8 mV). Meanwhile, Tafel analysis of these electrodes in 0.5 M H₂SO₄ gave a slope of 64 ± 2 mV decade⁻¹ as shown in Figure 5.11. These data were collected by linear sweep voltammetry at slow scan rates (2 mV s⁻¹) instead of multipotential steps due to delamination issues. However, in the lower panel of the same figure we show that a Tafel plot obtained from steady-state current density readings collected by controlled potential electrolysis at various potentials, gave a value of 66 mV decade⁻¹, in close agreement with that obtained by linear sweep voltammetry.

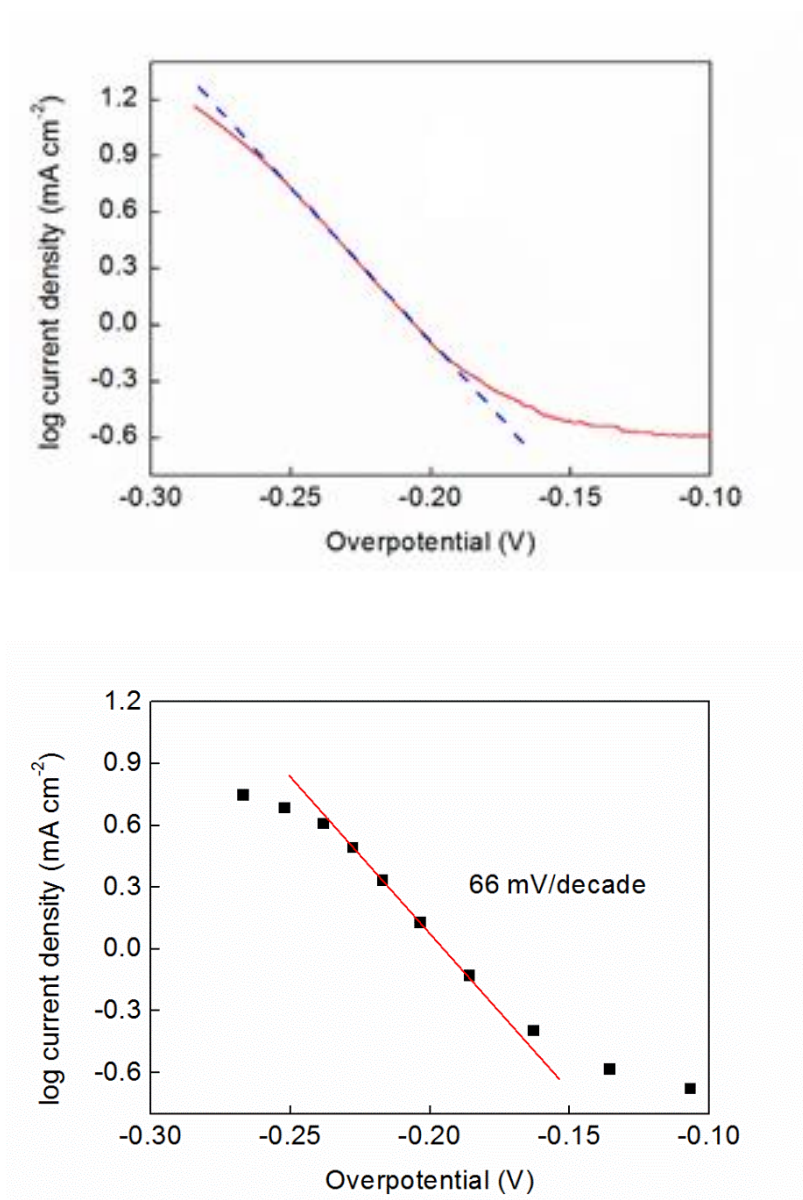


Figure 5.11 Top: A representative Tafel plot collected for a $\text{Co}_2\text{Mo}_9\text{S}_{26}$ film in $0.5 \text{ M H}_2\text{SO}_4$ by linear sweep voltammetry (see Section 5.5.4 for details). The blue dashed line is provided as a guide to the eye. **Bottom:** Tafel plot of a 300 nm-thick film collected as per the conditions stipulated in the Experimental Section whereby the current density was recorded after 5 min of electrolysis at each of the potentials denoted. A Tafel slope of 66 mV was obtained. Some delamination of the film was observed at overpotentials more negative than 250 mV in this case. In both panels, an Ag/AgCl reference electrode and carbon cloth counter electrode were used at room temperature. Overpotentials have been corrected for resistance.

5.3.2 Study of the performance of 150 nm thick films at low pH

Thinner (150 nm-thick films) evinced marginally poorer performance, requiring 300 mV overpotential to deliver a current density of 10 mA cm^{-2} , with a Tafel slope in the region of $85 \text{ mV decade}^{-1}$ (see Figure 5.12 and 5.13 respectively).

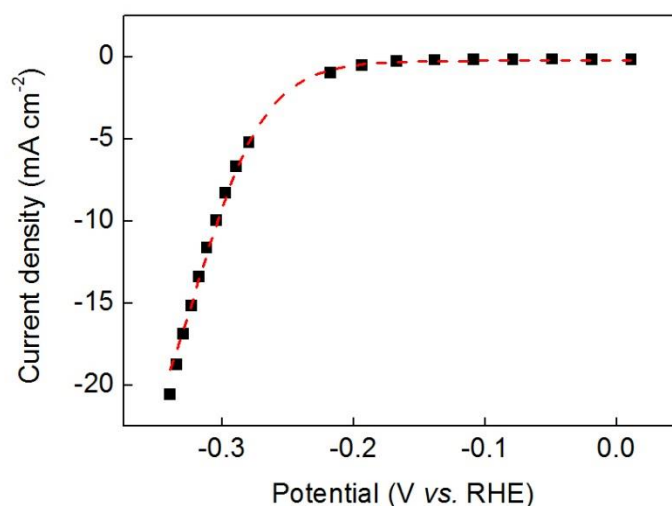


Figure 5.12 A representative trace showing the current density at pH 0 delivered by a 150 nm-thick $\text{Co}_2\text{Mo}_9\text{S}_{26}$ film. RE= Ag/AgCl, CE = carbon cloth. All current densities have been corrected for resistance. Black squares indicate steady-state current densities obtained after 5 min of polarization at the potentials indicated and the red dashed line is provided as a guide to the eye.

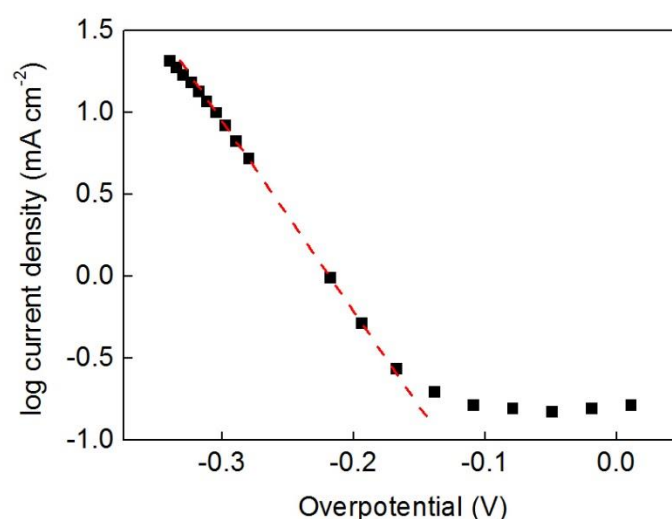


Figure 5.13 A representative Tafel plot collected for a 150 nm-thick $\text{Co}_2\text{Mo}_9\text{S}_{26}$ film in $0.5 \text{ M H}_2\text{SO}_4$ as per the conditions stipulated in the Experimental Section whereby the current density was recorded after 5 min of electrolysis at each of the potentials denoted (black squares). A Tafel slope of 85 mV was obtained (indicated by the red dashed line).

The fact that the 150 nm thick films show an activity $\sim 50\%$ that of the 300 nm ones may imply that this material is somehow permeable, with the active catalytic sites not limited just to the surface, so that upon lowering the catalyst mass loading to make a thinner film the overall activity decreases more or less proportionally to the decrease in mass loading, since the number of active catalytic sites has also diminished.

5.3.3 Study of the performance of 150 nm thick films at other pH

The performance of these films was also tested in 0.5 M sodium phosphate buffer (pH 7) and 1 M NaOH (pH 14). At pH 7, the films exhibited distinctly poorer performance compared to pH 0, achieving a current density of 1 mA cm^{-2} at $\sim 210 \text{ mV}$ overpotential, or 10 mA cm^{-2} at $\sim 460 \text{ mV}$ overpotential (see Figure 5.14). These films thus show similar performance at pH 7 to the electrodeposited Co-doped MoS_3 films reported by Hu and co-workers²⁰ on glassy carbon substrates (although we note that these authors do not report current densities higher than 1 mA cm^{-2} for their materials at this pH).

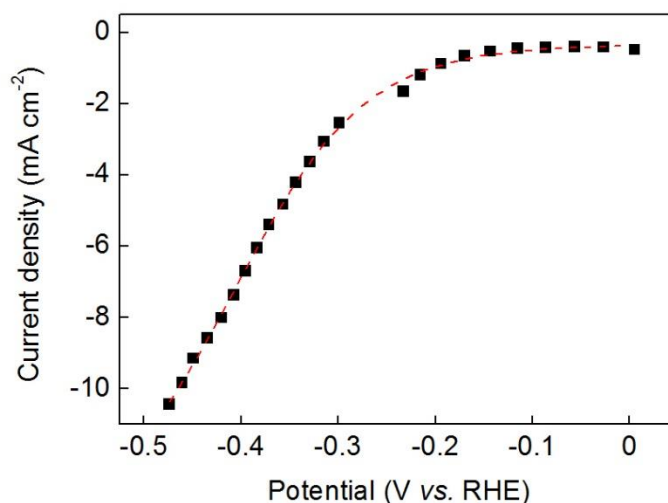


Figure 5.14 A representative trace showing the current density at pH 7 delivered by a 150 nm-thick $\text{Co}_2\text{Mo}_9\text{S}_{26}$ film prepared by the methods described in the main text on an FTO support. An Ag/AgCl reference electrode and carbon cloth counter electrode were used at room temperature. All current densities have been corrected for resistance. Black squares indicate steady-state current densities obtained after 5 min of polarization at the potentials indicated and the red dashed line is provided as a guide to the eye.

Meanwhile, the Tafel slope for our cathodes within the current density range -0.5 to -5 mA cm^{-2} was on the order 220 mV , as can be seen in Figure 5.15,

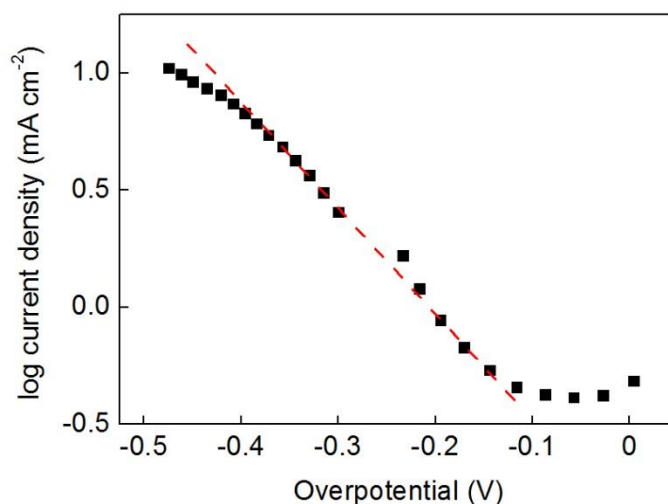


Figure 5.15 A representative Tafel plot collected for a 150 nm -thick $\text{Co}_2\text{Mo}_9\text{S}_{26}$ film in 0.5 M sodium phosphate buffer whereby the current density was recorded after 5 min of electrolysis at each of the potentials denoted (black squares). A Tafel slope of around 220 mV was obtained (indicated by the red dashed line).

At pH 14 on the other hand, our $\text{Co}_2\text{Mo}_9\text{S}_{26}$ -on-FTO cathodes exhibited very poor stability and the catalyst material was observed to exfoliate into solution rather rapidly during electrochemical analysis, precluding the collection of meaningful hydrogen evolution data.

A comparison of Tafel slope data and overpotential requirements to achieve a benchmark current density³⁷ of 10 mA cm^{-2} for a range of recently-reported metal-chalcogenide HER catalysts on FTO substrates is shown in Table 5.1. At pH 7, the mixed Co/Mo sulfides prepared on FTO by electrodeposition by Tran *et al.*²³ (Table 5.1, entry 1) exhibit significantly superior performance to our $\text{Co}_2\text{Mo}_9\text{S}_{26}$ -on-FTO materials at the same pH (see above). At pH 0, however, $\text{Co}_2\text{Mo}_9\text{S}_{26}$ -on-FTO achieves a current density for the hydrogen evolution reaction of 10 mA cm^{-2} at an overpotential that is essentially the same as that for the aforesaid electrodeposited catalyst at pH 7. Overall, these data suggest that the hydrothermal synthesis method

described herein is a viable route for the production of mixed Mo/Co chalcogenides directly on FTO substrates, producing materials that are competent hydrogen evolution electrocatalysts.

Table 5.1 Tafel slopes and overpotentials required to reach a benchmark current density of 10 mA cm⁻² for a selection recently reported metal-chalcogenide HER catalysts on FTO substrates.

Entry	Catalytic Material	pH	η at 10 mA cm ⁻² (mV)	Tafel slope ^a	Catalyst deposition method	Ref
1	CoMoS _x	7	250	85	Electrodeposition	23
2	Cu ₂ MoS ₄	0	300	95	Precipitation of simple salts	38
3	Cobalt sulfides	7	150	93	Electrodeposition	39
4	MoS ₂ on activated carbon	0	210 (5 mA cm ⁻²)	-	Electrodeposition	40
5	MoS ₂ on rGO ^b	13	250 (dark)	-	Solvothermal, then dip-coat	41 ^b
6	MoS ₂	0	230	50	Electrodeposition	35
7	Amorphous MoS ₃	0	170	-	Electrodeposition	36
8	Amorphous MoS ₂	0	200 (14 mA cm ⁻²)	40	Electrodeposition	42
9	MoS ₂ and MoS ₃ particles	0	220	50-60	Various, none hydrothermal	43
10	Mo ₂ S ₁₂	0	160	39	Drop casting	44
11	Co ₂ Mo ₉ S ₂₆	0	260	64	Direct Hydrothermal	This work

^aTafel slopes in mV/decade ^bSubstrate is FTO/reduced graphene oxide (FTO/rGO).

5.3.4 Gas analysis and stability

To confirm that the current density thus obtained with the $\text{Co}_2\text{Mo}_9\text{S}_{26}$ cathodes was due to the production of hydrogen, gas chromatography was performed on the headspace of sealed cells after extended time electrolysis, an example of which can be seen in Figure 5.16. This clearly indicated that hydrogen was the dominant reduction product, with a Faradaic yield of 89% ($\pm 6\%$).

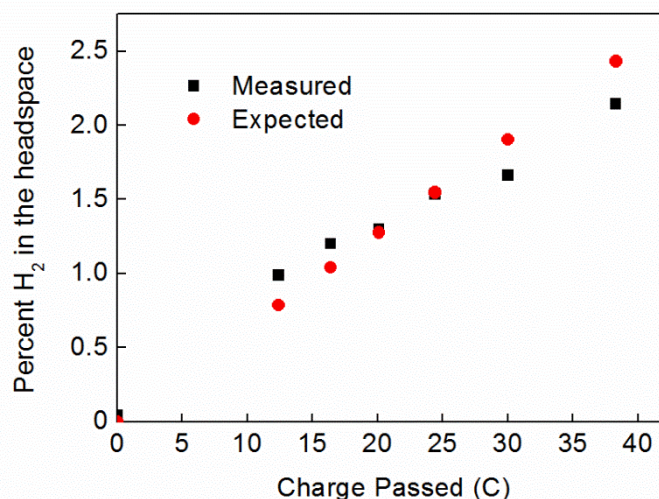


Figure 5.16 A representative trace showing gas chromatographic analysis of the headspace of airtight cells during electrolysis of a solution of 0.5 M sulfuric acid according to the general procedure given in the main text. An overpotential for proton reduction of 0.25 V was used. The red points indicate the % of hydrogen expected in the cell headspace based on the charge passed during electrolysis (38 C in this case). Black squares indicate actual measurements of the % of H_2 in the cell headspace as determined by gas chromatography.

These extended time electrolysis experiments also indicated that the activity of the films falls off somewhat over the course of several hours of polarisation at pH 0, as can be seen more clearly in Figure 5.17. In many cases, this drop-off in performance was accompanied by extensive bubble formation on the electrodes which acted to accelerate the cracking and exfoliation of the deposited material. Hence future studies will aim to improve the longevity of these catalysts by tuning film thicknesses (by, for example, adjusting the hydrothermal conditions and reaction times) and also by exploring the effect of additives as a means to deliver superior adhesion of the catalyst to the electrode.

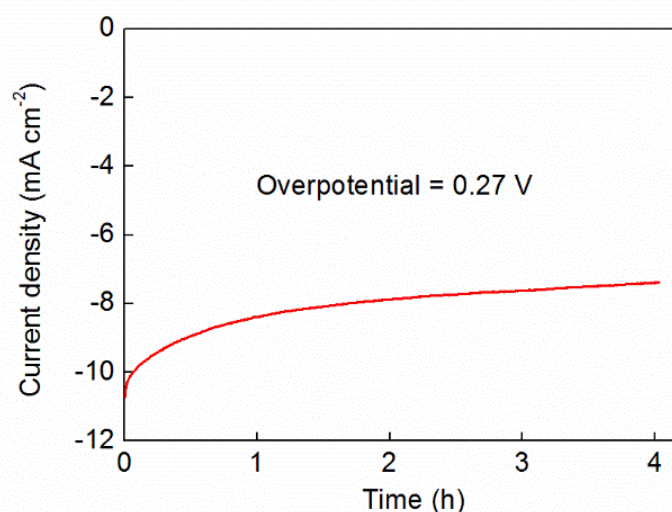


Figure 5.1 Controlled potential bulk electrolysis with stirring of a 300 nm-thick $\text{Co}_2\text{Mo}_9\text{S}_{26}$ film on an FTO support at a fixed, resistance-corrected overpotential for the hydrogen evolution reaction of 270 mV. A large surface area carbon felt was used as the counter electrode, and an Ag/AgCl (NaCl, 3 M) reference electrode (RE 5B, BASi) was used. The working electrode was washed with deionized water prior to use and had an area of 1.4 cm^2 .

5.4 Conclusions

In conclusion, we have developed a general synthetic procedure for the direct hydrothermal formation of cobalt-doped molybdenum sulfide on FTO, despite the fact that the FTO substrate is otherwise degraded under hydrothermal conditions in the absence of metal salts. Films of composition $\text{Co}_2\text{Mo}_9\text{S}_{26}$ were formed using this method, and the thicknesses of these films was tuned somewhat by varying the concentrations of the metal salts and thiourea in the hydrothermal deposition solution. These films were found to be good proton reduction electrocatalysts under cathodic bias in 0.5 M H_2SO_4 , generating hydrogen at a current density of 10 mA cm^{-2} at 260 mV overpotential and displaying a Tafel slope of $64 \text{ mV decade}^{-1}$. Some of the thinner films had substantial translucency, which (combined with their electrochemical performance) renders electrodes produced in this way potential candidates for solar-to-hydrogen applications.

5.5 Experimental section

5.5.1 Materials and reagents

$\text{CoSO}_4 \cdot 7\text{H}_2\text{O}$ (99 %) and $(\text{NH}_4)_6(\text{Mo}_7\text{O}_{24}) \cdot 4\text{H}_2\text{O}$ (99 %) were purchased from Sigma Aldrich while $\text{SC}(\text{NH}_2)_2$ (99 %) was supplied by Alfa Aesar. All chemical reagents and solvents were used as purchased. All electrolyte solutions were prepared with reagent grade water (18.2 M Ω -cm resistivity), obtained from a Sartorius Arium Comfort combined water system. pH determinations were made with a Hanna HI 9124 waterproof pH meter. UV-Vis spectra were collected in the solid state on a Shimadzu UV-2101PC spectrophotometer. Fluorine-doped tin oxide on glass (FTO) coated plain float electrodes (7 ohms per sheet) were purchased from Hartford Glass Co., Inc. All other materials were obtained as stated in the text. Experiments performed at “room temperature” were carried out at 20 °C.

5.5.2 Preparation of $\text{Co}_2\text{Mo}_9\text{S}_{26}$ -on-FTO

FTO substrates were prepared by being soaked for 10 minutes in a KOH/iso-propanol base bath, after which they were rinsed with a 1 M solution of HCl and a copious amount of distilled water. 300 nm-thick films of $\text{Co}_2\text{Mo}_9\text{S}_{26}$ -on-FTO were prepared by making a stock solution by mixing together 4.66 mL of an aqueous 50 mM solution of $\text{CoSO}_4 \cdot 7\text{H}_2\text{O}$, 28 mL of an aqueous 7.1 mM solution of $(\text{NH}_4)_6\text{Mo}_7\text{O}_{24} \cdot 4\text{H}_2\text{O}$, and 70 mL of an aqueous 50 mM solution of $\text{SC}(\text{NH}_2)_2$ with rigorous stirring (giving a Co:Mo:S ratio of 1:6:15). Hence this stock solution contained Co, Mo and S in the following overall concentrations: 2.3 mM Co, 13.6 mM Mo and 34.1 mM S. In a typical procedure, 15 mL of this stock solution was poured into a 20 mL Teflon liner, in which a $2.5 \times 1 \text{ cm}^2$ FTO substrate was placed with the conductive side facing down at an angle of *ca.* 45° angle. The Teflon liner was then sealed inside a stainless steel reaction vessel and heated at a rate of 1 °C min⁻¹ in a convection oven to 180 °C. After 72 h at this temperature, the vessel was cooled at a rate of 10 °C min⁻¹ to room temperature. The vessel was opened in air revealing a colourless solution with pH = *ca.* 8. The product was formed as a grey-black, translucent film on the conductive part of the substrate. The substrate with the film was washed with distilled water and dried in a desiccator over freshly regenerated silica gels at 100 °C. Subsequent annealing of these films at 300 °C under a stream of Ar did not produce any significant improvement in the electrochemical performance of these materials, and so all the results reported herein were obtained without any such annealing.

Thinner films (150 nm-thick) were prepared by the same method, except that the stock solution was prepared by mixing 4.66 mL of an aqueous 20 mM solution of $\text{CoSO}_4 \cdot 7\text{H}_2\text{O}$, 28 mL of an aqueous 2.9 mM solution of $(\text{NH}_4)_6\text{Mo}_7\text{O}_{24} \cdot 4\text{H}_2\text{O}$, and 70 mL of an aqueous 20 mM solution of $\text{SC}(\text{NH}_2)_2$ together with rigorous stirring (again giving a Co:Mo:S ratio of 1:6:15). 15 mL of this stock solution were then poured into a 20 mL Teflon liner containing an FTO substrate and heated as above.

5.5.3 Morphological and Compositional Characterisation

Raman spectroscopy was carried out with a wavelength of 532 nm on Horiba Jobin-Yvon LabRam Raman HR800. To prevent degradation of the sample, a 10 % filter and 200 mm hole was used. The focus on the surface of the sample was achieved using the controls, with the aid of a microscope with 10 \times and 50 \times magnification. Before the measurement the instrument was calibrated using a piece of Si as a standard. Powder X-ray diffraction (PXRD) measurements were performed using a Panalytical XPert-pro diffractometer ($\text{CuK}\alpha$ radiation corresponding to $\lambda = 1.54178 \text{ \AA}$ wavelength), operating in a Bragg-Bretano reflection geometry. SEM was performed in conjunction with EDX on a Philips XL30 ESEM with an attached Oxford Instruments x-act EDX detector. All the SEM pictures and the EDX analysis were recorded using a beam current of 20 kV. Initially, the SEM images were recorded by using the following magnifications: 20 \times , 100 \times , 800 \times and 4000 \times . The selected areas were then probed by EDX spectroscopy to obtain the elemental composition of the samples. Before running the EDX measurements a Cu foil standard was used for calibrating the measurements. XPS: As-prepared Co-doped molybdenum sulfide-on-FTO samples were carefully packed and sent to the National EPSRC XPS Users' Service (NEXUS) at Newcastle University, UK. XPS spectra were acquired with a K-Alpha instrument (Thermo Scientific, East Grinstead, UK), using a micro-focused monochromatic $\text{AlK}\alpha$ source (X-ray energy 1486.6 eV, spot size 400 x 800 microns). The emission angle was zero degrees and the pass energy was 200 eV for surveys and 40 eV for high resolution. Charge neutralization was enabled. The resulting spectra were referenced to the adventitious C 1s peak (285.0 eV) and were analyzed using the free-to-download CasaXPS software package. Atomic Force Microscopy (AFM) measurements were obtained using a Bruker Dimension Icon AFM. Film steps relative to the FTO substrate were measured over a scan area of 20 $\mu\text{m} \times 6.7 \mu\text{m}$. The step edges for AFM measurements were generated by electrolyzing films for extended time periods in 0.5 M H_2SO_4 according to the general

electrochemical methods described below until limited exfoliation of the catalyst material from the FTO substrate had occurred. The relative height of the non-exfoliated catalyst material compared to the bare substrate exposed by exfoliation was then measured. Three different areas were analysed per sample and the data reported are average values for the step sizes that were measured. The thicknesses of the films were measured to ± 50 nm thickness. For example, a step measurement on a 300 nm-thick film (taking a 4 μm cut each side of the step) gave a height of 270 nm. The film itself gave an average roughness of 26 nm, whilst for the substrate the roughness was 20 nm Ra.⁴⁵ Hence the roughness of the underlying FTO and the roughness of the deposit track reasonably closely. Errors associated with the AFM instrument itself were minimized by using a new tip for each measurement. Atomic absorption spectroscopy (AAS) was performed on a Perkin Elmer Aanalyst400 instrument as follows. To an accurate weight of material (carefully scraped from the FTO substrate) was added 5 mL of aqua regia and the sample was then boiled at 120 °C for 30 minutes, allowed to cool, and transferred to a 25 mL volumetric flask, rinsing all the glassware with deionized water. The samples were diluted to bring them into the linear range to be measured by AAS. A blank sample was also prepared using 5 mL of aqua regia. A series of standards were prepared in the range 0 – 5 mg L⁻¹ for cobalt and 0 – 50 mg L⁻¹ for molybdenum. The standards were prepared in water to match the diluted samples. Cobalt was measured at 240.7 nm using an air acetylene flame. Molybdenum was measured at 313.3 nm using a nitrous oxide/acetylene flame.

5.5.4 Electrochemical Methods

Electrochemical studies were performed in a three-electrode configuration (unless otherwise stated) using a CH Instruments CHI760D potentiostat in 0.5 M H₂SO₄, unless otherwise stated. A large surface area carbon felt (Alfa Aesar) was used as the counter electrode (unless otherwise stated), and an Ag/AgCl (NaCl, 3 M) reference electrode (RE 5B, BASi) was used. Working electrodes were washed with deionized water prior to use. Carbon felt counter electrodes were not re-used. Three-electrode potentials were converted to the NHE reference scale using $E(\text{NHE}) = E(\text{Ag}/\text{AgCl}) + 0.209$ V. The active area of all working electrodes was on the order of 1 cm².

Bulk electrolysis and linear sweep voltammetry: These were performed in a three-electrode configuration (unless otherwise stated) in single compartment electrochemical cells. Solutions were stirred, keeping the same stirring rate for all experiments. Where voltages have been corrected for ohmic resistances, the effective voltage ($V_{\text{effective}}$) has been calculated as stated in Section 3.5.2. Linear sweep voltammograms were recorded at a scan rate of 2 mV s^{-1} unless otherwise stated.

Tafel Plots: Tafel plots were obtained in single chamber cells with stirring according to the general methods described above. Plots were generally collected by linear sweep voltammetry at a scan rate of 2 mV s^{-1} , and the reported Tafel slopes are averages of several runs. Where specified, Tafel plots were also constructed by running bulk electrolyses at various potentials. In these cases, the current density was allowed to stabilize for 5 min at each potential before being recorded. The overpotentials reported have been corrected for resistive losses.

5.5.5 Headspace Hydrogen determination

Gas chromatography was conducted in airtight cells according to the general electrochemical procedure given above and using an Agilent Technologies 7890A GC system. During electrolysis, the solution was stirred and the headspace was sampled by gas-tight syringe (volume taken per sampling event = $50 \mu\text{L}$) and introduced onto the GC column by direct injection at various intervals. The column used was a 30 metre-long 0.320 mm widebore HP-molesieve column (Agilent). The GC oven temperature was set to $27 \text{ }^\circ\text{C}$ and the carrier gas was Ar. The front inlet was set to $100 \text{ }^\circ\text{C}$. The GC system was calibrated for H_2 using certified standards of hydrogen at a range of volume % in argon supplied by CK Gas Products Limited (UK). Linear fits of volume % vs. peak area were obtained, which allowed peak areas to be converted into volume % of H_2 in the cell headspace. Total system headspaces were calculated by filling the cells with water at room temperature. Charges passed were converted into expected volume percentages of hydrogen in the headspace by converting charges to an expected number of moles of gas (by dividing by $2F$ for H_2 , where F is the Faraday constant), and then taking the volume of 1 mole of an ideal gas at room temperature and pressure to be 24.5 L . Faradaic efficiencies were then calculated by taking the ratio of gas volume % based on the charge passed to the gas volume % measured by gas

chromatography. Faradaic efficiencies were based on the total amount of charge passed, uncorrected for any background or capacitance currents. All gas determinations were performed at least twice, and average Faradaic efficiencies are reported in the main text.

5.6 References

- (1) Chen, Y. Y.; Dong, M.; Wang, J.; Jiao, H. *J. Phys. Chem. C* **2012**, *116*, 25368.
- (2) Mortensen, P. M.; Grunwaldt, J.-D.; Jensen, P.A.; Knudsen, K.G.; Jensen, A. D. *Appl. Catal. A-Gen.* **2011**, *407*, 1.
- (3) Paul, J.-F. ; Cristol, S.; Payen, E. *Catal. Today* **2008**, *130*, 139.
- (4) Pumera, M.; Sofer, Z.; Ambrosi, A. *J. Mater. Chem. A* **2014**, *2*, 8981.
- (5) Min, Y.; Moon, G. D.; Kim, C.-E.; Lee, J.-H.; Yang, S.; Soon, A.; Jeong, U. *J. Mater. Chem. C* **2014**, *2*, 6222.
- (6) Roy, P.; Srivastava, S.K. *J. Mater. Chem. A* **2015**, *3*, 2454.
- (7) Bissett, M. A.; Worrall, S. D.; Kinloch, I. A.; Dryfe, R. A. W. *Electrochim. Acta* **2016**, *201*, 30.
- (8) Heine, T. *Acc. Chem. Res.* **2015**, *48*, 65.
- (9) Zhao, W.; Ribeiro, R. M.; Eda, G. *Acc. Chem. Res.* **2015**, *48*, 91.
- (10) Xu, X.; Yao, W.; Xiao, D.; Heinz, T. F. *Nature Phys.* **2014**, *10*, 343.
- (11) Lhuillier, E.; Pedetti, S.; Ithurria, S.; Nadal, B.; Heuclin, H.; Dubertret, B. *Acc. Chem. Res.* **2015**, *48*, 22.
- (12) Marks, T. J.; Hersam, M. C. *Nature* **2015**, *520*, 631.
- (13) Koppens, F. H. L.; Mueller, T.; Avouris, Ph.; Ferrari, A. C.; Vitiello, M. S.; Polini, M. *Nat. Nanotechnol.* **2014**, *9*, 780.
- (14) Buscema, M.; Island, J. O.; Groenendijk, D. J.; Blanter, S. I.; Steele, G. A.; van der Zant, H. S. J.; Castellanos-Gomez, A. *Chem. Soc. Rev.* **2015**, *44*, 3691.
- (15) For recent reviews of this topic, see: Laursen, A. B.; Kegnæs, S.; Dahl, S.; Chorkendorff, I. *Energy Environ. Sci.* **2012**, *5*, 5577; Yan, Y.; Xia, B.; Xu, Z.; Wang, X. *ACS Catal.* **2014**, *4*, 1693; Benck, J. D.; Hellstern, T. R.; Kibsgaard, J.; Chakthranont, P.; Jaramillo, T. F.; *ACS Catal.* **2014**, *4*, 3957; Yang, J.; Shin, H. S. *J. Mater. Chem. A* **2014**, *2*, 5979; Lu, Q.; Yu, Y.; Ma, Q.; Chen, B.; Zhang, H. *Adv. Mater.* **2016**, *28*, 1917; Voiry, D.; Yang, J.; Chhowalla, M. *Adv. Mater.* **2016**, *28*, 6197; Faber, M. S.; Jin, S. *Energy Environ. Sci.* **2014** *7*, 3519; Zeng, M.; Li, Y. *J.*

- Mater. Chem. A* **2015**, *3*, 14942; Benck, J. D.; Chen, Z.; Kuritzky, L. Y.; Forman, A. J.; Jaramillo, T. F. *ACS Catal.* **2012**, *2*, 1916; Lukowski, M. A.; Daniel, A. S.; Meng, F.; Forticaux, A.; Li, L.; Jin, S. *J. Am. Chem. Soc.* **2013**, *135*, 10274.
- (16) Jaramillo, T. F.; Jørgensen, K. P.; Bonde, J.; Nielsen, J. H.; Horch, S.; Chorkendorff, I. *Science* **2007**, *317*, 100.
- (17) Nørskov, J. K.; Bligaard, T.; Rossmeisl, J.; Christensen, C. H. *Nature Chem.* **2009**, *1*, 37.
- (18) Bonde, J.; Moses, P. G.; Jaramillo, T. F.; Nørskov, J. K.; Chorkendorff, I. *Faraday Discuss.* **2008**, *140*, 219.
- (19) Zhang, J.; Wang, T.; Liu, P.; Liu, S.; Dong, R.; Zhuang, X.; Chen, M.; Feng, X. *Energy Environ. Sci.* **2016**, *9*, 2789.
- (20) Merki, D.; Vrubel, H.; Rovelli, L.; Fierro, S.; Hu, X. *Chem. Sci.* **2012**, *3*, 2515.
- (21) Staszak-Jirkovský, J.; Malliakas, C. D.; Lopes, P. P.; Danilovic, N.; Kota, S. S.; Chang, K.-C.; Genorio, B.; Strmcnik, D.; Stamenkovic, V. R.; Kanatzidis, M. G.; Markovic, N. M. *Nat. Mater.* **2016**, *15*, 197.
- (22) Zhang, H.; Li, Y.; Xu, T.; Wang, J.; Huo, Z.; Wan, P.; Sun, X. *J. Mater. Chem. A* **2015**, *3*, 15020.
- (23) Tran, P. D.; Chiam, S. Y.; Boix, P. P.; Ren, Y.; Pramana, S. S.; Fize, J.; Artero, V.; Barber, J. *Energy Environ. Sci.* **2013**, *6*, 2452.
- (24) Zhu, H.; Zhang, J.; Yanzhang, R.; Du, M.; Wang, Q.; Gao, G.; Wu, J.; Wu, G.; Zhang, M.; Liu, B.; Yao, J.; Zhang, X. *Adv. Mater.* **2015**, *27*, 4752.
- (25) Xie, J.; Zhang, H.; Li, S.; Wang, R.; Sun, X.; Zhou, M.; Zhou, J.; Lou, X. W.; Xie, Y. *Adv. Mater.* **2013**, *25*, 5807.
- (26) Yan, Y.; Xia, B.; Ge, X.; Liu, Z.; Wang, J.-Y.; Wang, X. *ACS Appl. Mater. Interfaces* **2013**, *5*, 12794.
- (27) Deng, J.; Li, H.; Xiao, J.; Tu, Y.; Deng, D.; Yang, H.; Tian, H.; Li, J.; Ren, P.; Bao, X. *Energy Environ. Sci.* **2015**, *8*, 1594.
- (28) Bian, X.; Zhu, J.; Liao, L.; Scanlon, M. D.; Ge, P.; Ji, C.; Girault, H. H.; Liu, B. *Electrochem. Commun.* **2012**, *22*, 128.
- (29) Xie, J.; Zhang, J.; Li, S.; Grote, F.; Zhang, X.; Zhang, H.; Wang, R.; Lei, Y.; Pan, B.; Xie, Y. *J. Am. Chem. Soc.* **2013**, *135*, 17881.
- (30) Tang, Y.-J.; Gao, M.-R.; Liu, C.-H.; Li, S.-L.; Jiang, H.-L.; Lan, Y.-Q.; Han, M.; Yu, S.-H. *Angew. Chem. Int. Ed.* **2015**, *54*, 12928.

- (31) Diamond - Crystal and Molecular Structure Visualization, Crystal Impact, H. Putz and K. Brandenburg GbR, Kreuzherrenstr. 102, 53227 Bonn, Germany
<http://www.crystalimpact.com/diamond> (accessed June 2016).
- (32) Payen, E.; Kasztelan, S.; Houssenbay, S.; Szymanski, R.; Grimblot, J. *J. Phys. Chem.* **1989**, *93*, 6501.
- (33) Anastassakis, E.; Perry, C. H. *J. Chem. Phys.* **1976**, *64*, 3604.
- (34) Li, H.; Zhang, Q.; Yap, C. C. R.; Tay, B. K.; Edwin, T. H. T.; Olivier, A.; Baillargeat, D. *Adv. Funct. Mater.* **2012**, *22*, 1385.
- (35) Kibsgaard, J.; Chen, Z.; Reinecke, B. N.; Jaramillo, T. F. *Nat. Mater.* **2012**, *11*, 963.
- (36) Vrubel, H.; Hu, X. *ACS Catal.* **2013**, *3*, 2002.
- (37) McCrory, C. C. L.; Jung, S.; Ferrer, I. M.; Chatman, S. M.; Peters, J. C.; Jaramillo, T. F. *J. Am. Chem. Soc.* **2015**, *137*, 4347.
- (38) Tran, P. D.; Nguyen, M.; Pramana, S. S.; Bhattacharjee, A.; Chiam, S. Y.; Fize, J.; Field, M. J.; Artero, V.; Wong, L. H.; Loo, J.; Barber, J. *Energy Environ. Sci.* **2012**, *5*, 8912.
- (39) Sun, Y.; Liu, C.; Grauer, D. C.; Yano, J.; Long, J. R.; Yang, P.; Chang, C. J. *J. Am. Chem. Soc.* **2013**, *135*, 17699.
- (40) Laursen, A. B.; Vesborg, P. C. K.; Chorkendorff, I. *Chem. Commun.* **2013**, *49*, 4965.
- (41) Meng, F.; Li, J.; Cushing, S. K.; Zhi, M.; Wu, N. *J. Am. Chem. Soc.* **2013**, *135*, 10286.
- (42) Merki, D.; Fierro, S.; Vrubel, H.; Hu, X. *Chem. Sci.* **2011**, *2*, 1262.
- (43) Vrubel, H.; Merki, D.; Hu, X. *Energy Environ. Sci.* **2012**, *5*, 6136.
- (44) Huang, Z.; Luo, W.; Ma, L.; Yu, M.; Ren, X.; He, M.; Polen, S.; Click, K.; Garrett, B.; Lu, J.; Amine, K.; Hadad, C.; Chen, W.; Asthagiri, A.; Wu, Y. *Angew. Chem. Int. Ed.* **2015**, *54*, 15181.
- (45) Leach, R. K. *Good Practice Guide No. 37: The Measurement of Surface Texture using Stylus Instruments*. National Physical Laboratory Publications (UK),
http://publications.npl.co.uk/npl_web/pdf/mgpg37.pdf (accessed September, 2016).

CONCLUSIONS AND FUTURE WORK

The work detailed in this thesis has covered a detailed study on the effect of metal impurities in the oxygen and the hydrogen evolution half-reactions on the one hand and the electrochemical testing of Co-doped MoS₂ films which were deposited on FTO by direct hydrothermal synthesis on the other. We have shown that nickel impurities in trace levels coming from the salts used to prepare the buffers can act as a water oxidation catalyst in mildly basic aqueous solutions, achieving stable (tens of hours) current densities of 1 mA cm⁻² at overpotentials as low as 540 mV at pH 9.2 and 400 mV at pH 13. The importance of this finding lies in the fact that these values of overpotential are at the same level as many recently reported catalysts tested for the water oxidation reaction in similar conditions, which makes us think that in some of these cases the activity may be due mostly to trace nickel and not to the materials reported as WOCs. In this sense, basically all reports proposing copper oxides as water oxidation catalysts are quite suspicious, in particular the work performed by Du *et al.*¹ and that of Sun *et al.*². We have seen in Chapter 1 how the discovery and improvement of water oxidation catalysts that work at near neutral pH is crucial for the development of solar-to-fuels devices, and how so far only nickel and cobalt oxides have shown promising results at this pH. As a result, many efforts are being directed to the study of other materials to serve as WOCs at mild pH, including Mn, Cu and Fe oxides, but also other transition metal oxides and other kinds of materials such as polyoxometalates. The novelty of these studies often results in their publication with overpotentials to get 1 mA cm⁻² at the same level or even higher than the baselines we have traced in Chapter 3. Now that we have seen the extent to which trace nickel can catalyze water oxidation, it is important to be able to exclude them as the cause of any observed water oxidation activity when reporting new materials, otherwise this could lead researchers to dedicate time and effort to materials that do not have any activity for this reaction, and to propose wrong theories about the kind of materials and structures that can catalyze water oxidation. In summary, any new materials proposed as water oxidation catalysts need to be able to surpass the baselines we have set and/or prove to have been tested in buffers exempt of trace nickel.

The effect of silver leaking from Ag/AgCl reference electrodes for the HER is not as striking as that of the nickel impurities for the OER due to the fact that the baseline we set in this second case is easily surpassed by most HECs, as seen in Table 1.1 and Chapter 5. However, this is still an important work because once again it shows the

lack of rigor in the field when studying new materials as water reduction and water oxidation catalysts. We are not claiming to have discovered that silver ions can leak from Ag/AgCl reference electrodes, or that silver can catalyze the HER; both have already been reported. One may even find it mentioned in some old electrochemistry textbooks or elsewhere that Ag/AgCl reference electrodes should not be used at low pH, and while no specifications as to the suitability of these electrodes for any pH range can be found in either the documents that come with commercial reference electrodes or at the suppliers' websites, direct enquiries to them are answered with the recommendation not to use them outside the pH range 3 to 10. And yet, as we have shown in Section 4.1, many researchers routinely use these reference electrodes in aqueous buffers at low pH. This can only mean that we are talking of something that is either not common knowledge in the HER electrocatalysis community, or else is widely ignored. As a consequence, the potential for silver from the reference electrode to interfere in electrocatalytic reactions (and in the HER in particular) is very real. We have shown how easy it is to make new reference electrodes leak at room temperature experiments after using them for just a few hours at 40 °C. That is not such a high temperature, and these electrodes are meant to be used up to 100 °C. This work therefore serves to call for more rigor in any electrochemical work, and we offer guidelines as to how to achieve this and how to exclude silver impurities from being responsible for any activity observed for the HER.

Together, Chapters 3 and 4 have addressed the important yet neglected topic of interferences and impurities in electrochemical measurements, and in particular in the two water splitting half-reactions. Future work could be addressed to the study of the effect of silver leaking from Ag/AgCl reference electrodes at higher pH, since silver oxides have been shown to catalyze the OER at pH 9.2,³ close to the 10 – 11 upper limit of the pH range in which these electrodes are not recommended to be used.

In Chapter 5 we have addressed another topic that is also sometimes overlooked, which is the need to focus on electrocatalysts whose preparation can be easily scaled up to large surface areas, suitable for mass production. In this sense, a direct hydrothermal method to grow MoS₂ films onto transparent conductive substrates is a useful advance. However, as mentioned at the end of this chapter, the Co-doped MoS₂ prepared in this way had stability problems, so future work will be aimed to optimize

the conditions used in the hydrothermal synthesis and/or the addition of additives to prevent the exfoliation of the catalyst from the FTO.

A lot of work needs to be done in the field in order for solar-to-hydrogen devices in any of the architectures discussed in Chapter 1 to become a reality. Over the last two decades many electrocatalysts for the HER and the OER based on Earth-abundant elements have been reported, yet as we have seen in Chapter 1 they are neither ready to substitute precious metal-based catalysts in PEMEs nor to be integrated in photoelectrochemical devices. But not only electrocatalysts need to be improved; at present the low efficiencies and stability issues of light harvesting materials constitute a heavy anchor that prevents photoelectrochemical devices from reaching higher solar-to-hydrogen efficiencies. One only has to look at the papers describing the solar-to-hydrogen devices discussed in Section 1.6 to see that the component that is both lowering the overall efficiency and accounting for the device's high cost is the semiconductor material. If we intend solar-to-hydrogen devices to be the key to increase the use of solar energy in total energy production there is need to lower both the cost of the materials and increase their efficiency (and to start testing photoelectrochemical devices bigger than 1 cm²!). Or otherwise the public will keep thinking only of batteries neglecting such a promising energy storage system as is photoelectrochemical water splitting. May the work discussed in this thesis serve to some extent to help in the solar fuels field, so that one day, hopefully sometime soon, these devices are ready to be implemented in our lives.

References

- (1) Liu, X.; Jia, H.; Sun, Z.; Chen, H.; Xu, P.; Du, P. *Electrochem. Commun.* **2014**, *46*, 1.
- (2) Yu, F.; Li, F.; Zhang, B.; Li, H.; Sun, L. *ACS Catal.* **2015**, *5*, 627
- (3) Wang, W.; Zhao, Q.; Dong, J.; Li, J. *Int. J. Hydrogen Energ.* **2011**, *36*, 7374